

2011

Search for Effects Beyond the Born Approximation in Polarization Transfer Observables in ep Elastic Scattering

Mehdi Meziane

College of William & Mary - Arts & Sciences

Follow this and additional works at: <https://scholarworks.wm.edu/etd>



Part of the [Physics Commons](#)

Recommended Citation

Meziane, Mehdi, "Search for Effects Beyond the Born Approximation in Polarization Transfer Observables in ep Elastic Scattering" (2011). *Dissertations, Theses, and Masters Projects*. Paper 1539623582.

<https://dx.doi.org/doi:10.21220/s2-vseh-k159>

This Dissertation is brought to you for free and open access by the Theses, Dissertations, & Master Projects at W&M ScholarWorks. It has been accepted for inclusion in Dissertations, Theses, and Masters Projects by an authorized administrator of W&M ScholarWorks. For more information, please contact scholarworks@wm.edu.

Search for Effects Beyond the Born Approximation
in Polarization Transfer Observables in $\vec{e}p$ Elastic Scattering

Mehdi Meziane

Metz, Moselle, France

B.S. Physics, Université de Metz, 2004

M.S. Physics, Université Joseph Fourier, 2006

M.S. Physics, College of William and Mary, 2007

A Dissertation presented to the Graduate Faculty
of the College of William and Mary in Candidacy for the Degree of
Doctor of Philosophy

Department of Physics

The College of William and Mary
May, 2011

COPYRIGHT PAGE

©2011, Mehdi Meziane
All Right Reserved

APPROVAL PAGE

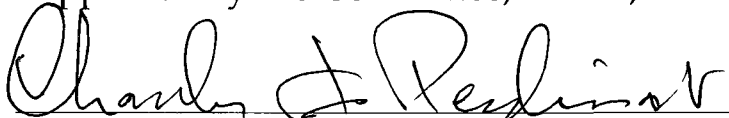
This Dissertation is submitted in partial fulfillment of
the requirements for the degree of

Doctor of Philosophy



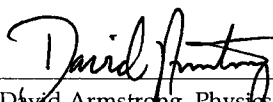
Mehdi Meziane

Approved by the Committee, March, 2011



Committee Chair

Professor Charles F. Perdrisat, Physics, The College of William and Mary



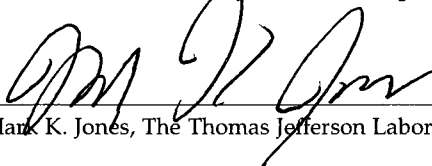
Professor David Armstrong, Physics, The College of William and Mary



Professor Todd Averett, Physics, The College of William and Mary



Associate Professor Joshua E. Erlich, Physics, The College of William and Mary



Mark K. Jones, The Thomas Jefferson Laboratory

ABSTRACT PAGE

Intensive theoretical and experimental efforts over the past decade have aimed at explaining the discrepancy between data for the proton electric to magnetic form factor ratio, G_E/G_M , obtained separately from cross section and polarization transfer measurements. One possible explanation for this difference is a two-photon-exchange (TPEX) contribution. In an effort to search for effects beyond the one-photon-exchange or Born approximation, this thesis reports measurements, of the GEp2 γ experiment, of polarization transfer observables in the elastic $H(\vec{e}, e' \vec{p})$ reaction for three different beam energies at a fixed squared momentum transfer $Q^2 = 2.5 \text{ GeV}^2$, spanning a wide range of the virtual photon polarization parameter, ϵ . The scattered electrons were detected in coincidence with the protons by the new electromagnetic lead-glass calorimeter BigCal and the High Momentum Spectrometer (HMS), respectively. We extract the polarization of the recoil proton by measuring the azimuthal asymmetry in the angular distribution after a secondary scattering in the CH₂ analyzer blocks of the new, double focal plane polarimeter (FPP) installed in the detector hut of the HMS.

Contents

List of Tables	iv
List of Figures	v
Acknowledgements	viii
Prolegomenon	1
1 Beyond the Born Approximation: Generalized Form Factors and Two Photon Exchange	4
1.1 Second-order electron-proton scattering	4
1.2 Generalized Form Factors	9
1.3 Unpolarized cross section and polarization components	12
1.3.1 Breit Frame kinematics	12
1.3.2 Leptonic and hadronic tensors	15
1.3.3 Unpolarized cross section	23
1.3.4 Transferred polarization components	25
1.3.5 Single-spin observables	34
2 Theoretical Models	36
2.1 Partonic Model	36
2.1.1 General Parton Distributions (GPD) Formalism	36
2.1.2 Results	40
2.2 Hadronic Model	43
2.2.1 Formalism	43
2.2.2 Unpolarized Cross Section and Form Factor Ratio Results	45
2.2.3 Polarized electron-proton scattering results	47
2.2.4 Excited Intermediate States	50
2.3 Perturbative Quantum Chromodynamic Calculations	51
2.4 Structure Function Calculation	56
3 Experimental Apparatus	58
3.1 The continuous Electron Beam Accelerator	58
3.1.1 Polarized electron source	59
3.1.2 Beam energy Measurement	62
3.1.3 Beam current Measurement	63
3.1.4 Beam position Measurement	63
3.1.5 Polarization Measurement	64

3.2	The Hall-C cryogenic target	65
3.3	The detector package	67
3.3.1	High Momentum Spectrometer (HMS)	68
3.3.2	Focal Plane Polarimeter (FPP)	74
3.3.3	Electromagnetic Calorimeter (BigCal)	79
3.4	Electronics and Trigger Set-up	82
3.4.1	BigCal trigger	83
3.4.2	HMS trigger	84
3.4.3	Main coincidence trigger	84
4	Data Analysis Part One: Tracking, Reconstruction and Event Selection	86
4.1	Kinematics	86
4.2	HMS Hodoscope Calibration	91
4.3	HMS Tracking and Reconstruction	92
4.3.1	HMS Tracking Algorithm	92
4.3.2	HMS Transport Matrix (Optics)	96
4.4	FPP Tracking and Reconstruction	101
4.4.1	FPP tracking algorithm	102
4.4.2	Left-Right Ambiguities	105
4.4.3	FPP Alignment	106
4.4.4	Track Multiplicity	106
4.4.5	Scattering Quantities	109
4.4.6	BigCal Reconstruction	112
4.5	Elastic Events Selection	114
4.5.1	Source of Inelastic Background	116
5	Data Analysis Part Two: Focal Plane Asymmetries, Spin Precession and Polarization	
	Observables Extraction	118
5.1	Angular Distributions and Asymmetries	118
5.2	Spin Precession	122
5.2.1	Dipole Model	122
5.2.2	Geometric Model	123
5.2.3	COSY Model	124
5.3	Maximum Likelihood Method	127
5.4	False Asymmetries	130
5.5	CH ₂ Analyzing power at $p_0 = 2.0676$ GeV/c	132
6	Results	137
6.1	Matching Acceptance Cut	137
6.2	Z_{close} Dependence of A_y and R	139
6.3	Final Cuts	140
6.4	False Asymmetry Correction	143
6.5	Radiative Corrections	143
6.6	Polarization Component Ratio Results	145
6.7	Longitudinal Component Polarization Results	145
6.8	Systematic Uncertainties	147
6.9	Summary and Discussion of the Results	151
6.10	Empirical Determination of the TPEX amplitudes.	159

Epilogue	162
A Dirac Matrices, Dirac Equation and Trace Identities	164
A.1 Dirac Formalism	164
A.2 Dirac Equation	166
A.3 Useful Trace theorems	168
B Unpolarized cross section calculation using the trace technique	169
B.1 General definitions	169
B.2 Trace calculation	171
B.3 Kinematic identities	172
B.4 Leptonic-hadronic tensor contraction	173
B.5 Unpolarized cross Section	177
C FPP Scattering Quantities Reconstruction	179
C.1 Tracks Equations	179
C.2 z-coordinate z_{close} of the point of closest approach	180
C.3 Distance of closest approach s_{close}	181
C.4 Polar scattering angle ϑ_{FPP}	181
C.5 Azimuthal scattering angle φ_{FPP}	181
C.6 Cone-test	182
Bibliography	185

List of Tables

3.1	Beam energy measurements performed during the GE _p -2 γ .	63
3.2	Properties of the HMS quadrupole system.	69
3.3	Parameters of the HMS dipole.	69
3.4	Performance of the HMS.	70
3.5	Characteristics of the wires used in the FPP drift chambers.	78
3.6	Main characteristics of the TF0-1 glass.	81
4.1	Kinematic Table of the GE2 γ experiment, with E_e the beam electron energy, E'_e the scattered elastic electron energy, p_p the proton momentum, θ_e the electron scattering angle and θ_p the scattered proton angle.	87
4.2	Jacobian and BigCal-target distance of the GE _p 2 γ experiment.	90
4.3	Thin multi-foil targets used during the dedicated optics runs.	96
4.4	Detail of the track multiplicity of the FPP at $Q^2 = 2.5 \text{ GeV}^2$ and $\epsilon = 0.152$.	107
4.5	Fit results of the fraction of single and multiple track events for both FPPs and for the three kinematics.	109
5.1	Fit results of helicity difference distribution in the focal plane.	121
5.2	Central precession angle χ_θ for the HMS at $Q^2 = 2.5 \text{ GeV}^2$.	123
5.3	False asymmetry ϑ_{FPP} bins.	132
6.1	Average Q^2 with and without the FP cut.	138
6.2	Ratio of the average proton momenta with and without matching acceptance cuts.	139
6.3	Elastic event selection cuts used in the final analysis.	142
6.4	Shift ΔR in R induced by the false asymmetries.	143
6.5	Shift ΔP_ℓ in the longitudinal polarization component P_ℓ induced by the false asymmetries.	143
6.6	Radiative corrections to R obtained from the program MASCARAD.	145
6.7	Results for R corrected for the false asymmetries with and without the FP cut.	145
6.8	P_ℓ/P_ℓ^{Born} results corrected for the false asymmetries with and without the z_{close} cut.	147
6.9	Offsets applied in θ_{bend} , ϕ_{bend} , E_{beam} , δ and φ_{FPP} in the determination of the systematic uncertainties.	149
6.10	Absolute systematic uncertainties in R .	149
6.11	Absolute systematic uncertainties in P_ℓ/P_ℓ^{Born} .	150
6.12	Point-to-point systematic uncertainties for R relative to the highest $\epsilon = 0.785$ point.	150
6.13	Point-to-point systematic uncertainties for P_ℓ/P_ℓ^{Born} relative to the smallest $\epsilon = 0.152$ point.	150
6.14	Ratio R and P_ℓ/P_ℓ^{Born} final results.	151

List of Figures

1	Discrepancy between the polarization transfer and Rosenbluth results of the proton form factor ratio.	2
1.1	Direct box diagram and Crossed box diagram.	6
1.2	Box diagram and Cross diagram.	9
1.3	Elastic scattering in the Breit frame	13
2.1	Handbag diagram.	37
2.2	Two-photon exchange diagram to the electron-quark scattering.	38
2.3	Scaled cross section prediction based on a GPD calculation from A. Afanasev <i>et al.</i>	41
2.4	Rosenbluth and polarization data with two-photon exchange correction based on a GPD calculation from A. Afanasev <i>et al.</i>	42
2.5	Ratio of the longitudinal polarization component P_ℓ relative to the Born Approximation value versus ϵ	43
2.6	Two-photon exchange corrections to the scaled reduced cross section obtained from the hadronic model of P.G. Blunden <i>et al.</i>	46
2.7	Two-photon exchange corrections to the form factor ratio measured using the Rosenbluth separation technique based on the hadronic model of P.G. Blunden <i>et al.</i>	46
2.8	Ratio of the longitudinal and transverse cross section relative to the Born unpolarized cross section based on the hadronic model of P.G. Blunden <i>et al.</i>	48
2.9	Proton form factor ratio from polarization data with and without the two-photon exchange corrections using the hadronic model of P.G. Blunden <i>et al.</i>	49
2.10	Two-photon exchange correction to the real part of \tilde{G}_M , \tilde{G}_M and $Y_{2\gamma}$ amplitudes at $Q^2 = 1, 3$ and 6 GeV^2 using the hadronic model of P.G. Blunden <i>et al.</i>	50
2.11	Nucleon and Δ contributions to the two-photon exchange correction to the cross section using the model of S. Kondratyuk <i>et al.</i>	51
2.12	Diagram for the elastic ep scattering with two hard photon exchanges.	52
2.13	Two-photon exchange amplitude $\delta\tilde{G}_M/G_M$ versus ϵ at $Q^2 = 10 \text{ GeV}^2$ in the pQCD model of D. Borisyuk and A. Kobushkin.	54
2.14	Two-photon exchange amplitude $\delta\tilde{G}_M/G_M$ versus Q^2 at $\epsilon = 0.5$ and $\epsilon = 0.1$ using the pQCD model of D. Borisyuk and A.Kobushkin.	54
2.15	Proton form factor ratio as a function of ϵ at $Q^2 = 2.5 \text{ GeV}^2$ based on proton distribution amplitudes models COZ and BLW.	55
2.16	ϵ -dependence of the ratio of the unpolarized and polarized cross section at $Q^2 = 1, 3$ and 5 GeV^2 using the structure function method of Bystritskiy <i>et al.</i>	56
2.17	Q^2 dependence of the polarization component ratio and of the proton form factor ratio using the structure function model of Bystritskiy <i>et al.</i>	57

3.1	Cartoon of the CEBAF accelerator.	59
3.2	GaAs band structure and energy levels.	60
3.3	Layout of the Hall C Möller polarimeter.	66
3.4	Beam raster pattern during the E04-109 experiment.	67
3.5	Layout of the Jlab HallC during the E04-109 experiment.	68
3.6	Side view of the HMS.	69
3.7	Side view of the standard HMS detector package.	71
3.8	Schematic of the HMS drift chambers.	72
3.9	Schematic of a polarized proton scattering off an CH_2 analyzer nucleus.	75
3.10	Evolution of $r - \vec{P} $ vs φ	76
3.11	Schematic of an elementary cell of the FPP drift chambers. The dimensions are not to scale.	79
3.12	Design drawing of the FPP with the HMS drift chambers and the trigger planes.	80
3.13	The 1744 lead-glass bars of BigCal ordered in several groups (in colors) for the trigger.	81
3.14	Schematic of the HMS trigger.	84
3.15	Schematic of the main coincidence trigger.	85
4.1	Coordinate systems used during the GEp2 γ experiment.	88
4.2	HMS drift time and HMS drift distance distribution.	93
4.3	Flow chart of the HMS tracking and reconstruction algorithm.	95
4.4	Schematic of the thin foil target and sieve slit collimator system.	97
4.6	Difference y'_{diff} between the known angles y'_{foil} and the reconstructed angles y'_{rec} versus y'_{foil} for the 3 foil-Aluminum target and 2 foil-Carbon target.	99
4.7	Difference y_{diff} between the known coordinate y_{foil} and the reconstructed coordinate y_{rec} versus y_{foil} for the 3 foil-Aluminum target 2 foil-Carbon target.	100
4.8	Difference in term of fraction of central momentum p_0 , between the reconstructed momentum and the proton momentum from the proton angle as a function of the focal plane coordinates x_{fp} , y_{fp} and angles x'_{fp} , y'_{fp}	101
4.9	FPP drift time and FPP drift distance distribution.	102
4.10	Flow chart of the FPP tracking and reconstruction algorithm.	104
4.11	Diagram showing the left-right ambiguity in the vicinity of the chamber center.	105
4.12	Fraction of the single and multiple track events as a function of the run number for the three kinematics for FPP ₁ and FPP ₂	108
4.13	z_{close} versus ϑ_{FPP} distribution for both FPPs.	109
4.14	Scattering angle ϑ_{FPP} distributions for both FPPs.	110
4.15	Distance of closest approach s_{close} distributions for both FPPs.	110
4.16	p_{miss}^p distributions for $Q^2 = 2.5 \text{ GeV}^2$ at $\epsilon=0.152, 0.635$ and 0.785 without any cuts	114
4.17	Δ_y versus Δ_x at $Q^2 = 2.5 \text{ GeV}^2$ and $\epsilon = 0.152$	115
4.18	p_{miss}^p distributions for $Q^2 = 2.5 \text{ GeV}^2$ at $\epsilon=0.152, 0.635$ and 0.785 after the elliptical cut.	116
5.1	Helicity difference distribution in the focal plane $f^+ - f^-$ for $\epsilon = 0.152, 0.635, 0.773$ and 0.791 and for $1.7^\circ \leq \vartheta \leq 38^\circ$	120
5.2	Helicity sum distribution in the focal plane $f^+ + f^-$ for $\epsilon = 0.152, 0.635, 0.773$ and 0.791 and for $1.7^\circ \leq \vartheta \leq 38^\circ$	122
5.3	Analyzing power distribution as a function of the transverse momentum p_T at $Q^2 = 2.5 \text{ GeV}^2$ for all single and multi-track events and all (single + multi).	134

5.4	Momentum corrected for energy loss p_{corr} as a function of z_{close} for FPP ₁ and FPP ₂	135
5.5	CH ₂ Analyzing power versus $1/p$.	136
6.1	x_{fp} versus y_{fp} distribution showing the matching acceptance cut.	138
6.2	\bar{A}_y versus z_{close} for FPP ₁ and FPP ₂ .	139
6.3	R versus z_{close} for FPP ₁ and FPP ₂ .	140
6.4	φ_{FPP} versus z_{close} distribution for the first analyzer block.	141
6.5	P_ℓ^{Born} versus R	146
6.6	Kinematic factor K versus ϵ .	148
6.7	R and $A_y P_l$ versus δ , y_{tgt} and the dispersive θ_{tgt} , non-dispersive ϕ_{tgt} angles for $\epsilon = 0.152$ using the COSY model and the dipole model.	152
6.8	R and $A_y P_l$ versus δ , y_{tgt} and the dispersive θ_{tgt} , non-dispersive ϕ_{tgt} angles for $\epsilon = 0.635$ using the COSY model and the dipole model.	153
6.9	R and $A_y P_l$ versus δ , y_{tgt} and the dispersive θ_{tgt} , non-dispersive ϕ_{tgt} angles for $\epsilon = 0.785$ using the COSY model and the dipole model.	154
6.10	R as a function of ϵ .	156
6.11	P_ℓ / P_ℓ^{Born} as a function of ϵ .	157
6.12	Ratio of the ϑ_{FPP} distributions between the different kinematics.	158
6.13	δ distribution of the three kinematics.	158
6.14	Results of P_ℓ / P_ℓ^{Born} obtained with various combinations of cuts in ϑ_{FPP} and δ .	159
6.15	TPEX amplitudes as a function of ϵ for the two fits of P_ℓ , with their 1σ statistical error bands.	160
C.1	Diagram showing the cone-test in the FPP.	184

Acknowledgements

First, I would like to thank my advisor Charles Perdrisat for giving me the opportunity of doing my Ph.D. at the College of William and Mary. It has been an honour and privilege to learn from his boundless culture. I am also grateful for his confidence, guidance and strong mentorship. I also thank him for sending me all over the US to present the results of the experiment at various conferences. Merci beaucoup Charles.

I would of course like to thank the different members of the GEpIII and GEp2 γ team. Frank Wesselmann for teaching me what I know about drift chambers, polarimeter and the data acquisition system. Lubomir Pentchev for checking my work on the GEp2 γ analysis. Mark Jones for his incredible knowledge about nearly everything related to experimental physics and for his incommensurable patience when I bugged him with naive questions. Vina Punjabi and Edward Brash for their useful comments and suggestion in the analysis. I am indebted as well to the other graduate students who worked on the GEpIII and GEp2 γ experiments. Andrew Puckett for his tremendous help and rigorous expertise in the data analysis and for his encyclopedic knowledge. Wei Luo, for answering any questions I had about computing science. It was a pleasure to have him as an office mate.

I am thankful to Professor Carl Carlson for his precious help in electron-proton scattering theory and for giving me so much of his time to answer all of my interrogations.

I would like to thank Paula Perry for her precious help in making me more familiar with the rules and customs of the american student life.

I am grateful to my family for its unconditional support and for sending me parcels, across the Atlantic, full of treats that made my life easier in the delicate moments.

I wish to thank my girlfriend Amanda for making everything easier and sweeter.

Prolegomenon

The measurement of the magnetic moment of the proton by Stern in 1933 [1] made the idea of the proton being a point-like particle obsolete. Stern found an anomalous value 2.8 times larger than expected for a spin-1/2, point-like particle. This was the first evidence of a proton internal structure.

Later in the 1950's, Hofstadter [2] introduced a technique to access the proton substructure: electron scattering. For the first time, two form factors G_E and G_M were used to describe the distribution of charge and magnetization, respectively, and thus to account for the proton structure. Until the 1990's the only method to measure the proton form factors and extract their ratio was the unpolarized cross section measurement based on the Rosenbluth separation technique [3]. The square of both form factors is extracted from the angular dependence of the reduced cross section at constant value of the momentum transfer Q^2 . It was found [4, 5, 6] that the form factor ratio G_E/G_M remained approximately constant with increasing Q^2 .

In the late 1990's, when polarized beams and targets became available, a new method to measure the form factors became practical: double polarization measurements. The form factor ratio is accessible from experiment using a polarized electron beam with a polarized proton target or measuring the polarization transfer to the recoil proton in $\vec{e}p$ elastic scattering. The results of the polarization experiments [7, 8, 9, 10] were surprisingly and strikingly different from the cross section measurements [11] as shown in Figure 1. They depict a form factor ratio falling monotonically with Q^2 .

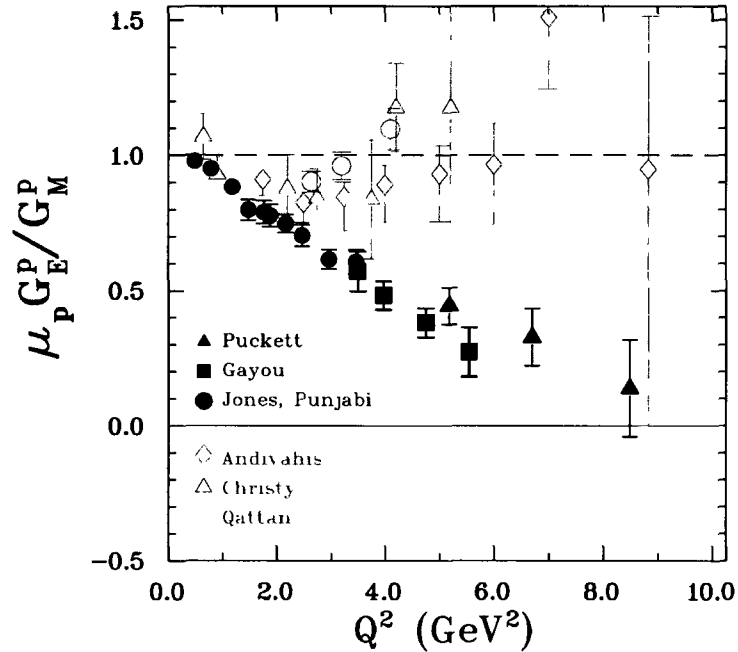


Figure 1: Discrepancy between the polarization transfer results (filled circles from [7, 8], squares from [9] and triangles from [10]) and Rosenbluth (opened diamonds from [4], triangles from [5] and circles [6]) results of the proton form factor ratio.

This discrepancy led to intensive theoretical and experimental efforts aiming at reconciling the results of the two techniques. A set of “standard” radiative corrections [12, 13] must be applied to the Rosenbluth data changing the slope of the reduced cross section by as much as 30% for large Q^2 . In contrast, the effect of these first-order corrections on the polarization measurement is almost negligible [14]. As a consequence, attention turned to the validity of the theoretical assumptions used in the analysis of both sets of measurement. In both cases, the extraction is based on the exchange of a single photon, commonly called the Born Approximation. It turned out that a possible explanation of the discrepancy is a higher order radiative process which includes the exchange of two photons. Nevertheless, the available data do not have sufficient precision to exhibit any sensitivity to the two photon exchange mechanism. Experiment E04-019 (Gep2 γ) which is the subject of this thesis, aiming at looking for a possible kinematical dependence of the polarization transfer observables, is an effort to provide such data. A detailed study of the results

is the core of this thesis.

The thesis is organized around six chapters. In the first chapter, we will establish the theoretical framework necessary for the calculation of the polarization transfer observables. In the second chapter, an overview of the theoretical models of the two-photon exchange mechanism will be given. The experimental apparatus used during the experiment will be described in the third chapter. The fourth and fifth chapters describe in details the data analysis involving the tracking, the event selection and the extraction of the polarization observables. In the sixth and last chapter, we will present the final results of the GEp2 γ experiment.

Chapter 1

Beyond the Born Approximation: Generalized Form Factors and Two Photon Exchange

In this chapter, we will give the formalism of electron-proton elastic scattering to the second order. We will derive also the complete calculation of the reduced unpolarized cross section and of the recoil polarization components, for processes including the exchange of at least two photons.

1.1 Second-order electron-proton scattering

The lowest order in power of the electromagnetic coupling constant [15] $\alpha = \frac{e^2}{4\pi} \approx \frac{1}{137}$ of electron-proton scattering is the one photon exchange mechanism (OPEX). It is also called the *Born Approximation*. In what follows, we will consider electron-proton scattering to the second order, in which the two photon exchange (TPEX) process takes place. We will see that two types of diagrams need to be considered.

The second order contribution to the perturbation expansion of the S-matrix is given by:

$$S_{fi}^{(2)} = -ie^2 \int d^4x d^4y \bar{\psi}_f(x) \mathcal{A}(x) S_F(x-y) \mathcal{A}(y) \psi_i(y) \quad , \quad (1.1)$$

where f and i stand for final and initial state respectively. $A(x)$ is the electromagnetic potential produced by the proton and S_F the electron propagator. From (1.1) we can write the second order electron current as:

$$j_{\mu\nu}^{(2)}(x, y) = ie^2 \bar{\psi}_f(x) \gamma_\mu S_F(x-y) \gamma_\nu \psi_i(y) \quad . \quad (1.2)$$

We consider the second order contribution of the proton in (1.1) i.e. the product of the electromagnetic potentials $A_\mu(x)A_\nu(y)$:

$$\begin{aligned} A_\mu(x)A_\nu(y) &= \int d^4X d^4Y D_F(x-X) D_F(y-Y) J_{\mu\nu}^{(2)}(X, Y) \\ &= ie^2 \int d^4X d^4Y D_F(x-X) D_F(y-Y) \bar{\psi}_f^p(X) \Gamma_\mu S_F^p(X-Y) \Gamma_\nu \psi_i^p(Y) \end{aligned} \quad (1.3)$$

where the upper-script p stands for the proton, $J_{\mu\nu}^{(2)}$ is the second order proton current, D_F is the photon propagator and Γ_μ is the hadronic or proton vertex function. More details about the vertex function will be given in the next section. Gathering (1.2) and (1.3) we obtain for the amplitude of second-order electron-proton scattering:

$$\begin{aligned} S_{fi}^{(2)} &= e^4 \int d^4x d^4y d^4X d^4Y \left(\bar{\psi}_f(x) \gamma^\mu S_F(x-y) \gamma^\nu \psi_i(y) \right) \\ &\quad \times \left(D_F(x-X) D_F(y-Y) \bar{\psi}_f^p(X) \Gamma_\mu S_F^p(X-Y) \Gamma_\nu \psi_i^p(Y) \right) \end{aligned} \quad (1.4)$$

Note that X, Y are the space-time point (vertices) where the photons are emitted by the proton and x, y the space-time point where the photons are absorbed by the electron. This process is described by the *Direct box* diagram in Figure 1.1 left. Nevertheless, this amplitude does not totally represent the second order amplitude. Due to the indistinguishability of the photons, we need to consider another contribution. Indeed, for an electron at the space-point x , a photon emitted at the space-point X or Y is equivalent. This is done by adding a contribution in (1.4) with the exchange $X \rightarrow Y$

and $Y \rightarrow X$ in the photon propagators and $\mu \rightarrow \nu$ in the proton vertex functions. This process is described by the *Crossed box* diagram in figure 1.1 right. The total second-order electron-proton scattering amplitude is then:

$$\begin{aligned}
S_{fi}^{(2)} &\equiv S_{fi}^{(2),Box} + S_{fi}^{(2),Cross} \\
&= e^4 \int d^4x d^4y d^4X d^4Y \left(\bar{\psi}_f(x) \gamma^\mu S_F(x-y) \gamma^\nu \psi_i(y) \right) \\
&\quad \times \left[D_F(x-X) D_F(y-Y) \left(\bar{\psi}_f^p(X) \Gamma_\mu S_F^p(X-Y) \Gamma_\nu \psi_i^p(Y) \right) \right. \\
&\quad \left. + D_F(x-Y) D_F(y-X) \left(\bar{\psi}_f^p(X) \Gamma_\nu S_F^p(X-Y) \Gamma_\mu \psi_i^p(Y) \right) \right] \quad (1.5)
\end{aligned}$$

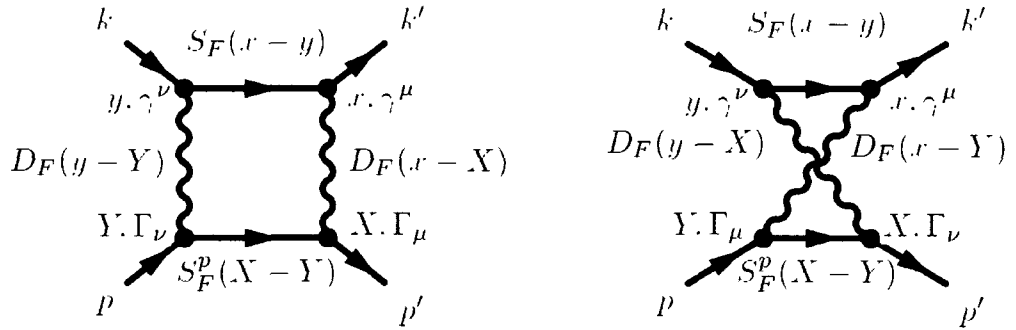


Figure 1.1: Direct box diagram (left) and Crossed box diagram (right).

We expand the ψ_i ($\bar{\psi}_f$) of the electron of mass m in plane waves of momentum k (k') and spin s (s') respectively. We perform a similar expansion for the proton of mass M and we obtain:

$$\psi_i = \sqrt{\frac{m}{E_e V}} u(k, s) e^{-ik \cdot x} \quad \bar{\psi}_f = \sqrt{\frac{m}{E'_e V}} \bar{u}(k', s') e^{ik' \cdot x} \quad (1.6)$$

$$\psi_i^p = \sqrt{\frac{M}{E_p V}} u(p, S) e^{-ip \cdot x} \quad \bar{\psi}_f^p = \sqrt{\frac{M}{E'_p V}} \bar{u}(p', S') e^{ip' \cdot x} \quad (1.7)$$

with V the box normalization volume.

The electron propagator is given by:

$$S_F(x-y) = \int \frac{d^4 p}{(2\pi)^4} \frac{e^{-ip(x-y)}}{\not{p} - m + i\epsilon} \quad (1.8)$$

The proton propagator has a similar expression by changing m into M . The photon propagator is defined by:

$$D_F^{\mu\nu}(x-y) = -4\pi \int \frac{d^4 q}{(2\pi)^4} g^{\mu\nu} \frac{e^{-iq(x-y)}}{q^2 + i\epsilon} \quad (1.9)$$

Having all those definitions we can re-write the box diagram term of (1.5) as:

$$\begin{aligned} S_{fi}^{(2),Box} &= C \int d^4 x d^4 y d^4 X d^4 Y \frac{m}{\sqrt{E'_e E_e}} \frac{M}{\sqrt{E'_p E_p}} \int \frac{d^4 q_1}{(2\pi)^4} \frac{d^4 q_2}{(2\pi)^4} \frac{d^4 K}{(2\pi)^4} \frac{d^4 P}{(2\pi)^4} \frac{e^{-iq_1(x-X)} e^{-iq_2(y-Y)}}{q_1^2 + i\epsilon} \frac{1}{q_2^2 + i\epsilon} \\ &\times e^{ik'x} \bar{u}(k', s') \gamma^\mu \frac{e^{-iK(x-y)}}{\not{K} - m + i\epsilon} \gamma^\nu u(k, s) e^{-iky} \\ &\times e^{ip'X} \bar{u}(p', S') \Gamma_\mu(q_1) \frac{e^{-iP(X-Y)}}{\not{P} - M + i\epsilon} \Gamma_\nu(q_2) u(p, S) e^{-ipY} \end{aligned} \quad (1.10)$$

with $C = \frac{(4\pi)^2 e^4}{V^2}$. The integration over the space coordinates will give four 4-dimensional delta functions which ensure the energy-momentum conservation at each vertex:

$$\begin{aligned} &\int d^4 x d^4 y d^4 X d^4 Y e^{-iq_1(x-X)} e^{-iq_2(y-Y)} e^{ik'x} e^{-iK(x-y)} e^{-iky} e^{ip'X} e^{-iP(X-Y)} e^{-ipY} \\ &= (2\pi)^4 \delta^4(q_1 + p - k') (2\pi)^4 \delta^4(q_2 - p + k) (2\pi)^4 \delta^4(-q_2 - P + p) (2\pi)^4 \delta^4(-q_1 + P - p') \end{aligned} \quad (1.11)$$

Finally, integrating over the momentum q_2 , K and P , with $q \equiv k' - k = p - p'$ we obtain for the box diagram contribution:

$$\begin{aligned}
S_{fi}^{(2),Box} &= C(2\pi)^4 \delta^4(p' + k' - p - k)^4 \frac{m}{\sqrt{E'_e E_e}} \frac{M}{\sqrt{E'_p E_p}} \int \frac{d^4 q_1}{(2\pi)^4} \frac{1}{q_1^2 + i\epsilon} \frac{1}{(q - q_1)^2 + i\epsilon} \\
&\times \bar{u}(k', s') \gamma^\mu \frac{1}{\not{k}' - \not{q}_1 - m + i\epsilon} \gamma^\nu u(k, s_i) \bar{u}(p', S') \Gamma_\mu(q_1) \frac{1}{\not{p}' + \not{q}_1 - M + i\epsilon} \Gamma_\nu(q - q_1) u(p, s)
\end{aligned} \tag{1.12}$$

A similar calculation can be carried out for the cross diagram contribution. More "practical" Feynman diagrams of the scattering are given in Figure 1.2. The total second-order electron-proton scattering amplitude is given by:

$$\begin{aligned}
S_{fi}^{(2)} &= \frac{(4\pi)^2 e^4}{V^2} (2\pi)^4 \delta^4(p' + k' - p - k)^4 \frac{m}{\sqrt{E'_e E_e}} \frac{M}{\sqrt{E'_p E_p}} \int \frac{d^4 q_1}{(2\pi)^4} \frac{1}{q_1^2 + i\epsilon} \frac{1}{(q - q_1)^2 + i\epsilon} \\
&\times \bar{u}(k', s') \gamma^\mu \frac{1}{\not{k}' - \not{q}_1 - m + i\epsilon} \gamma^\nu u(k, s_i) \left[\bar{u}(p', S') \Gamma_\mu(q_1) \frac{1}{\not{p}' + \not{q}_1 - M + i\epsilon} \Gamma_\nu(q - q_1) u(p, s) \right. \\
&\left. + \bar{u}(p', S') \Gamma_\nu(q - q_1) \frac{1}{\not{k} - \not{q}_1 - M + i\epsilon} \Gamma_\mu(q_1) u(p, s) \right]
\end{aligned} \tag{1.13}$$

The remaining loop integral comes from the fact that there is no definite ratio between the momenta of the two photons. As a consequence, we need to integrate over all the possible momenta q_1 . The evaluation of the loop integral is delicate and won't be performed here. Instead, in the next chapter, we will present some theoretical model used to solve this loop integral within some approximations and more generally aiming at giving the two-photon exchange contribution to the electron-proton scattering. In the next section we will concentrate on the proton vertex function Γ_μ and we will derive it for processes including the exchange of at least two photons.

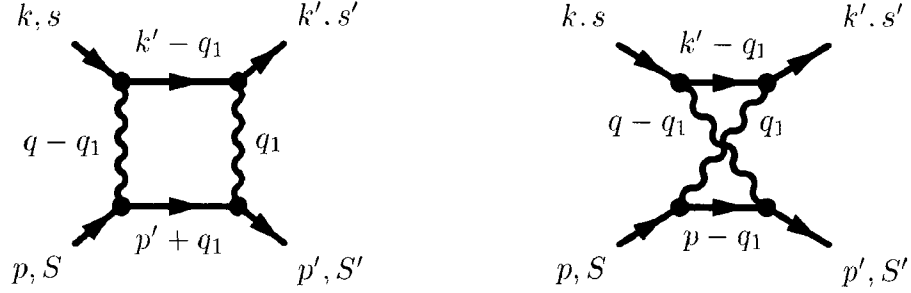


Figure 1.2: Box diagram (left) and Cross diagram (right).

1.2 Generalized Form Factors

We consider the elastic electron-proton scattering:

$$e(k, h) + p(p, \lambda_p) \rightarrow e(k', h') + p(p', \lambda'_p) \quad (1.14)$$

where h, h', λ_p and λ'_p are the helicities and k, p are the momenta of the initial electron and proton. The primed momenta refer to the final particles. We set:

$$q = k - k' = p' - p, \quad q^2 = -Q^2, \quad P = \frac{p + p'}{2}, \quad K = \frac{k + k'}{2} \quad (1.15)$$

The Mandelstam variables are given by:

$$s = (p + k)^2, \quad t = q^2 = -Q^2 = (k - k')^2, \quad u = (p - k')^2 = (k - p')^2 \quad (1.16)$$

We choose as the independent kinematical variables of the scattering:

$$q^2 = -Q^2, \quad \nu = K \cdot P = \frac{s - u}{4} \quad (1.17)$$

A general expansion of the amplitude matrix, M with respect to a set of Dirac bilinears in the spinor space of the proton is:

$$M = A1^{(p)} + B\gamma_5^{(p)} + C_\mu\gamma_\mu^{(p)} + D_\mu\gamma_5^{(p)}\gamma_\mu^{(p)} + E_{\mu\nu}\sigma_{\mu\nu}^{(p)} \quad (1.18)$$

where the coefficients A, B, C, \dots are matrices in the spinor space of the electron and are functions of P, K and q .

We can show, by decomposing the coefficients C_μ, D_μ and $E_{\mu\nu}$ with respect to a vector basis defined by P_μ, K_μ, q_μ and $L_\mu = \epsilon_{\mu\nu\alpha\beta}K_\nu P_\alpha Q_\beta$, that M takes the form [16]:

$$M = a1^{(p)} + b\gamma_5^{(p)} + c\gamma^{(p)} \cdot K + d\gamma_5^{(p)}\gamma^{(p)} \cdot K \quad (1.19)$$

A similar expansion of the coefficients a, b, c and d with respect to matrices in the electron spinor space can be evaluated. This operation will give a total of 16 amplitudes, but terms containing only one γ_5 will violate parity conservation. Requiring parity conservation, this reduces to the 8 following terms:

$$\begin{array}{lll} i\gamma^{(e)} \cdot P i\gamma^{(p)} \cdot K & 1^{(e)} i\gamma^{(p)} \cdot K & \gamma_5^{(e)} i\gamma^{(e)} \cdot P \gamma_5^{(p)} i\gamma^{(p)} \cdot K \\ 1^{(e)} 1^{(p)} & \gamma_5^{(e)} \gamma_5^{(p)} & i\gamma^{(e)} \cdot P 1^{(p)} \\ \gamma_5^{(e)} i\gamma_5^{(p)} \gamma^{(p)} \cdot K & & \gamma_5^{(e)} \gamma^{(e)} \cdot P \gamma_5^{(p)} \end{array} \quad (1.20)$$

The last two terms change sign under inversion of motion, therefore they are not invariant under Wigner time reversal. This reduces further to 6 amplitudes and the term $\gamma_5^{(e)} i\gamma^{(e)} \cdot P \gamma_5^{(p)} i\gamma^{(p)} \cdot K$ can be replaced by $\gamma_\mu^{(e)} \gamma^\mu^{(p)}$ and a combination of the other five structures. Using the spinor notation and keeping tacit the helicities for clarity, the remaining amplitudes are:

$$\begin{array}{lll} \bar{u}(k')u(k) \cdot \bar{u}(p')u(p) & \bar{u}(k')u(k) \cdot \bar{u}(p')\gamma \cdot Ku(p) & \bar{u}(k')\gamma_5 u(k) \cdot \bar{u}(p')\gamma_5 u(p) \\ \bar{u}(k')\gamma \cdot Pu(k) \cdot \bar{u}(p')\gamma \cdot Ku(p) & \bar{u}(k')\gamma \cdot Pu(k) \cdot \bar{u}(p')u(p) & \bar{u}(k')\gamma_\mu u(k) \cdot \bar{u}(p')\gamma^\mu u(p) \end{array} \quad (1.21)$$

Due to the vector nature of the coupling in QED, in the limit $m_e \rightarrow 0$, all the above structures conserve the helicity of the electron. In other words they are invariant under the chirality transformation. We see that the first three terms in (1.21) change sign under the operation $u(k) \rightarrow \gamma_5 u(k)$ and $\bar{u}(k') \rightarrow -\bar{u}(k')\gamma_5$ and then must be proportional to m_e . Therefore they will vanish in the limit $m_e \rightarrow 0$.

The general elastic electron-proton scattering amplitude, considering at least the exchange of two photons and introducing a factor $\frac{e^2}{Q^2}$ for convenience, is then given by [17]:

$$T = \frac{e^2}{Q^2} \bar{u}(k', h) \gamma_\mu u(k, h) \times \bar{u}(p', \lambda'_p) \left(\tilde{G}_M \gamma^\mu - \tilde{F}_2 \frac{P^\mu}{M} + \tilde{F}_3 \frac{\gamma \cdot K P^\mu}{M^2} \right) u(p, \lambda_p) \quad (1.22)$$

where M is the mass of the proton, the three independent Lorentz structures \tilde{G}_M , \tilde{F}_2 and \tilde{F}_3 are complex and are functions of the kinematical parameter $\epsilon \equiv [v^2 - M^4 \tau(1 + \tau)] / [v^2 + M^4 \tau(1 + \tau)]$ (understood as the longitudinal polarization of the virtual photon in the Born approximation) and the momentum transfer Q^2 . They are called the generalized form factors. Defining $\tilde{G}_E = \tilde{G}_M - (1 + \tau)\tilde{F}_2$, $\tau = \frac{Q^2}{4M^2}$, we exhibit the effect of the exchange of at least two photons by writing the generalized form factors as :

$$\tilde{G}_M(Q^2, \epsilon) = G_M(Q^2) + \delta\tilde{G}_M(Q^2, \epsilon) \quad (1.23)$$

$$\tilde{G}_E(Q^2, \epsilon) = G_E(Q^2) + \delta\tilde{G}_E(Q^2, \epsilon) \quad (1.24)$$

$$\tilde{F}_3(Q^2, \epsilon) \equiv \delta\tilde{F}_3(Q^2, \epsilon) \quad (1.25)$$

G_M and G_E are form factors in the Born approximation (exchange of one photon) called the Sachs form factors. They are real and depend on Q^2 only. The complex amplitudes $\delta\tilde{G}_M$, $\delta\tilde{G}_E$ and \tilde{F}_3 exist only at the 2γ level and beyond, and are of order e^2 relative to the factor e^2 in (1.22)

1.3 Unpolarized cross section and polarization components

In this section, we will derive the unpolarized cross section of the $\bar{e}p \rightarrow e\bar{p}$ scattering and the transferred polarization components of the recoil proton by calculating the leptonic and hadronic tensors in the Breit frame. The electron is longitudinally polarized.

1.3.1 Breit Frame kinematics

In the Breit frame, also called the brick-wall frame, the momenta of the initial and final proton are equal in magnitude and opposite in direction. Let the transferred momentum be along the z-axis. A boost along the transferred momentum allows us to pass from the lab frame to the Breit frame. The momentum transfer \vec{q}_B , the momenta of the initial (final) electron \vec{k}_B (\vec{k}'_B) and of the initial (final) proton \vec{p}_B (\vec{p}'_B) are:

$$\vec{k}_B = \begin{pmatrix} k_x \\ 0 \\ \frac{Q}{2} \end{pmatrix}, \quad \vec{k}'_B = \begin{pmatrix} k_x \\ 0 \\ -\frac{Q}{2} \end{pmatrix}, \quad \vec{q}_B = \begin{pmatrix} 0 \\ 0 \\ Q \end{pmatrix}$$

$$\vec{p}_B = \begin{pmatrix} 0 \\ 0 \\ -\frac{Q}{2} \end{pmatrix}, \quad \vec{p}'_B = \begin{pmatrix} 0 \\ 0 \\ \frac{Q}{2} \end{pmatrix}$$

It follows that:

$$Q^2 = -q^2 = 4p^2 \Rightarrow |p| = \frac{Q}{2} \tag{1.26}$$

$$E_{pB} = E'_{pB} = \sqrt{p^2 + M^2} = \sqrt{\frac{Q^2}{4} + M^2} = M\sqrt{1 + \tau}, \tag{1.27}$$

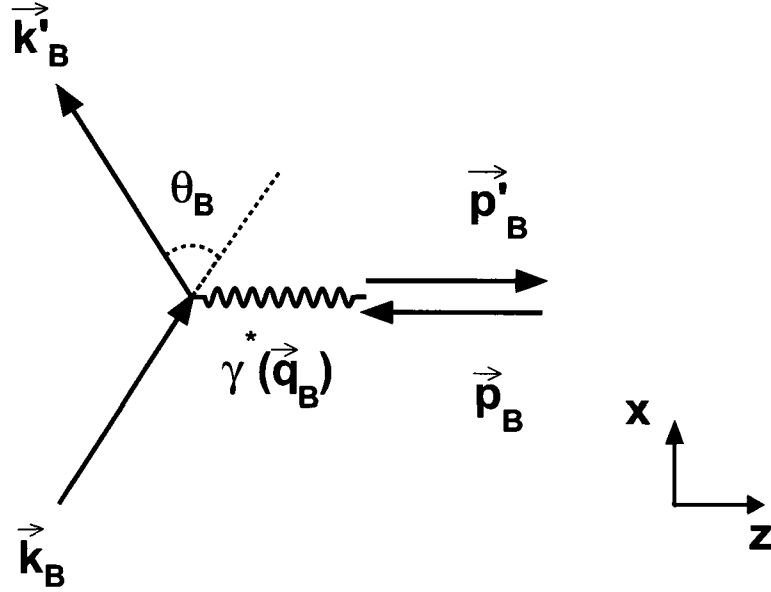


Figure 1.3: Elastic scattering in the Breit frame

so that the energy transfer $\omega = E_{pB} - E'_{pB}$ equals zero. Thus, we write the four-momenta of the initial and final proton in the Breit frame as:

$$p^\mu = \begin{pmatrix} M\sqrt{1+\tau} \\ 0 \\ 0 \\ -\frac{Q}{2} \end{pmatrix}, \quad p'^\mu = \begin{pmatrix} M\sqrt{1+\tau} \\ 0 \\ 0 \\ \frac{Q}{2} \end{pmatrix} \quad (1.28)$$

We next derive the coordinates of the 4-momenta of the initial and final electron in the Breit frame. As k_y and k'_y are equal to zero (by definition) and $\vec{q} = Q\vec{z}$, k_x is conserved so that: $k_x = k'_x$. The four-momenta z-components are calculated using the facts that the energy transfer is equal to zero and the momentum transferred is along the z-axis:

$$\left. \begin{aligned} q_z = k_z - k'_z = Q &\Rightarrow k_z = k'_z + Q \\ \omega = E_{pB} - E'_{pB} = 0 &\Rightarrow |k'| = |k| \Rightarrow k_z^2 = k_z'^2 \end{aligned} \right\} \quad k'_z = -\frac{Q}{2}, k_z = \frac{Q}{2} \quad (1.29)$$

The four-momenta x-components are expressed in terms of the scattering angle in the Breit frame and of the momentum transfer:

$$k \cdot k' = |k||k'| \cos \theta_B \Rightarrow \cos \theta_B = \frac{k_x^2 - \frac{Q^2}{4}}{k_x^2 + \frac{Q^2}{4}} \Rightarrow k_x = k'_x = \frac{Q}{2} \cot \frac{\theta_B}{2} \quad (1.30)$$

The time components are simply given by:

$$k_0 = k'_0 = \sqrt{k_x^2 + \frac{Q^2}{4}} = \frac{Q}{2 \sin \frac{\theta_B}{2}} \quad (1.31)$$

We then write the initial/final electron four-momenta as:

$$k^\mu = \begin{pmatrix} \frac{Q}{2 \sin \frac{\theta_B}{2}} \\ \cot \frac{\theta_B}{2} \\ 0 \\ \frac{Q}{2} \end{pmatrix}, \quad k'^\mu = \begin{pmatrix} \frac{Q}{2 \sin \frac{\theta_B}{2}} \\ \cot \frac{\theta_B}{2} \\ 0 \\ -\frac{Q}{2} \end{pmatrix} \quad (1.32)$$

The derivation of the four-momenta of the initial/final electron/proton is now complete.

Next we derive a relation between the scattering angle in the Breit frame and the scattering angle in the Lab frame.

We start by writing the z and x-components of the four-momentum vector of the initial electron in the lab frame. Because the transferred momentum is along the z-axis:

$$k_z^2 = \frac{\vec{k} \cdot \vec{q}}{q^2}, \quad \text{so} \quad k_x^2 = \frac{\vec{k}^2 \cdot q^2 - \vec{k} \cdot \vec{q}}{q^2} \quad (1.33)$$

Using: $Q^2 = \bar{q}^2 - v^2 \Rightarrow \bar{q}^2 = Q^2(1 + \frac{Q^2}{4M^2}) = Q^2(1 + \tau)$ the x-component becomes:

$$\begin{aligned}
 k_x^2 &= \frac{E_e^4 - 2E_e^3 E_e' \cos \theta_e + E_e^2 E_e'^2 - (E_e^4 - 2E_e^3 E_e' \cos \theta_e + E_e^2 E_e'^2 \cos^2 \theta_e)}{Q^2(1 + \tau)} \\
 &= \frac{E_e^2 E_e'^2 \sin^2 \theta_e}{Q^2(1 + \tau)} \\
 &= \frac{4E_e^2 E_e'^2 \sin^2 \frac{\theta_e}{2} \cos^2 \frac{\theta_e}{2}}{Q^2(1 + \tau)} \\
 &= \frac{Q^2}{4(1 + \tau)} \cot^2 \frac{\theta_e}{2}
 \end{aligned} \tag{1.34}$$

By comparing (1.30) and (1.34), the relation between the Breit and lab frame scattering angles is:

$$\cot^2 \frac{\theta_B}{2} = \frac{\cot^2 \frac{\theta_e}{2}}{(1 + \tau)} \tag{1.35}$$

Using trigonometric identities we can rewrite (1.35) as:

$$\frac{1}{\cos^2 \frac{\theta_B}{2}} = \tan^2 \frac{\theta_e}{2} \left(\frac{1}{\sin^2 \frac{\theta_e}{2}} + \tau \right) \tag{1.36}$$

From the kinematic relations (B.29) of the appendix, we find:

$$\begin{aligned}
 \frac{1}{\cos \frac{\theta_B}{2}} &= \tan \frac{\theta_e}{2} \frac{E_e + E_e'}{Q} \\
 &= \tan \frac{\theta_e}{2} \frac{2v}{MQ}
 \end{aligned} \tag{1.37}$$

1.3.2 Leptonic and hadronic tensors

Considering the T-matrix expansion (1.22), we define the leptonic $L_{\mu\nu}$ and hadronic $W^{\mu\nu}$ by:

$$\begin{aligned}
 L_{\mu\nu} &= j_\mu j_\nu^* \\
 W^{\mu\nu} &= J^\mu J^{\nu*}
 \end{aligned}$$

where $j_{\mu\nu}$ and $J^{\mu\nu}$ are the leptonic and hadronic currents, respectively. Those currents are given by:

$$\begin{aligned} j_\mu &= \bar{v}(k', h') \gamma_\mu v(k, h) \\ J^\mu &= \bar{u}(p', \lambda'_N) \Gamma^\mu u(k, \lambda_N) = \bar{u}(p', \lambda'_N) \left(\tilde{G}_M \gamma^\mu - \tilde{F}_2 \frac{P^\mu}{M} + \tilde{F}_3 \frac{\gamma \cdot KP^\mu}{M^2} \right) u(k, \lambda_N) \end{aligned} \quad (1.38)$$

where Γ^μ is the proton vertex function. This structure, of some complexity, contains the electromagnetic structure of the proton. The leptonic tensor is equal to:

$$\begin{aligned} L_{\mu\nu} &= \sum_{\alpha\beta\delta\epsilon} \sum_{h, h'} \bar{v}_\alpha(k', h') \gamma_{\mu\alpha\beta} v_\beta(k, h) \bar{v}_\delta(k, h) \gamma_{\nu\delta\epsilon} v_\epsilon(k', h') \\ &= \sum_{\alpha\beta\delta\epsilon} \gamma_{\mu\alpha\beta} \underbrace{\sum_h v_\beta(k, h) \bar{v}_\delta(k, h)}_{\left[(\not{k} + m_e) \left(\frac{1 - h\gamma_5}{2} \right) \right]_{\beta\delta} = \left[\not{k} \left(\frac{1 - h\gamma_5}{2} \right) \right]_{\beta\delta}} \gamma_{\nu\delta\epsilon} \sum_{h'} \bar{v}_\alpha(k', h') v_\epsilon(k', h') \\ &= \sum_{\alpha\epsilon} \sum_{h'} \underbrace{\bar{v}_\alpha(k', h') v_\epsilon(k', h')}_{(\not{k}' + m_e)_{\epsilon\alpha} = (\not{k}')_{\epsilon\alpha}} \left[\gamma_\mu \not{k} \left(\frac{1 - h\gamma_5}{2} \right) \gamma_\nu \right]_{\alpha\epsilon} \\ &= \text{Tr} \left[\not{k}' \gamma_\mu \not{k} \left(\frac{1 - h\gamma_5}{2} \right) \gamma_\nu \right] \\ &= \frac{1}{2} \text{Tr} [\not{k}' \gamma_\mu \not{k} \gamma_\nu] - \frac{h}{2} \text{Tr} [\not{k}' \gamma_\mu \not{k} \gamma_5 \gamma_\nu] \\ &= 2 \left(k'_\mu k'_\nu + k_\nu k'_\mu - (k \cdot k') g_{\mu\nu} \right) + \frac{h}{2} \text{Tr} [\gamma_5 \not{k}' \gamma_\mu \not{k} \gamma_\nu] \\ &= 2 \left(k'_\mu k'_\nu + k_\nu k'_\mu - (k \cdot k') g_{\mu\nu} \right) - \frac{h}{2} \text{Tr} [\gamma_5 \gamma_\mu \gamma_\nu \not{k}' \not{k}] \\ &= 2 \left(\left(k'_\mu k'_\nu + k_\nu k'_\mu - (k \cdot k') g_{\mu\nu} \right) + ih\epsilon_{\mu\nu\alpha\beta} k^\alpha k'^\beta \right) \end{aligned} \quad (1.39)$$

We used the standard trace technique of γ -matrices (A.22) to carry out this calculation. From line 2 to line 3, we summed over the initial spin and used the completeness relation for polarized Dirac particles (A.20), neglecting the electron mass. From line 3 to line 4, we summed over the final spin and used the completeness relation (A.19). The unpolarized trace has been evaluated in appendix (B.9).

We develop the leptonic tensor using the Breit frame components of the initial/final electron

four-momenta (1.32) to obtain:

$$\begin{aligned}
L_{\mu\nu} &= 2 \begin{pmatrix} 2k_0k'_0 - (k \cdot k') & k_0k'_1 + k_1k'_0 & 0 & k_0k'_3 + k_3k'_0 \\ k_0k'_1 + k_1k'_0 & 2k_1k'_1 + (k \cdot k') & 0 & k_1k'_3 + k_3k'_1 \\ 0 & 0 & (k \cdot k') & 0 \\ k_3k'_0 + k_0k'_3 & k_3k'_1 + k_1k'_3 & 0 & 2k_3k'_3 + (k \cdot k') \end{pmatrix} \\
&+ 2i\hbar \begin{pmatrix} 0 & 0 & -k_3k'_1 + k_1k'_3 & 0 \\ 0 & 0 & k_3k'_0 - k_0k'_3 & 0 \\ -k_1k'_3 + k_3k'_1 & k_0k'_3 - k_3k'_0 & 0 & -k_0k'_1 + k_1k'_0 \\ 0 & 0 & k_0k'_1 - k_1k'_0 & 0 \end{pmatrix} \\
&= Q^2 \underbrace{\begin{pmatrix} \cot^2 \frac{\theta_B}{2} & \frac{\cot \frac{\theta_B}{2}}{\sin \frac{\theta_B}{2}} & 0 & 0 \\ \frac{\cot \frac{\theta_B}{2}}{\sin \frac{\theta_B}{2}} & \frac{1}{\sin^2 \frac{\theta_B}{2}} & 0 & 0 \\ 0 & 0 & 1 & 0 \\ 0 & 0 & 0 & 0 \end{pmatrix}}_{\text{real and symmetric}} + i\hbar Q^2 \underbrace{\begin{pmatrix} 0 & 0 & \cot \frac{\theta_B}{2} & 0 \\ 0 & 0 & \frac{-1}{\sin \frac{\theta_B}{2}} & 0 \\ -\cot \frac{\theta_B}{2} & \frac{1}{\sin \frac{\theta_B}{2}} & 0 & 0 \\ 0 & 0 & 0 & 0 \end{pmatrix}}_{\text{imaginary and antisymmetric}} \quad (1.40)
\end{aligned}$$

We see that the unpolarized part of the leptonic tensor is given by a real and symmetric tensor, whereas the polarization information is in a complex and antisymmetric tensor.

In order to express the hadronic tensor in the Breit frame we will need to evaluate currents of the form: $\bar{u}(p)u(p)$, $\bar{u}(p)\gamma^0 u(p)$ and $\bar{u}\gamma_0(p)\gamma^i u(p)$, $i = 1\dots 3$.

From (1.28) it follows that:

$$P^\mu = \frac{p^\mu + p'^\mu}{2} = \frac{M}{2} \sqrt{1 + \tau} g^{\mu 0} \quad (1.41)$$

As a consequence, the \tilde{F}_2 and \tilde{F}_3 terms will only give a timelike contribution to the current. The \tilde{G}_M term, by the presence of a γ^μ will give both timelike and spacelike contribution. We decompose the hadronic current into a sum of three terms:

$$J^\mu \equiv J_M^\mu + J_2^0 + J_3^0 \quad (1.42)$$

By recalling the expressions for the Dirac spinors:

$$u(p) = \sqrt{E+M} \begin{pmatrix} \xi \\ \frac{\vec{\sigma} \cdot \vec{p}}{E+M} \xi \end{pmatrix}, \quad \bar{u}(p) = \left(\zeta'^{\dagger}, \zeta'^{\dagger} \frac{\vec{\sigma} \cdot \vec{p}'}{E+M} \right) \gamma^0$$

Using $\vec{p} = -\vec{p}'$ and $E = E'$ we have:

$$\begin{aligned} \bar{u}(p)u(p) &= \sqrt{E'+M} \left(\zeta'^{\dagger}, \zeta'^{\dagger} \frac{\vec{\sigma} \cdot \vec{p}'}{E+M} \right) \gamma^0 \sqrt{E+M} \begin{pmatrix} \xi \\ \frac{\vec{\sigma} \cdot \vec{p}}{E+M} \xi \end{pmatrix} \\ &= (E'+M) \left(\zeta'^{\dagger}, -\zeta'^{\dagger} \frac{\vec{\sigma} \cdot \vec{p}}{E+M} \right) \begin{pmatrix} \xi \\ -\frac{\vec{\sigma} \cdot \vec{p}}{E+M} \xi \end{pmatrix} \\ &= \zeta'^{\dagger} \xi \left(1 + \frac{p^2}{(E+M)^2} \right) \\ &= \zeta'^{\dagger} \xi (E+M + (E-M)) \\ &= 2E \zeta'^{\dagger} \xi \\ &= 2M \sqrt{1 + \tau} \zeta'^{\dagger} \xi \end{aligned} \quad (1.43)$$

So:

$$J_2^0 = -4M^2 \frac{\tilde{F}_2}{2M} (1 + \tau) = 2M(\tilde{G}_E - \tilde{G}_M) \quad (1.44)$$

J_M^μ is obtained by calculating the $\bar{u}(p)\gamma^0 u(p)$ and $\bar{u}(p)\gamma^i u(p)$ terms. For the timelike part we have:

$$\begin{aligned}
\bar{u}(p)\gamma^0 u(p) &= (E+M) \left(\zeta'^{\dagger}, -\zeta'^{\dagger} \frac{\vec{\sigma} \cdot \vec{p}}{E+M} \right) \gamma^0 \gamma^0 \begin{pmatrix} \zeta \\ \frac{\vec{\sigma} \cdot \vec{p}}{E+M} \zeta \end{pmatrix} \\
&= \zeta'^{\dagger} \zeta \left(1 + \frac{p^2}{(E+M)^2} \right) \\
&= \zeta'^{\dagger} \zeta (E+M - (E-M)) \\
&= 2M \zeta'^{\dagger} \zeta
\end{aligned} \tag{1.45}$$

For the spacelike part we find:

$$\begin{aligned}
\bar{u}(p)\gamma^i u(p) &= (E+M) \left(\zeta'^{\dagger}, -\zeta'^{\dagger} \frac{\vec{\sigma} \cdot \vec{p}}{E+M} \right) \underbrace{\gamma^0 \gamma^i}_{\begin{pmatrix} 0 & \sigma^i \\ \sigma^i & 0 \end{pmatrix}} \begin{pmatrix} \zeta \\ \frac{\vec{\sigma} \cdot \vec{p}}{E+M} \zeta \end{pmatrix} \\
&= (E+M) \left(\zeta'^{\dagger}, -\zeta'^{\dagger} \frac{\vec{\sigma} \cdot \vec{p}}{E+M} \right) \begin{pmatrix} \sigma^i \frac{\vec{\sigma} \cdot \vec{p}}{E+M} \zeta \\ \sigma^i \zeta \end{pmatrix} \\
&= \zeta'^{\dagger} \left(\sigma^i \vec{\sigma} \cdot \vec{p} - \vec{\sigma} \cdot \vec{p} \sigma^i \right) \zeta \\
&= 2i \zeta'^{\dagger} \vec{p} \times \vec{\sigma} \zeta
\end{aligned} \tag{1.46}$$

As a result we obtain:

$$J_M^0 = 2M \bar{G}_M \tag{1.47}$$

$$\vec{J}_M = 2i \bar{G}_M \zeta'^{\dagger} \vec{p} \times \vec{\sigma} \zeta \tag{1.48}$$

The J_3^0 current requires more attention since it contains a $\gamma \cdot K$ factor. This factor can be expressed by:

$$\gamma \cdot K = \mathcal{K} = \begin{pmatrix} K_0 & 0 \\ 0 & K_0 \end{pmatrix} + \begin{pmatrix} 0 & -\vec{\sigma} \cdot \vec{K} \\ \vec{\sigma} \cdot \vec{K} & 0 \end{pmatrix} \quad (1.49)$$

where $K_0 = \frac{k_0 + k'_0}{2} = \frac{Q}{2 \sin \frac{\theta_B}{2}}$

We can then write:

$$J_3^0 \equiv J_{3,0}^0 + J_{3,i}^0 \quad (1.50)$$

The first term is equal to:

$$\begin{aligned} J_{3,0}^0 &= (E+M) \begin{pmatrix} \zeta'^{\dagger} & -\zeta'^{\dagger} \frac{\vec{\sigma} \cdot \vec{p}}{E+M} \end{pmatrix} \underbrace{\tilde{F}_3}_{Id} (\gamma^0)^2 K_0 \frac{2M\sqrt{1+\tau}}{2M^2} \begin{pmatrix} \zeta \\ -\frac{\vec{\sigma} \cdot \vec{p}}{E+M} \zeta \end{pmatrix} \\ &= \frac{E+M}{M} \frac{Q}{2 \sin \frac{\theta_B}{2}} \sqrt{1+\tau} \tilde{F}_3 \zeta'^{\dagger} \underbrace{\left[1 - \left(\frac{\vec{\sigma} \cdot \vec{p}}{E+M} \right)^2 \right]}_{1 - \frac{\sigma_x^2 |\vec{p}|^2}{(E+M)^2} = 1 - \frac{E^2 - M^2}{(E+M)^2} = \frac{2M}{E+M}} \zeta \\ &= \frac{Q\sqrt{1+\tau}}{\sin \frac{\theta_B}{2}} \tilde{F}_3 \zeta'^{\dagger} \zeta \end{aligned} \quad (1.51)$$

We find for the second term:

$$\begin{aligned} J_{3,i}^0 &= \frac{E+M}{M} \sqrt{1+\tau} \tilde{F}_3 \begin{pmatrix} \zeta'^{\dagger} & -\zeta'^{\dagger} \frac{\vec{\sigma} \cdot \vec{p}}{E+M} \end{pmatrix} \begin{pmatrix} 0 & -\vec{\sigma} \cdot \vec{K} \\ \vec{\sigma} \cdot \vec{K} & 0 \end{pmatrix} \begin{pmatrix} \zeta \\ -\frac{\vec{\sigma} \cdot \vec{p}}{E+M} \zeta \end{pmatrix} \\ &= \frac{E+M}{M} \sqrt{1+\tau} \tilde{F}_3 \begin{pmatrix} \zeta'^{\dagger} & -\zeta'^{\dagger} \frac{\vec{\sigma} \cdot \vec{p}}{E+M} \end{pmatrix} \begin{pmatrix} \frac{\vec{\sigma} \cdot \vec{K} \vec{\sigma} \cdot \vec{p}}{E+M} \zeta \\ \vec{\sigma} \cdot \vec{K} \zeta \end{pmatrix} \end{aligned} \quad (1.52)$$

$$\begin{aligned}
\bar{J}_{3,i}^0 &= \frac{\sqrt{1+\tau}}{M} \bar{F}_3 \bar{\zeta}'^\dagger (\vec{\sigma} \cdot \vec{K} \vec{\sigma} \cdot \vec{p} - \vec{\sigma} \cdot \vec{p} \vec{\sigma} \cdot \vec{K}) \bar{\zeta} \\
&= \frac{\sqrt{1+\tau}}{M} \bar{F}_3 \bar{\zeta}'^\dagger (\sigma_x K^x \sigma_z p^z - \sigma_z p^z \sigma_x K^x) \bar{\zeta} \\
&= \frac{\sqrt{1+\tau}}{M} \bar{F}_3 \bar{\zeta}'^\dagger K^x p^z (\sigma_x \sigma_z - \sigma_z \sigma_x) \bar{\zeta} \\
&= \frac{\sqrt{1+\tau}}{M} \bar{F}_3 \bar{\zeta}'^\dagger K^x p^z (-2i\sigma_y) \bar{\zeta} \\
&= i \frac{Q^2 \sqrt{1+\tau}}{2M} \cot \frac{\theta_B}{2} \bar{F}_3 \bar{\zeta}'^\dagger \sigma_y \bar{\zeta}
\end{aligned} \tag{1.53}$$

Finally, by regrouping the expressions (1.44), (1.48), (1.51) and (1.53) we find for the hadronic current in the Breit frame:

$$J^\mu = \begin{pmatrix} \left(2\bar{G}_E + \frac{Q\sqrt{1+\tau}}{\sin \frac{\theta_B}{2}} \bar{F}_3 \right) \bar{\zeta}'^\dagger \bar{\zeta} + i \frac{Q^2 \sqrt{1+\tau}}{2M} \cot \frac{\theta_B}{2} \bar{F}_3 \bar{\zeta}'^\dagger \sigma_y \bar{\zeta} \\ iQ\bar{G}_M \bar{\zeta}'^\dagger \sigma_y \bar{\zeta} \\ -iQ\bar{G}_M \bar{\zeta}'^\dagger \sigma_x \bar{\zeta} \\ 0 \end{pmatrix}$$

And its hermitian conjugate is given by:

$$J^{\nu\dagger} = \left(\left(2\bar{G}_E^* + \frac{Q\sqrt{1+\tau}}{\sin \frac{\theta_B}{2}} \bar{F}_3^* \right) \bar{\zeta}^\dagger \bar{\zeta}' - i \frac{Q^2 \sqrt{1+\tau}}{2M} \cot \frac{\theta_B}{2} \bar{F}_3^* \bar{\zeta}^\dagger \sigma_y \bar{\zeta}', \quad -iQ\bar{G}_M^* \bar{\zeta}^\dagger \sigma_y \bar{\zeta}', \quad iQ\bar{G}_M^* \bar{\zeta}^\dagger \sigma_x \bar{\zeta}', \quad 0 \right)$$

Having the current and its hermitian conjugate, we can build the hadronic tensor in the Breit

frame to obtain:

$$W^{\mu\nu} = \frac{1}{2} \begin{pmatrix} 4M^2\tilde{G}_E\tilde{G}_E^* + 4M[A\Re(\tilde{G}_E\tilde{F}_3^*) - B\Im(\tilde{G}_E\tilde{F}_3^*)\langle\sigma_y\rangle] & -iQ[(A\langle\sigma_y\rangle + iB)\tilde{F}_3 + 2M\tilde{G}_E\langle\sigma_y\rangle]\tilde{G}_M^* & -iQ\tilde{G}_M^*[(A - iB\langle\sigma_y\rangle)\tilde{F}_3 + 2M\tilde{G}_E]\langle\sigma_x\rangle & 0 \\ iQ[(A\langle\sigma_y\rangle - iB)\tilde{F}_3 + 2M\tilde{G}_E^*\langle\sigma_y\rangle]\tilde{G}_M & Q^2\tilde{G}_M\tilde{G}_M^* & iQ^2\tilde{G}_M\tilde{G}_M^*\langle\sigma_z\rangle & 0 \\ iQ\tilde{G}_M[(A + iB\langle\sigma_y\rangle)\tilde{F}_3 + 2M\tilde{G}_E^*]\langle\sigma_x\rangle & -iQ^2\tilde{G}_M\tilde{G}_M^*\langle\sigma_z\rangle & Q^2\tilde{G}_M\tilde{G}_M^* & 0 \\ 0 & 0 & 0 & 0 \end{pmatrix} \quad (1.54)$$

Where:

$$A = \frac{Q\sqrt{1+\tau}}{\sin\frac{\theta_B}{2}}$$

$$B = \frac{Q^2\sqrt{1+\tau}}{2M} \cot\frac{\theta_B}{2}$$

\Re and \Im stand for the real and imaginary part, respectively. The overall $\frac{1}{2}$ factor comes from the average over the initial spin states. We adopted the notation $\zeta'\sigma_X\zeta'^{\dagger} \equiv \langle\sigma_X\rangle$ for clarity. We also used the normalization relations of the spinors $\zeta\zeta^{\dagger} = 1$, $\zeta'\zeta'^{\dagger} = 1$ and the completeness relation:

$$\sum_{s=1,2} \zeta^s \zeta^{s\dagger} = 1 \quad (1.55)$$

The contraction of the leptonic and hadronic tensor is then:

$$\begin{aligned}
L_{\mu\nu}W^{\mu\nu} &= 4Q^2 \cot^2 \frac{\theta_B}{2} \left[M^2 \tilde{G}_E \tilde{G}_E^* + MA \Re(\tilde{G}_E \tilde{F}_3^*) - MB \Im(\tilde{G}_E \tilde{F}_3^*) \langle \sigma_y \rangle \right] \\
&+ \frac{Q^2 \cot^2 \frac{\theta_B}{2}}{\sin \frac{\theta_B}{2}} \left\{ 2QB \Re(\tilde{G}_M \tilde{F}_3^*) + 2Q \Im[(A \tilde{F}_3^* + 2M \tilde{G}_E^*) \tilde{G}_M] \langle \sigma_y \rangle \right\} \\
&- 2hQ^3 \cot^2 \frac{\theta_B}{2} \left\{ \Re[\tilde{G}_M^* (A \tilde{F}_3 + 2M \tilde{G}_E)] \langle \sigma_x \rangle + 2 \Re(B \tilde{G}_M^* \tilde{F}_3) \langle \sigma_z \rangle \right\} \\
&+ \frac{2hQ^4}{\sin \frac{\theta_B}{2}} \Re(\tilde{G}_M \tilde{G}_M^*) \langle \sigma_z \rangle + Q^4 \tilde{G}_M \tilde{G}_M^* \left(\frac{1}{\sin^2 \frac{\theta_B}{2}} + 1 \right)
\end{aligned} \tag{1.56}$$

We see that the contraction is a sum of unpolarized and polarized (proportional to $\langle \sigma_x \rangle$, $\langle \sigma_y \rangle$ and $\langle \sigma_z \rangle$) terms:

$$L_{\mu\nu}W^{\mu\nu} \equiv L_{\mu\nu}W_{unpol}^{\mu\nu} + L_{\mu\nu}W_{\langle \sigma_x \rangle}^{\mu\nu} + L_{\mu\nu}W_{\langle \sigma_y \rangle}^{\mu\nu} + L_{\mu\nu}W_{\langle \sigma_z \rangle}^{\mu\nu} \tag{1.57}$$

1.3.3 Unpolarized cross section

We will first consider the unpolarized terms of the contraction only:

$$\begin{aligned}
L_{\mu\nu}W_{unpol}^{\mu\nu} &= 2Q^2 \cot^2 \frac{\theta_B}{2} \left(M^2 |\tilde{G}_E|^2 + \frac{MQ}{\sin \frac{\theta_B}{2}} \sqrt{1+\tau} \Re(\tilde{G}_E \tilde{F}_3^*) \right) \\
&+ \frac{Q^5 \sqrt{1+\tau} \cot^2 \frac{\theta_B}{2}}{2M \sin \frac{\theta_B}{2}} \Re(\tilde{G}_M^* \tilde{F}_3) + \frac{Q^4}{2} |\tilde{G}_M|^2 \left(\frac{1}{\sin^2 \frac{\theta_B}{2}} + 1 \right)
\end{aligned} \tag{1.58}$$

Using: $\Re(\tilde{G}_E \tilde{F}_3^*) = G_E \Re(\tilde{F}_3)$ and $\Re(\tilde{G}_M^* \tilde{F}_3) = G_M \Re(\tilde{F}_3)$, the above expression becomes:

$$\begin{aligned}
L_{\mu\nu}W_{unpol}^{\mu\nu} &= 2M^2 Q^2 \left[\cot^2 \frac{\theta_B}{2} \left(|\tilde{G}_E|^2 + \tau \frac{|\tilde{G}_M|^2}{\cos^2 \frac{\theta_B}{2}} \right) + \tau |\tilde{G}_M|^2 + \frac{\cot^2 \frac{\theta_B}{2}}{\sin \frac{\theta_B}{2}} \sqrt{1+\tau} \right. \\
&\times \left. \left(\frac{Q}{M} G_E \Re(\tilde{F}_3) + \frac{Q^3}{4M^3} G_M \Re(\tilde{F}_3) \right) \right] \\
&= 2M^2 Q^2 \left\{ \frac{\cot^2 \frac{\theta_B}{2}}{1+\tau} \left[|\tilde{G}_E|^2 + \tau |\tilde{G}_M|^2 \left(1 + (1+\tau) \tan^2 \frac{\theta_B}{2} \right) \right] \right. \\
&\left. + \frac{\cot^2 \frac{\theta_B}{2}}{\sin \frac{\theta_B}{2}} \sqrt{1+\tau} \left(\frac{Q}{M} G_E \Re(\tilde{F}_3) + \frac{Q^3}{4M^3} G_M \Re(\tilde{F}_3) \right) \right\}
\end{aligned} \tag{1.59}$$

Using (1.35) and (1.37) we find:

$$\frac{\cot^2 \frac{\theta_B}{2}}{\sin \frac{\theta_B}{2}} = \frac{2\nu}{MQ\sqrt{1+\tau}} \frac{\cot^2 \frac{\theta_e}{2}}{1+\tau} \quad (1.60)$$

Plugging this into (1.59), the unpolarized contraction becomes:

$$\begin{aligned} L_{\mu\nu} W_{unpol}^{\mu\nu} &= 2M^2 Q^2 \cot^2 \frac{\theta_e}{2} \left[\frac{|\tilde{G}_E|^2 + \tau |\tilde{G}_M|^2}{1+\tau} \left(1 + 2(1+\tau) \tan^2 \frac{\theta_e}{2} \right) \right. \\ &\quad \left. + \frac{2\nu \cot^2 \frac{\theta_e}{2}}{M(1+\tau)} \left(\frac{1}{M} G_E \Re(\tilde{F}_3) + \frac{Q^2}{4M^3} G_M \Re(\tilde{F}_3) \right) \right] \\ &= \frac{2\tau M^2 Q^2 \cot^2 \frac{\theta_e}{2}}{\epsilon(1+\tau)} \underbrace{\left[|\tilde{G}_E|^2 \frac{\epsilon}{\tau} + |\tilde{G}_M|^2 + 4\epsilon \left(\frac{G_E \Re(\tilde{F}_3)}{M} + \frac{\nu}{2M^2} G_M \Re(\tilde{F}_3) \right) \right]}_{\sigma_r} \end{aligned} \quad (1.61)$$

The use of

$$\begin{aligned} |\tilde{G}_E|^2 &= G_E^2 + 2G_E \Re(\delta\tilde{G}_E) \\ |\tilde{G}_M|^2 &= G_M^2 + 2G_M \Re(\delta\tilde{G}_M) \\ \tau &= \frac{\nu}{2M} \end{aligned}$$

gives

$$\sigma_r = G_M^2 + \frac{\epsilon}{\tau} G_E^2 + \frac{2\epsilon}{\tau} G_E \Re\left(\delta\tilde{G}_E + \frac{\nu}{M^2} \tilde{F}_3\right) + 2G_M \Re\left(\delta\tilde{G}_M + \frac{\epsilon\nu}{M^2} \tilde{F}_3\right) + \mathcal{O}(e^4) \quad (1.62)$$

σ_r is called the reduced cross section. The same expression has been calculated in the appendix (B.52) using the standard trace techniques.

1.3.4 Transferred polarization components

In order to extract the polarization components from the polarized contraction, it is necessary to evaluate the products $\bar{\zeta}'\sigma_x\zeta'^{\dagger} = \langle\sigma_x\rangle$, $\bar{\zeta}'\sigma_y\zeta'^{\dagger} = \langle\sigma_y\rangle$ and $\bar{\zeta}'\sigma_z\zeta'^{\dagger} = \langle\sigma_z\rangle$. Then we write the Pauli matrices (σ_x , σ_y and σ_z) and their eigenvectors for a scattered proton with positive or negative helicity state.

$$\sigma_x = \begin{pmatrix} 0 & 1 \\ 1 & 0 \end{pmatrix}, \quad \zeta'_{(\mathbf{x},+|\lambda'_p|)} = \begin{pmatrix} \frac{1}{\sqrt{2}} \\ \frac{1}{\sqrt{2}} \end{pmatrix}, \quad \zeta'_{(\mathbf{x},-|\lambda'_p|)} = \begin{pmatrix} \frac{1}{\sqrt{2}} \\ -\frac{1}{\sqrt{2}} \end{pmatrix} \quad (1.63)$$

$$\sigma_y = \begin{pmatrix} 0 & -i \\ i & 0 \end{pmatrix}, \quad \zeta'_{(\mathbf{y},+|\lambda'_p|)} = \begin{pmatrix} \frac{1}{\sqrt{2}} \\ \frac{i}{\sqrt{2}} \end{pmatrix}, \quad \zeta'_{(\mathbf{y},-|\lambda'_p|)} = \begin{pmatrix} \frac{1}{\sqrt{2}} \\ -\frac{i}{\sqrt{2}} \end{pmatrix} \quad (1.64)$$

$$\sigma_z = \begin{pmatrix} 1 & 0 \\ 0 & -1 \end{pmatrix}, \quad \zeta'_{(\mathbf{z},+|\lambda'_p|)} = \begin{pmatrix} 1 \\ 0 \end{pmatrix}, \quad \zeta'_{(\mathbf{z},-|\lambda'_p|)} = \begin{pmatrix} 0 \\ 1 \end{pmatrix} \quad (1.65)$$

For example, $\zeta'_{(\mathbf{x},+|\lambda'_p|)}$ describes a scattered proton with positive helicity $+|\lambda'_p|$ along the x -axis. Therefore, for a scattered proton in a positive (negative) helicity state along the x -axis, meaning a final spin-up (down) state in the reaction plane but transverse to the momentum transfer, we find the following products:

$$\langle\sigma_x\rangle_{\mathbf{x}} = \bar{\zeta}'_{(\mathbf{x},\pm|\lambda'_p|)}\sigma_x\zeta'_{(\mathbf{x},\pm|\lambda'_p|)} = \pm 1 \quad (1.66)$$

$$\langle\sigma_y\rangle_{\mathbf{x}} = \bar{\zeta}'_{(\mathbf{x},\pm|\lambda'_p|)}\sigma_y\zeta'_{(\mathbf{x},\pm|\lambda'_p|)} = 0 \quad (1.67)$$

$$\langle\sigma_z\rangle_{\mathbf{x}} = \bar{\zeta}'_{(\mathbf{x},\pm|\lambda'_p|)}\sigma_z\zeta'_{(\mathbf{x},\pm|\lambda'_p|)} = 0 \quad (1.68)$$

This describes the transverse polarization of the recoil proton.

For a scattered proton in a positive (negative) helicity state along the y -axis, meaning a final

spin-up (down) state in the out of plane direction (normal to the scattering plane), we have:

$$\langle \sigma_x \rangle_{\mathbf{y}} = \xi_{(\mathbf{y}, \pm | \lambda'_p |)}'^{\dagger} \sigma_x \xi'_{(\mathbf{y}, \pm | \lambda'_p |)} = 0 \quad (1.69)$$

$$\langle \sigma_y \rangle_{\mathbf{y}} = \xi_{(\mathbf{y}, \pm | \lambda'_p |)}'^{\dagger} \sigma_y \xi'_{(\mathbf{y}, \pm | \lambda'_p |)} = \pm 1 \quad (1.70)$$

$$\langle \sigma_z \rangle_{\mathbf{y}} = \xi_{(\mathbf{y}, \pm | \lambda'_p |)}'^{\dagger} \sigma_z \xi'_{(\mathbf{y}, \pm | \lambda'_p |)} = 0 \quad (1.71)$$

This describes the normal polarization of the recoil proton.

Finally, for a scattered proton in a positive (negative) helicity state along the z-axis, meaning a final spin-up (down) state along the momentum transfer, we obtain:

$$\langle \sigma_x \rangle_{\mathbf{z}} = \xi_{(\mathbf{z}, \pm | \lambda'_p |)}'^{\dagger} \sigma_x \xi'_{(\mathbf{z}, \pm | \lambda'_p |)} = 0 \quad (1.72)$$

$$\langle \sigma_y \rangle_{\mathbf{z}} = \xi_{(\mathbf{z}, \pm | \lambda'_p |)}'^{\dagger} \sigma_y \xi'_{(\mathbf{z}, \pm | \lambda'_p |)} = 0 \quad (1.73)$$

$$\langle \sigma_z \rangle_{\mathbf{z}} = \xi_{(\mathbf{z}, \pm | \lambda'_p |)}'^{\dagger} \sigma_z \xi'_{(\mathbf{z}, \pm | \lambda'_p |)} = \pm 1 \quad (1.74)$$

This describes the longitudinal polarization of the recoil proton.

Therefore, we obtain:

$$\begin{aligned} L_{\mu\nu} W_{(x, \pm | \lambda'_p |)}^{\mu\nu} &= -2hQ^3 \cot \frac{\theta_B}{2} \Re(\tilde{G}_M^* \tilde{G}_E) - hQ^4 \frac{\cot \frac{\theta_B}{2}}{\sin \frac{\theta_B}{2}} \sqrt{1 + \tau} G_M \Re(\tilde{F}_3) \\ L_{\mu\nu} W_{(y, \pm | \lambda'_p |)}^{\mu\nu} &= 2hMQ^3 \frac{\cot \frac{\theta_B}{2}}{\sin \frac{\theta_B}{2}} \Im(\tilde{G}_M \tilde{G}_E^*) + hQ^4 \frac{\cot \frac{\theta_B}{2}}{\sin^2 \frac{\theta_B}{2}} \sqrt{1 + \tau} \Im(\tilde{G}_M \tilde{F}_3^*) \\ &\quad - hQ^4 \cot^3 \frac{\theta_B}{2} \sqrt{1 + \tau} \Im(\tilde{G}_E \tilde{F}_3^*) \\ L_{\mu\nu} W_{(z, \pm | \lambda'_p |)}^{\mu\nu} &= \frac{hQ^4}{\sin \frac{\theta_B}{2}} |\tilde{G}_M|^2 + \frac{hQ^5}{2M} \sqrt{1 + \tau} \cot^2 \frac{\theta_B}{2} G_M \Re(\tilde{F}_3) \end{aligned} \quad (1.75)$$

The polarization components are defined by the ratio of the different polarized terms of (1.75) over the unpolarized term (1.61):

$$P_t \equiv \frac{L_{\mu\nu} W_{(x,\pm|\lambda'_p|)}^{\mu\nu}}{L_{\mu\nu} W_{unpol}^{\mu\nu}} \quad (1.76)$$

$$P_n \equiv \frac{L_{\mu\nu} W_{(y,\pm|\lambda'_p|)}^{\mu\nu}}{L_{\mu\nu} W_{unpol}^{\mu\nu}} \quad (1.77)$$

$$P_l \equiv \frac{L_{\mu\nu} W_{(z,\pm|\lambda'_p|)}^{\mu\nu}}{L_{\mu\nu} W_{unpol}^{\mu\nu}} \quad (1.78)$$

where t , n , and l stand for transverse, normal and longitudinal respectively, as explained above.

Transverse polarization

From (1.76) the transverse polarization components is given by

$$P_t = \frac{-2hQ^3 \cot \frac{\theta_B}{2} \Re(\tilde{G}_M^* \tilde{G}_E) - hQ^4 \frac{\cot \frac{\theta_B}{2}}{\sin \frac{\theta_B}{2}} \sqrt{1 + \tau} G_M \Re(\tilde{F}_3)}{2 \frac{M^2 Q^2}{(1 + \tau)} \frac{\tau}{\epsilon} \cot^2 \frac{\theta_e}{2} \sigma_r} \quad (1.79)$$

Using the relations between the scattering angle in the Breit frame and the scattering angle in the lab frame (1.35) and (1.37), we have:

$$\begin{aligned} \frac{\cot \frac{\theta_B}{2}}{\sin \frac{\theta_B}{2}} &= \frac{\cot^2 \frac{\theta_B}{2}}{\cos \frac{\theta_B}{2}} \\ &= \frac{\cot^2 \frac{\theta_e}{2}}{1 + \tau} \tan \frac{\theta_e}{2} \frac{2\nu}{MQ} \\ &= \frac{2\nu}{MQ(1 + \tau)} \cot \frac{\theta_e}{2} \end{aligned} \quad (1.80)$$

Therefore:

$$P_t = -h \frac{Q}{M} \frac{\epsilon \sqrt{1 - \tau}}{\tau \sigma_r} \frac{1}{\cot \frac{\theta_e}{2}} \left(\Re(\tilde{G}_M^* \tilde{G}_E) + \frac{\nu}{M^2} G_M \Re(\tilde{F}_3) + \mathcal{O}(e^4) \right) \quad (1.81)$$

By noticing that:

$$\Re(\tilde{G}_M^* \tilde{G}_E) = G_E G_M + G_E \Re(\delta \tilde{G}_M) + G_M \Re(\delta \tilde{G}_E) + \mathcal{O}(e^4) \quad (1.82)$$

and by expressing the tangent of the incident electron angle as a function of ϵ :

$$\epsilon = \frac{1}{1 + 2(1 + \tau) \tan^2 \frac{\theta_e}{2}} \Rightarrow \tan \frac{\theta_e}{2} = \sqrt{\frac{1 - \epsilon}{2\epsilon(1 + \tau)}} \quad (1.83)$$

we obtain for the transverse polarization component the following expression:

$$P_t = -h \sqrt{\frac{\epsilon(1 - \epsilon)}{\tau}} \frac{1}{\sigma_r} \left[G_E G_M + G_M \Re\left(\delta \tilde{G}_E + \frac{\nu}{M^2} \tilde{F}_3\right) + G_E \Re(\delta \tilde{G}_M) + \mathcal{O}(e^4) \right] \quad (1.84)$$

Longitudinal polarization

From (1.78), the longitudinal polarization component is given by:

$$\begin{aligned} P_l &= \frac{\frac{hQ^4}{\sin \frac{\theta_e}{2}} |\tilde{G}_M|^2 + \frac{hQ^5}{2M} \sqrt{1 + \tau} \cot^2 \frac{\theta_B}{2} G_M \Re(\tilde{F}_3)}{2 \frac{M^2 Q^2}{(1 + \tau)} \frac{\tau}{\epsilon} \cot^2 \frac{\theta_e}{2} \sigma_r} \\ &= \frac{\epsilon(1 + \tau)}{\tau \sigma_r} \left(\frac{h}{\sin \frac{\theta_B}{2} \cot^2 \frac{\theta_e}{2}} \frac{Q^2}{2M^2} |\tilde{G}_M|^2 + h \underbrace{\frac{Q}{M}}_{2\sqrt{\tau}} \underbrace{\frac{Q^2}{4M^2}}_{\tau} \sqrt{1 + \tau} \underbrace{\frac{\cot^2 \frac{\theta_B}{2}}{\cot^2 \frac{\theta_e}{2}}}_{(1 + \tau)^{-1}} G_M \Re(\tilde{F}_3) \right) \end{aligned} \quad (1.85)$$

Looking at the first term in the above expression, we have:

$$\begin{aligned} \frac{1}{\sin \frac{\theta_B}{2} \cot^2 \frac{\theta_e}{2}} &= \frac{1}{(1 + \tau) \cos \frac{\theta_B}{2} \cot \frac{\theta_B}{2}} \\ &= \frac{1}{1 + \tau} \tan \frac{\theta_e}{2} \frac{2\nu}{MQ} \frac{\sqrt{1 + \tau}}{\cot \frac{\theta_e}{2}} \\ &= \frac{1}{\sqrt{\tau(1 + \tau)}} \frac{\nu}{M^2} \tan^2 \frac{\theta_e}{2} \\ &= \frac{1}{\sqrt{\tau(1 + \tau)}} \frac{\nu}{M^2} \frac{1 - \epsilon}{2\epsilon(1 + \tau)} \end{aligned} \quad (1.86)$$

A useful relation between ν , τ and the kinematical parameter ϵ is :

$$\frac{\nu}{M^2} = \sqrt{\frac{\tau(1+\tau)(1+\epsilon)}{1-\epsilon}} \Rightarrow \sqrt{\tau(1+\tau)} = \frac{\nu}{M^2} \sqrt{\frac{1-\epsilon}{1+\epsilon}} \quad (1.87)$$

The longitudinal polarization then becomes:

$$\begin{aligned} P_l &= h \frac{\sqrt{1-\epsilon^2}}{\sigma_r} |\tilde{G}_M|^2 + 2h\epsilon \frac{\nu}{M^2} \sqrt{\frac{1-\epsilon}{1+\epsilon}} G_M \Re(\tilde{F}_3) + \mathcal{O}(e^4) \\ &= h \frac{\sqrt{1-\epsilon^2}}{\sigma_r} \left[G_M^2 + 2G_M \Re \left(\delta \tilde{G}_M + \frac{\nu}{M^2} \frac{\epsilon}{1+\epsilon} \tilde{F}_3 \right) + \mathcal{O}(e^4) \right] \end{aligned} \quad (1.88)$$

Normal polarization

From (1.77), the normal polarization components given by:

$$\begin{aligned} P_n &= h \left[\underbrace{2MQ^3 \frac{\cot \frac{\theta_B}{2}}{\sin \frac{\theta_B}{2}} \Im(\tilde{G}_M \tilde{G}_E^*)}_{(1)} + \underbrace{Q^4 \frac{\cot \frac{\theta_B}{2}}{\sin^2 \frac{\theta_B}{2}} \sqrt{1+\tau} \Im(\tilde{G}_M \tilde{F}_3^*)}_{(2)} \right. \\ &\quad \left. \underbrace{-Q^4 \cot^3 \frac{\theta_B}{2} \sqrt{1+\tau} \Im(\tilde{G}_E \tilde{F}_3^*)}_{(3)} \right] \frac{1}{2 \frac{M^2 Q^2}{(1+\tau)} \frac{\tau}{\epsilon} \cot^2 \frac{\theta_E}{2} \sigma_r} \end{aligned} \quad (1.89)$$

Note that the three terms (1), (2) and (3) contained the division by the unpolarized term.

Plugging (1.83) into (1.80) we find:

$$\frac{\cot \frac{\theta_B}{2}}{\sin \frac{\theta_B}{2}} = \frac{\nu}{MQ(1+\tau)} \sqrt{\frac{2\epsilon(1+\tau)}{1-\epsilon}} \quad (1.90)$$

The first term of (1.89) becomes:

$$\begin{aligned}
(1) &= h \frac{4Q^2 v}{1+\tau} \sqrt{\frac{2\epsilon(1+\tau)}{1-\epsilon}} \frac{\epsilon(1+\tau)}{\tau} \frac{\tan^2 \frac{\theta_e}{2}}{2M^2 Q^2} \Im(\tilde{G}_M \tilde{G}_E^*) \\
&= 2h \sqrt{\frac{\tau(1+\tau)(1+\epsilon)}{1-\epsilon}} \sqrt{\frac{2\epsilon(1+\tau)}{1-\epsilon}} \frac{\epsilon(1-\epsilon)}{2\tau\epsilon(1+\tau)} \Im(\tilde{G}_M \tilde{G}_E^*) \\
&= h \sqrt{\frac{2\epsilon(1+\epsilon)}{\tau}} \Im(\tilde{G}_M \tilde{G}_E^*)
\end{aligned} \tag{1.91}$$

Noticing that: $\frac{\cot \frac{\theta_B}{2}}{\sin^2 \frac{\theta_B}{2}} = \frac{\cot^3 \frac{\theta_B}{2}}{\cos^2 \frac{\theta_B}{2}}$, we find for the second term (2):

$$\begin{aligned}
(2) &= hQ^4 \sqrt{1+\tau} \frac{\cot^3 \frac{\theta_B}{2}}{\cos^2 \frac{\theta_B}{2}} \frac{\epsilon}{2M^2 Q^2 \tau \cot^2 \frac{\theta_B}{2}} \Im(\tilde{G}_M \tilde{F}_3^*) \\
&= hQ^4 \sqrt{1+\tau} \frac{4v^2}{M^2 Q^2 \sqrt{1+\tau}} \tan \frac{\theta_e}{2} \frac{\epsilon}{2M^2 Q^2 \tau} \Im(\tilde{G}_M \tilde{F}_3^*) \\
&= h \frac{2v^2 \epsilon}{M^4 \tau} \sqrt{\frac{1-\epsilon}{2\epsilon(1+\tau)}} \Im(\tilde{G}_M \tilde{F}_3^*) \\
&= h \frac{2v\epsilon}{M^2 \tau} \sqrt{\frac{\tau(1+\tau)(1+\epsilon)}{1-\epsilon}} \sqrt{\frac{1-\epsilon}{2\epsilon(1+\tau)}} \Im(\tilde{G}_M \tilde{F}_3^*) \\
&= h \frac{v}{M^2} \sqrt{\frac{2\epsilon(1+\epsilon)}{\tau}} \Im(\tilde{G}_M \tilde{F}_3^*)
\end{aligned} \tag{1.92}$$

In the second to last step, we used the relation (1.87) to express $\frac{v}{M^2}$.

Finally, the evaluation of the third term of (1.89) is straightforward:

$$\begin{aligned}
(3) &= -hQ^4 \frac{\cot^3 \frac{\theta_e}{2}}{1+\tau} \frac{\epsilon(1+\tau)}{2M^2 Q^2 \tau \cot^2 \frac{\theta_e}{2}} \Im(\tilde{G}_E \tilde{F}_3^*) \\
&= -h \underbrace{\frac{Q^2}{2M^2}}_{2\tau} \frac{\epsilon}{\tau} \cot \frac{\theta_e}{2} \Im(\tilde{G}_E \tilde{F}_3^*) \\
&= -2h\epsilon \sqrt{\frac{2\epsilon(1+\tau)}{1-\epsilon}} \times \frac{\sqrt{\tau}}{\sqrt{\tau}} \Im(\tilde{G}_E \tilde{F}_3^*) \\
&= -h \sqrt{\frac{2\epsilon(1+\epsilon)}{\tau}} \left(\frac{2\epsilon}{1+\epsilon} \frac{v}{M^2} \right) \Im(\tilde{G}_E \tilde{F}_3^*)
\end{aligned} \tag{1.93}$$

In the last step, we used again the relation (1.87), but to express this time the term $\sqrt{\tau(1+\tau)}$ as a function of ν , M and ϵ .

The different imaginary parts contained in the expression (1.89) are given by:

$$\begin{aligned}\Im(\tilde{G}_M \tilde{G}_E^*) &= \Im[(G_M + \delta\tilde{G}_M)(G_E + \delta\tilde{G}_E^*)] \\ &= -G_M \Im(\delta\tilde{G}_E) + G_E \Im(\delta\tilde{G}_M) + \mathcal{O}(e^4)\end{aligned}\quad (1.94)$$

$$\Im(\tilde{G}_M \tilde{F}_3^*) = -G_M \Im(\tilde{F}_3) + \mathcal{O}(e^4) \quad (1.95)$$

$$\Im(\tilde{G}_E \tilde{F}_3^*) = -G_E \Im(\tilde{F}_3) + \mathcal{O}(e^4) \quad (1.96)$$

Therefore, the normal polarization component becomes:

$$P_n = h\sqrt{\frac{2\epsilon(1+\epsilon)}{\tau}} \frac{1}{\sigma_r} \left[-G_M \Im\left(\delta\tilde{G}_E + \frac{\nu}{M^2} \tilde{F}_3\right) + G_E \Im\left(\delta\tilde{G}_M \frac{2\epsilon}{1+\epsilon} \frac{\nu}{M^2} \tilde{F}_3\right) + \mathcal{O}(e^4) \right] \quad (1.97)$$

Summarizing the different results, we obtain:

$$\begin{aligned}P_t &= -h\sqrt{\frac{\epsilon(1-\epsilon)}{\tau}} \frac{1}{\sigma_r} \left[G_E G_M + G_M \Re\left(\delta\tilde{G}_E + \frac{\nu}{M^2} \tilde{F}_3\right) + G_E \Re(\delta\tilde{G}_M) + \mathcal{O}(e^4) \right] \\ P_n &= h\sqrt{\frac{2\epsilon(1+\epsilon)}{\tau}} \frac{1}{\sigma_r} \left[-G_M \Im\left(\delta\tilde{G}_E + \frac{\nu}{M^2} \tilde{F}_3\right) + G_E \Im\left(\delta\tilde{G}_M \frac{2\epsilon}{1+\epsilon} \frac{\nu}{M^2} \tilde{F}_3\right) + \mathcal{O}(e^4) \right] \\ P_l &= h\frac{\sqrt{1-\epsilon^2}}{\sigma_r} \left[G_M^2 + 2G_M \Re\left(\delta\tilde{G}_M + \frac{\nu}{M^2} \frac{\epsilon}{1+\epsilon} \tilde{F}_3\right) + \mathcal{O}(e^4) \right]\end{aligned}\quad (1.98)$$

where the reduced cross section σ_r is given by:

$$\sigma_r = G_M^2 + \frac{\epsilon}{\tau} G_E^2 + \frac{2\epsilon}{\tau} G_E \Re\left(\delta\tilde{G}_E + \frac{\nu}{M^2} \tilde{F}_3\right) + 2G_M \Re\left(\delta\tilde{G}_M + \frac{\epsilon\nu}{M^2} \tilde{F}_3\right) + \mathcal{O}(e^4)$$

We define the polarization component ratio by: $R \equiv -\mu_p \sqrt{\frac{\tau(1+\epsilon)}{2\epsilon}} \frac{P_t}{P_l}$. Using the expressions just above and defining $R_{Born} \equiv \frac{G_E}{G_M}$ we obtain:

$$\begin{aligned}
\frac{P_t}{P_l} &= -\sqrt{\frac{2\epsilon(1-\epsilon)}{\tau}} \frac{1}{\sqrt{1-\epsilon^2}} \frac{G_M \left[G_E + \Re\left(\delta\tilde{G}_E + \frac{\nu}{M^2} \tilde{F}_3\right) + R_{Born} \Re(\delta\tilde{G}_M) \right]}{G_M \left[G_M + 2\Re\left(\delta\tilde{G}_M + \frac{\nu}{M^2} \frac{\epsilon}{1+\epsilon} \tilde{F}_3\right) \right]} + \mathcal{O}(e^4) \\
&= -\sqrt{\frac{2\epsilon}{\tau(1+\epsilon)}} \frac{1}{G_M} \left[G_E + \Re\left(\delta\tilde{G}_E + \frac{\nu}{M^2} \tilde{F}_3\right) + R_{Born} \Re(\delta\tilde{G}_M) \right] \\
&\quad \times \left[1 - \frac{2}{G_M} \Re\left(\delta\tilde{G}_M + \frac{\nu}{M^2} \frac{\epsilon}{1+\epsilon} \tilde{F}_3\right) \right] + \mathcal{O}(e^4) \\
&= -\sqrt{\frac{2\epsilon}{\tau(1+\epsilon)}} \Re\left(R_{Born} + \frac{R_{Born}}{G_M} \delta\tilde{G}_M + \frac{\delta\tilde{G}_E}{G_M} + \frac{\nu\tilde{F}_3}{G_M M^2} - \frac{2R}{G_M} \delta\tilde{G}_M - \frac{\nu}{M^2} \frac{R_{Born}\epsilon}{1+\epsilon} \tilde{F}_3 \right) + \mathcal{O}(e^4) \\
&= -\sqrt{\frac{2\epsilon}{\tau(1+\epsilon)}} \Re\left[R_{Born} \left(1 - \frac{\delta\tilde{G}_M}{G_M} - \frac{\nu}{M^2} \frac{2\epsilon}{1+\epsilon} \frac{\tilde{F}_3}{G_M} \right) + \frac{\delta\tilde{G}_E}{G_M} + \frac{\nu\tilde{F}_3}{G_M M^2} \right] + \mathcal{O}(e^4) \\
&= -\sqrt{\frac{2\epsilon}{\tau(1+\epsilon)}} R_{Born} \Re\left[1 - \frac{\delta\tilde{G}_M}{G_M} + \frac{\delta\tilde{G}_E}{G_E} + \frac{\nu\tilde{F}_3}{M^2} \left(\frac{1}{G_E} - \frac{2\epsilon}{1+\epsilon} \frac{1}{G_M} \right) \right] + \mathcal{O}(e^4) \tag{1.99}
\end{aligned}$$

So R is given by:

$$\begin{aligned}
R &= -\sqrt{\frac{\tau(1+\epsilon)}{2\epsilon}} \frac{P_t}{P_l} \\
&= R_{Born} \left[1 + \frac{\Re(\delta\tilde{G}_M)}{G_M} - \frac{\Re(\delta\tilde{G}_E)}{G_E} - \frac{\nu\Re(\tilde{F}_3)}{M^2} \left(\frac{1}{G_E} - \frac{2\epsilon}{G_M(1+\epsilon)} \right) \right] + \mathcal{O}(e^4) \tag{1.100}
\end{aligned}$$

From the above equations (1.98) and (1.100) we see that the ϵ -dependence appears as an interference between the Sachs form factors G_E and G_M and the real part of the TPEX amplitudes $\delta\tilde{G}_M$, $\delta\tilde{G}_E$ and $\delta\tilde{F}_3$.

In the Born approximation for electron-proton elastic scattering, the hermiticity of the Hamiltonian implies that the proton electromagnetic form factors are real and depend only on the momentum transfer. Therefore the TPEX contributions $\delta\tilde{G}_M$, $\delta\tilde{G}_E$ and $\delta\tilde{F}_3$ vanish. The usual expressions for the polarization components, the reduced cross section and the form factor ratio in

the Born approximation are recovered [18, 19]:

$$\begin{aligned}
P_t^{Born} &= -h\sqrt{\frac{\epsilon(1-\epsilon)}{\tau}}\frac{1}{\sigma_r}G_E G_M \\
P_n^{Born} &= 0 \\
P_\ell^{Born} &= h\frac{\sqrt{1-\epsilon^2}}{\sigma_r}G_M^2 \\
\sigma_r^{Born} &= G_M^2 + \frac{\epsilon}{\tau}G_E^2
\end{aligned} \tag{1.101}$$

The latter equation is the foundation of the Rosenbluth separation technique which extracts the square of the form factors by linear interpolation of the measured cross section. The slope and the intercept of the graph σ_{red} vs $\frac{\epsilon}{\tau}$ will give G_E^2 and G_M^2 respectively. Due to the $\frac{\epsilon}{\tau}$ multiplying G_E^2 , the cross section will be dominated by G_M^2 with increasing Q^2 , whereas the contribution of G_E^2 becomes delicate to measure.

In the experiment, we extract the ratio R and the longitudinal polarization component P_ℓ . In what follows, we will then only study these two quantities. In order to make additional quantitative comments about the TPEX contribution to the polarization observables, it is convenient to express the real parts of the TPEX amplitude relative to the magnetic form factor:

$$Y_M \equiv \Re\left(\frac{\delta\tilde{G}_M}{G_M}\right), \quad Y_E \equiv \Re\left(\frac{\delta\tilde{G}_E}{G_M}\right), \quad Y_3 \equiv \frac{\nu}{M^2}\Re\left(\frac{\delta\tilde{F}_3}{G_M}\right) \tag{1.102}$$

We rewrite the expression of R , P_ℓ and σ_r :

$$\frac{\sigma_r}{G_M^2} = 1 + \frac{\epsilon}{\tau}R_{Born}^2 + 2Y_M + 2\frac{\epsilon}{\tau}R_{Born}Y_E + 2\epsilon\left(1 + \frac{R_{Born}}{\tau}\right)Y_3 + \mathcal{O}(e^4) \tag{1.103}$$

$$R = R_{Born} + Y_E - R_{Born}Y_M + \left(1 - \frac{2\epsilon}{1+\epsilon}R_{Born}\right)Y_3 \tag{1.104}$$

$$P_\ell = h\frac{\sqrt{1-\epsilon^2}}{\sigma_r}G_M^2\left(1 + 2Y_M + \frac{2\epsilon}{1+\epsilon}Y_3\right) \tag{1.105}$$

It is also more convenient to study P_ℓ relative to its Born value P_ℓ^{Born} . The ratio P_ℓ/P_ℓ^{Born} expressed

as a function of the Y amplitudes is given by:

$$\begin{aligned}
\frac{P_\ell}{P_\ell^{\text{Born}}} &= h \frac{\sqrt{1-\epsilon^2} G_M^4 \left(1 + 2Y_M + \frac{2\epsilon}{1+\epsilon} Y_3\right)}{1 + \frac{\epsilon}{\tau} R_{\text{Born}}^2 + 2Y_M + 2\frac{\epsilon}{\tau} R_{\text{Born}} Y_E + 2\epsilon \left(1 + \frac{R_{\text{Born}}}{\tau}\right) Y_3} \times \frac{1 + \frac{\epsilon}{\tau} R_{\text{Born}}^2}{h\sqrt{1-\epsilon^2} G_M^4} \\
&= \left(1 + 2Y_M + \frac{2\epsilon}{1+\epsilon} Y_3\right) \left[1 - \frac{2Y_M + 2\frac{\epsilon}{\tau} R_{\text{Born}} Y_E + 2\epsilon \left(1 + \frac{R_{\text{Born}}}{\tau}\right) Y_3}{1 + \frac{\epsilon}{\tau} R_{\text{Born}}^2}\right] \\
&= 1 + \frac{1}{1 + \frac{\epsilon}{\tau} R_{\text{Born}}^2} \left[2 \left(1 + \frac{\epsilon}{\tau} R_{\text{Born}}^2\right) Y_M - 2Y_M - \frac{2\epsilon}{\tau} R_{\text{Born}} Y_E \right. \\
&\quad \left. + 2\epsilon Y_3 \left(\frac{1 + \frac{\epsilon}{\tau} R_{\text{Born}}^2}{1+\epsilon} - 1 - \frac{R_{\text{Born}}}{\tau}\right)\right] \\
&= 1 + \frac{1}{1 + \frac{\epsilon}{\tau} R_{\text{Born}}^2} \left[2 \left(\frac{\epsilon}{\tau} R_{\text{Born}}^2 Y_M - \frac{\epsilon}{\tau} R_{\text{Born}} Y_E\right) + \frac{2\epsilon}{1+\epsilon} Y_3 \left(\frac{\epsilon}{\tau} R_{\text{Born}}^2 - \epsilon - \frac{R_{\text{Born}}}{\tau}\right)\right] \\
&= 1 - \frac{2\epsilon}{1 + \frac{\epsilon}{\tau} R_{\text{Born}}^2} \left[\left[\frac{R_{\text{Born}}}{\tau} + \frac{\epsilon}{1+\epsilon} \left(1 - \frac{R_{\text{Born}}^2}{\tau}\right)\right] Y_3 + \frac{R_{\text{Born}}}{\tau} [Y_E - R_{\text{Born}} Y_M]\right] \quad (1.106)
\end{aligned}$$

Neglecting the terms proportional to the $R_{\text{Born}} = G_E/G_M$ term, we see that the TPEX contributions to σ_τ and R are proportional to $Y_M + \epsilon Y_3$ and $Y_M + Y_E$ respectively. In contrast, the TPEX corrections to P_ℓ will be entirely dominated by Y_3 .

1.3.5 Single-spin observables

The single-spin observable P_n is directly and specifically proportional to the imaginary part (absorptive part) of the TPEX (or multi-photon exchange) and is of order e^2 (relative to the factor e^2 in (1.22)). It vanishes in the OPEX approximation due to time reversal invariance [20]. We can measure this single spin observable by elastic electron-proton scattering with either the target or the electron beam spin polarized normal to the scattering plane. Another single-spin asymmetry could be accessed by considering the general expansion of the T -matrix including lepton-helicity flip. We obtain a scattering amplitude involving six invariant amplitudes. We derived already the structures that give rise to those six independent amplitudes in (1.21). Thus, using those results a

general expansion of the lepton helicity flip T -matrix is given by [21]:

$$T^{flip} = \frac{e^2}{Q^2} \frac{m}{M} \left[\bar{u}(k', h) u(k, h) \cdot \bar{u}(p', \lambda'_p) \left(\tilde{F}_4 + \tilde{F}_5 \frac{\gamma \cdot K}{M} \right) u(p, \lambda_p) + \tilde{F}_6 \bar{u}(k', h) \gamma_5 u(k, h) \cdot \bar{u}(p', \lambda'_p) \gamma_5 u(p, \lambda_p) \right] \quad (1.107)$$

As well as \tilde{G}_M , \tilde{G}_E and \tilde{F}_3 , the amplitudes \tilde{F}_4 , \tilde{F}_5 and \tilde{F}_6 are complex and depend on ϵ and Q^2 . The extracted factor $\frac{m}{M}$ emphasizes the fact that the lepton helicity-flip amplitude vanishes in the limit of a massless lepton ($m \rightarrow 0$). This single-spin asymmetry could be measured in low energy elastic muon-proton scattering.

Chapter 2

Theoretical Models

In this chapter, we will present the different theoretical calculations aimed at explaining the discrepancy observed between the proton form factor ratio data obtained by the Rosenbluth separation method, and recoil polarization technique. We will particularly dwell on the partonic and hadronic calculations. Other models based on a pQCD approach will also be described.

2.1 Partonic Model

2.1.1 General Parton Distributions (GPD) Formalism

The partonic calculation of A. V. Afanasev *et al.* [22, 23] gives an estimation of the two-photon contribution to elastic electron-proton scattering using a quark-parton representation of virtual Compton scattering.

The partonic mechanism is described by the handbag diagram shown in Figure 2.1. It consists of a hard scattering H of a lepton l off a massless quark. The quarks are “embedded” in the nucleon through the nucleon’s GPDs represented by the blob in Figure 2.1. The T -matrix of the electron-quark scattering $e(k) + q(p_q) \rightarrow e(k') + q(p'_q)$ is given by:

$$H_{h,\lambda}^{hard} = \frac{e^2 e_q^2}{Q^2} \bar{u}(k', h) \gamma_\mu u(k, h) \times \bar{u}(p'_q, \lambda) \left(\tilde{f}_1 \gamma^\mu + \tilde{f}_3 \gamma \cdot K P_q^\mu \right) u(p_q, \lambda) \quad (2.1)$$

with $P_q \equiv \frac{p_q + p'_q}{2}, K \equiv \frac{k + k'}{2}$ and where e_q is the fractional quark charge for a flavour q . The quark helicity $\lambda = \pm \frac{1}{2}$ is conserved in the hard process.

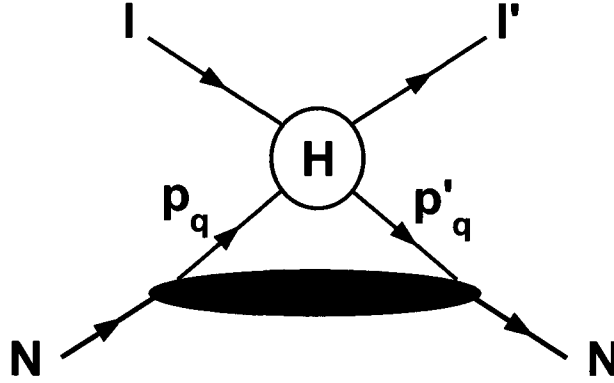


Figure 2.1: Handbag diagram.

The first step in this model is to calculate the partonic subprocess (the upper part of the handbag diagram). This hard scattering is described by the TPEX diagrams of Figure 2.2. The amplitude \tilde{f}_1 is separated into a soft and hard part: $\tilde{f}_1 = \tilde{f}_1^{soft} + \tilde{f}_1^{hard}$ [24]. In the soft part situation, one of the exchanged photons in Figure 2.2 carries zero four-momentum. This soft part is obtained by replacing the four-momentum of the other photon by q in the numerator and in the denominator in the loop integral [24]. One obtains that the real parts, $\Re(\tilde{f}_1^{hard})$ and $\Re(\tilde{f}_3)$, are infrared (IR) finite whereas $\Re(\tilde{f}_1^{soft})$, which contains a term proportional to $\ln \lambda^2$ (where λ is an infinitesimal photon mass) is IR divergent. A similar result is obtained for the imaginary parts. However, it can be shown [25] that the IR part of the imaginary part of the soft contribution of \tilde{f}_1^{soft} does not contribute to the single spin asymmetry calculation.

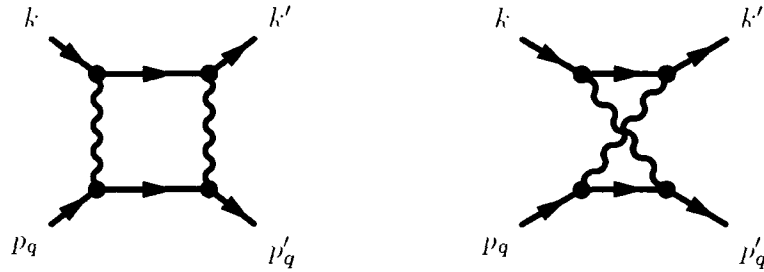


Figure 2.2: Two-photon exchange diagram to the electron-quark scattering.

After the calculation of the partonic scattering process, the second step is to describe how the quark are embedded in the nucleon. In the handbag diagram, both photons are coupled to the same quark. However, contributions exist from processes where the photons interact with different quarks. It can be shown that the sum of the resulting IR contributions of these processes and the soft contributions from the handbag diagrams give the same result as the IR contribution calculated with just a nucleon intermediate state, satisfying the low energy theorem for Compton scattering [26]. The IR divergence in the real part is cancelled when the Bremsstrahlung contribution is taken into consideration. The Bremsstrahlung originates from the interference processes where a soft photon is emitted from the electron and the proton. This implies a radiative correction term in addition to the soft part term from the direct and crossed diagrams:

$$\sigma_{R,soft} = \sigma_{1\gamma}(1 + \delta_{2\gamma,soft} + \delta_{Brems}) \quad (2.2)$$

with $\sigma_{1\gamma}$ the one-photon exchange cross section.

The finite hard parts of the handbag diagram are evaluated using the nucleon's General Parton

Distributions. The T -matrix of the reaction (1.14) is given by:

$$\begin{aligned}
T_{h,\lambda_p,\lambda_p}^{hard} &= \int_{-1}^1 \frac{dx}{x} \sum_q \frac{1}{2} (H_{h,+1/2}^{hard} + H_{h,-1/2}^{hard}) \frac{1}{2} \left[H^q(x, 0, q^2) \bar{u}(p', \lambda'_p) \gamma \cdot nu(p, \lambda_p) \right. \\
&\quad \left. + E^q(x, 0, q^2) \bar{u}(p', \lambda'_p) \frac{i\sigma^{\mu\nu} n_\mu q_\nu}{2M} u(p, \lambda_p) \right] \\
&\quad + \int_{-1}^1 \frac{dx}{x} \sum_q \frac{1}{2} (H_{h,+1/2}^{hard} - H_{h,-1/2}^{hard}) \frac{1}{2} \text{sgn}(x) \tilde{H}^q(x, 0, q^2) \bar{u}(p', \lambda'_p) \gamma \cdot n \gamma_5 u(p, \lambda_p) \quad (2.3)
\end{aligned}$$

Details about the GPDs' kinematic are given in [23]. H^q , E^q and \tilde{H}^q are the GPDs for a quark of flavor q in the proton. Furthermore, defining $\nu = P_q \cdot \hat{K}$ the hard two-photon exchange contributions are given by:

$$\delta \tilde{G}_M^{hard} = C, \quad \delta \tilde{G}_E^{hard} = - \left(\frac{1+\epsilon}{2\epsilon} \right) (A - C) + \sqrt{\frac{1+\epsilon}{2\epsilon}} B \quad \text{and} \quad \tilde{F}_3 = \frac{M^2}{\nu} \left(\frac{1+\epsilon}{2\epsilon} \right) (A - C) \quad (2.4)$$

with A , B and C defined as:

$$\begin{aligned}
A &\equiv \int_{-1}^1 \frac{dx}{x} \frac{[(\hat{s} - \hat{u}) \tilde{f}_1^{hard} - \hat{s} \hat{u} \tilde{f}_3]}{s - u} \sum_q e_q^2 (H^q - E^q) \\
B &\equiv \int_{-1}^1 \frac{dx}{x} \frac{[(\hat{s} - \hat{u}) \tilde{f}_1^{hard} - \hat{s} \hat{u} \tilde{f}_3]}{s - u} \sum_q e_q^2 (H^q - \tau E^q) \\
C &\equiv \int_{-1}^1 \tilde{f}_1^{hard} \text{sgn}(x) \sum_q e_q^2 \tilde{H}^q \quad (2.5)
\end{aligned}$$

The cross section including the two-photon corrections obtained in this GPD-based calculation can then be written as:

$$\sigma_R = \sigma_{R,soft} + \sigma_{R,hard} \quad \text{with} \quad \sigma_{R,hard} = (1 + \epsilon) G_M \Re(A) + \sqrt{2\epsilon(1 + \epsilon)} \frac{1}{\tau} G_E \Re(B) + (1 - \epsilon) G_M \Re(C) \quad (2.6)$$

The polarization components are given by:

$$\begin{aligned}
 P_t &= -\sqrt{\frac{\epsilon(1-\epsilon)}{\tau}} \frac{1}{\sigma_r} \left[G_E G_M + G_E \Re(C) + G_M \sqrt{\frac{1+\epsilon}{2\epsilon}} \Re(B) + \mathcal{O}(e^4) \right] \\
 P_n &= \sqrt{\frac{2\epsilon(1+\epsilon)}{\tau}} \frac{1}{\sigma_r} \left[G_E \Im(A) - G_M \sqrt{\frac{1+\epsilon}{2\epsilon}} \Im(B) + \mathcal{O}(e^4) \right] \\
 P_l &= \frac{\sqrt{1-\epsilon^2}}{\sigma_r} \left[G_M^2 + G_M \Re(A+C) + \mathcal{O}(e^4) \right]
 \end{aligned}$$

The models of GPDs used to estimate the hard amplitudes in (2.4) are a Gaussian model and a modified Regge model. The parametrization of these models is given in [23].

2.1.2 Results

Cross Section

The effect of the two-photon correction on the cross section are displayed on the Figure 2.3 for different values of Q^2 . The straight dotted line shows the results using the extracted values of G_{Ep}/G_{Mp} from the polarization data [7, 9]. They are not compatible with the Rosenbluth data [4] corrected only for the standard Mo and Tsai radiative corrections [13]. This is another representation of the discrepancy of the form factor ratio results obtained from cross section and polarization measurements. By including the TPEX correction based on a GPD calculation, the Rosenbluth plots presents some non-linearity at the largest values of ϵ . In particular, the observed change of slope agrees with the experimental data and allows a partial reconciliation of the Rosenbluth and polarization transfer data.

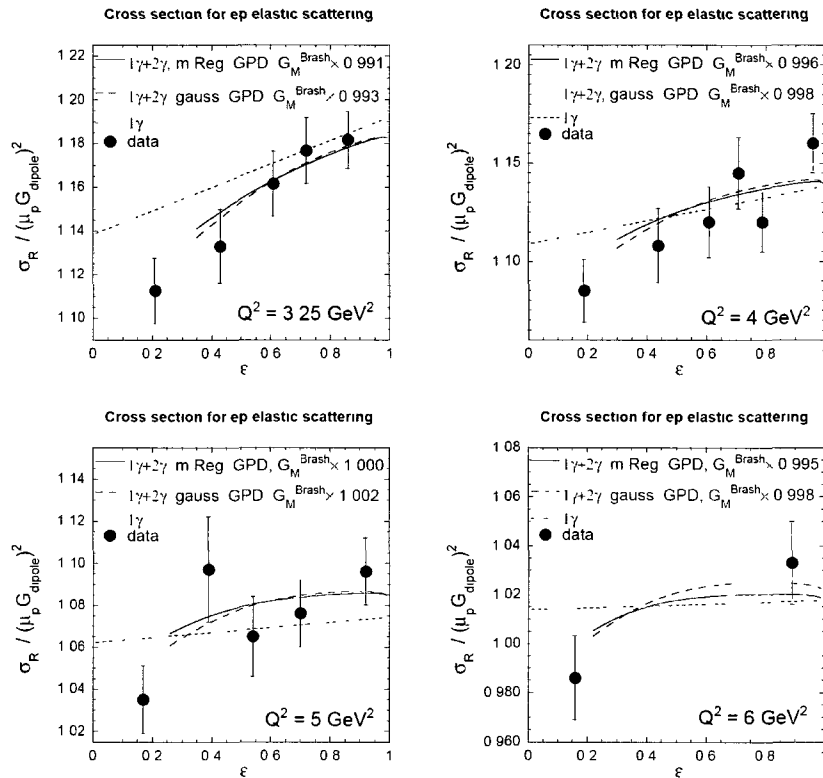


Figure 2.3: Scaled cross section prediction based on a GPD calculation from A. Afanasev *et al.* [23]. The dashed and solid curves display the results using the Gaussian GPD and the modified Regge GPD models, respectively. In both models, the parametrization of G_{Mp} of [27] was used. The data are from A. Andivahis [4]

Form Factor Ratio

Figure 2.4 shows the effect of the hard two-photon correction on the the Rosenbluth form factor ratio data. The Regge model is not shown here for reason of clarity, but gives results similar to the Gaussian GPD model. The form factor ratio results extracted using the Rosenbluth separation method including the hard two-photon corrections agree with the polarization transfer data for a Q^2 range of 2 – 3 GeV^2 . For higher Q^2 , the agreement of the two methods is partial. The slope of the Rosenbluth data remains unchanged.

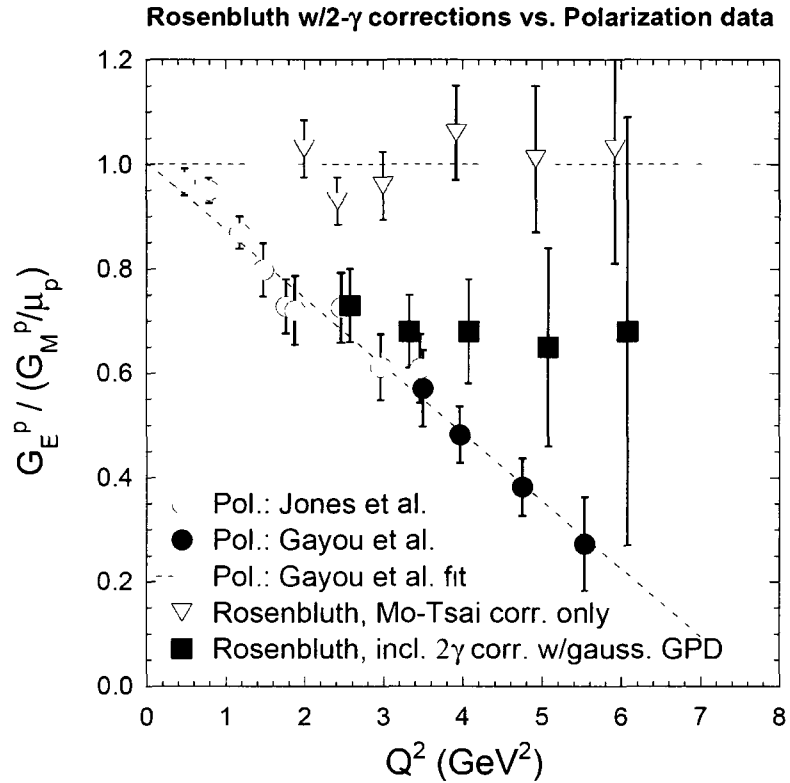


Figure 2.4: Rosenbluth and polarization data with two-photon exchange correction based on a GPD calculation from A. Afanasev *et al.* [23]. The open triangles show the Rosenbluth data [28] corrected with the standard Mo and Tsai radiative corrections. The polarization data [7, 9] are displayed with open and solid circles and include Mo and Tsai radiative corrections. The solid squares show the results obtained with the Rosenbluth data [4] and hard two-photon corrections using the Gaussian GPD-based calculation.

Longitudinal Polarization Component

The effect of the TPEX corrections on the longitudinal polarization component are very small in the GPD model as shown in Figure 2.5. Indeed, the effect on the ratio between the full calculation (including the TPEX corrections) and the OPEX calculation is less than 0.5%. Results obtained with both the Gaussian and the modified Regge GPD models are displayed in Figure 2.5.

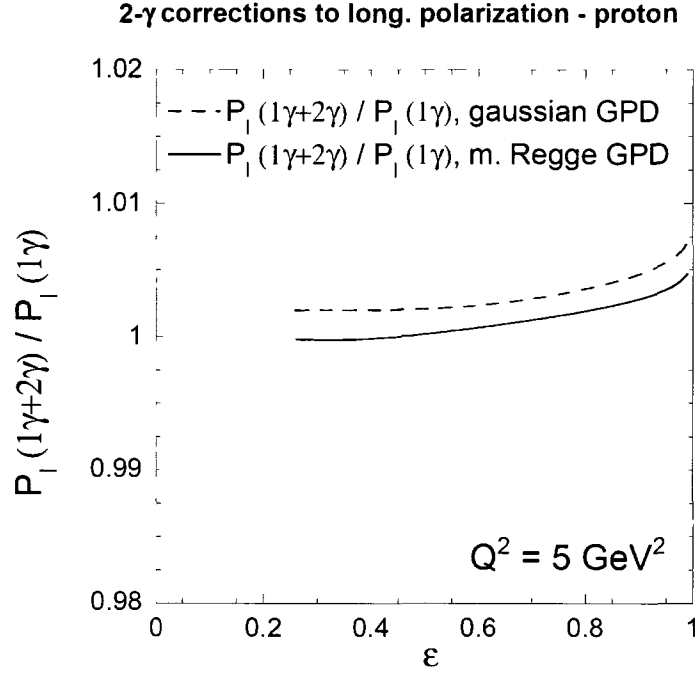


Figure 2.5: Ratio of the longitudinal polarization component P_ℓ relative to the Born Approximation value versus ϵ obtained from the two GPD models: Gaussian (dashed line) and Regge (solid line).

2.2 Hadronic Model

2.2.1 Formalism

The hadronic model of P.G. Blunden *al* [29, 30] investigates the two-photon exchange correction in elastic electron-nucleon scattering by keeping just the elastic nucleon intermediate state. Let $\frac{d\sigma_0}{d\Omega}$ be the cross section for elastic scattering (1.14) in the Born Approximation. When radiative corrections of order α are taken into consideration, the cross section can be expressed by: $\frac{d\sigma}{d\Omega} = \frac{d\sigma_0}{d\Omega}(1 + \delta)$. δ is given by calculating the one-loop integral virtual corrections (electron and proton vertex correction, vacuum polarization and two-photon exchange corrections) and also the inelastic bremsstrahlung with real photon emission [13]. With the inclusion of the radiative correction δ , one expects a better understanding of the ϵ -dependence of the Rosenbluth plot for increasing Q^2 . The corresponding amplitude \mathcal{M}_1 is given by the sum of a factorizable term

proportional to the Born amplitude \mathcal{M}_0 and a nonfactorizable term $\bar{\mathcal{M}}_1$:

$$\mathcal{M}_1 = f(\epsilon, Q^2)\mathcal{M}_0 + \bar{\mathcal{M}}_1 \quad (2.7)$$

The Born amplitude is given by:

$$\mathcal{M}_0 = -i\frac{e^2}{q^2}\bar{u}(k')\gamma_\mu u(k)\bar{u}(p')\Gamma^\mu(q)u(p) \quad \text{with} \quad q = p' - p = k - k' \quad (2.8)$$

The proton vertex Γ^μ function is expressed in terms of Dirac (F_1) and Pauli (F_2) form factors as follows: $\Gamma^\mu = F_1(q^2)\gamma^\mu + \frac{i\sigma^{\mu\nu}q^\nu}{2M}F_2(q^2)$. The ratio of the cross section (to order α) to the Born cross section is then given by:

$$\frac{|\mathcal{M}_0 + \mathcal{M}_1|^2}{|\mathcal{M}_0|^2} = 1 + \delta \quad \text{with} \quad \delta = 2f(\epsilon, Q^2) + \frac{2\Re(\mathcal{M}_0^\dagger\bar{\mathcal{M}}_1)}{|\mathcal{M}_0|^2} \quad (2.9)$$

The dominant factorizable term is essentially independent of the hadronic structure. It contains the electron vertex and the vacuum polarization corrections, the IR divergent parts of both the two-photon exchange and the nucleon vertex corrections. However, the latter three contributions depend on Q^2 only and therefore are not important to the ϵ -dependence of the Rosenbluth plot. Thus, the remaining contributions for the study of the ϵ -dependence of the virtual photon corrections are the IR divergent parts of the two-photon exchange. The model dependent term $\bar{\mathcal{M}}_1$ includes the two-photon exchange and the finite proton vertex corrections. It has been shown [31] that the latter correction presents a weak ϵ -dependence and will be neglected here. The inelastic bremsstrahlung contribution to the cross section are well understood, they present an important ϵ -dependence already accounted in the experimental analysis and won't be discussed here. Thus, the corrections that can lead to a non-negligible epsilon dependence can be written as follows:

$$\delta^{full} \equiv \delta^{IR} + \delta^{2\gamma} \quad (2.10)$$

The δ^{IR} have been calculated in [13], therefore a quantity of particular interest is the difference Δ between the full two-photon exchange obtained by the computation of the loop integral (1.1)

under the assumption of an on-shell nucleon, and the IR divergent corrections of Mo and Tsai:

$$\Delta \equiv \delta^{full} - \delta_{Mo-Tsai}^{IR} \quad (2.11)$$

Since the IR behaviour of δ^{full} and $\delta_{Mo-Tsai}^{IR}$ is the same [30], the difference Δ will then be IR finite. It is possible to solve the integral analytically in terms of 4-point Passarino-Veltman functions [32] calculated using Spence functions [33].

2.2.2 Unpolarized Cross Section and Form Factor Ratio Results

Figure 2.6 displays the effect of the two-photon exchange corrections on the unpolarized cross section in this model. The cross section is scaled by a factor $1/G_D^2$ with $G_D = \left(1 + \frac{Q^2}{(0.84 \text{ GeV})^2}\right)$ the dipole form factor. On both panels, the dotted curves are the expected values of the reduced cross section in the Born Approximation and do not fit the data well. The parametrization of E. Brash *et al.* [27] is used to determine the electric form factor of the proton G_E from a fit to the polarization data [7, 9, 8]. By contrast, the corrected results (solid curves) are in better agreement with the data, with a larger slope and a non-linear region at small ϵ . The influence of the two-photon exchange correction on the proton form factor ratio is shown in Figure 2.7. Those results are obtained by fitting the correction $(1 + \Delta)$ to a linear function of ϵ ($a + b\epsilon$) for each value of Q^2 at which the ratio is measured. Implementing this procedure in the reduced cross section follows:

$$\sigma_r \approx aG_M^2 \left[1 + \frac{\epsilon}{\mu_p^2 \tau} \left[R^2(1 + \epsilon b/a) + \mu_p^2 \tau b/a \right] \right] \quad (2.12)$$

where μ_p is the proton magnetic moment and R is the proton form factor ratio given by:

$$R^2 = \frac{\bar{R}^2 - \mu_p^2 \tau b/a}{1 + \bar{\epsilon} b/a} \quad (2.13)$$

$\bar{\epsilon}$ is the average value of epsilon over the fitted ϵ range and \bar{R} is the measured form factor ratio which contains the two-photon exchange effect. The results for the form factor ratio are displayed in Figure 2.7. The effect of the two-photon exchange corrections on R is evident; they have the proper sign to bring down the cross section data (LT)[28] closer to the polarization data (PT) [7].

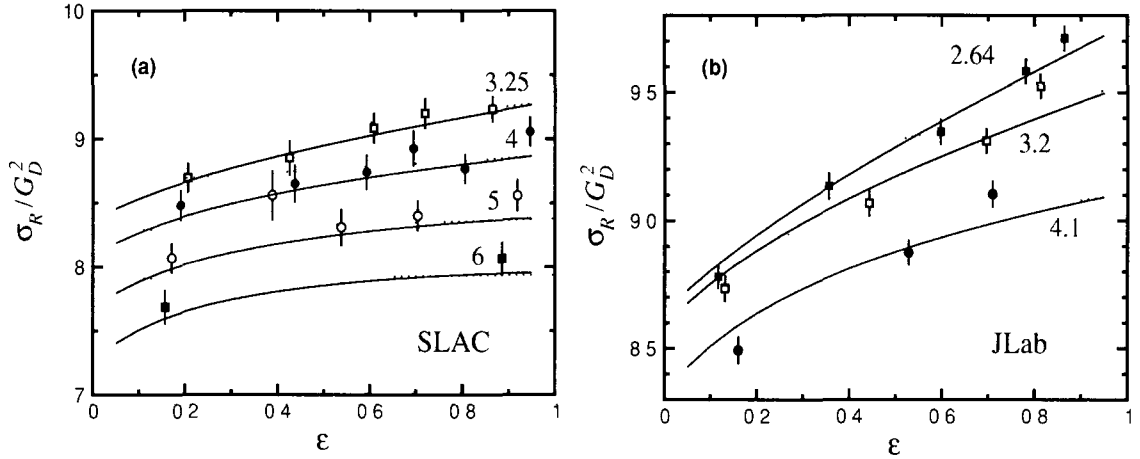


Figure 2.6: Two-photon exchange corrections to the reduced cross section (scaled by the dipole form factor) using the hadronic model of P.G. Blunden *et al.* [30]. The dotted lines shows the Born cross sections. The solid lines include the TPEX contributions. The left panel shows the data from SLAC [4] at $Q^2 = 3.25$ GeV² (open squares), $Q^2 = 4$ GeV² (filled circles), $Q^2 = 5$ GeV² (open circles) and $Q^2 = 6$ GeV² (filled squares). The right panel displays the data from the "Super Rosenbluth" experiment at JLab [6] at $Q^2 = 2.64$, 3.2 and 4.1 GeV² (filled squares, open squares and filled circles respectively).

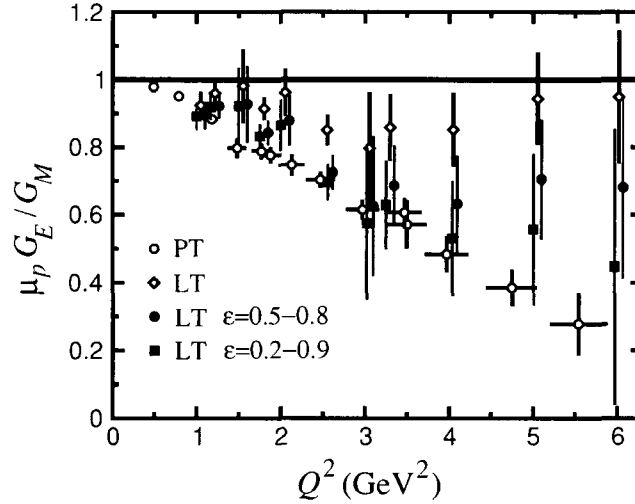


Figure 2.7: Two-photon exchange corrections to the form factor ratio measured using the Rosenbluth separation technique based on the hadronic model of P.G. Blunden *et al.* [30]. The filled circles and filled squares are the corrected Rosenbluth data (LT) [28] obtained by fitting over an ϵ range of 0.5-0.8 and 0.2-0.9 respectively. The open diamonds represent the uncorrected data and the open circles represent the polarization data (PT) [7].

Up to $Q^2 \approx 3 \text{ GeV}^2$, the corrected Rosenbluth data are in good agreement with the polarization results. Above $Q^2 \approx 3 \text{ GeV}^2$, the reconciliation between the two data sets is only partial and the slope of the polarization results is not recovered. Depending on the fitted ϵ range, the 2γ corrections can have a smaller or larger effect.

2.2.3 Polarized electron-proton scattering results

A similar loop integration can be evaluated including the case when the initial electron and the final proton are polarized. It results in a correction to the longitudinal (Δ_L) and transverse (Δ_T) cross section. As the Mo-Tsai radiative corrections are independent of the polarization, the 2γ corrections for polarized electron-proton scattering are given by the IR finite quantity:

$$\Delta_{L,T} \equiv \delta_{L,T}^{full} - \delta_{Mo-Tsai}^{IR} \quad (2.14)$$

It is more convenient to look at the ratio of the longitudinal and transverse cross section that contains the two-photon exchange effect, relative to the Born unpolarized cross section. This is defined as:

$$\frac{P_{L,T}^{1\gamma+2\gamma}}{P_{L,T}^{1\gamma}} = \frac{1 + \Delta_{L,T}}{1 + \Delta} \quad (2.15)$$

Figure 2.8 shows the two-photon exchange contribution to the longitudinal and transverse cross section ratio. The correction to P_L is small overall in this model (less than one percent) with an enhancement at forward angles (large ϵ) whereas it is large for the transverse polarization ratio and becomes significant at backward angles (small ϵ). The correction to P_T increases systematically with Q^2 . The effect of the 2γ corrections on the proton form factor ratio can be expressed as:

$$\tilde{R} = R \frac{1 + \Delta_T}{1 + \Delta_L} \quad (2.16)$$

where R is the corrected ratio and \tilde{R} the measured form factor ratio which contained the two-photon exchange effect as in (2.2.2). The results are shown in Figure 2.9. The corrected polarization data (PT corrected) are displayed with solid circles (with a horizontal offset applied for clarity) and the uncorrected ones (PT) with opens circles. The uncorrected Rosenbluth data (LT) of Figure

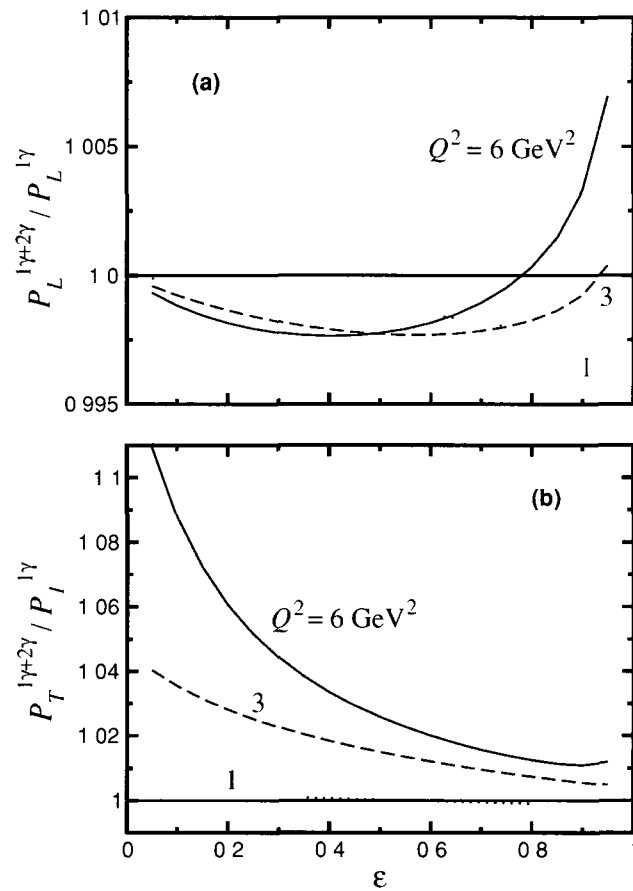


Figure 2.8: Ratio of the longitudinal and transverse cross section relative to the Born unpolarized cross section based on the hadronic model of P.G. Blunden *et al.* [30]. The dotted, dashed and solid curves correspond to the Q^2 values of 1, 3 and 6 GeV^2 respectively.

2.7 are shown with open diamonds for comparison. The correction to the proton form factor ratio data measured by the polarization transfer technique is very small, $\lesssim 3\%$, as expected since the polarization transfer experiments have $\epsilon \approx 0.7 - 0.8$.

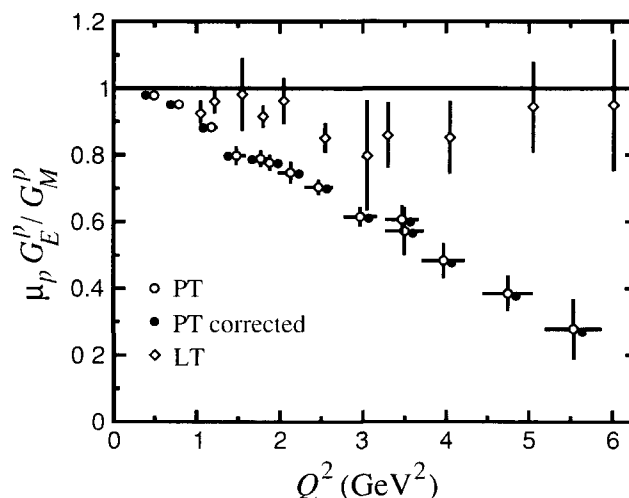


Figure 2.9: Proton form factor ratio from polarization data with (solid circles) and without (open circles) the two-photon exchange corrections using the hadronic model of P.G. Blunden *et al.* [30]

Figure 2.10 displays the two-photon exchange contributions $\delta\tilde{G}_M/G_M$, $\delta\tilde{G}_E/G_E$ to the real part of the generalized form factors \tilde{G}_M , \tilde{G}_E respectively, and the amplitude $Y_{2\gamma} = \nu \frac{\tilde{F}_3}{G_M}$. Both corrections to \tilde{G}_M and \tilde{G}_E are large, have a positive slope in ϵ and increase with Q^2 even if the latter becomes shallower for intermediate values of ϵ with increasing Q^2 . The amplitude $Y_{2\gamma}$ is significantly smaller than the other two contributions, depends weakly on Q^2 and has a slight negative slope in ϵ . Very similar results were obtained in a more general hadronic calculation [34] (in the sense that it can use any proton form factor parametrization) based on the analytic properties of the proton form factors.

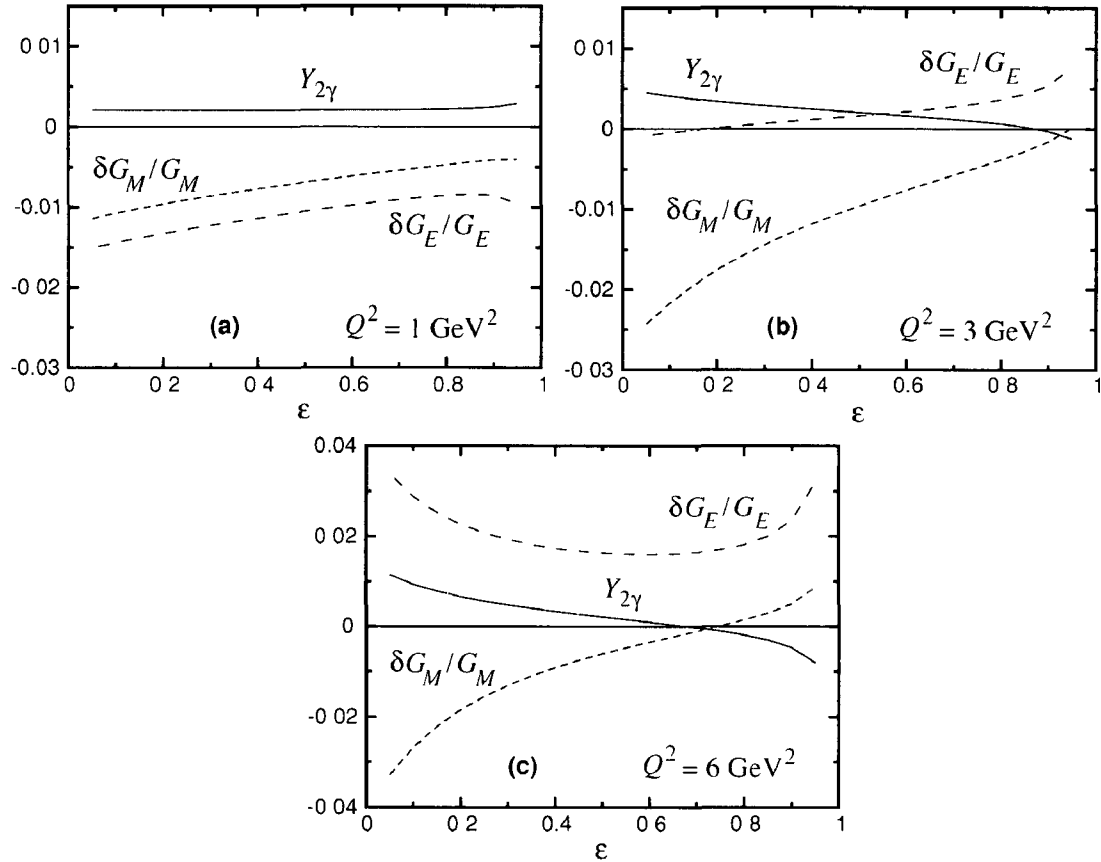


Figure 2.10: Two-photon exchange correction to the real part of \tilde{G}_M , \tilde{G}_M and $Y_{2\gamma}$ amplitudes at $Q^2 = 1, 3$ and 6 GeV^2 using the hadronic model of P.G. Blunden *et al.*

2.2.4 Excited Intermediate States

Up to this point, two-photon exchange diagrams contained only nucleons in the intermediate state. This section describes the contribution δ_Δ of another hadron: the Δ resonance. Reference [35] gives details of the calculation which is similar to the one carried throughout the previous section. A modified vertex function is introduced, expressed in terms of the Δ form factor F_Δ (necessary for ultraviolet regularization of the loop integrals) and the magnetic, electric and Coulomb coupling constants. The F_Δ form factor is given by the simple dipole form $F_\Delta = \frac{\Lambda_\Delta^4}{(\Lambda_\Delta^2 - q^2)^2}$, where Λ_Δ is a cutoff and q^2 is the square of the momentum transfer. The cross section is factorized as follows:

$\sigma_r = \sigma_r^{Born}(1 + \delta_N + \delta_\Delta)$ with $\sigma_r^{Born} = G_M^2(Q^2) + \frac{\epsilon}{\tau}G_E^2(Q^2)$ and δ_N and δ_Δ are the contributions obtained from two-photon exchange diagram containing nucleons and the Δ resonance in the intermediate state, respectively.

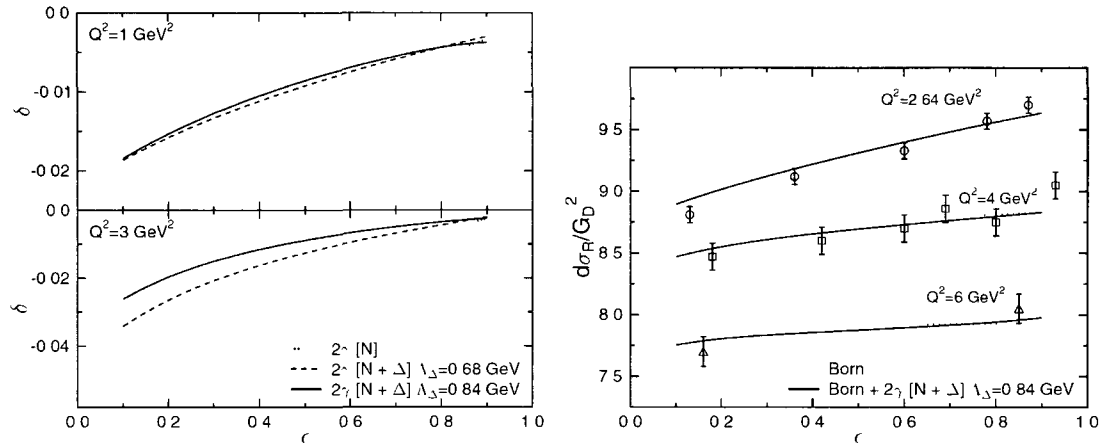


Figure 2.11: Nucleon and Δ contributions to the two-photon exchange correction to the cross section (left panel) in the model of [35]. Effect of the two-photon exchange correction including the Δ resonance to the Born cross section (scaled by the inverse of the square of the dipole form factor) (right panel). The data points are from the references [6, 12]

The nucleon and Δ contributions to the two-photon exchange correction to the cross section for two values of the cut Λ_Δ are shown in the left panel of Figure 2.11. The inclusion of the resonance makes a small difference compared to the case with only the nucleon in the intermediate state. As a consequence the results obtained for the cross section (right panel of Figure 2.11) are similar to the ones of Figure 2.6.

2.3 Perturbative Quantum Chromodynamic Calculations

The model of D. Borisyuk and A. Kobushkin [36] studies the two-photon exchange effect in elastic electron-proton scattering at high Q^2 using a perturbative quantum chromodynamic (pQCD) formalism. In the Born Approximation (*i.e.* the exchange of one photon), at least two hard gluons need to be exchanged between the quarks. The remaining quark interacts with the virtual photon. The one-photon exchange amplitudes are therefore of the order: $\frac{\alpha\alpha_s^2}{Q^6}$, where α_s is the strong

coupling constant. When one considers the exchange of two photons, one gluon exchange between the quarks is sufficient. Thus the leading order pQCD contribution to the TPEX amplitude is proportional to $\frac{\alpha^2 \alpha_s}{Q^6}$. It follows that the TPEX amplitude is of order $\frac{\alpha}{\alpha_s}$ relative to the Born amplitude, and not α as described in the other models. Using the simple parametrization for α_s :

$$\alpha_s = \frac{4\pi}{\beta_0 \ln \frac{Q^2}{\Lambda^2}} \quad (2.17)$$

with $\Lambda = 0.2 \text{ GeV}$ and $\beta_0 = 11 - \frac{2}{3}n_f$ is the β -function with n_f the number of quarks with mass less than the energy scale Λ . One notices that the two-photon exchange contribution increases logarithmically with Q^2 .

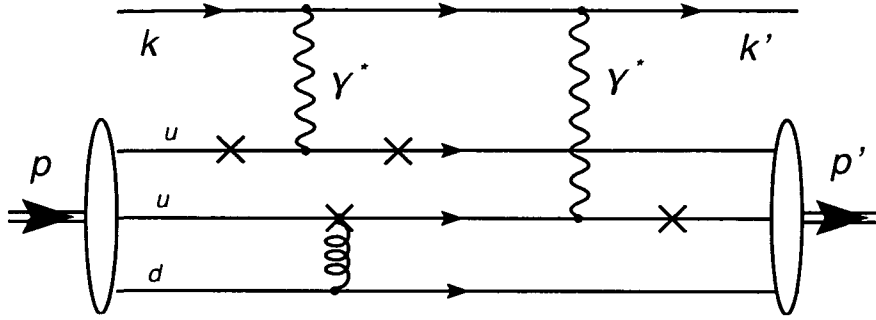


Figure 2.12: Diagram for the elastic ep scattering with two hard photon exchanges. The crosses indicates the other possibilities to attach the gluon. Other diagrams are possible where one photon is coupled to the d-quark but they are not shown here for simplicity.

It is important to point out that the partonic model [23] only considers diagrams where both photons interact with the same quark (see Figure 2.12). The resulting amplitudes will be of the order $\frac{\alpha^2 \alpha_s^2}{Q^6}$ and thus will be subleading in α_s . These diagrams are not taken into consideration in the present calculation. For large Q^2 , the term proportional to the magnetic form factor dominates in the cross section. The reduced cross section can then be rewritten as:

$$\sigma_r \approx \frac{Q^2}{4M^2} G_M^2 \left[1 + 2\Re \left(\frac{\delta \tilde{G}_M}{G_M} \right) \right] \quad (2.18)$$

By neglecting the term of order $\frac{M^2}{Q^2}$, the longitudinal polarization component becomes:

$$P_l \approx h\sqrt{1-\epsilon^2} \left[1 - \frac{2\epsilon^2}{1+\epsilon} \Re \left(\frac{\delta\tilde{F}_3}{G_M} \right) \right] \quad (2.19)$$

Under the assumptions that a nucleon of momentum p consists of three collinearly moving quarks with momenta $x_i p$ (with $0 < x_i < 1$, $\sum_{i=1}^3 x_i = 1$) and that the masses of the quarks and of the nucleon can be neglected, the amplitude of the process can be written as the following matrix element:

$$\mathcal{M} = \langle \phi(y_i) | T(y_i, x_i) | \phi(y_i) \rangle \quad (2.20)$$

where T is the hard scattering amplitude at the quark level, $\phi(x_i)$, and $\phi(y_i)$ are the initial and final nucleon spin-flavour-coordinate wave functions, also called the quark distribution amplitudes. It is clear that the x_i 's are the fractions of the nucleon momentum carried by the quarks. The details of the calculation of the two-photon exchange amplitudes and the parametrization of the wave functions are given in [36]. The calculations were carried out using different forms of distribution amplitudes: Chernyack-Ogloblin-Zhitnitsk (COZ) [37], Gari-Stefanis (GS) [38] and heterotic (Het) [39]. Figure 2.13 shows the ϵ -dependence of the two-photon exchange amplitude $\delta\tilde{G}_M$ at $Q^2 = 10 \text{ GeV}^2$. Both COZ (solid curve) and Het model (dashed curve) give a quasi-linear ϵ -dependence except at low and high ϵ . The amplitude obtained is up to 3.5% of the corresponding Born amplitude at low ϵ . Besides slow logarithmic evolution, which is neglected here, this behaviour was found to be the same for all Q^2 .

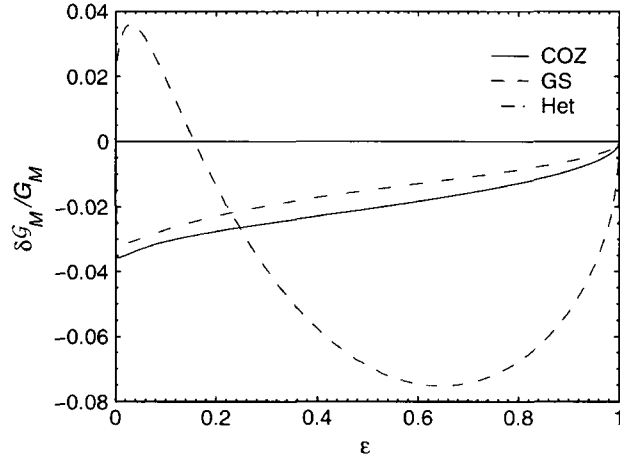


Figure 2.13: Two-photon exchange amplitude $\delta\tilde{G}_M/G_M$ versus ϵ at $Q^2 = 10$ GeV² in the pQCD model of D. Borisyuk and A. Kobushkin.

On the contrary, the GS (dashed curve) model gives a larger and strongly non-linear amplitude. It has been shown [40] that for the Rosenbluth plot to remain linear, a linear ϵ -dependence of $\delta\tilde{G}_M$ is the necessary and sufficient condition. A non-linearity in the Rosenbluth plots [41] has yet to be observed experimentally, therefore the GS model will no longer be considered here.

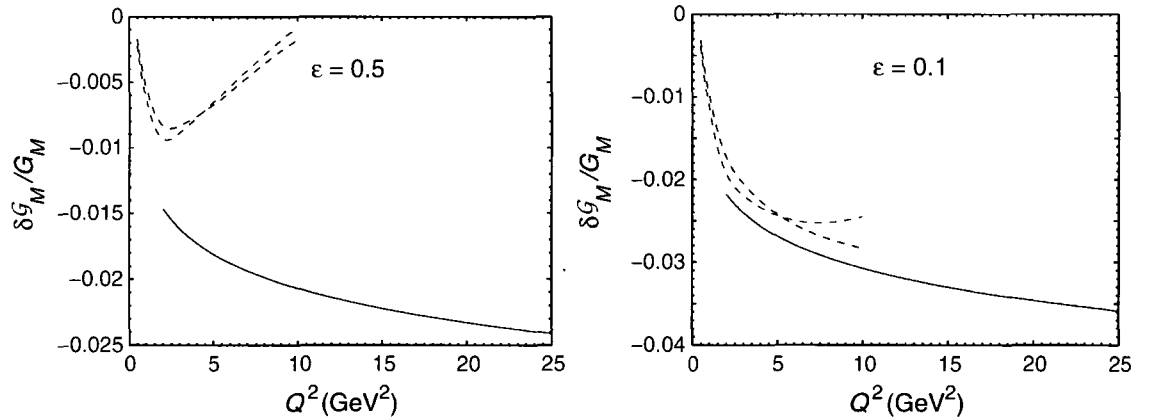


Figure 2.14: Two-photon exchange amplitude $\delta\tilde{G}_M/G_M$ versus Q^2 at $\epsilon = 0.5$ (left) and $\epsilon = 0.1$ (right) using the pQCD model [36]. The dashed curves display the hadronic calculations: dipole parametrization in red and [29, 30] in black.

Figure 2.14 displays the two-photon exchange amplitude $\delta\tilde{G}_M/G_M$ versus Q^2 at $\epsilon = 0.5$ (left

panel) and $\epsilon=0.1$ (right panel). The results of the hadronic calculations [34, 42] are also shown. The red dashed curve corresponds to the dipole parametrization of the form factors and the black curve to the calculation in [29, 30]. A smooth interpolation between the pQCD and the hadronic curves is possible especially at low ϵ . Nevertheless, there is a strong disagreement between these two calculations for Q^2 above 3 GeV^2 at $\epsilon = 0.5$.

Another pQCD based model has been developed by M. Vanderhaeghen and N. Kivel [43] using the proton distribution amplitude COZ, the BLW [44] parametrization and the Gock08 [45] model based on recent lattice QCD calculations. Figure 2.15 shows the correction on the proton form factor ratio predicted by these two models at $Q^2 = 2.5 \text{ GeV}^2$. The dashed line shows the one-photon exchange expectation, the solid and dotted lines correspond to the COZ and BLW calculations respectively. The dotted-dashed curve displays the results with the amplitude from the Gock08 model. The data point in the figure is from the JLAB/HALL A experiments [7, 8]. The three calculations give the same trend for a negative correction which increases for decreasing ϵ . A non-linearity arises for low ϵ . However, the applicability limit, above which the QCD approach is valid, is represented by a vertical line in the Figure 2.15.

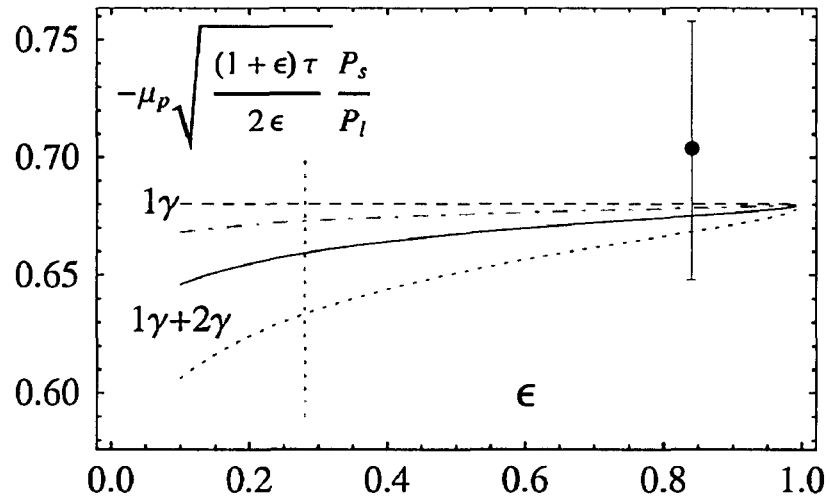


Figure 2.15: Proton form factor ratio as a function of ϵ at $Q^2 = 2.5 \text{ GeV}^2$ based on proton distribution amplitudes models COZ and BLW.

2.4 Structure Function Calculation

The model of Bystritskiy *et al.* [46] aims at giving a high order calculation of the radiative-corrected (including the two-photon exchange) cross section in both unpolarized and polarized situations. The calculation is based on the structure function method [13] using a Drell-Yan picture of the electron. Figure 2.16 displays the results of the unpolarized (left) and polarized (right) cross section as a function of ϵ at $Q^2 = 1, 3$ and 5 GeV^2 (from top to bottom). In the kinematic range considered here, the structure function method decreases the slope of the reduced cross section.

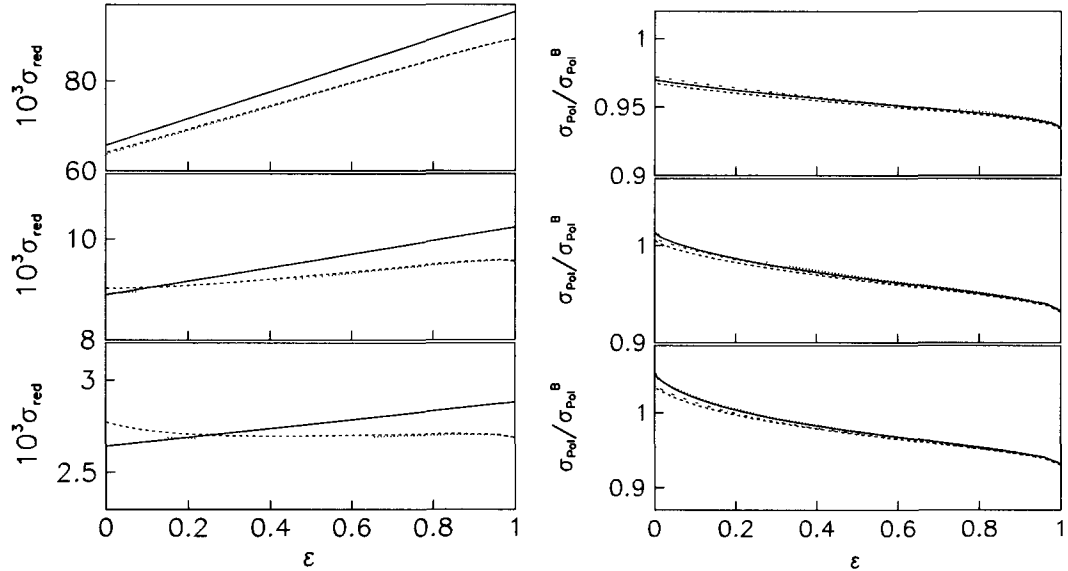


Figure 2.16: ϵ -dependence of the ratio of the unpolarized cross section at $Q^2 = 1, 3$ and 5 GeV^2 from top to bottom (left). ϵ -dependence of the ratio of the polarized cross section, corrected by the structure function method of Bystritskiy *et al.* [46], to the corresponding component of the Born cross section at $Q^2 = 1, 3$ and 5 GeV^2 from top to bottom (right). On the left panel, the solid line represents the Born calculation, the dashed line corresponds to the calculation using only the structure function, whereas for the dotted line the two-photon exchange contribution is included. On the right panel, the dotted (dash dotted) lines correspond to the calculation that includes only the structure functions for the transverse (longitudinal) component of the cross section. The calculation that includes the two-photon exchange contribution is shown as solid (dashed) line for the transverse (longitudinal) component.

This effect grows with Q^2 . Some small non-linearities in the reduced cross section arise at low and high ϵ at high Q^2 . The inclusion of the two-photon exchange effect has little influence on

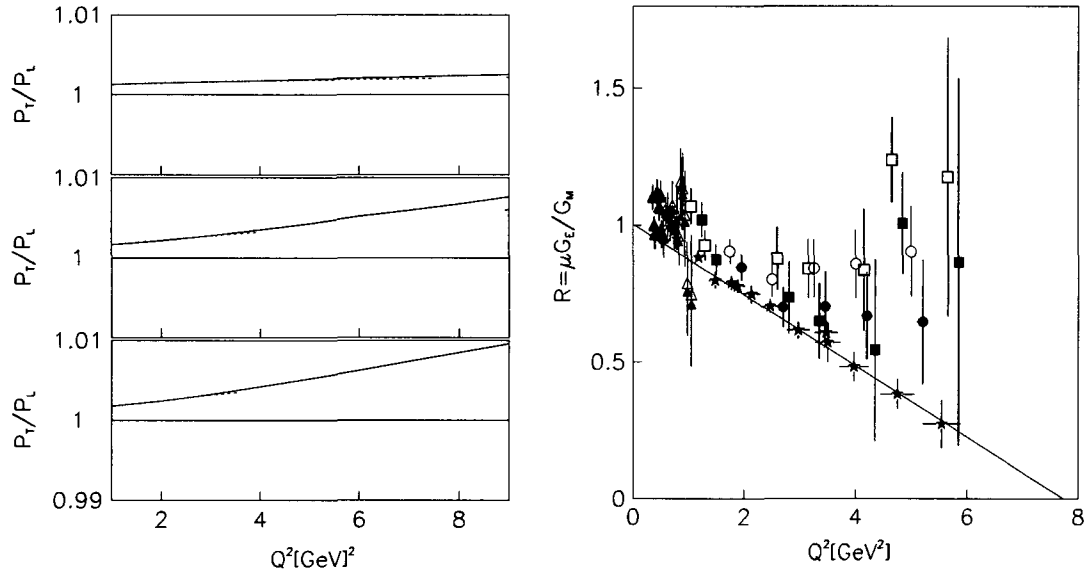


Figure 2.17: Q^2 dependence of the ratio of the transverse to longitudinal polarization components, normalized to the Born values for $\theta_e = 85^\circ$, 60° , and 20° from top to bottom (left). Q^2 dependence of the proton form factor ratio (right), obtained by the Rosenbluth separation method [4] (squares), [5] (circles) and, [47] (triangles), using the structure function model of Bystritskiy *et al.* [46]. The open and solid symbols correspond to the uncorrected and corrected results respectively. The polarization data [7, 8, 9] are represented with stars.

the result. The same effect is seen in the polarized case (right panel). The ratio of the polarized cross section to the corresponding component of the Born cross section is plotted. Again, the TPEX effect is very small. The results for the proton form factor ratio are displayed in Figure 2.17. The left panel shows the ratio of the transverse to longitudinal polarization components, calculated with the structure method (dashed lines), normalized to the Born values to compensate the kinematical factor at different values of the electron scattering angle $\theta_e = 20^\circ$, 60° , and 85° . The 2γ -correction is very small: at most 1% for $Q^2 = 10 \text{ GeV}^2$. The correction is too small to be noticed on the graph. The effect of the structure function calculation on the cross section based data is clearly visible and thus partially solves the discrepancy between the proton form factor ratio extracted by the Rosenbluth method and the recoil polarization transfer technique.

Chapter 3

Experimental Apparatus

The E04-019 (GEp2 γ) experiment was carried out from October 2007 until January 2008, jointly with the E04-108 (GEpIII) experiment. It took place in the experimental Hall-C of the Thomas Jefferson National Accelerator Facility (TJNAF, also called JLab), The accelerator consists of an superconducting recirculation linear electron accelerator (CEBAF) which can accelerate electrons to energies up to 6 GeV. In this chapter, we will present the experimental setup with descriptions of the beam line instrumentation and of the detector package specific to the E04-019 and E04-108 experiments.

3.1 The continuous Electron Beam Accelerator

The CEBAF accelerator consists of an injector, two linacs, two recirculation arcs, extraction elements, which guide and transport the beam into the three different halls, and three beam dumps (see Figure 3.1). The electrons, produced by photo-emission on a gallium arsenide (GaAS) photocathode (more details about the production of polarized electrons will be given in the next section), are injected at 67 MeV and accelerated in the North and South linacs by superconducting radio-frequency (RF) resonant cavities tuned to 1497 MHz. An RF chopping system "divides" the beam into bunches so that each hall receives a 499 MHz pulsed beam. After each pass through both linacs, the energy of the electron increases by 1.14 GeV (570 MeV per linac). As many as

5 successive passes are possible for the total reachable energy of 5.767 GeV at the time of the GEp(2 γ) experiment. The procedure gives some flexibility in the beam delivery to the different hall. Simultaneously, beams with different energy, polarization and current can be sent to each hall. Nevertheless, the beam energy can only be a multiple of the energy available after one pass through the linacs, the total current delivered to the three halls cannot exceed 180 μA and the polarization is defined by the precession of the electron spin through the recirculating arcs and transport lines.

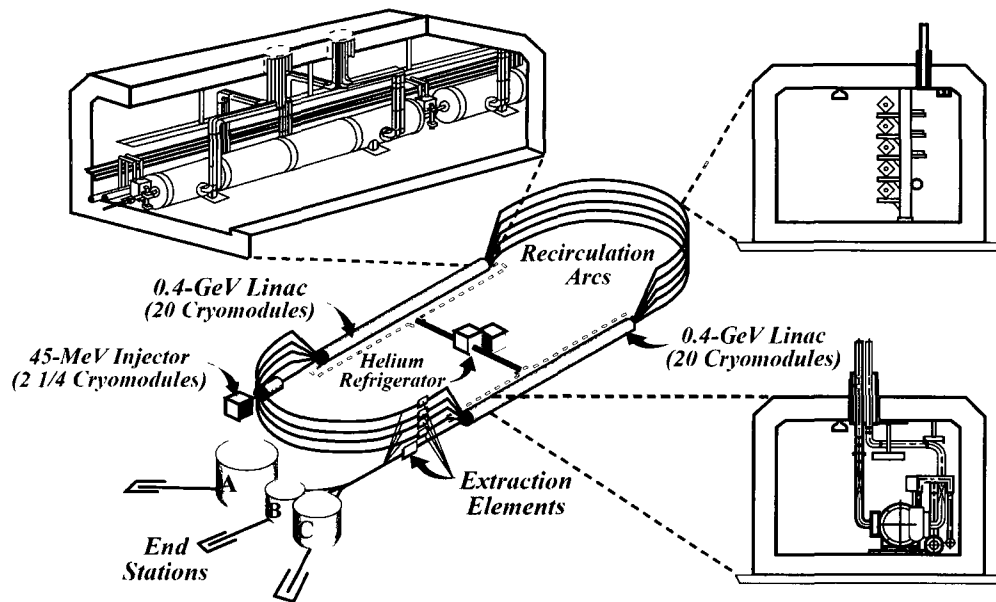


Figure 3.1: Cartoon of the CEBAF accelerator.

3.1.1 Polarized electron source

The production of the polarized beam at JLab is based on electron extraction by photoemission induced by laser light on a GaAs crystal [48]. The circularly polarized photons, emitted by the laser, of energy just above the gap threshold, will excite electrons from the p-states of the valence band to the s-states of the conduction band of the GaAs crystal. These electrons will then migrate through the crystal to the "vacuum" where they can be transported and accelerated through the

linacs. The whole process is based on the spin-orbit splitting of the valence p-energy levels into a fourfold degenerate $P_{3/2}$ and twofold $P_{1/2}$ levels. The energy gap between these two levels is $\Delta = 0.34 \text{ eV}$. For circularly polarized light, the selection rules are $\Delta m_j = \pm 1$ for right (σ^+) or left (σ^-) polarization respectively. The different relative transition probabilities (calculated from the Clebsch-Gordan coefficients), represented by numbers in circle on figure 3.2, between the P-states and the conduction band S-states are at the origin of the spin polarization. Indeed, for a σ^+ light, the photons will excite preferentially (in a ratio of 3 to 1) electrons with $\Delta m_j = +1$. The theoretically obtainable polarizations are in that case -50% and +50% for σ^- light. Furthermore, one can split the $P_{3/2}|j, m_j\rangle$ levels into $|3/2, \pm 3/2\rangle$ and $|3/2, \pm 1/2\rangle$ levels separated by an energy gap of $\delta = 0.065 \text{ eV}$ [49]. So that by choosing a laser energy between E_{gap} and $E_{gap} + \delta$, one can select the transitions $|3/2, \pm 3/2\rangle \rightarrow |1/2, \pm 1/2\rangle$ only.

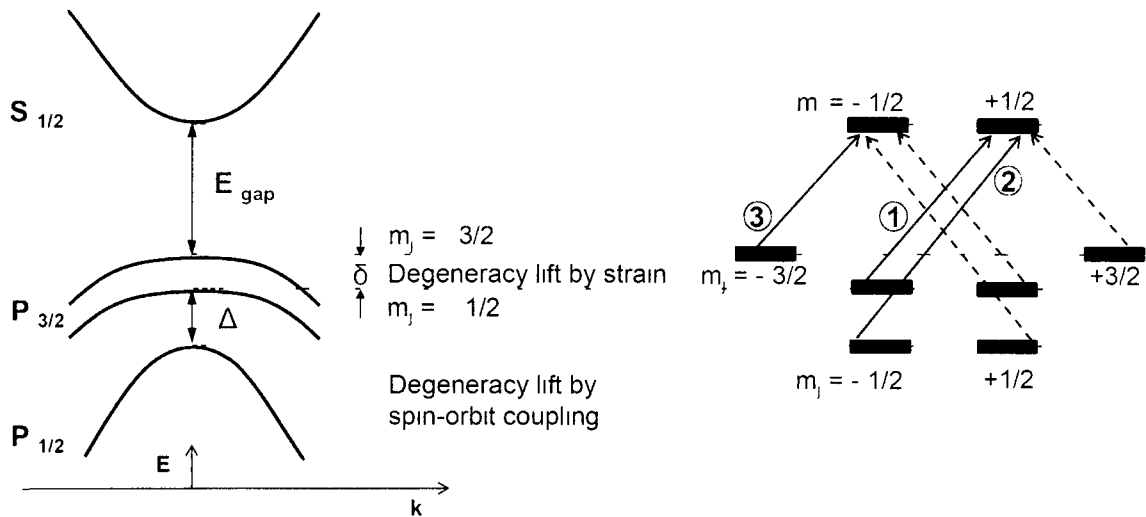


Figure 3.2 GaAs band structure and energy levels

The degeneracy is lifted by breaking the crystalline symmetry, growing the GaAs crystal on a GaAsP substrate, which has different lattice constants. The polarization given by

$$P = \frac{N_e^+ - N_e^-}{N_e^+ + N_e^-} \quad (3.1)$$

where N_e^+ and N_e^- are the number of electrons with spin parallel and anti-parallel to the light direction respectively has a theoretical limit of 100% since one selects a specific transition only. However, depolarization of the electrons in the conduction band affects this theoretical yield. The GaAs photocathodes used at JLab, at the time of the experiment, provided a 85% polarized electron beam.

In order to leave the crystal, electrons need a sufficient energy to overcome the electron affinity which the potential barrier between the conduction band and the vacuum. Thus for a laser light of energy between E_{gap} and $E_{gap} + \delta$, the available kinetic energy of the electron after the gap is at most δ , not enough to exceed the electron affinity which is about 4 eV for a GaAs semiconductor. In practice, to overcome this problem, one oxydises the conduction band by adding, for example, a layer of CsF which decreases the electron affinity and even makes it negative so that electrons at the conduction band are free to leave the crystal to be accelerated.

An important property of a photocathode is its quantum efficiency (QE). This is defined as ratio of the number of emitted electrons to the number of incident photons. It depends on the thickness of the crystal; the thicker the crystal, the greater the QE. Nevertheless the larger the thickness, the lower will be the polarization since electrons will be more likely to interact on their way out of the crystal. At JLab, superlattice GaAs photocathodes, consisting in thin multi-layered (few nm) GaAs and GaAsP semiconductors, are used to achieve a QE near 1%.

Three different lasers, one for each experimental hall, allow the delivery of beams with different intensities and polarizations. They are pulsed at the third subharmonic (499 MHz) of the accelerator. The circularly polarized light is obtained by adding "Pockels" cells on the optical bench. These cells consist of a birefringent crystal whose refraction indices depend linearly upon the applied electric field. The phaseshift between the two light components is given by:

$$\phi = \frac{2\pi n_0^3 r_{63}}{\lambda} V \quad (3.2)$$

where n_0 is the nominal refraction index of the crystal, V is the applied voltage and r_{63} is the electro-optic tensor coupling constant specific of the crystal structure. The Pockels cells at JLab are used to obtain a polarization reversal; in this experiment the standard 30 Hz reversal rate

between right and left circular polarization was used. A Wein filter is used to correct for the spin precession in the magnetic elements of the injector and of the recirculation arcs.

3.1.2 Beam energy Measurement

The beam energy is measured with the Hall-C arc magnets operated in a spectrometer mode [50]. Passing through the magnets, the electrons undergo a Lorentz force which bends their trajectories. The energy or momentum (by neglecting the electron mass) is written as:

$$p = \frac{e}{\theta} \int Bdl \quad (3.3)$$

where $\int Bdl$ is the magnetic field integral over the path of the beam, e is the electron charge and θ is the arc bend angle. A precise knowledge of the field map as a function of the current is required. The precision of this measurement is given by:

$$\frac{\delta p}{p} = \sqrt{\left(\frac{\delta \int Bdl}{\int Bdl}\right)^2 + \left(\frac{\delta \theta}{\theta}\right)^2} \quad (3.4)$$

and is of the order $\frac{\delta p}{p} \approx 5 \times 10^{-4}$. The beam position and angles are measured with the superharps at the entrance and exit of the arc. The superharps are detectors made of 3 tungsten wires, one oriented horizontally and the other two vertically, that can sweep through the area where the beam is present. Photons emitted from the interaction between the beam and the wires are detected by photomultipliers (PMT). Thus the current is recorded as a function of the harp position. Note that it is not possible to perform a beam energy measurement and take data at the same time, the calibration is intrusive. Table 3.1 present the different arc energy measurements performed during the GE_p-2 γ experiment.

Day	Energy, MeV
11/28/2007	1873.02 ± 1.09
12/11/2007	2847.16 ± 1.19
01/06/2008	3680.23 ± 1.31
01/23/2008	1868.13 ± 1.09
estimated	3549 ± 1.29

Table 3.1: Beam energy measurements performed during the $GE_p-2\gamma$.

No beam energy measurement was performed for the first part of the highest ϵ kinematic but the beam energy was estimated from the beam injector energy and the number of passes.

3.1.3 Beam current Measurement

Two types of detectors are used to measure the beam current in Hall-C. The first one, the Unser, is a parametric DC transformer which allows non-destructive measurements (i.e one can take data as well as measuring the current at the same time) and gives absolute value of the current. The Unser has a very stable and well-known gain but suffers from slow gain drift so it cannot be used as continuous current monitor. It also has a poor signal to noise ratio. To measure the beam current continuously two more stable resonant cavities are used: the Beam Current Monitors (BCM). They are calibrated using the known gain and the measured offset of the Unser and perform a non destructive measurement of both the beam current and accumulated charge. They consist of cylindrical wave guides designed so that the 499 MHz structure of the beam resonates in the 1497 MHz (frequency of the RF cavities) TM_{010} mode. Antennas are placed inside the guide and convert the RF power of the resonances to an analog voltage signal when the beam passes through the guide. The resonant frequency is very sensitive to any temperature change, which is why the BCM are kept in a thermally insulated environment at 43.3°C .

3.1.4 Beam position Measurement

The position of the beam is known through a non destructive measurement by the Beam Position Monitor (BPM). The principle of a BPM is very similar to the BCM. It consists of a cylindrical resonant cavity designed so that its resonant frequency matches the fundamental frequency of

the accelerator and the Hall-C beam. Inside the cavities, four antennas are placed at 45° with respect to the horizontal and vertical axes to attenuate the synchrotron radiation damage. The sum over difference signals from opposite (with respect to the beam) antenna, read out by a sampling Analog to Digital Converter (ADC), are proportional to the distance to the beam. The measurement is independent of the intensity of the beam since the position is measured from a ratio of signals. The overall accuracy of beam position measurements is of the order ± 1 mm. A more precise but destructive measurement of the beam position can be performed by using the superharps as described in the previous beam energy measurement section.

3.1.5 Polarization Measurement

The beam polarization in Hall C is measured with a Möller polarimeter [51]. It is based on the scattering of polarized electrons off a polarized electron target like magnetized iron, of known polarization; ($\vec{e}\vec{e} \rightarrow ee$) whose cross section is analytically well-known from QED. In the center-of-mass (c.m.) frame, for a longitudinally polarized beam of polarization P_b^\parallel , the cross section is given by the expression:

$$\frac{d\sigma}{d\Omega} = \frac{d\sigma_0}{d\Omega} \left(1 + P_b^\parallel P_t^\parallel A_{zz}(\theta) \right) \quad (3.5)$$

$\frac{d\sigma_0}{d\Omega}$ is the unpolarized cross section of the same reaction, P_t^\parallel is the polarization of the target and A_{zz} is the analyzing power of the reaction which depends upon the (c.m.) scattering angle θ and is maximum for $\theta = 90^\circ$ ($A_{zz} = -7/9$). The beam polarization is then extracted by measuring the cross section asymmetry \mathcal{F} for parallel (\Rightarrow) and anti-parallel (\Leftarrow) beam and target spins:

$$\mathcal{F} = \frac{\frac{d\sigma_{\Rightarrow} - d\sigma_{\Leftarrow}}{d\Omega} - \frac{d\sigma_{\Leftarrow}}{d\Omega}}{\frac{d\sigma_{\Rightarrow} + d\sigma_{\Leftarrow}}{d\Omega}} = |P_b^\parallel| |P_t^\parallel| |A_{zz}| \quad (3.6)$$

The target is a foil of pure iron polarized to saturation using a superconducting split-coil solenoid which applies a 4T field perpendicular to the foil. A 90° c.m. scattering angle corresponds to forward scattering at small, opposite and equal angles in the lab frame. The scattered electrons pass through a pair of quadrupoles, Q_1 and Q_2 , and adjustable collimators (see figure 3.3) for a better spread, separation and selection of the 90° c.m. events. In order to reduce the background

coming mostly from scatterings on the iron nuclei, both electrons are detected in coincidence by two lead-glass total absorption shower counters. Using (3.6), the asymmetry in the coincidence counting rates gives the beam polarization. The Mott polarimeter allows one to measure the beam polarization with a typical 1% statistical uncertainty and with $\approx 1\%$ systematic uncertainty. Since the beam is used to scatter off a different target than the one used for the experiment, it is clear that a beam polarization measurement is destructive. Even if the beam polarization cancels out in the polarization component ratio measured in the experiment described here, it is very important to perform frequent measurements for the extraction of the longitudinal polarization component.

3.2 The Hall-C cryogenic target

In experiment E04-109, the standard Hall-C target ladder, placed in a cylindrical vacuum scattering chamber, was used. It consists of several different solid targets and a three loop cryogenic target system which can be raised or lowered to place the desired target in the beam path. The scattering chamber is directly connected to the beam line and has thin aluminium windows for the scattered particles to exit the chamber. A 20 cm liquid hydrogen target connected to a recirculating hydrogen loop was used during the production runs. A 60 Hz fan circulated the liquid hydrogen through the loop. A heat exchanger, operating with 14K helium, cools the cryogen (hydrogen) to the temperature of 19 K. A Joule-Thompson valve is used to control the helium flow. In order to compensate for fluctuations of the beam power deposition in the target, a high-power heater is used to regulate and maintain the temperature of the cryogen through the loop at 19K. Additional low-power heaters are used for correcting small changes in temperature due to small fluctuations in beam current. Due to the small spot size ($<100 \mu\text{m}$) and high intensity currents, typically $\approx 85 \mu\text{A}$ for this experiment, the target windows could undergo serious damages and the liquid target might start boiling, resulting in significant fluctuation of the density. To avoid this situation and spread out the heat over the target, the beam is steered to a transverse size of $2 \times 2 \text{ mm}^2$ by a fast raster system [52] (see Figure 3.4). The raster consists of two sets of dipole magnets, one for the horizontal direction and the other for the vertical direction. They are located 25 m upstreams

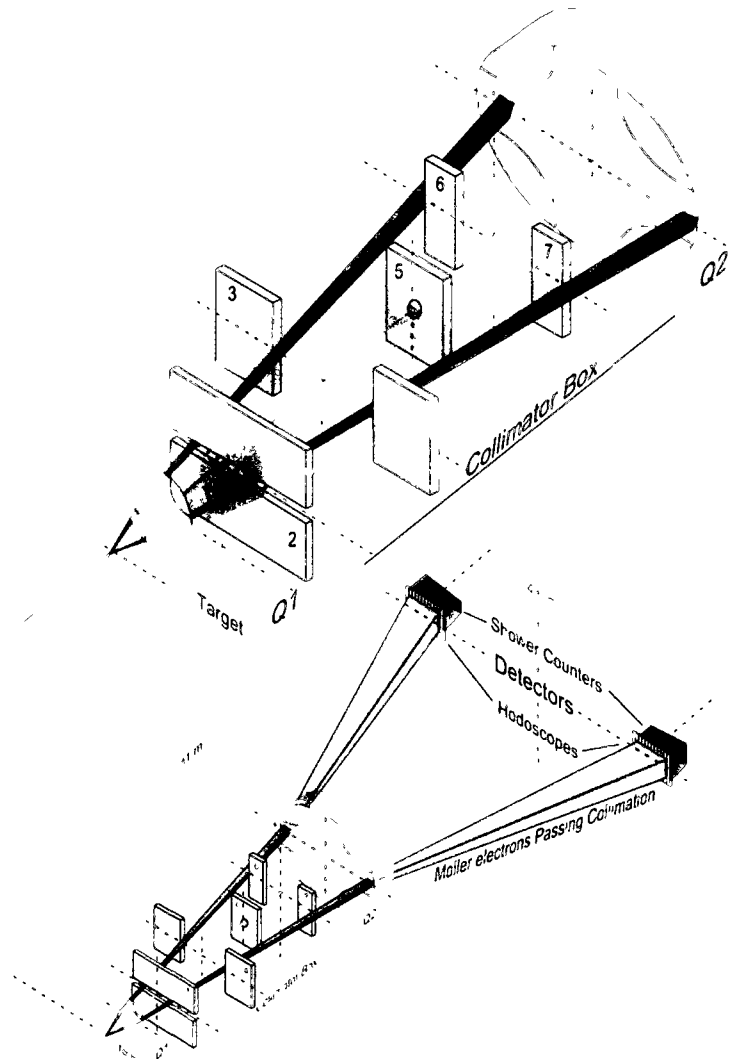


Figure 3.3: Layout of the Hall C Möller polarimeter.

from the target.

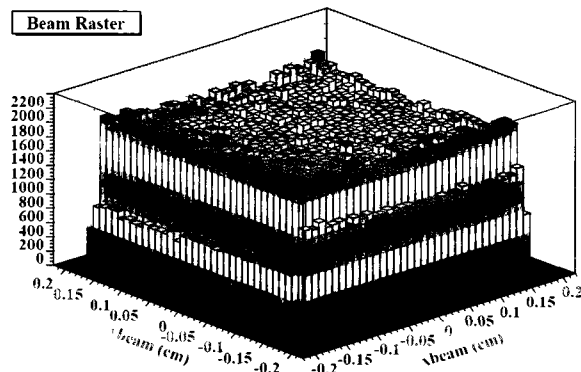


Figure 3.4: Beam raster pattern during the E04-109 experiment.

A number of multi-foil solid targets were used to perform optics calibration of the detector. The z positions of the foils were: $z = 0 \pm 7.5$ cm, $z = \pm 2$ cm and $z = \pm 3.8$ cm for the three-foil Aluminium target, two-foil Carbon target and the two-foil Aluminium target, respectively. A 20 cm dummy target, made of two Aluminium foils at $z = 3.84 \pm 10$ cm, was used to determine the background contribution of the target walls and to perform optics calibrations [53].

3.3 The detector package

In this experiment, the scattered electrons were detected by the new, large acceptance electromagnetic calorimeter (BigCal) located on the left of the beam. The scattered protons were detected in a superconducting magnetic spectrometer: the High Momentum Spectrometer (HMS). A new focal plane polarimeter (FPP) was built to measure the polarization of the proton. The FPP is housed inside the HMS shielded concrete detector hut. Another detector, which was not used here, is also located in Hall C: the Short Orbit Spectrometer (SOS). spectrometer is made for detecting particles with momentum < 2 GeV/c. The SOS can be used either Figure 3.5 shows a cartoon of the layout of Jlab Hall C. In this section, we will describe and give the characteristics and performances of the different detectors used during the GEp2 γ experiment.

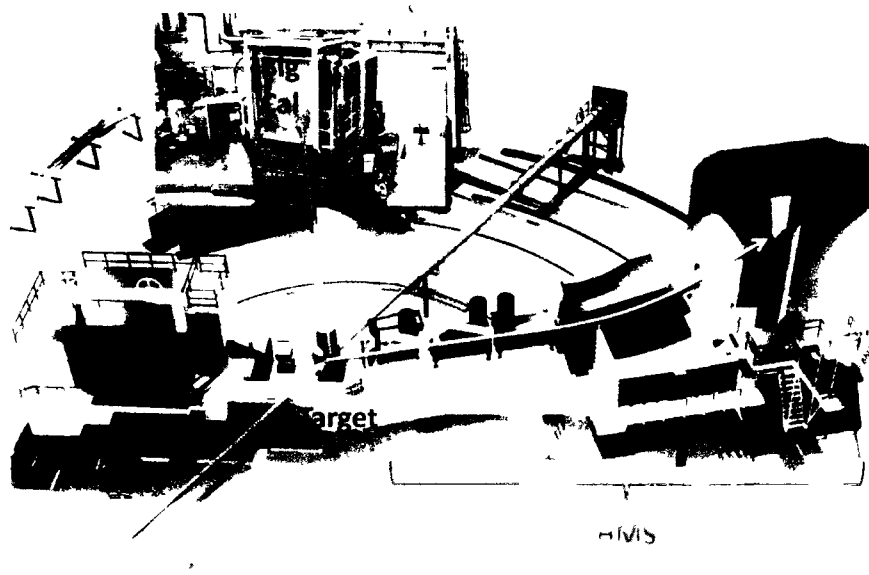


Figure 3.5: Layout of the Jlab HallC during the E04-109 experiment.

3.3.1 High Momentum Spectrometer (HMS)

The High Momentum Spectrometer (HMS) [54] consists of a QQQD magnetic system and concrete hut, where a set of detectors are located and used to track and identify the charged particles coming from the target. The hut and the magnets are supported on different carriages. However, the whole structure, mounted on a pair of concentric rails, can rotate around a rigid central bearing to the desired angle. During the experiment, the HMS magnetic system operated in a point-to-point tune.

Magnets

The three quadrupoles and the dipole of the HMS are all superconducting magnets and are cooled with a 4K liquid Helium cryogen supplied by the End Station Refrigerator (ESR). The acceptance of the HMS is determined by the quadrupoles whereas the dipole sets its central momentum. The quadrupoles are labeled Q1, Q2 and Q3. Q1 and Q3 focus in the dispersive direction and

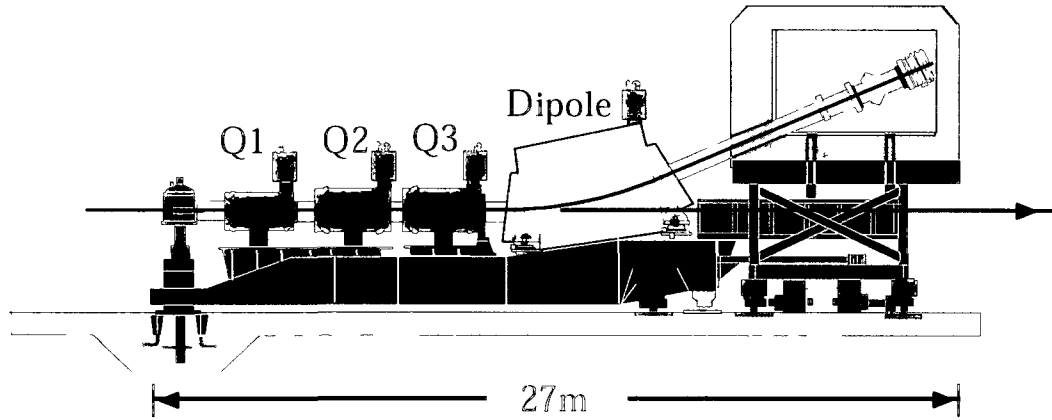


Figure 3.6: Side view of the HMS.

Q2 focuses in the non-dispersive (transverse) direction. The properties of the HMS quadrupole system are given in Table 3.2.

	Length (cm)	Pole Rad. (cm)	Warm Rad. (cm)	Pole Field (T)	Gradient (G/cm)
Q1	189	25	22	1.5	605
Q2 / Q3	210	35	30	1.56	445

Table 3.2: Properties of the HMS quadrupole system.

The dipole, which deflects the charged particle vertically into the hut, has a central bending angle of 25° and flat poles with an edge focusing effect due the 6° inclination of the pole face with respect to the normal of the central ray. The dipole field is regulated by a Nuclear Magnetic Resonance (NMR) probe, while the quadrupole magnetic fields are monitored by current. The basic parameter of the HMS dipole are given in Table 3.3.

Length (cm)	Gap (cm)	Pole face rotation	Max. Pole Tip Field (T)	Bend angle
526	42.1	$+6^\circ, -6^\circ$	1.66	25°

Table 3.3: Parameters of the HMS dipole.

During the experiment, for an HMS central momentum of $2.0676 \text{ GeV}/c$, the magnets were set at: 269.31 A, 214.36 A, 104.34 A and 0.56830 T for Q1, Q2, Q3 and the dipole, respectively.

Collimators

A set of three collimators, mounted at the entrance of Q1, are available in the HMS for distinct purposes. Two octagonal collimators (a large and a small one), made of machinable Tungsten with 10% CuNi, are used to prevent particle loss in the magnets and thus to shape the HMS solid angle acceptance. The larger one of the collimators was used during the experiment. The other type, the Sieve slit collimator, is used for the HMS optics calibration of the different magnetic elements. It consist of a grid of small holes of 0.508 cm in diameter (the central sieve hole is 0.254 cm in diameter) spaced by 2.54 cm in the vertical direction and 1.524 in the horizontal direction. Two holes are missing on the plate to check its orientation. The performances of the HMS are summarized in Table 3.4.

Max. Central Momentum (Gev/c)	7.4
Momentum Bite, $(p_{max} - p_{min})/p_0$	18%
Momentum Resolution, $\delta p/p$	< 0.1%
Solid Angle Acceptance (msr)	6.74
In plane scattering angle resolution (mrad)	0.8
Out of plane scattering angle resolution (mrad)	1.0
Useful target length from the spectrometer (cm)	10

Table 3.4: Performance of the HMS.

The detector package

The different elements used for detecting, tracking, and identifying the scattered particles are shown in figure 3.7. The standard HMS detector package is a compound of a pair of drift chambers to track the charged particles, gas and aerogel (not shown in the figure) Cerenkov detectors for particle identification, four planes of scintillator hodoscopes (S1X, S1Y, S2X and S2Y) for triggering and timing and a lead glass calorimeter for energy information as well as further particle identification. In the GEp(2γ) experiment, the Cerenkov detector and the S2X and S2Y scintillator plane needed to be removed in order to install the new FPP. An additional scintillator, named S0, was placed in front of the drift chambers to form the HMS trigger with the remaining hodoscope planes.

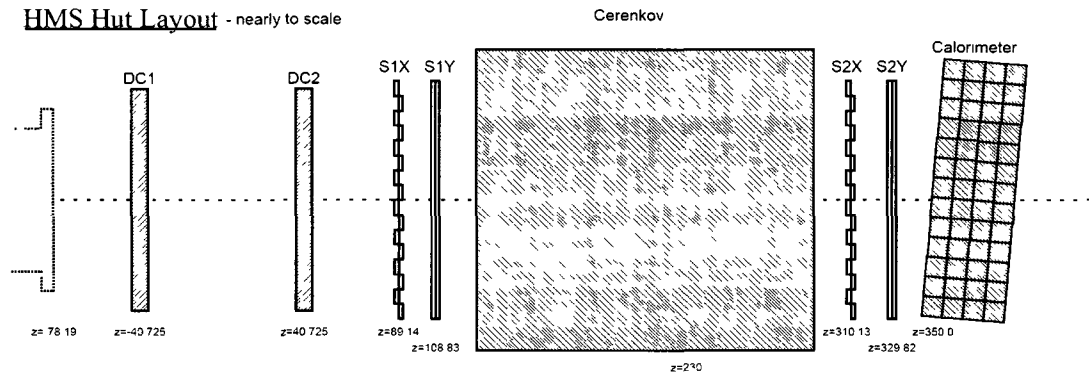


Figure 3.7: Side view of the standard HMS detector package.

The HMS drift chambers

The drift chambers are gas (or gas mixture) filled detectors. A basic drift chamber consists of an anode plane made of regularly spaced thin wires (sense wires) between two cathode planes. A high voltage is applied between the cathode and anode wires. In order to make the field more uniform, other wires, called field wires, are placed between each sense wire to define an elementary cell (a sense wire surrounded by cathode and field wires). The motion of a charged particle passing through the gas will produce a primary ionization. The ejected electron-ion pairs drift towards the sense wire due to the electric field. In the vicinity of the sense wire where the electric field gradient becomes very high, electrons have enough energy to create a second and a third etc. ionization which lead to a multiplicative avalanche and then a detectable and recordable signal on the sense wire. Measuring the elapsed time (drift time) between the trigger and the avalanche allows one to determine the distance between the particle track and the sense wire with a typical resolution of $100 \mu m$. The spatial and angular coordinates of the particle track can be obtained by adding several planes of detection in a row.

The HMS drift chambers consist of 6 parallel planes of wires arranged in order X,Y,U,V,Y' and X' spaced apart by 1.8 cm. The dimensions of the elementary HMS drift chamber cell are 1.0 cm (horizontal) \times 0.8 cm (in the direction of motion of the particle). The sense wires are connected to the ground while the field and cathode wires are kept to a negative high voltage. The X (X') planes give information in the dispersive direction (vertical), the Y (Y') planes give information in

the non dispersive direction (horizontal), and the U and V plane are rotated by $\pm 15^\circ$ with respect to the X and X' plane. A schematic view of the HMS drift chambers is shown in figure 3.8.

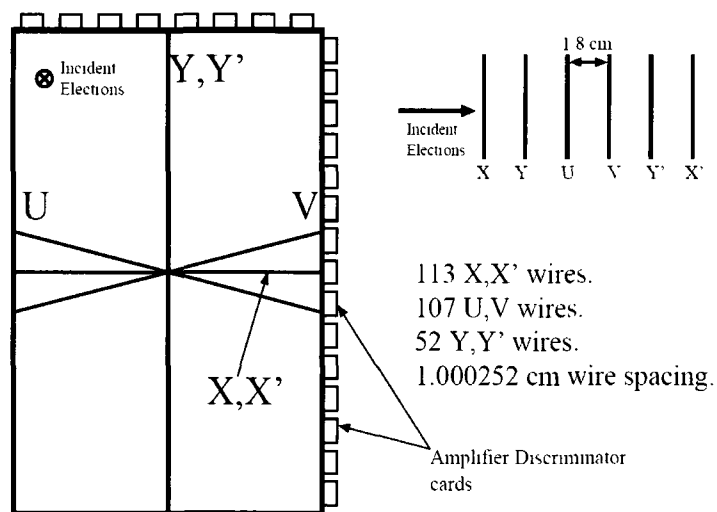


Figure 3.8: Schematic of the HMS drift chambers.

The gas used in the chambers is a mixture of Argon and Ethane 50%/50% bubbled through isopropyl alcohol, resulting in a 1% doping. Argon is a good avalanche starter whereas Ethane quenches the avalanche to prevent a continuous discharge on the sense wire. Ionized Ethane fragments can form a polymer which agglomerates on the different wires and affects the chamber performances over time. The addition of alcohol helps to delay the polymer formation and improve the lifetime of the chambers.

LRS 2735 and Nanometrics N-227 amplifier/discriminator cards are used to read out the signal on the sense wires. The signal is transmitted to multi-hit Lecroy 1877 fastbus TDC modules where a stop signal is generated.

The hodoscopes

In the HMS standard configuration, the triggering and timing informations based on the time of flight calculation, are given by 4 planes, S1X, S1Y, S2X and S2Y, of scintillator hodoscopes. The scintillators are made of BC-404 plastic which emits light when a charged particle passes through.

The X paddles are 75.5 cm long, the Y paddles are 120.5 cm long. All are 8 cm wide and 1 cm thick. The scintillation light propagates through the material by total internal reflection to Photonis XP2262 photomultipliers (PMTs) located at both ends of the paddles. The paddle and the PMTs are coupled by UVT lucite light guide. In order to avoid light "leaks", each paddle and lightguide is wrapped in a layer of aluminized Mylar and then covered with a layer of Tedlar to ensure a good light-tightness. Once the light reaches the photo-cathode of the PMT, electrons will be emitted by the photoelectric effect and a series of dynodes will increase the number of electrons and thus amplify the electric signal. The HMS hodoscope time resolution is about 0.3 ns.

In the $GEp2\gamma$ experiment, the S2 planes had to be removed to make room for the proton polarimeter. The S1 paddles then were used only to define the trigger and give the start time for the HMS drift time determination. The S1X and S1Y planes being very close together, would not create an efficient trigger by themselves, as they do not restrict the tracks that go through the HMS chambers. Furthermore, the trigger rate, even in coincidence with the electron trigger, would exceed the capabilities of the data acquisition system. Consequently, a new scintillator paddle, called "S0", was built to create a coincidence trigger with the S1 plane. It was located right before the first HMS drift chamber. Its dimensions are 30.5 cm \times 38cm \times 1 cm. It is composed of two paddles, named "S0X1" and "S0X2". Each paddle is coupled to two XP2020 PMTs with bars of wavelength-shifter which degrades significantly the timing resolution. As a result, the S1 signal, delayed relative to the S0 signal, was used to form the S0-S1 coincidence trigger. S0X2 was located to detect the elastically scattered proton, and thus centered on the optical axis of the spectrometer. S0X1 catches the events of the radiative tail and inelastic events.

A copy of each of the S1 and S0 signals was sent to charge integrating LeCroy 1881M fastBus Analog to Digital Converters (ADC) to measure the integral of the pulse. The other copy was discriminated through leading-edge discriminators and sent to VME scalers and TDCs for timing information.

If S0 improves the triggering rate, being located before the HMS chambers, it unfortunately affects the angular resolution of the HMS due multiple scattering in its 1 cm thickness. At a Q^2 of 2.5 GeV² and a proton momentum $p = 2.0676$ GeV/c, the width of the angular distribution of multiple scattering in the 1 cm thick scintillator plastic is $\theta \approx 1$ mrad. This induces a smearing in

the angular resolution of 2.9 mrad in the vertical direction and 2.6 mrad in the horizontal direction, as obtained by a convolution of the first order coefficients of the HMS transport matrix (which will be described in section 4.3.2) and the width of the angular distribution of multiple scattering.

3.3.2 Focal Plane Polarimeter (FPP)

The new Focal Plane Polarimeter (FPP), located in the HMS hut in place of the Cerenkov detector and the S2 scintillator hodoscope planes, measures the polarization of the recoil proton. It consists of two CH_2 analyzer blocks mounted in series (to increase the efficiency) each followed by a pair of drift chambers. Before going further into technical details about the polarimeter, it is appropriate to explain the principle of a proton polarimetry measurement.

Proton Polarimetry principle

The polarization measurement takes advantage of the spin orbit coupling ($\vec{L} \cdot \vec{S}$) in the scattering of polarized protons off an analyzer nuclei which induces an azimuthal asymmetry in the angular distribution of the scattered protons. Figure 3.9 shows the special case where the polarized proton, with its spin \vec{S}_x along the x axis, has an angular momentum \vec{L} along the $+x$ or $-x$ axis depending on whether it scattered on the left or right off the CH_2 analyser nucleus at fixed impact parameter. The spin orbit coupling $\vec{L} \cdot \vec{S}$ then will be of opposite sign for these two cases inducing an attractive potential on one side and a repulsive one on the other side. Setting that $\vec{L} \cdot \vec{S} > 0$ gives a repulsive potential, there will be more protons scattered on the left than on the right. Having more protons with spin along the x direction than in the opposite direction will lead to a left-right asymmetry in the azimuthal angular distribution. In practice, of course only one state of polarization of the beam is available at a time. As the beam polarization is never 100%, we measure the asymmetry between the polarized proton and the remaining unpolarized protons. However, by flipping the helicity of the beam and taking the difference between the two angular distributions the contribution of the unpolarized protons is removed.

An easy way to understand the asymmetry process is to look at the probability vector \vec{P} on Figure 3.9 with its origin at 0. Its magnitude represents the probability for the polarized proton to scatter at an angle φ . In the unpolarized case, as there is no asymmetry, all the angles are equally

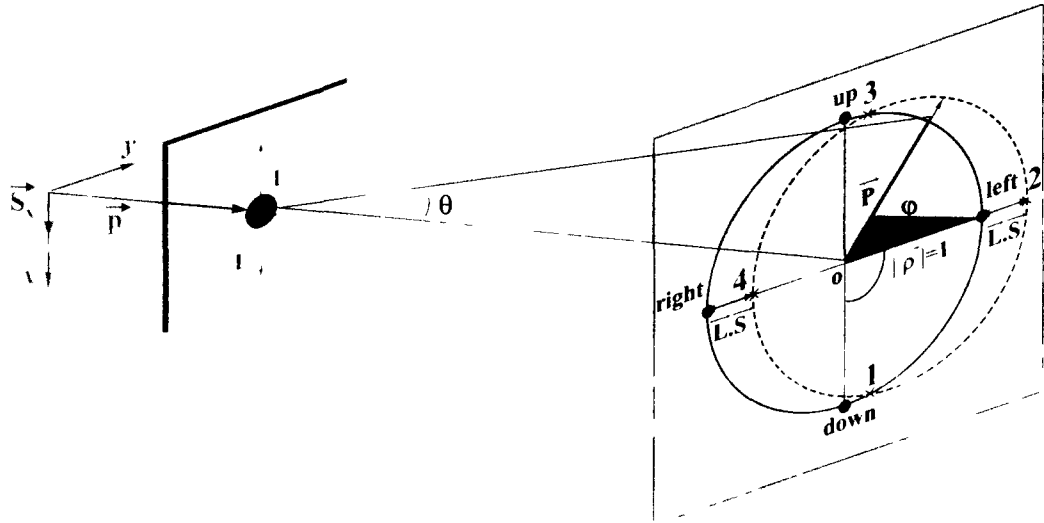


Figure 3.9: Schematic of a polarized proton scattering off an CH_2 analyzer nucleus.

likely, the tip of \vec{P} would lie on a circle (the green circle in the figure) of radius $|\vec{\rho}| = 1$ versus φ . Now, considering a left-right asymmetry due to the spin-orbit coupling, the tip of \vec{P} lies on another circle (dotted red) shifted to the left by an amount proportional to $\vec{L} \cdot \vec{S}$. We see that its magnitude is larger in the left half than in the right half. So the protons would more likely scatter with an angle φ between 0 and π . This shows why a left-right asymmetry leads to a continuous azimuthal angular asymmetry. Figure 3.10 shows the evolution of the probability to scatter at an angle φ relative to the unpolarized case given by $\frac{|\vec{P}| - |\vec{\rho}|}{|\vec{\rho}|} = |\vec{P}| - 1$ as a function of φ when the tip of \vec{P} moves from the points 1 to 4. Points 2 and 4 are the points where the asymmetry is maximum. Points 1 and 3 is where the probabilities in the polarized and unpolarized case are identical (intersection of the green and red dotted circles), $|\vec{P}| - 1 = 0$ and there is no asymmetry.

In general, for an incident proton propagating along the arbitrary direction of vector \vec{k} , with transverse polarization $\vec{\Pi} = S_x \hat{x} + S_y \hat{y}$, the azimuthal angular distribution of the yield I of scattered protons is given by:

$$I = I_0 \left(1 + A_y(p, \vartheta) \vec{\Pi} \cdot \hat{n} \right) \quad (3.7)$$

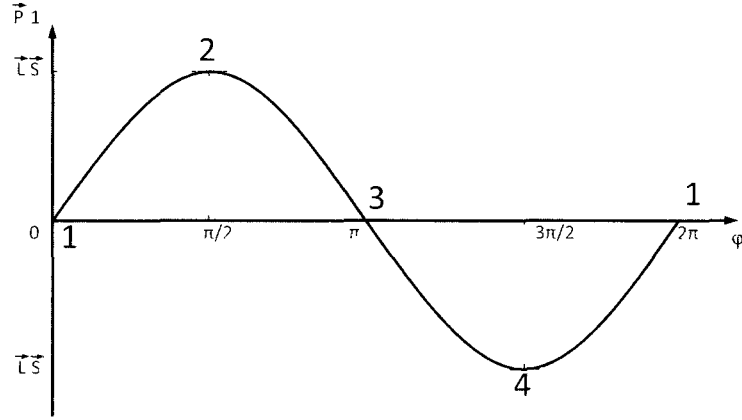


Figure 3.10: Evolution of $|\vec{P}| - 1$ vs φ .

where I_0 is the unpolarized yield, \hat{n} is the unit vector normal to the scattering plane defined as $\hat{n} = \hat{k} \times \hat{k}' / |\hat{k} \times \hat{k}'|$, with k (k') the unit vector in the direction of the incident (scattered) proton. The quantity $A_y(p, \vartheta)$, which depends upon the incident proton momentum prior to the interaction and the polar scattering angle ϑ , is the CH₂ analyzing power. From equation 3.7, we can see that A_y is the "size" of the asymmetry, described by $\vec{\Pi} \cdot \hat{n}$, relative to the unpolarized case for 100% polarization. The polar and azimuthal angles are defined by:

$$\sin \vartheta = |\hat{k} \times \hat{k}'|, \quad \sin \varphi = -\hat{x} \cdot \hat{n}, \quad \cos \varphi = \hat{y} \cdot \hat{n} \quad (3.8)$$

From these definitions, the angular probability distribution of scattered protons is given by:

$$f(p, \vartheta, \varphi) = \frac{\epsilon(p, \vartheta)}{2\pi} (1 + A_y(p, \vartheta) S_y \cos \varphi - A_y(p, \vartheta) S_x \sin \varphi) \quad (3.9)$$

with $\epsilon(p, \vartheta)$ the efficiency off the polarimeter which describes the proportionality of the scattered protons relative to the incident protons. The factor $1/2\pi$ comes from the normalization of the probability f .

The analyzing power is an important quantity because it defines the performance of the polarime-

ter through the figure of merit \mathcal{F} given by:

$$\mathcal{F}^2 = \int_{\theta} \frac{d\epsilon}{d\theta} A_y^2(\theta) d\theta \quad (3.10)$$

with $d\epsilon/d\theta$ the differential efficiency of the process, defined as the number of "good" scattered particles relative to the total number of incident particles N_0 . The figure of merit enters directly in the statistical uncertainty of a measurement of the polarization ΔP given by:

$$\Delta P = \sqrt{\frac{2}{N_0 \mathcal{F}^2}} \quad (3.11)$$

From this expression we see that for a given number of incident particles the choice of material is important. A material with high analyzing power will reduce the statistical uncertainty more than a low analyzing power material. Consequently, the running time of the experiment will also be reduced.

Analyzer

The FPP analyzer is made, as mentioned above, of polyethylene (CH_2). It consists of two retractable doors each made of two blocks, allowing the data taking of straight through trajectories for calibration and alignment studies of the FPP. Each block pair is 145 cm (tall) \times 111 cm (wide) \times 55 cm (thick) and made of several layers of CH_2 held together by an outer aluminium frame. To reduce the occurrence of leakage through the seam when the doors are inserted, an overlapping step was designed into the edge; and being significantly heavy, the blocks are supported on a different frame than the detector and attached directly to the floor of the shield house. This ensures that while inserting the doors the other detectors do not move. The doors can be inserted and retracted by a hand crank mechanism installed in the HMS hut.

The choice of CH_2 as the analyzer material is a compromise between best analyzing power, cost and a system that could fit in the confined space of the HMS hut. Even if hydrogen would be the perfect candidate in term of analyzing power, it is evident that it is the worst when it comes to safety. Furthermore, an experiment carried in Dubna, Russia [55], aiming at measuring the

analyzing power of the reaction $\vec{p} + CH_2 \rightarrow \text{one charged particle} + X$ at proton momenta up to 5.3 GeV/c revealed two important features: the CH_2 analyzing power is larger than the one in carbon; increasing the target thickness above the nuclear collision length (56.1 g/cm² for the CH_2) and the polarimeter acceptance in $p_T \equiv p \sin \theta$ above 0.7 GeV/c does not improve significantly the figure of merit. p_T is called the transverse momentum, p is the proton momentum corrected for energy loss up to the interaction point in the material, θ is the scattering angle. These arguments lead to the actual design of the FPP analyzer.

FPP drift chambers

The tracking system of the FPP consists of two drift chamber pairs, one after each analyzer block. They were made by the team of Y. Zanevsky at the Joint Institute for Nuclear Research (JINR) in Dubna, Russia. The active area of the chamber is 164 cm (tall) \times 132 cm (wide). Each chamber contains three detection planes sandwiched and interspersed with cathode layers, with outer 30 μm thick aluminized mylar windows for the gas-tightness of the chambers and an outermost aluminium frame on either side to ensure the mechanical rigidity of the whole system. A field wire is positioned between each sense wire (spaced 2 cm apart from each other). The cathode wires, spaced 0.3 cm apart, are located at 0.8 cm in front of and behind (in the transverse direction of the chambers) the sense and field wire layer. The characteristics of the different wire are given in table 3.5.

	Material	Diameter (μm)	Tension (g)
Sense	gold plated Tungsten	30	70
Field	Beryllium-Bronze-alloy	100	150
Cathode	Beryllium-Bronze alloy	80	120

Table 3.5: Characteristics of the wires used in the FPP drift chambers.

The dimension of the resulting FPP drift chamber elementary cell are 1.6 cm (tall) \times 2.0 cm (wide) as shown on figure 3.11. The three layers of detection of a chamber have different orientation: $+45^\circ$, 0° and -45° relative to the x axis which points down. The $\pm 45^\circ$ layers have 104 sense wires each, the 0° layer has 83 wires. The same order is repeated for all chambers, which are identical. The 50%/50% Argon-Ethane gas mixture used to fill the chambers is supplied by the same system

as for the HMS. A high voltage of 2400V was applied on cathode and field wires; the sense wires were at ground potential.

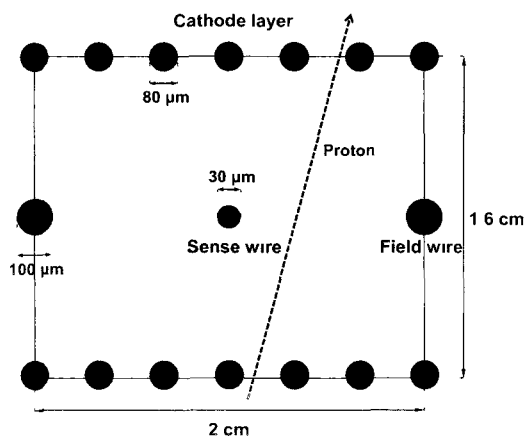


Figure 3.11: Schematic of an elementary cell of the FPP drift chambers. The dimensions are not to scale.

The readout system consists in amplifier/read-out cards, manufactured in Dubna, Russia, attached to the left and right sides of the chambers with special connectors. Each card connects to 8 sense wires and they output ECL logic signal. The signals are transmitted via a standard 34-pair ribbon cable (with two cards per cable) to VME-based F1 TDC modules which measure the event time. A design drawing of the FPP with the HMS drift chambers and the trigger planes is shown on figure 3.12.

3.3.3 Electromagnetic Calorimeter (BigCal)

A new electromagnetic calorimeter (BigCal) was designed and built to help the separation of “ep” elastic events from the inelastic background, by detecting the electron in coincidence with the scattered proton and determining the shower coordinates of the electron.

BigCal is made of a total of 1744 TF0-1 lead glass bars split into two different part as shown in figure 3.13. The bottom part is composed of 1024 lead glass blocks of dimensions $3.8 \times 3.8 \times 45 \text{ cm}^3$, stacked in an array of 32×32 , coming from the Institute for High Energy Physics (IHEP)

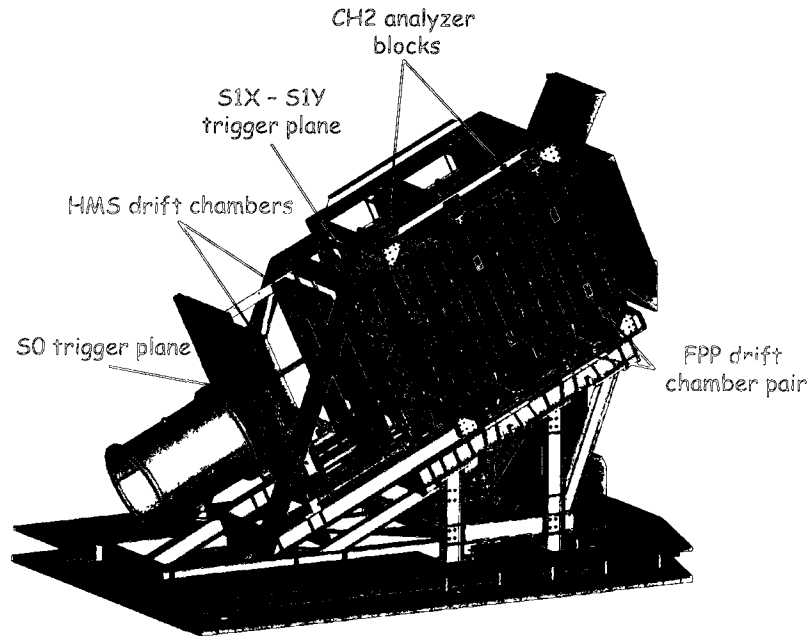


Figure 3.12: Design drawing of the FPP with the HMS drift chambers and the trigger planes.

in Protvino, Russia. The 720 blocks of the upper part have different dimensions: $4 \times 4 \times 40 \text{ cm}^3$ and are stacked in a 30 (horizontal) \times 24 (vertical) array. They were made at the Yerevan Physics Institute, Armenia and were previously used in the Real Compton Scattering (RCS) experiment in Jlab Hall A. The whole calorimeter block array has then 56 rows and 32(30) columns for the bottom (upper) part, respectively, resulting in an active area of approximately $122 \times 218 \text{ cm}^2$. The main characteristics of the TF0-1 glass are given in table 3.6. The glass stack is placed in a frame attached to the BigCal platform. The total weight of the glass is about 4300 kg. Each bar is individually wrapped in a thin aluminized mylar sheet and connected to a 12-stage, venetian blind Russian FEU-84 PMT through a 5 mm thick Si-pad (called a "cookie"). PMTs and cookies are attached to a 2" thick aluminium adjustable cross bar. Each bar supports 4 rows of PMTs. In the upper part of the calorimeter each then supports 120 PMTs, while in the lower part, a bar holds 128 PMTs.

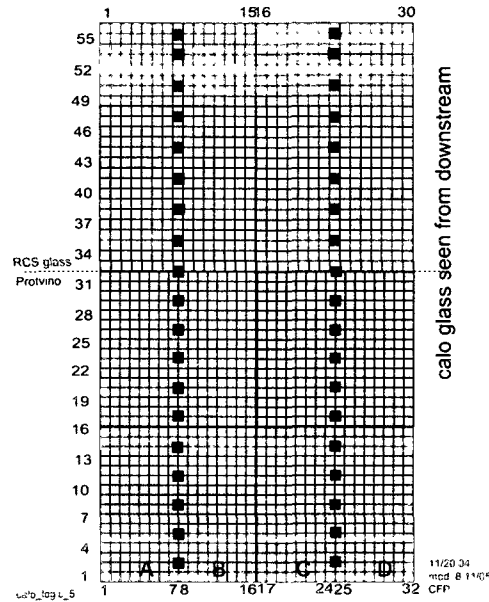


Figure 3.13: The 1744 lead-glass bars of BigCal ordered in several groups (in colors) for the trigger.

Density, ρ ($\text{g}\cdot\text{cm}^{-3}$)	3.86
Index of refraction, n	1.6522
Radiation length, X_0 ($\text{g}\cdot\text{cm}^{-2}$)	2.74
Nuclear absorption length, (cm)	22

Table 3.6: Main characteristics of the TF0-1 glass.

An electron hitting the lead glass surface of the calorimeter produces an electromagnetic cascade: the primary electron losing energy in the glass produces Bremsstrahlung photons. Those photons then produce electron-positron pairs which in turn produce other photons and so on, until the primary electron and the secondary pair-produced particles lose enough energy to reach the critical energy. After what, they will mainly lose energy by ionization and then will get absorbed. The incident and secondary electrons, moving faster than the lead-glass speed of light c/n , with n the refraction index given in Table 3.6, emit Cerenkov light in the glass, which is collected and transformed into an electric signal by the PMTs, sent into Lecroy 1881M Fastbus ADCs.

An LED and lucite system is located in front of the glass bars. This system consists of a 0.5-inch-

thick aluminium plate drilled with 1744 0.25-inch-diameter holes to let the light, coming from a 0.5-inch-thick lucite plate, go through the lead glass bars. The light is generated by an LED and propagates through optic fibres coupled to the lucite plate. This LED system was, of course, turned off during the production runs. Instead, it was used to perform rough calibrations mainly during the test phase in the Testlab. In order to protect the glass bars from low energy photons, a series of four 1-inch-thick aluminium plates could be placed at the very front of the calorimeter. All four plates were used during the experiment, except at the lowest energy point where only one was in place.

An extensive GEANT Monte Carlo simulation performed at Protvino estimated the coordinate resolution of BigCal to be $dx \approx 0.54 \text{ cm} / \sqrt{E'_e}$ with E'_e the energy of the scattered electron in GeV. The simulation takes into consideration the features of the photocathodes of the PMTs, the coefficient of reflection of the Mylar sheet used to wrap the bars, the lead glass absorption length and refraction index and the plates of material in front of the glass. The scattering of the electrons in air during their travel from the target to BigCal was not included in the simulation. The angular resolution is the result of two contributions. There is of course a contribution coming from the shower coordinate resolution but also a contribution from the fact that the target is extended. To the shower coordinate given above corresponds an angular resolution of 0.7 to 2.3 mrad for the different kinematics of the GEp(2γ) experiment. Despite the absorber in the front, the lead-glass suffered from serious radiation damage over time, that altered significantly the energy resolution, but only slightly the position resolution. At the beginning of the experiment, the energy resolution was $\approx 10\% / \sqrt{E}$. At the end it decreased to $\approx 20\% / \sqrt{E}$. The presence of the absorber has also a non-negligible effect on the energy resolution.

3.4 Electronics and Trigger Set-up

The main data acquisition system was located on a platform in the hall, shielded from radiation by a concrete bunker. The BigCal trigger and the main trigger were created on this platform whereas the HMS trigger was formed inside the HMS hut.

3.4.1 BigCal trigger

The generation of the BigCal trigger comes from a succession of three summing levels. The signal from the 1744 PMTs are fed to 224 NIM summing modules each with 8 inputs and 4 outputs. The summing modules perform two tasks with the 8 inputs. One task is to amplify the individual inputs by a factor 4.2 and output the individual signals sent to 28 LeCroy 19881M ADC modules. The second task is to sum the 8 signals and produce 4 summed output signals.

The *first level* trigger consists of the analog sum of eight signals, discriminated (corresponding to a group of 8 blocks in the same row) and sent to 3 Lecroy 1877 TDC modules of 224 channels each. Another output (sum of eight) of each NIM module is sent to another bank of identical modules.

The *second level* trigger is formed from 38 sums of 64 signals used to define the BigCal trigger. The calorimeter is divided as follows: into 2 parts horizontally, each part being a compound of 19 overlapping groups of 4 rows and 16 columns. In figure 3.13, the sum of 64 are shown by color groups overlapping each other vertically by one row (starting from the bottom). The 38 output signals are represented by 19 black and 19 blue squares for the left and right part respectively. This vertical overlapped pattern is used to increase the trigger efficiency. Indeed, without this overlap, if a shower is created at the border of two rows, half of its energy will be deposited in the upper row and the other half in the lower row. As a consequence, if the BigCal trigger threshold was set to about the full shower energy, the later event would be lost. The overlapping pattern allows then to increase the trigger threshold without significant loss in efficiency.

Finally, the sum of 64 signals are sent to 4 discriminator modules (one for each quarter of BigCal), each with a remotely adjustable threshold and 16 inputs, creating the *third* and last trigger level. The 4 logical outputs of the discriminator are sent to 4 Fanin/Fanout NIM units, where a final logical OR on all the 38 second level sums is applied. So any signals above the threshold coming from any quarters of BigCal is sufficient to generate a trigger.

3.4.2 HMS trigger

The HMS trigger consists of the coincidence between the S1 HMS trigger signal and either one of the two signals coming from the two S0 paddles (figure 3.14). A S1 trigger is generated when both the X and Y planes give a signal. For each plane, this requires both PMTs in at least one scintillator paddle to fire. The S0 trigger is generated when both PMTs of either the S0X1, or the S0X2 paddle fire. Two different trigger signals could then be generated: HMS1(2) which are the coincidence signals between the S1 trigger and the S0X1(2) paddle respectively. Having two different triggers

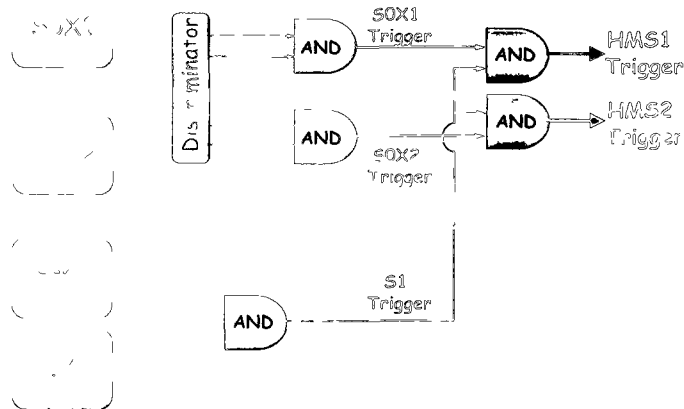


Figure 3.14: Schematic of the HMS trigger.

allows us to prescale them independently. The S0 detector was designed and placed in the HMS hut so that the elastic event distribution for most of the kinematics would fit in one paddle. So for a high rate kinematic, like the lowest energy one in this experiment, one paddle (S0X2) triggers mainly on the elastic events, while the other triggers mainly on the inelastic events. The two paddles being prescaled separately, this improves the trigger rate. The discriminators used to build the HMS trigger had a fixed 40 mV threshold and a 30 ns output pulse width.

3.4.3 Main coincidence trigger

From the two HMS triggers and the single BigCal trigger, five different triggers were available: HMS1, HMS2, BigCal and the coincidence triggers HMS1 & BigCal = COIN1, HMS2 & BigCal =

COIN2. The timing, at all times, was set by the HMS signals arriving last and the BigCal trigger arriving first. All these five triggers were sent to the trigger supervisor and could be prescaled separately, which is very handy to prevent the data acquisition system from being overwhelmed by too high rates. The COIN2 trigger corresponds to the S0X2 paddle, where almost all the elastic events are originating from; it was always prescaled with a factor of 1. Depending on the kinematic COIN1 was prescaled by a factor 1 to 10. The BigCal trigger was always prescaled by a large factor due to its very high raw rate. A schematic of the trigger is shown in figure 3.15.

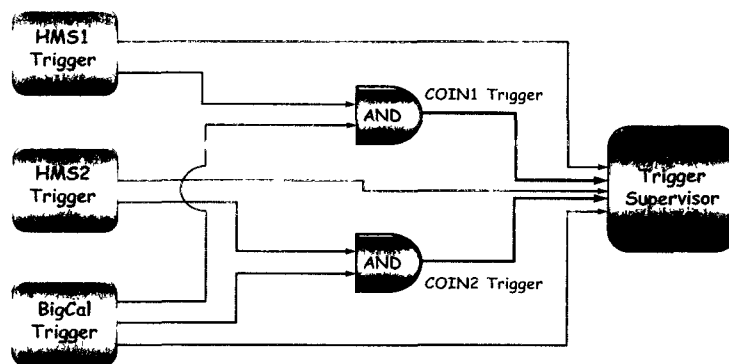


Figure 3.15: Schematic of the main coincidence trigger.

Chapter 4

Data Analysis Part One: Tracking, Reconstruction and Event Selection

In this chapter, we will describe and explain the data analysis process which leads to the polarization component ratio. We will first dwell on the event reconstruction in the HMS and in the FPP. Then in a second step the separation of the elastic events from the inelastic background will be detailed. In the third and last step, we will explain the extraction of the polarization components through the spin transport calculation. Before doing so, it is appropriate to present the different kinematics of the GEp(2γ) experiment.

4.1 Kinematics

The goal of the GEp(2γ) experiment was to search for a possible kinematical dependence in elastic $\vec{e}p$ scattering of the proton polarization component ratio $R \equiv -\mu_p \sqrt{\frac{\tau(1+\epsilon)}{2\epsilon}} \frac{P_t}{P_l}$ and of the ratio of the longitudinal polarization component to its Born value P_ℓ/P_ℓ^{Born} . Three values of ϵ were chosen: 0.152, 0.635 and 0.785. Looking at the theoretical models (which predict a bigger effect at small ϵ) one might wonder why two points at high ϵ were chosen. These choices were driven by the beam time allowed: the cross section dropping by a factor 20 going from $\epsilon = 0.785$ to 0.152, replacing the middle ϵ point by a smaller one would have required much more beam time. These

choices were also constrained by the available beam energy: as other experiments were running in Hall A and B, only certain energies were available, thereby restricting the choice in ϵ since the proton momentum was fixed ($p_0=2.0676$ GeV/c). These compromises and constraints lead to the kinematic table 4.1:

E_e , GeV	E_e' , GeV	p_p , GeV/c	θ_e , °	θ_p , °	ϵ
1.875	0.543	2.0676	105.16	14.495	0.152
1.868	0.536	2.0676	105.08	14.495	0.152
2.848	1.516	2.0676	44.9	30.985	0.635
3.549	2.207	2.0676	32.579	35.395	0.773
3.680	2.348	2.0676	30.778	36.105	0.791

Table 4.1: Kinematic Table of the $GE_p-2\gamma$ experiment, with E_e the beam electron energy, E_e' the scattered elastic electron energy, p_p the proton momentum, θ_e the electron scattering angle (BigCal angle) and θ_p the scattered proton angle (spectrometer (HMS) angle).

Before presenting the calculation of some kinematic expressions of two-body elastic scattering, we need to present the main coordinate systems used during the experiment. In the Hall-C coordinate system the z -axis is along the beam direction with the x -axis pointing left when looking downstream. The y -axis then points up so that the Hall-C system is right-handed. In the right-handed BigCal system, the z_{cal} -axis is along the scattered electron direction. The x_{cal} and y_{cal} point left and up when looking downstream, respectively. In the right-handed focal plane systems, the z -axis is along the direction of motion of the recoil proton. Looking downstream x_{fp} (y_{fp}) point down (left) in the focal system. The azimuthal scattering angle φ_{FPP} is defined from positive x to positive y (clockwise). Figure 4.1 presents the different coordinate systems.

It is now appropriate to derive the useful expressions of two-body elastic scattering. We first consider an electron moving along the z direction which scatters in the xz plane off a proton at rest. After the scattering, the electron and the proton are at angles θ_e and θ_p with respect to the z -axis, respectively. Neglecting the electron mass, the four-vectors of the incident (scattered)

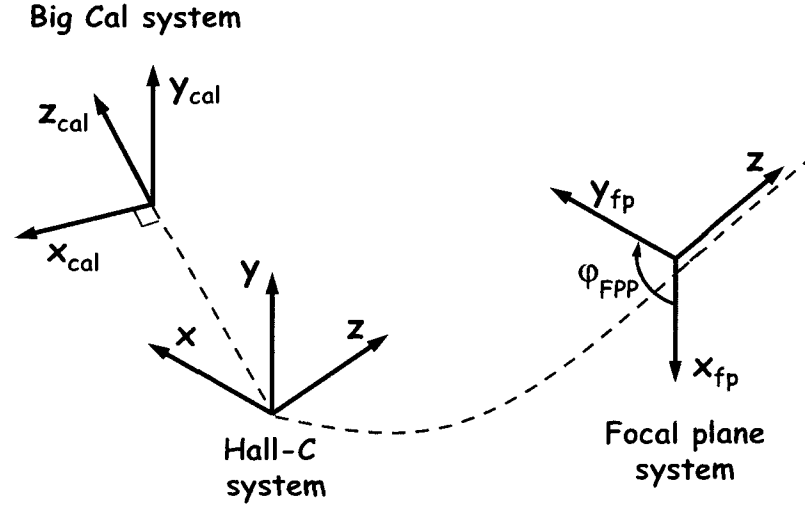


Figure 4.1: Coordinate systems used during the GEp2 γ experiment.

electron k_μ (k'_μ) and of the rest (scattered) proton p_μ (p'_μ) are given in the lab frame by:

$$\vec{k}^\mu = \begin{pmatrix} E_e \\ 0 \\ 0 \\ E_e \end{pmatrix}, \quad \vec{k}'^\mu = \begin{pmatrix} E'_e \\ E'_e \sin \theta_e \\ 0 \\ E'_e \cos \theta_e \end{pmatrix}$$

$$\vec{p}^\mu = \begin{pmatrix} M \\ 0 \\ 0 \\ 0 \end{pmatrix}, \quad \vec{p}'^\mu = \begin{pmatrix} E'_p \\ -p_p \sin \theta_p \\ 0 \\ p_p \cos \theta_p \end{pmatrix}$$

with p_p the scattered proton momentum and M its mass. The conservation of energy gives:

$$E_e + M = E'_e + E'_p \Rightarrow E'_e = E_e + M + \sqrt{p_p^2 + M^2} \quad (4.1)$$

The momentum conservation is given by:

$$\text{along x: } 0 = E'_e \sin \theta_e - p_p \sin \theta_p \Rightarrow E_e'^2 \sin^2 \theta_e = p_p^2 \sin^2 \theta_p \quad (4.2)$$

$$\text{along y: } 0 = 0 \quad (4.3)$$

$$\text{along z: } E_e = E'_e \cos \theta_e + p_p \cos \theta_p \quad (4.4)$$

Extracting $E_e'^2 \sin^2 \theta_e$ from 4.4 and plugging it into 4.2 it follows that:

$$E_e'^2 - p_p^2 \sin^2 \theta_p = (E_e - p_p \cos \theta_p)^2 \quad (4.5)$$

Using 4.1 to replace $E_e'^2$, we obtain:

$$(E_e + M) \sqrt{p_p^2 + M^2} = M(E_e + M) + E_e p_p \cos \theta_p \quad (4.6)$$

Taking the square of this expression and solving for p_p we finally get:

$$p_p = \frac{2E_e M(E_e + M) \cos \theta_p}{M^2 + 2E_e M + E_e^2 \sin^2 \theta_p} \quad (4.7)$$

This relation gives the proton momentum as a function of the beam energy and the scattered proton angle. The momentum transfer squared Q^2 is given by:

$$Q^2 = 2k \cdot k' = 2M \sqrt{p_p^2 + M^2} = 2E_e E'_e (1 - \cos \theta_e) = 4E_e E'_e \sin^2 \frac{\theta_e}{2} \quad (4.8)$$

The different quantities derived above allow one to calculate the Jacobian of the reaction and thus the distance from the target at which the calorimeter needs to be located in order to have a matching acceptance between the electron and proton arms. The Jacobian \mathcal{J} of the elastic electron-proton scattering is defined as the ratio of the electron solid-angle $d\Omega_e (= \sin \theta_e d\theta_e d\phi_e)$ to the proton solid-angle $d\Omega_p (= \sin \theta_p d\theta_p d\phi_p)$ with $\phi_p(\phi_e)$ the electron(proton) azimuthal angle:

$$\mathcal{J} \equiv \frac{d\Omega_e}{d\Omega_p} \quad (4.9)$$

It can be shown that the Jacobian is given by the expression:

$$\mathcal{J} = \frac{p_p^2}{E_e'^2} \left| \frac{\cos \theta_p \tan \theta_p \sin \theta_p - \sin^2 \theta_p \frac{p_p E_e}{M(E_e + M)}}{\cos \theta_e - \frac{E_e'}{M} \sin^2 \theta_e} \right| \quad (4.10)$$

The proton solid-angle is known and defined by the HMS acceptance: $\Delta\Omega_p = 6.74$ msr. The distance from the target to the calorimeter d is given by:

$$d = \sqrt{\frac{\mathcal{A}}{\Delta\Omega_e}} \quad (4.11)$$

with \mathcal{A} ($= 122 \times 218$ cm²) the lead-glass area of the calorimeter. The distance calculated with Eq. 4.11 and the actual distance at which the calorimeter was located during the experiment were different due to physical obstacles in the hall such as the rail of the spectrometer, the length of the BigCal cables (signal and HV) or the Hall C AC units. Nonetheless, it is only when the calorimeter is placed further than the distance required by acceptance matching that some elastic events start to miss hitting the calorimeter. No elastic events were lost when the calorimeter was located closer to the target than the matching acceptance suggested. The spot on the surface of the calorimeter was just smaller. Table 4.2 summarizes the Jacobian, electron solid-angle, the calorimeter distance d calculated from 4.11 and d_{Hall} the actual distance for the different kinematics.

E_e , GeV	θ_e , °	\mathcal{J}	$\Delta\Omega_e$,msr	d , cm	d_{Hall} , cm	ϵ
1.875	105.16	14.72	99.2	517.7	493	0.152
1.868	105.08	15.26	102.9	508.5	494	0.152
2.848	44.9	2.09	14.1	1373	1200	0.635
3.539	32.579	0.99	6.7	1997	1116	0.773
3.680	30.778	0.88	5.9	2115	1102	0.791

Table 4.2: Jacobian and BigCal-target distance of the GEp2 γ experiment.

It is important to add that the order of the kinematics in the table is not chronological. The seconds parts of the lowest ($\epsilon=0.152$) and highest ($\epsilon=0.791$) ϵ points were done after the Christmas break of 2008. The two parts of each kinematic were then merged and averaged. An individual study of each part is interesting to check the stability of the detectors and the consistency of the

results. The two parts of the smallest point being kinematically very close from each other will not be analyzed separately. It has been checked that the results from those two samples were very compatible.

4.2 HMS Hodoscope Calibration

We have seen in the previous chapter that the HMS hodoscopes defined the HMS trigger, and measure and set the start time of the HMS and FPP drift chambers. A good calibration is essential to obtain a clean trigger. Several corrections are applied to the hodoscopes information. First, we needed to convert the TDC signal into a time. A conversion factor of 25.9 ps per TDC count was applied. We also needed to account for different signal cable length.

Since the PMT signals are sent to a discriminator with a fixed threshold, a dependence between the amplitude of the pulse and the time at which the threshold is exceeded exists. A pulse high correction, also known as walk correction, of the form t_1/\sqrt{ADC} is applied, where the parameter t_1 is determined for each PMT.

Another correction, was required to take into account the different light velocity in each individual PMT. From the time difference between opposite PMTs, the coordinate d (along the scintillator axis) of the point at which the particle went through the paddle is determined. Then a correction of the form d/v_{PMT} , with v_{PMT} the light propagation velocity of each individual PMT, is taken into consideration to obtain the average scintillator time. In the calibration procedure v_{PMT} is treated as a parameter.

Finally, as the start time of the drift chambers is defined at the focal plane ($z = 0$), we need to account for a correction of the form $z/\beta c$ for each average scintillator time, where z is the position of each paddle with respect to the focal plane. In the relativistic factor β , the reconstructed momentum of the spectrometer p is used.

The calibration is done by using a code written by Peter Bosted. It allows one to determine by a minimization procedure the t_1 , v_{PMT} and zero offset t_0 parameters for each of the 52 PMTs. A timing resolution of 0.25 ns was reached.

4.3 HMS Tracking and Reconstruction

4.3.1 HMS Tracking Algorithm

The proton trajectories entering the HMS drift chambers are very nearly perpendicular to the wire planes, so that the distance of closest approach between a track and a wire is in the plane of the anode wire. The drift time is corrected for the propagation along the wire and difference in signal cable length between the chambers and the TDC modules.

The first step in the tracking algorithm is to identify the hit clusters or *space points* in the chamber. A hit is defined as the intersection in the xy plane of wires that have fired. For two hits to be grouped with each other, and then define the very first space-point of coordinates x,y , the distance between the two hits (in the xy plane) needs to be smaller than a hard-coded value ($= \sqrt{2}$ cm in the analysis). Other hits are added to the space point if they satisfy the above distance requirement with respect to the coordinates of the space point. A minimum of 5 hits per space-point is required. For space-points with more than one hit per plane, a routine is used to create new space-points. A limit of 20 space-points and 3 planes with multiple hits per space-point cannot be exceeded. In the situation where some planes still have multiple hits, the hit with the shortest drift time in each plane is kept.

The next step in the track reconstruction is the fitting of a *stub* for each space point using the drift time information. We assumed a uniform distribution of the drift position (in other words distribution of events) after averaging over all the cells. A time-to-distance map (drift map) is then generated for each wire plane. The drift distance \mathcal{D} is obtained by integrating the drift time distribution $\mathcal{T}(\tau)$ up to the drift time T_d given by the TDC:

$$\mathcal{D}(T_d) = \mathcal{D}_{max} \frac{\int_{T_{min}}^{T_d} \mathcal{T}(\tau) d\tau}{\int_{T_{min}}^{T_{max}} \mathcal{T}(\tau) d\tau} = \mathcal{D}_{max} \int_{T_{min}}^{T_d} \mathcal{T}(\tau) d\tau \quad (4.12)$$

since T_{min} and T_{max} define the allowed time window so that $\int_{T_{min}}^{T_{max}} \mathcal{T}(\tau) d\tau = 1$. \mathcal{D}_{max} is the maximum drift distance and equal to half of the wire spacing (0.5 cm). Since all the possible drift positions are equally likely within a cell, the drift distance distribution is expected to be flat as

in figure 4.2. The drift distance gives the absolute value of the distance between the track and the wire but does not provide information about the relative position with respect to the wire: whether the track passed on the right or the left of the wire. To resolve this so called left-right ambiguity and assign the correct sign to the drift distance, a routine is used to test all the possible left-right combinations of hits within a point. All the possible stubs ($2^6 = 64$) are fitted and the one with the smallest χ^2 is selected. Since all the tracks are nearly perpendicularly to the wire plane, a small angle approximation for the Y and Y' plane is used. These planes being offset by 0.5 cm, the left-right combination that makes the track go between the wires is the chosen one. This improves the speed of the algorithm by reducing the number of combinations to be analysed from 64 to $2^4 = 16$.

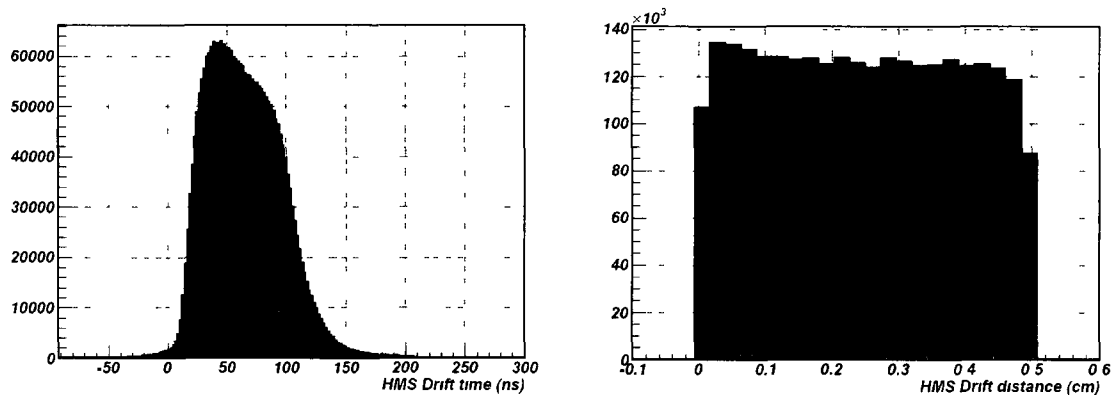


Figure 4.2: HMS drift time and HMS drift distance distribution.

The best stubs of both chambers are compared by grouping their space points together and testing all the combination in order to form a complete track. The stubs of the front and rear chamber are projected back to the focal plane. If their slope x' , the coordinates x_{fp} and y_{fp} satisfied some hard-coded requirements, a combination of two stubs is formed. For each of them, now made of 10 to 12 hits, all the possible left-right combinations are tested to define the best complete track. The fit parameters (slope in x' , y' and the x , y coordinates) and the χ^2 are stored.

At this point, it only remains to select the best complete track. All the tracks are reconstructed back to the target using the HMS transport matrix, the vertex position y_{tgt} , the vertical x'_{tgt} and

horizontal y'_{tgt} angles and $\delta = p - p_0/p_0$ the relative momentum of the spectrometer with respect to the central momentum $p_0 = 2.0676$ GeV/c. The timing is improved by using the track information. The tracks pass then through a pruning test, consisting of an ordered series of cuts:

- $|x'_{tgt}| \leq 100$ mrad
- $|y'_{tgt}| \leq 50$ mrad
- $|\delta| \leq 9\%$
- $|y_{tgt}| \leq 10$ cm
- $N_{PMT} \leq 3$
- $|t_{fp} - t_0| \leq 10$ ns

with N_{PMT} the number of PMTs on track and, t_{fp} the focal plane time of the track and t_0 the time determined from the hodoscopes. From all the tracks passing the pruning test, the one which has the smallest χ^2 is selected and considered as the best track of the HMS. Figure 4.3 shows a flow charts of the HMS tracking and reconstruction algorithm.

A resolution, obtained by comparing the position of the individual to the best fitted track (residuals) and averaged over all the planes, of $280 \mu\text{m}$ is achieved. This translates into a spatial resolution in $x(y)$ of $140 \mu\text{m}$ ($200 \mu\text{m}$) and angular resolution of 0.24 mrad (0.35) in $x'_{fp}(y'_{fp})$ respectively.

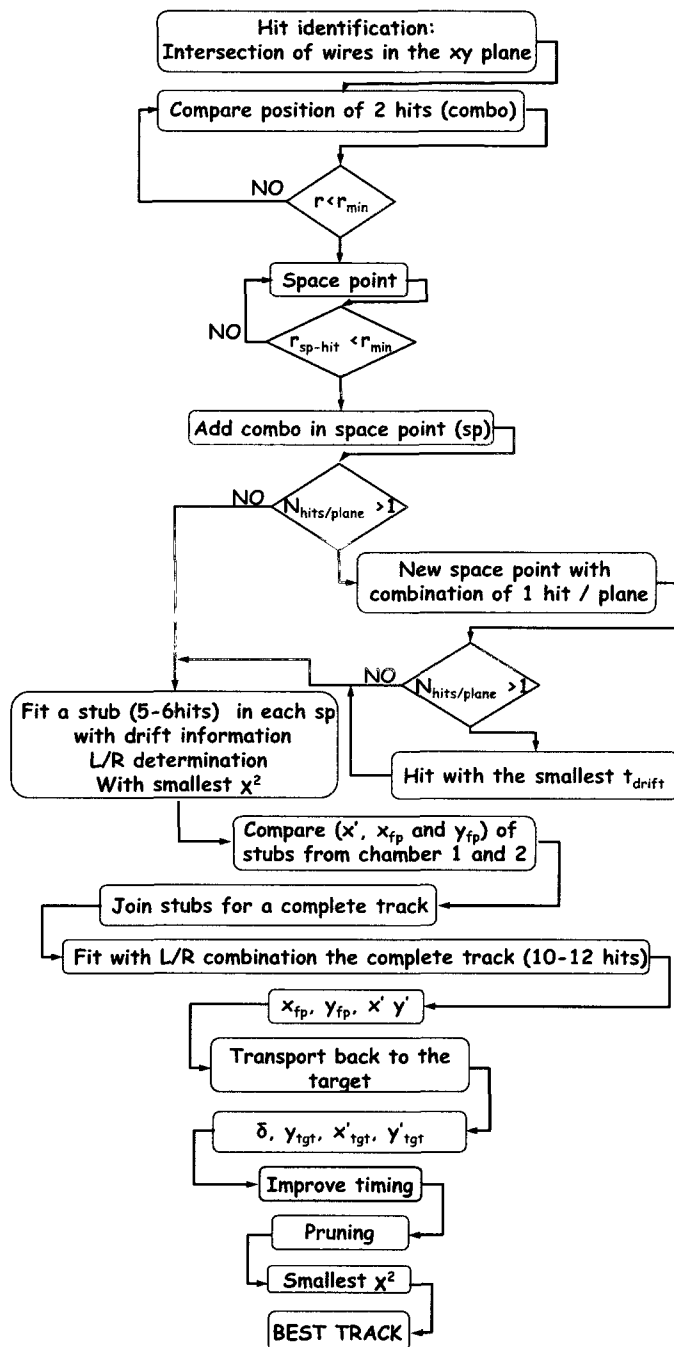


Figure 4.3: Flow chart of the HMS tracking and reconstruction algorithm.

4.3.2 HMS Transport Matrix (Optics)

As we have mentioned earlier, the five target coordinates $(x_{tgt}, y_{tgt}, x'_{tgt}, y'_{tgt}, \delta)$ are determined from the focal plane coordinates $(x_{fp}, y_{fp}, x'_{fp}, y'_{fp})$ using the HMS transport matrix. It is clear that this is an under-determined problem since the number of unknowns is greater than the number of measured variables. We can make the reasonable assumption that the vertical beam position y_b , known from the beam raster, corresponds to the vertical target coordinates x_{tgt} at $z_{spec} = 0$ ($x_{tgt} = -y_b$ since in the raster coordinate system, the $+y$ direction is oriented upward along the vertical). Knowing x_{tgt} , in other word fixing its value in the system of equations, allows us to solve for the other 4 target coordinates. If this assumption is very good for thin targets, additional corrections need to be applied for extended targets. The target coordinates can be expressed as a Taylor-series of the focal plane coordinates on an event-by-event basis. For the n^{th} -event we obtain:

$$(y, x', y', \delta)_{tgt}^n = \sum_{i,j,k,l,m=0}^{i+j+k+l+m \leq N} \Gamma_{(y,x',y',\delta),n}^{i,j,k,l,m} (x_{fp})^i (y_{fp})^j (x'_{fp})^k (y'_{fp})^l (x_{tgt})^m \quad (4.13)$$

The $\Gamma_{(y,x',y',\delta)}^{i,j,k,l,m}$ are the coefficients of the HMS optics matrix, calculated in an iterative fitting procedure [56] based on a starting model from the differential linear algebra based program COSY INFINITY [57]. In the analysis, the expansion was performed up to the $N = 6$ order. Specific runs using a sieve slit collimator on thin multi-foil targets were taken to perform the calibration of the coefficients. The different targets used during the optics runs are given in Table 4.3. The common 0.95 cm offset comes from a survey of the target positions.

Target	z position (cm)
Aluminum 3-foil	0.95, 0.95 \pm 7.5
Carbon 2-foil	0.95 \pm 2.0
Aluminum 2-foil	0.95 \pm 3.8

Table 4.3: Thin multi-foil targets used during the dedicated optics runs.

The sieve slit collimator consists of an array of seven columns spaced by 2.540 cm and nine rows separated by 1.524 cm of sieve holes. All the sieve holes are 0.508 cm in diameter except the

central one which has a diameter two times smaller of 0.254 cm. The combined use of surveyed thin foil targets and sieve holes provides point targets with fixed and known y_{tgt} and track with known angles ($x'_{tgt} = x'_{foil}, y'_{tgt} = y'_{foil}$) and $y_{tgt} = y_{foil}$. These coordinates are then compared to the ones reconstructed from the Taylor-series. From 4.13 we can see the coefficients Γ are specific to each reconstructed quantity. Thus the optimization procedure needs to be performed separately for each of them.

As mentioned before, the use of an extended target requires a correction to x_{tgt} given by Eq. 4.14.

$$x_{tgt} = -y_b - x'_{tgt} z_{int} \cos \theta_{spec} \quad (4.14)$$

with z_{int} , the position along the target of the interaction vertex.

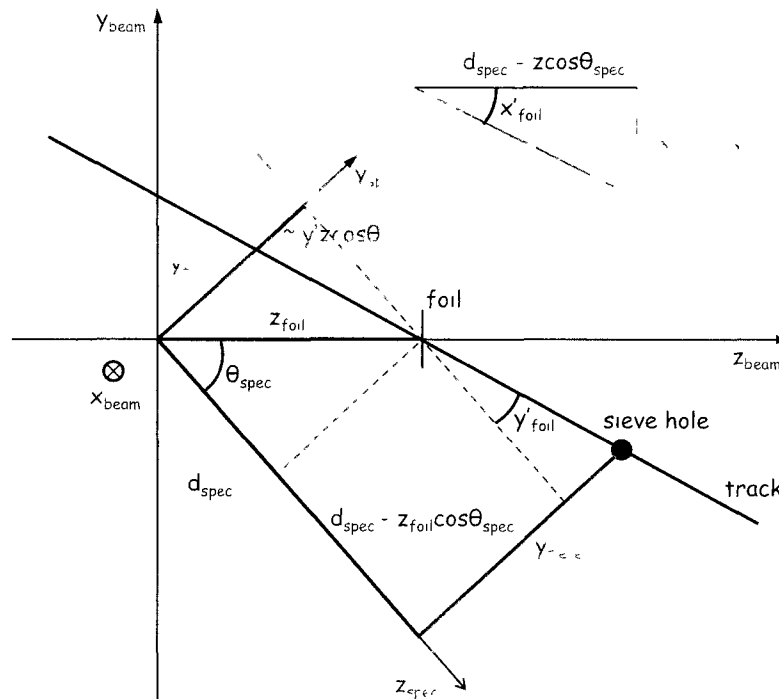


Figure 4.4: Schematic of the thin foil target and sieve slit collimator system.

From figure 4.4 it is clear that the coordinates of a track, originating from a foil target located at

z_{foil} , passing through a sieve hole located at (x_{sieve}, y_{sieve}) (in the spectrometer coordinate system) are given in the small angle approximation by:

$$\begin{aligned}
 y'_{foil} &\approx \frac{y_{sieve} - z_{foil} \sin \theta_{spec}}{d_{spec} - z_{foil} \cos \theta_{spec}} \\
 y_{foil} &= z_{foil} \left(\sin \theta_{spec} - y'_{foil} \cos \theta_{spec} \right) \\
 x'_{foil} &\approx \frac{x_{sieve} + y_{beam} \sin \theta_{spec}}{d_{spec} - z_{foil} \cos \theta_{spec}}
 \end{aligned} \tag{4.15}$$

with d_{spec} the distance from the origin to the center of the sieve slit collimator.

Data were taken at a central momentum value of 2.4 GeV/c with the HMS at a central angle of 22.0°. The results of the optimization on the angles are shown in Figures 4.5 and 4.6. Each plot displays the difference $x'_{diff}(y'_{diff})$ between the known angles $x'_{foil}(y'_{foil})$ and the reconstructed angles $x'_{rec}(y'_{rec})$ versus $x'_{foil}(y'_{foil})$:

$$\begin{aligned}
 x'_{diff} &= x'_{foil} - x'_{rec} \\
 y'_{diff} &= y'_{foil} - y'_{rec}
 \end{aligned} \tag{4.16}$$

The x'_{tgt} optimization was performed 3 times. For the first iteration, since x_{tgt} is not known, the y_{beam} value is used. This will give a rough estimate of y'_{tgt} , x'_{tgt} and y_{tgt} which will allow us to use the full correction and perform other iterations. The first, second and third iterations are shown in blue, green and red respectively. Data were collected using the 3 foil-Aluminum and 2 foil-Carbon targets. After each iteration, the calculated coefficients were used for the next iteration. Only one iteration was done for the y'_{tgt} and y_{tgt} optimization. On the $x'_{diff}(y'_{diff})$ plot, each column corresponds to a row(column) of sieve holes on the collimator and for each column, a symbol represents a sieve hole. In the ideal case, after the optimization procedure, $x'_{diff}(y'_{diff})$ would be equal to 0, resulting in all the symbols aligned on a line $x'_{diff} = 0$ on the different plots. In Figure 4.5, the slope in the x'_{diff} versus x'_{foil} plot of the outer foils of the Aluminum target shows a strong z_{tgt} dependence of x_{tgt} and thus exhibits the significance and the need for a x_{tgt} correction for extended targets. After the optimization, the slope in x'_{diff} and in y'_{diff} almost disappeared, showing the beneficial effect of the optimization.

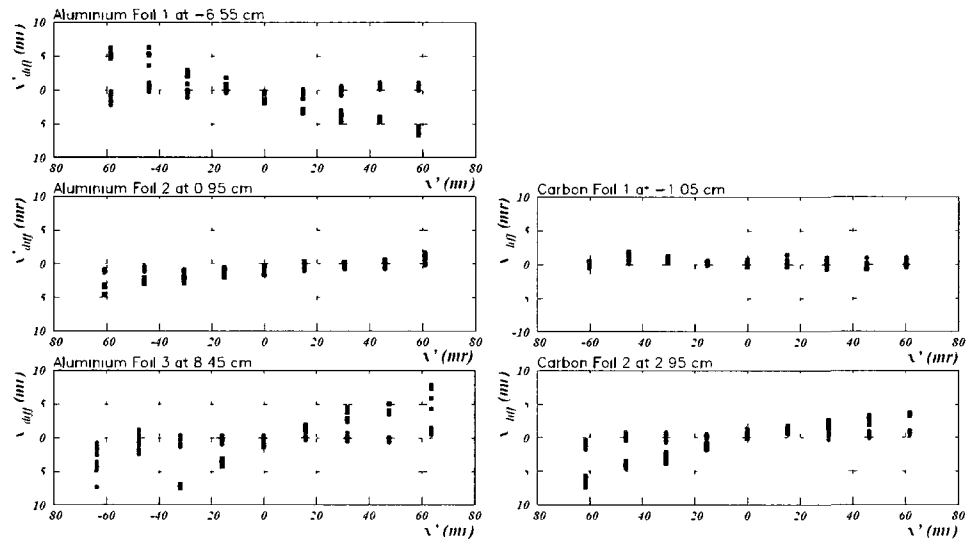


Figure 4.5: Difference x'_{diff} between the known angles x'_{foil} and the reconstructed angles x'_{rec} versus x'_{foil} for the 3 foil-Aluminum target (left) and 2 foil-Carbon target (right). In black using the original set of coefficients, in blue, green and red using the coefficients from the first, second and third iteration respectively.

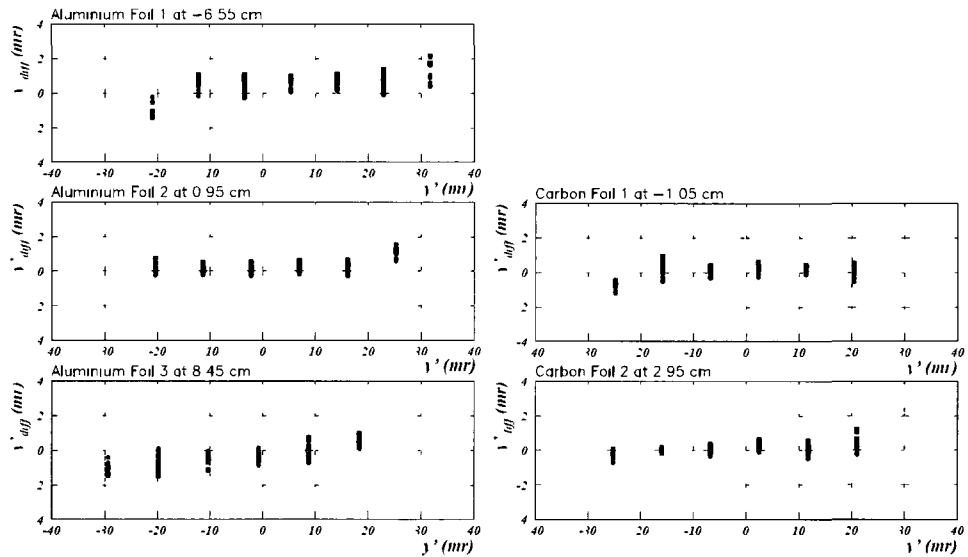


Figure 4.6: Difference y'_{diff} between the known angles y'_{foil} and the reconstructed angles y'_{rec} versus y'_{foil} for the 3 foil-Aluminum target (left) and 2 foil-Carbon target (right). In black using the original set of coefficients, in red those using the coefficients from the first iteration.

y_{tgt} was also optimized. The results for both the Aluminum and the Carbon targets are shown on the same Figure 4.7. The difference y_{diff} between the known coordinate y_{foil} and the reconstructed coordinate y_{rec} versus y_{foil} is plotted. Once again, the optimization improves the slope of the plot. It is important to say that the 3 foil-Aluminum target allows us to cover almost all the acceptance in y_{tgt}

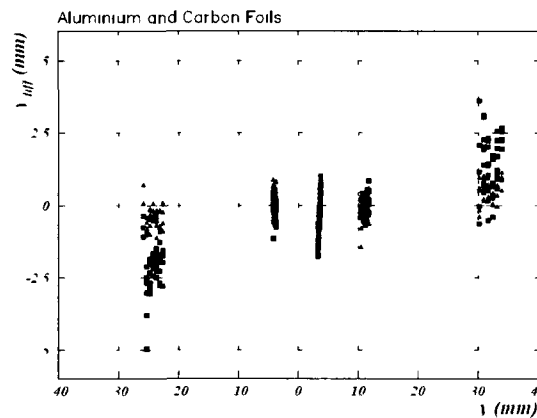


Figure 4.7: Difference y_{diff} between the known coordinate y_{foil} and the reconstructed coordinate y_{rec} versus y_{foil} for the 3 foil-Aluminum target 2 foil-Carbon target. In black, results obtained using the original set of coefficients, in red using the coefficients from the first iteration.

Dedicated runs on the 20 cm liquid hydrogen target were taken to check the momentum reconstruction. Data were taken at $E_{beam} = 4.109$ GeV and $p_0 = 2.02$ GeV/c. The calorimeter was located at $\theta_{cal} = 25.8^\circ$ and at 8.82 m from the target (position not surveyed but checked in software). Successive runs were taken in steps of 1° from $\theta_p = 36.5^\circ$ to 40.5° to cover the entire δ range of the HMS and scan over the entire effective target length y_{tgt} for each kinematics. The difference, in terms of the fraction of central momentum p_0 , between the reconstructed momentum and the proton momentum calculated from the proton angle using (4.7) versus the focal plane coordinates (x_{fp}, y_{fp}) and angles (x'_{fp}, y'_{fp}) is shown in Figure 4.8. There is no noticeable correlation between the momentum difference and the focal plane quantities which shows the very high quality of the momentum reconstruction. Based on these results no optimization was performed.

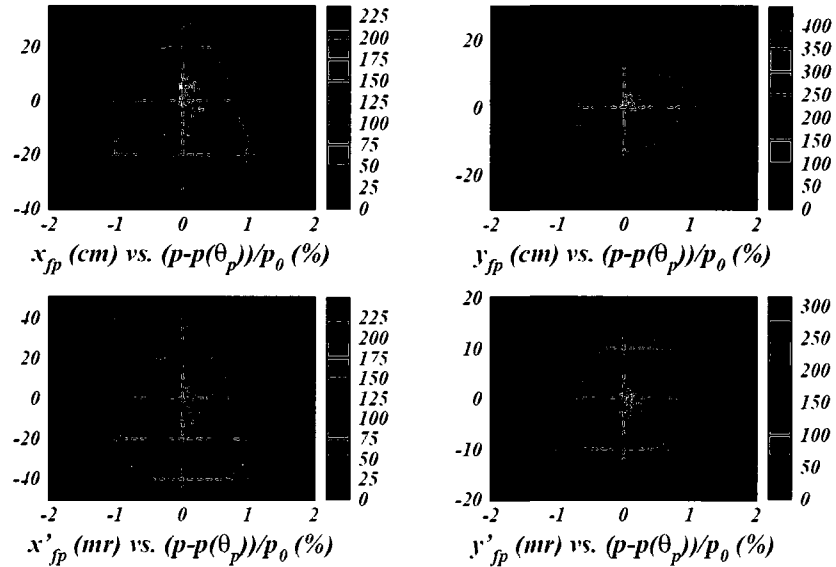


Figure 4.8: Difference in term of fraction of central momentum p_0 , between the reconstructed momentum and the proton momentum from the proton angle as a function of the focal plane coordinates x_{fp}, y_{fp} (top) and angles x'_{fp}, y'_{fp} (bottom).

4.4 FPP Tracking and Reconstruction

The FPP drift chambers are used to track protons after scattering in the CH_2 analyser blocks. The incident or reference trajectory is well known from the HMS tracking chambers. The tracks found with the FPP are then compared with the HMS track and the polar and azimuthal scattering angles, the distance of closest approach and the z-coordinate of the interaction point in the analyser are reconstructed. The fact that the HMS tracks are almost perpendicular to the chamber plane, simplifies and improves the speed of the reconstruction algorithm. This does not hold any more for the FPP since tracks with a scattering angle up to $\approx 40^\circ$ need to be reconstructed. Furthermore, FPP drift chambers are different in various aspects, mainly in the elementary cell size and number of planes, resulting in different tracking philosophies.

4.4.1 FPP tracking algorithm

The first step of the algorithm is to group hits from adjacent wires into clusters made of up to three adjacent wires per plane. Several clusters are allowed in one plane. In the case where more than three wires in one plane fired, the first three wires are selected to form the cluster. All combinations of one cluster per plane are taken into consideration. The algorithm first considers the combinations with six clusters and performs a rough fit based on the wire position. After finding all the six cluster combinations, the algorithm will consider combinations with only five clusters in case no hit had been recorded in one plane. This is the lowest acceptable limit for the number of clusters on a track. The algorithm requires at least five clusters per track and will ignore cases where only four or less planes fired. The rough tracks are then subjected to a χ^2 test defined as:

$$\chi^2 \equiv \sum_{i=1}^{N_{hit}} \left(\frac{p_{wire} - p_{track}}{\sigma_{w,i}} \right)^2 \quad (4.17)$$

with p_{wire} the position of the wire center, p_{track} the projection of the track along the wire that fired and σ_w the "wire resolution" given by the wire spacing ℓ divided by $\sqrt{12}$. In the case of clusters made of two or three hits, a first track is fitted with all the wire hits. After projecting the track on each individual plane, the residuals between the wire position and the track are computed. The wire which gives the smallest residual is selected for another fitting procedure with all the single hits per plane and the fitted track is also subjected to a χ^2 test. The χ^2 criterion is used to check if the wire-position based track is a good candidate to the drift-based tracking procedure.

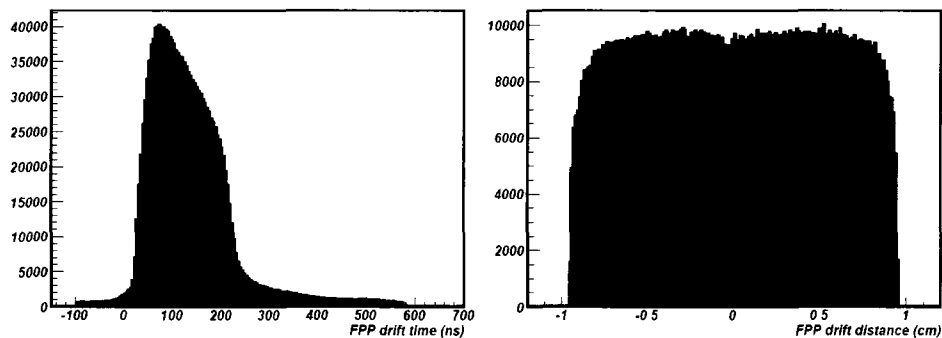


Figure 4.9: FPP drift time and FPP drift distance distribution.

Due to the high rates in the FPP and small number of detection planes, all the wire combinations that passed the χ^2 test are subjected to the drift based tracking algorithm. The drift time is corrected for the propagation in the wire and a drift map is generated. Figure 4.9 shows the drift time and distance distributions in the FPP. The 1σ resolution obtained from the FPP track residuals is about $125\mu\text{m}$.

A drift-based tracking procedure requires the determination of the correct left-right combination for each wire. For each wire combination, all of the 64 ($=2^6$) left-right combinations are tested and the one which gives the smallest χ^2 is chosen. The hits on this chosen track are marked as used. The remaining hits are then considered by the algorithm in the search of additional new tracks. These tracks need also to satisfy a χ^2 test. If a track fails to pass the test, the hit giving the worst contribution to the χ^2 is left aside and the track is refitted. This procedure is repeated until the track passes the test or the number of planes on the track passes below 5. In the analysis, we require tracks with at least five hits and exactly one hit per plane. For a 6-hit track with at least one multi-hit cluster, the hits originating from the multi-hit cluster are the first considered to be dropped in order to improve the χ^2 . For a 2-hit cluster, the algorithm forces the track to pass between the two wires and the left-right combination is then chosen accordingly. In a 3-hit cluster case, the middle hit is identified and paired with both of the outer hits. The outer hit of a combination outer-middle, that gives the worst χ^2 contribution, will be removed. The 3-hit cluster is then reduced to a 2-hit cluster and the left-right combination is chosen as explained above. For 5-hit tracks with at least one multi-hit cluster, all hits are kept as long as the track satisfies the χ^2 requirement.

The resulting tracks pass an ultimate pruning test based on the scattering angle ϑ_{FPP} , the z-coordinate z_{close} of the point and distance s_{close} of closest approach between the incident and scattered track. The method of derivation of those quantities as well as the azimuthal angle φ_{FPP} is given in the appendix. A summary of the FPP tracking algorithm is given in Figure 4.10.

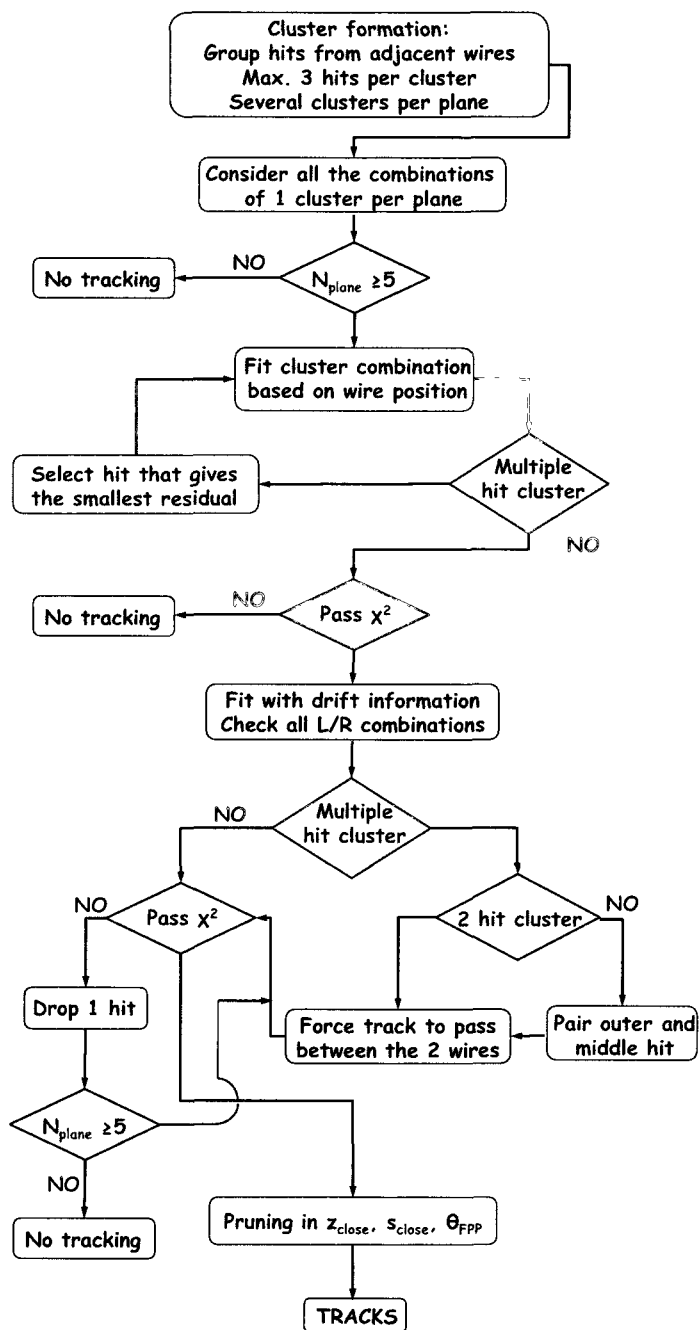


Figure 4.10: Flow chart of the FPP tracking and reconstruction algorithm.

4.4.2 Left-Right Ambiguities

The specific design of the FPP drift chambers has an intrinsic drawback that results in the code choosing the wrong left-right determination nearly half of the time in a limited region of the chamber. In the (x,y) plane, all the wires intersect at the center C of the chamber which acts as a center of symmetry. Therefore any track which intersects nearly perpendicularly to the (x,y) plane in the vicinity of C at M_1 with drift distances $(d_{x,1}, d_{u,1}, d_{v,1})$ will have a mirror image M_2 with the same valid set of drift distances $(d_{x,2}, d_{u,2}, d_{v,2})$ as shown in Figure 4.11. In this case, the code will have nearly 50% chance to assign the wrong drift sign. The three wires have also a common intersection along the central horizontal wire W_0 . Thus tracks having an intersection within a horizontal band of width equal to two wire spacings and centered along W_0 will be subject to a wrong left-right determination 50% of the time. However, the $\pm 45^\circ$ angles relative to the vertical of the u,v planes makes the wire spacing in the x direction equal to $2\sqrt{2}$ so that the irrationality of the spacing makes this pattern never repeat itself anywhere else in the chamber. Still it happens that the three wires intersect with each other nearly at the same point resulting in a potential wrong left-right determination.

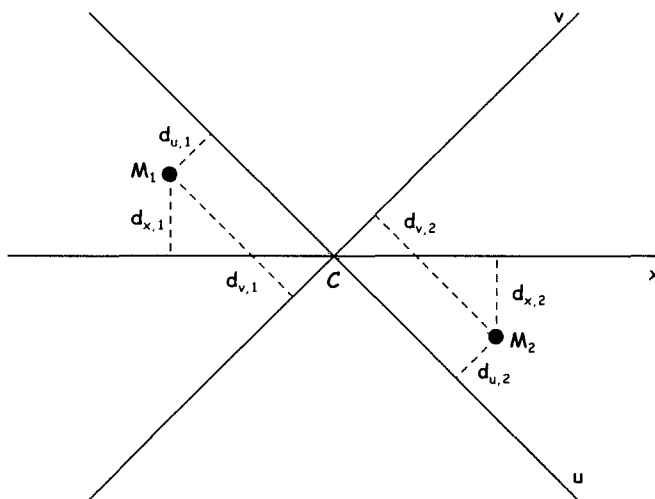


Figure 4.11: Diagram showing the left-right ambiguity in the vicinity of the chamber center.

As the track needs to be nearly perpendicular to the wire plane, this phenomenon will happen mainly at small angles. We will see in the next chapter the incidence of this effect on the track reconstruction and how it affects the analyzing power.

4.4.3 FPP Alignment

The code written by Stephen Strauch was used to optimize the alignment of the FPP. From 2.2 GeV "straight through" runs, where both of the CH₂ doors were retracted, the software minimized the difference between the track parameters (positions and slopes) of the HMS and FPP by a quadratic fit of each track's parameters. As a result, angular resolutions of 1.85 mrad in x' and 2.1 mrad in y' were achieved.

4.4.4 Track Multiplicity

The minimal design of the FPP drift chamber (only six planes of detection to define a track) and the possibility for the tracks to have nearly any angles ($0 \leq \theta \leq 90^\circ$) induce a rather high track multiplicity in the FPP. Table 4.4 presents a detailed study of the tracking statistics in both FPPs at $\epsilon = 0.152$. The columns are for the different event possibilities: *SINGLE* for one track per event, *MULTIPLE* for more than one track per event, *ZERO* when no track had been detected in the drift chambers and *ALL* regroups all the above cases. The rows are for the two FPPs and they are each subdivided into two main cases: *TOTAL* refers to the total number of events without any scattering cuts and *PASS* refers to the events passing the scattering cuts (z_{close} , θ_{FPP} , s_{close} and the cone-test)¹. The Coulomb scattering cases (abbreviated *Cb* in the table) is also shown for each FPP. The characterization of these events is presented in the next section. Finally, the row *N1=0* stand for events which did not have a track in FPP₁ but did or did not have one in FPP₂. In each box of the table, the number of events is given as well as a percentage relative to the number in the row *TOTAL* if no other indication is specified. For example, in FPP₁ there are 22,953,284 events or, in other words, 19.5% of the total number of events (117,832,388) that scattered producing only one track (*SINGLE*). This number also represents 71.2% of the events that passed all the scattering cuts (32,255,509).

¹The definitions of these variables are given in the next section.

Table 4.4: Detail of the track multiplicity of the FPP at $Q^2 = 2.5 \text{ GeV}^2$ and $e = 0.152$.

		ALL	SINGLE	MULTIPLE	ZERO	
FPP1	TOTAL	117832388	65600900 55.7%	22918653 19.5%	29312835 24.8%	
	PASS (zclose, sclose, theta, conetest)	32255509 27.4% 69.7% of Cb+Nuclear	22953284 19.5% 71.2% of CUT 65.3% of Cb+Nuclear	9302225 7.9% 28.8% of CUT 83.7% of Cb+Nuclear	0	
	Cb	TOTAL	22348846 19% of ALL	19487427	2861419	0
		PASS (zc, sc, cone)	14013775 11.9% of ALL 30.3% of Cb+Nuclear	12203940 34.7% of Cb+Nuclear	1809835 16.3% of Cb+Nuclear	0
FPP2	TOTAL	117832388	50919709 43.2%	14724112 12.5%	52188567 44.3%	
	PASS (zclose, sclose, theta, conetest)	14186281 12% 84.1% of Cb+Nuclear	10286625 8.7% 72.5% of CUT 81.3% of Cb+Nuclear	3899656 3.3% 27.4% of CUT 92.4% of Cb+Nuclear	0	
	Cb	TOTAL	10618014 9% of ALL	9345095	1272919	0
		PASS (zc, sc, cone)	2680364 2.2% of ALL 15.9% of Cb+Nuclear	2359862 18.7% of Cb+Nuclear	320502 7.6% of Cb+Nuclear	0
	N1=0	TOTAL	29312835 24.8% of ALL	9826505 8.3% of ALL 33.5% of N1=0	2747706 2.3% of ALL 9.4% of N1=0	16738624 12.8% of ALL 57.1% of N1=0
		PASS (zc, sc, th, cone)	2559072 2.2% of ALL 8.7% of N1=0	1868327 1.6% of ALL 6.4% of N1=0	690745 0.6% of ALL 2.4% of N1=0	0

The interesting cases are highlighted in the table. The orange boxes show the consistency of the single track event fraction in both FPPs which is around 72%. The red boxes give the complementary fraction (multiple track events). Coulombs events (blue boxes) represent 30.3% (15.9%) of the events that scattered in FPP₁ (FPP₂). An interesting number is the percentage of zeros (events with no track.). There are 24.8% of zeros in FPP₁ and 12.8% in FPP₂. This difference is explained by the fact that the particle will have to pass through almost twice as much material than in FPP₁ and thus is most likely to scatter in FPP₂. However we see that 57% of the zeros in FPP₁ do not give a track in FPP₂ which represent almost 13% of the total number of events. This number gives us information about the inefficiency of the chamber but also about the number of neutral produced in the CH₂ analyser blocks. Finally the overall efficiency of the polarimeter is given by the percentage of events that passed the scattering cuts in FPP₁ and FPP₂: $19.5\% + 8.7\% = 28.2\%$

Figure 4.12 show the fraction of single (darker colors) and multiple (lighter colors) track events as a function of the run number for the three kinematics and for both FPPs . This shows a good stability of this fraction over time and over the kinematics. The fit results are given in table 4.5. For $\epsilon = 0.152$ the results given in both tables are very similar but not strictly identical because of the fit procedure which induces some uncertainties.

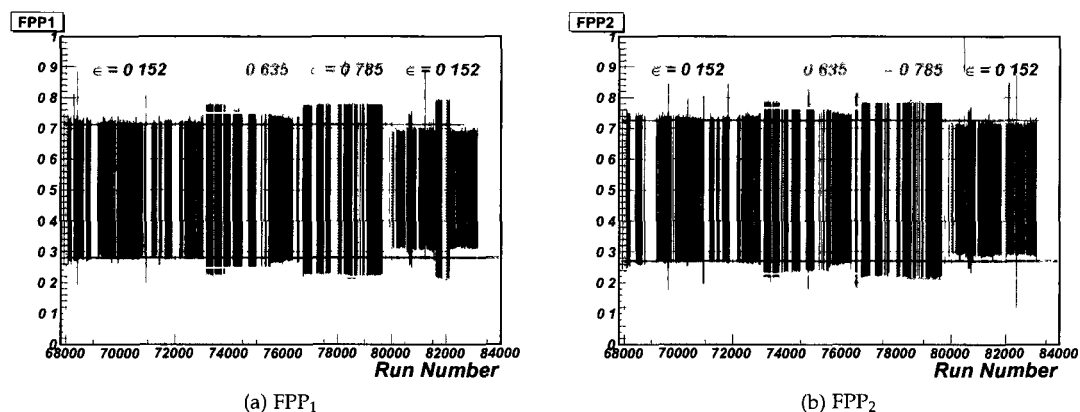


Figure 4.12: Fraction of the single (darker colors) and multiple (lighter colors) track events as a function of the run number for the three kinematics for FPP₁ (left) and FPP₂ (right).

	SINGLE		MULTI	
	FPP ₁	FPP ₂	FPP ₁	FPP ₂
$\epsilon = 0.152$	71.25% \pm 2.88	72.64% \pm 2.95	28.09 \pm 1.81	27.06% \pm 1.81
$\epsilon = 0.635$	75.00% \pm 4.43	76.78% \pm 4.46	24.84 \pm 2.55	22.91% \pm 2.43
$\epsilon = 0.785$	77.94% \pm 4.32	78.57% \pm 4.35	21.39 \pm 2.26	21.40% \pm 2.27

Table 4.5: Fit results of the fraction of single and multiple track events for both FPPs and for the three kinematics.

4.4.5 Scattering Quantities

The polar scattering angle ϑ_{FPP} , the azimuthal scattering angle ϕ_{FPP} , the distance of closest approach s_{close} , the z-coordinate of the point of closest approach z_{close} and the cone-test are calculated as in the appendix C. The effect of the latter is seen in the ϑ_{FPP} versus z_{close} distribution (figure 4.13).

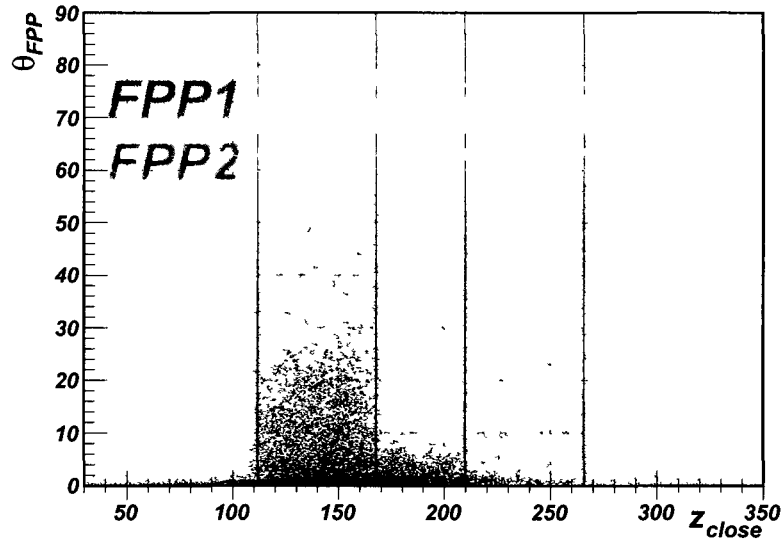


Figure 4.13: z_{close} versus ϑ_{FPP} distribution for both FPPs.

The red lines represent the physical width of the two analyser blocks. The "razor blade" shape of the distribution inside the CH₂ blocks is a sign of the tracks passing the cone test. The cone-test eliminates upstream tracks with large ϑ_{FPP} . The two sets of vertical lines represents the physical

width of the two CH_2 analyzer blocks. The vertical stripes outside the analyzer are due to bad reconstructed events which appear to have scattered in the drift chamber. A discussion about these events is done in section 6.2. The ϑ_{FPP} distribution of single track events and passing the cone-test is shown on figure 4.14. The peak at small angle is due to Coulomb scattering characterized by very low analysing power.

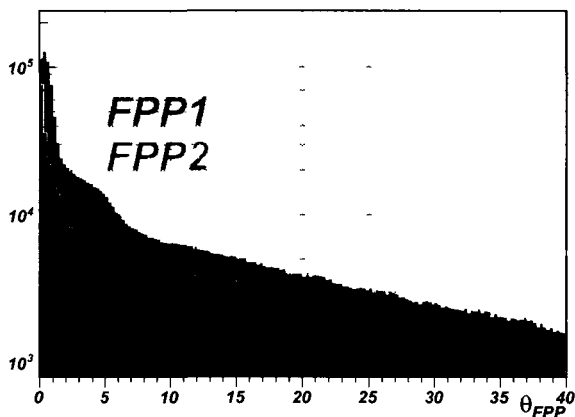


Figure 4.14: Scattering angle ϑ_{FPP} distributions for both FPPs.

The distance of closest approach distribution is displayed in Figure 4.15.

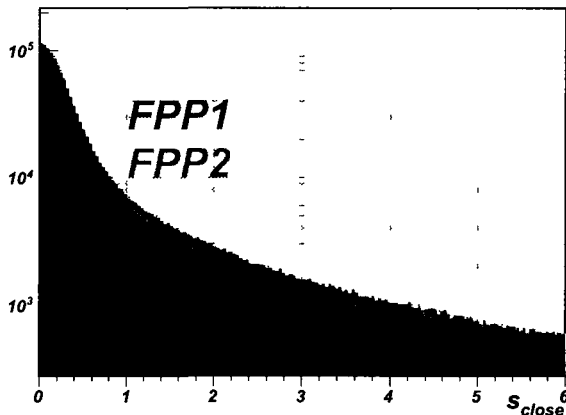


Figure 4.15: Distance of closest approach s_{close} distributions for both FPPs.

The width of these distributions is due to multiple scattering which tends to blow up the s_{close}

reconstruction. The s_{close} distribution is wider for FPP₂ since a proton has to go through almost twice as much material as in FPP₁. From these two figures 4.14 and 4.15, we notice that half as many events scatter in FPP₂ as in FPP₁.

FPP scattering cuts

This is an appropriate place to give the different FPP scattering cuts applied in the analysis. First we need to find the limit on the Coulomb scattering. The width θ_0 of the multiple scattering through small angle distribution is given by [58]:

$$\theta_0 = \frac{13.6 \text{ MeV}}{\beta c p} z \sqrt{\frac{x}{X_0}} \left[1 + 0.0038 \ln \left(\frac{x}{X_0} \right) \right] \quad (4.18)$$

where p , βc , and z are the momentum, the velocity and the charge number of the incident particle. x/X_0 is the thickness of the scattered medium expressed in radiation lengths. Therefore for a proton $z = 1$, with $p = 2.0676 \text{ GeV}/c$, $\beta c \approx 0.71$ and for an analyzer thickness of 54 (108) cm for FPP₁ (FPP₂) with $X_0^{CH_2} = 47.9 \text{ cm}$ the width of the distribution is $\theta_0^{FPP_1(FPP_2)} \approx 0.57(0.83)^\circ$. In the analysis we used a conservative 3σ cut:

$$\theta_{FPP_1} > 1.7^\circ \quad (4.19)$$

$$\theta_{FPP_2} > 2.5^\circ \quad (4.20)$$

A cut on the z -coordinate of the scattering vertex was applied. Events scattering outside the physical width of the analyzer $\pm 1\text{cm}$ were rejected leading to the cuts:

$$111.9 \text{ cm} \leq z_{close}^{FPP_1} \leq 167.9 \text{ cm} \quad (4.21)$$

$$209.8 \text{ cm} \leq z_{close}^{FPP_2} \leq 265.8 \text{ cm} \quad (4.22)$$

A loose cut on the distance of closest approach was applied:

$$s_{close}^{FPP_1} \leq 3 \text{ cm} \quad (4.23)$$

$$s_{close}^{FPP_2} \leq 6 \text{ cm} \quad (4.24)$$

The cut in FFP₂ is looser to account for the smearing of the s_{close} distribution.

The event failing the cone-test were rejected and we also selected single track events only:

$$N_{track}^{FFP_1} = 1 \quad (4.25)$$

$$N_{track}^{FFP_2} = 1 \quad (4.26)$$

We also always choose the HMS track as a reference track for FFP₂. This conservative analysis of the FFP₂ events in addition with the strict z_{close} cut eliminates the possible double counting in the case of a scattering in FFP₁ and in FFP₂.

4.4.6 BigCal Reconstruction

Up to this point, we only dwelled on the "proton side" of the experiment. On the "electron side", the BigCal calorimeter is used to reconstruct the electron angles and energy. The electron energy is determined by summing the hit energies of an array (cluster) of dimension up to 5×5 contiguous hits:

$$E_k = \sum_{k \in 5 \times 5} c_k A_k \quad (4.27)$$

where the c_k are the calibration constants and the A_k are the pedestal-subtracted ADC values. Each of the calibration constants are obtained by minimizing the difference between the reconstructed and known energies. In other words, minimizing the following χ^2 results in solving 1744 linear equations for the 1744 calibration constants:

$$\chi^2 = \sum_{i=1}^N \left(E_i^{known} - \sum_{k \in 5 \times 5} c_{k,i} A_{k,i} \right)^2 \quad (4.28)$$

Several calibration procedures were performed during the experiment in order to update the set of calibration constants and PMTs high voltages. An energy resolution σ_E/E of 10.5% was achieved at the beginning of the experiment. The resolution is altered over time due mainly to radiation damage. At the end of the GEpIII experiment, despite a UV curing, the energy resolution was found to be σ_E/E of 15.4%.

Since the angular resolution of the HMS is altered by the S0 detector, the scattered electron angle θ_e is calculated from the proton momentum p_p using:

$$\cos \theta_e = 1 - \frac{MT_p}{E_e (E_e - T_p)} \quad (4.29)$$

with $T_p = \sqrt{p_p^2 + M^2} - M$ the proton kinetic energy. The azimuthal electron angle ϕ_e is calculated by requiring co-planarity of the elastic scattering, thus:

$$\phi_e = \phi_p + \pi \quad (4.30)$$

Finally, the knowledge of these angles and the beam position allows one to calculate the expected electron coordinates (x_e, y_e) at the face of BigCal from two-body kinematics:

$$x_e = x_{beam} + s \sin \theta_e \sin \phi_e - z_{beam} + s \cos \theta_e \quad (4.31)$$

$$y_e = y_{beam} - s \sin \theta_e \cos \phi_e \quad (4.32)$$

with:

$$s = \frac{d_{cal} - x_{beam} \sin \theta_{cal} - z_{beam} \cos \theta_{cal}}{\sin \theta_e \sin \phi_e \sin \theta_{cal} + \cos \theta_e \cos \theta_{cal}} \quad (4.33)$$

d_{cal} is the distance from the target to the center of the face of BigCal. In the BigCal coordinate system, x and y are pointing in the direction of increasing θ_e and vertically upward respectively. A resolution of 0.55cm in the horizontal coordinate was obtained. Unlike the horizontal resolution which is dominated by the proton momentum, the vertical resolution is determined by x'_{tgt} altered by multiple scatterings in the S0 detector. As a result, the vertical resolution is 3 to 5 times larger than the horizontal one. A complete and very detailed study of the electron angles and energy reconstruction is done in [59].

4.5 Elastic Events Selection

The reconstruction of the electron and proton quantities being done, the last task of the first part of the analysis is the selection of the elastic event. There are different methods to isolate elastic events from inelastic background. We can study the proton momentum and proton angle correlation by looking at the relative momentum of the spectrometer p with respect to the momentum calculated from the proton angle p_{θ_p} (see in the equation 4.7). This difference p_{miss}^p is expressed as a percentage of the central momentum p_0 : $p_{miss}^p = 100 \times (p - p_{\theta_p}) / p_0$. Figure 4.16 shows the p_{miss}^p distributions for the three ϵ points. The elastic events peak around $p_{miss}^p = 0$.

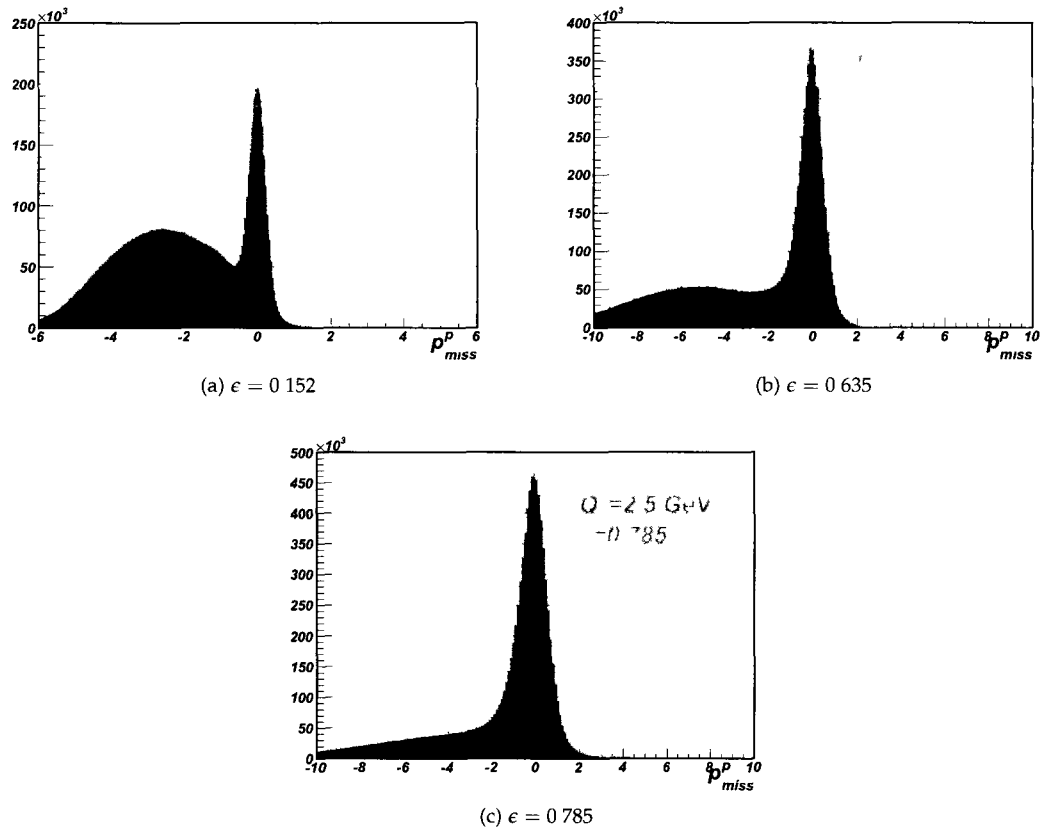


Figure 4.16: p_{miss}^p distributions for $Q^2 = 2.5 \text{ GeV}^2$ at $\epsilon = 0.152$ (a), 0.635 (b), and 0.785 (c) without any cuts, in percentage of the central momentum value.

However the angular resolution of the HMS is insufficient to properly select the elastic events. So

additional cuts on the electron side are needed. We could define a similar criterion of inelasticity p_{miss}^e by replacing p_{θ_p} by the proton momentum calculated from the electron angle p_{θ_e} and use in addition a coplanarity criterion $\Delta_\phi = \phi_e - \phi_p - \pi$. However in the final analysis we used an equivalent method by applying elliptical cuts on the horizontal (Δx) and vertical (Δy) differences between the measured shower coordinates and the coordinates predicted from the beam energy and the reconstructed proton momentum, angles and vertex coordinates assuming two-body kinematics. Cuts of the following form were used:

$$\left(\frac{\Delta x}{x_{max}}\right)^2 + \left(\frac{\Delta y}{y_{max}}\right)^2 \leq 1 \quad (4.34)$$

Figure 4.17 displays the Δ_x vs Δ_y distribution for the $\epsilon = 0.152$ kinematic.

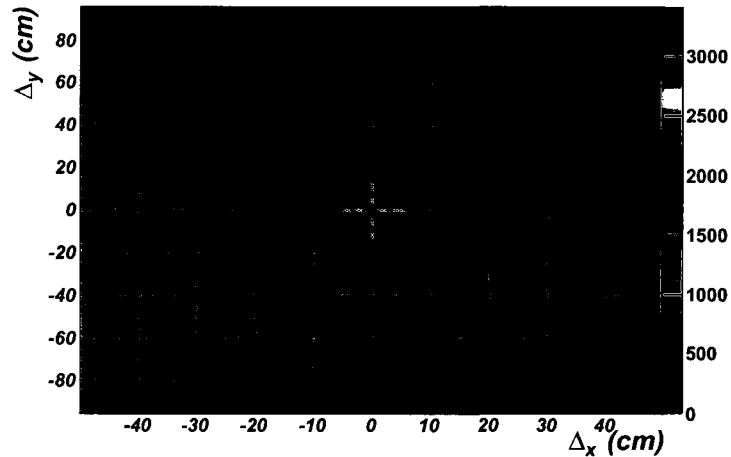


Figure 4.17: Δ_y versus Δ_x at $Q^2 = 2.5 \text{ GeV}^2$ and $\epsilon = 0.152$.

We can clearly see the elastic peak centered at $(\Delta_x, \Delta_y) = (0,0)$. The results of the elliptical cuts on the p_{miss}^p spectra are given in Figure 4.18. The inelastic background is efficiently suppressed. The different width of the spectra come from the different momentum spread of the three kinematics.

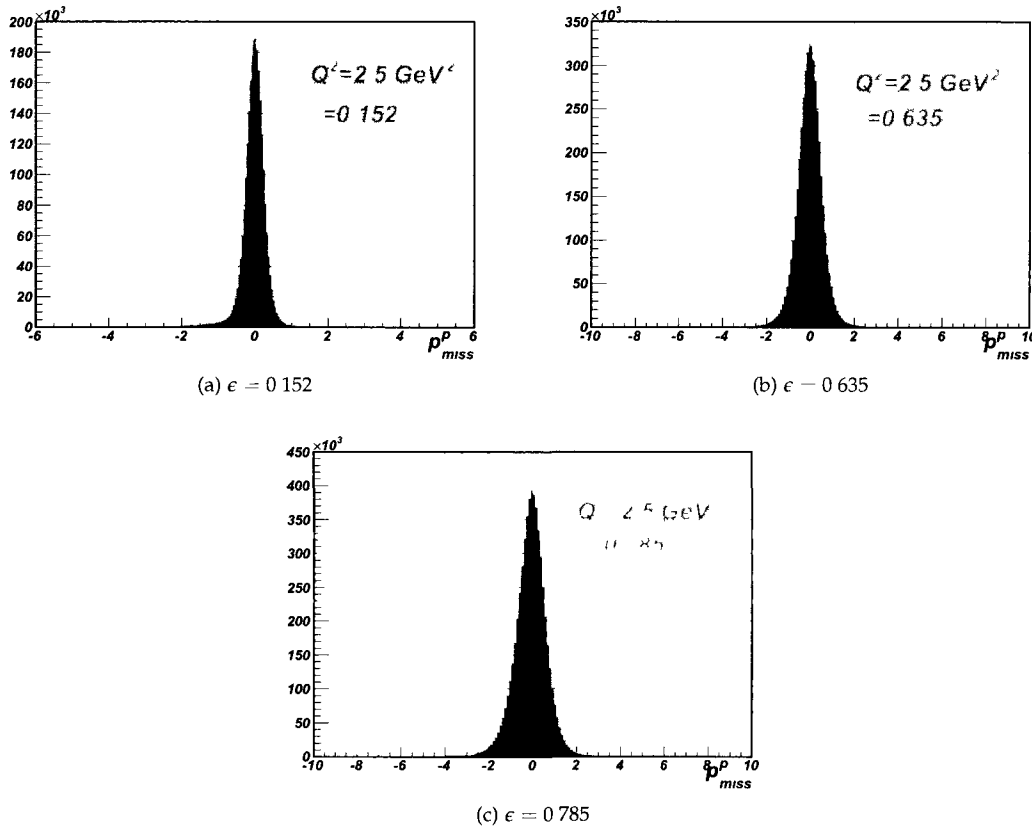


Figure 4.18: p_{miss}^p distributions for $Q^2 = 2.5 \text{ GeV}^2$ at $\epsilon = 0.152$ (a), 0.635 (b), and 0.785 (c) after the elliptical cut, as a percentage of the central momentum value.

4.5.1 Source of Inelastic Background

It is now appropriate to describe the different source of inelastic background. Super-elastic events, characterized by a higher momentum than the momentum (on the right of the elastic peak) expected from elastic $\bar{e}p$ scattering, have their origin in the target end-caps. They are far from being the main background contribution. On the left of the elastic peak in Figure 4.16a, b) and c), are the events having, this time, a momentum lower than the momentum expected by elastic scattering. They are due to π^0 electro-photoproduction and real Compton scattering. Both processes are initiated by hard Bremsstrahlung in the target. The latter reaction $\gamma + p \rightarrow \gamma + p$, does not give a significant contribution to the inelastic background because of its smaller cross

section compared to the one of π^0 photoproduction.

In the former, the interaction of the Bremsstrahlung photon with the proton produces a π^0 and a proton:



For this reaction to happen and the event to be in the experimental acceptance, the photon energy needs to be nearly equal to the electron beam energy. The produced π^0 decays immediately into two photons and each carry exactly half of the π^0 mass in the π^0 center of mass frame. In the lab frame, these two photons are emitted in a forward cone along the π^0 trajectory. One or both photons could then hit the calorimeter and if their energy is greater than the BigCal threshold they will be detected and produce very similar signals to the one from the $\vec{e}p$ elastic electron. The BigCal energy resolution being poor, it is crucial to eliminate the inelastic background by position correlation. A residual background fraction, computed with the SIMC Monte-Carlo simulation, of 0.7% under the elastic peak was found for the smallest ϵ point. The other two kinematics have even smaller contamination: 0.4% and 0.3% for $\epsilon = 0.635$ and $\epsilon = 0.785$, respectively.

Chapter 5

Data Analysis Part Two: Focal Plane Asymmetries, Spin Precession and Polarization Observables Extraction

The last step in the analysis toward the extraction of the polarization component ratio is the extraction of the physical azimuthal asymmetries. In the FPP, we measure these asymmetries at the focal plane after the proton underwent a spin precession through the HMS magnets. A precise understanding of the spin precession calculation, performed using a spin matrix determined by the software COSY, is needed to reconstruct the polarization observables at the target with a maximum likelihood method.

5.1 Angular Distributions and Asymmetries

The general angular distribution in the polarimeter based on Equation 3.9 is given by:

$$\begin{aligned}
N^\pm(p, \vartheta_{FPP}, \varphi) &= N_0^\pm \frac{\varepsilon(p, \vartheta_{FPP})}{2\pi} \left[1 + (c_1 \pm A_y P_y^{FPP}) \cos \varphi + \right. \\
&\quad \left. (s_1 \mp A_y P_x^{FPP}) \sin \varphi + \right. \\
&\quad \left. c_2 \cos(2\varphi) + s_2 \sin(2\varphi) + \dots \right]
\end{aligned} \tag{5.1}$$

where N_0^\pm is the number of protons corresponding to beam helicity ± 1 , A_y is the analyzing power of $\vec{p} + CH_2 \rightarrow$ one charged particle + X scattering, P_x^{FPP} and P_y^{FPP} are the transverse polarization components at the focal plane, $\varepsilon(p, \vartheta_{FPP})$ is the fraction of protons of momentum p scattered at an angle ϑ and producing one track. The terms c_1, s_1, \dots have been added in comparison with Equation 3.9. They are the Fourier coefficients of the false (or instrumental) asymmetry. These asymmetries arise from the acceptance (the geometry of the polarimeter) which in theory is independent of φ . We see that by taking the difference of the angular distribution of the two helicity states, we have access to the physical asymmetries, whereas by taking the sum, we obtain the false asymmetries. This separation is only possible because the false (physical) asymmetries are helicity independent (dependent). The difference and the sum of the angular distribution integrated over all momenta p and over a limited ϑ_{FPP} range, $1.7^\circ \leq \vartheta \leq 38^\circ$, to exclude both Coulomb and large angle scatterings for which $A_y \approx 0$, are given by:

$$\begin{aligned}
f^+ - f^- &= \frac{\pi}{\Delta\varphi} \left[\frac{N^+(\varphi)}{N_0^+} - \frac{N^-(\varphi)}{N_0^-} \right] \\
&= \frac{A_y}{\Delta\varphi} \left[P_y^{FPP} \cos \varphi - P_x^{FPP} \sin \varphi \right]
\end{aligned} \tag{5.2}$$

$$\begin{aligned}
f^+ + f^- &= \frac{\pi}{\Delta\varphi} \left[\frac{N^+(\varphi)}{N_0^+} + \frac{N^-(\varphi)}{N_0^-} \right] \\
&= \frac{1}{2\Delta\varphi} [1 + c_1 \cos \varphi + s_1 \sin \varphi + c_2 \cos 2\varphi + s_2 \sin 2\varphi + \dots]
\end{aligned} \tag{5.3}$$

with $\Delta\varphi$ the bin width. Figure 5.1 shows the measured helicity-dependent asymmetries for the three ε points.

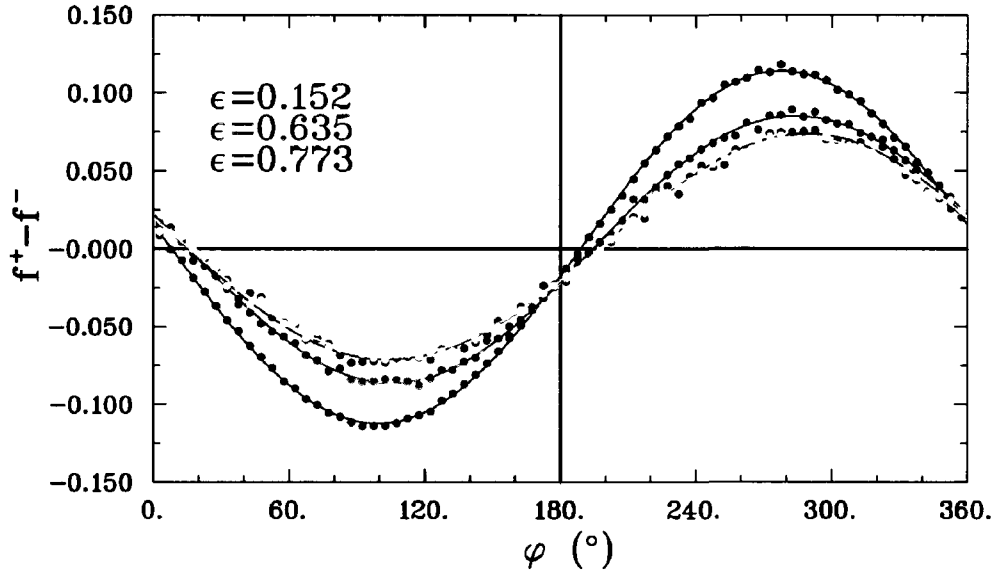


Figure 5.1: Helicity difference distribution in the focal plane $f^+ - f^-$ for $\epsilon = 0.152, 0.635, 0.773$ and 0.791 and for $1.7^\circ \leq \theta \leq 38^\circ$.

The distribution is fitted by a sum of sine and cosine in φ up to the third harmonic:

$$f^+ - f^- = C_0 + \sum_{i=1}^3 c_i \cos(i\varphi) + s_i \sin(i\varphi) \quad (5.4)$$

The results of the fits are given in Table 5.1.

ϵ	C_0	c_1	s_1
0.152	$-0.4084\text{E-}03 \pm 0.247\text{E-}03$	$0.1650\text{E-}01 \pm 0.242\text{E-}03$	$-0.1110\text{E-}00 \pm 0.245\text{E-}03$
0.635	$0.6255\text{E-}03 \pm 0.319\text{E-}03$	$0.6379\text{E-}02 \pm 0.319\text{E-}03$	$-0.2066\text{E-}01 \pm 0.321\text{E-}03$
0.773	$-0.1501\text{E-}02 \pm 0.547\text{E-}03$	$0.2043\text{E-}01 \pm 0.545\text{E-}03$	$-0.6951\text{E-}01 \pm 0.550\text{E-}03$
0.791	$0.1725\text{E-}03 \pm 0.393\text{E-}03$	$0.2015\text{E-}01 \pm 0.391\text{E-}03$	$-0.6697\text{E-}01 \pm 0.394\text{E-}03$
ϵ	c_2	s_2	
0.152	$-0.5044\text{E-}03 \pm 0.245\text{E-}03$	$0.2735\text{E-}03 \pm 0.244\text{E-}03$	
0.635	$-0.1559\text{E-}03 \pm 0.319\text{E-}03$	$-0.1546\text{E-}04 \pm 0.320\text{E-}03$	
0.773	$-0.2161\text{E-}03 \pm 0.547\text{E-}03$	$-0.1060\text{E-}02 \pm 0.549\text{E-}03$	
0.791	$-0.3347\text{E-}03 \pm 0.392\text{E-}03$	$-0.5744\text{E-}03 \pm 0.393\text{E-}03$	

ϵ	c_3	s_3
0.152	$-0.2205\text{E-}03 \pm 0.243\text{E-}03$	$0.7449\text{E-}03 \pm 0.244\text{E-}03$
0.635	$-0.1586\text{E-}03 \pm 0.354\text{E-}03$	$-0.9005\text{E-}04 \pm 0.354\text{E-}03$
0.773	$-0.1487\text{E-}02 \pm 0.548\text{E-}03$	$0.2177\text{E-}03 \pm 0.548\text{E-}03$
0.791	$0.1878\text{E-}03 \pm 0.393\text{E-}03$	$0.3732\text{E-}03 \pm 0.393\text{E-}03$

Table 5.1: Fit results of helicity difference distribution in the focal plane.

We can see that the helicity difference is really defined by the first harmonic in φ as expected. Looking closer at the coefficients, we notice that the shape of the distributions is a sine 1φ which gives an idea of the relative size of the polarization components. The fit coefficients of the second harmonic are an order of magnitude smaller. At this point, the polarization observables at the focal plane can be extracted by a Fourier analysis. However, we need to take into consideration the spin precession information in the HMS to determine them at the target.

The measured helicity-independent asymmetry is displayed on Figure 5.2. The distributions have been fitted by a Fourier series up to the eighth harmonic in order to account for the fine structure of the spectra:

$$f^+ + f^- = C_0 + \sum_{i=1}^8 c_i \cos(i\varphi) + s_i \sin(i\varphi) \quad (5.5)$$

The fit gives good quantitative results for all four kinematics and exhibits a strong cosine 2φ component. The fit coefficients corresponding to other components are about an order of magnitude smaller. Obviously this is not a perfect fit and we could have increased the number of harmonics, but the goal of this study was to characterize the shape of the instrumental asymmetries and check that they are independent of kinematics, as expected. The two parts of the smallest ϵ kinematic were analyzed separately and gave very similar results. Only the average results of these two parts is plotted.

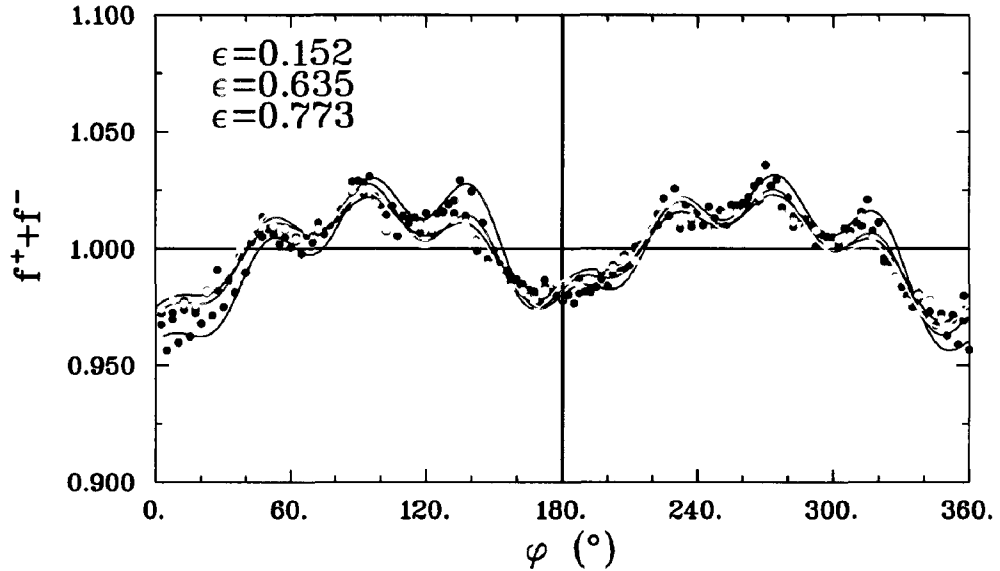


Figure 5.2: Helicity sum distribution in the focal plane $f^+ + f^-$ for $\epsilon = 0.152, 0.635, 0.773$ and 0.791 and for $1.7^\circ \leq \theta \leq 38^\circ$.

5.2 Spin Precession

On its way to the FPP, the proton spin precesses through the HMS superconducting magnets. Before studying the full calculation, we will present two simplified models of the HMS magnetic components: the dipole and geometric approximation.

5.2.1 Dipole Model

In this model, the HMS dipole is supposed to be an ideal dipole, with a uniform field and sharp edges. In this approximation, we also neglect any effects coming from the HMS quadrupole. In this situation, the proton spin precesses around the transverse dipole field by an angle χ_θ defined by:

$$\chi_\theta = \gamma \kappa_p \vartheta_{bend} \quad (5.6)$$

with γ the relativistic proton boost, $\kappa_p = \mu_p - 1 \approx 1.79$ the proton's anomalous magnetic moment and ϑ_{bend} the deflection angle of the trajectory given by:

$$\vartheta_{bend} = \theta_{HMS} + \theta_{igt} - \vartheta_{fp} \quad (5.7)$$

with θ_{HMS} the spectrometer angle and θ_{igt} (ϑ_{fp}) the reconstructed (measured) vertical angle. These angles are related to the vertical slopes at the target and at the focal plane respectively by: $\theta_{igt} = \arctan x'_{igt}$ and $\vartheta_{fp} = \arctan x'_{fp}$. The value of the central precession angle is given in Table 5.2.

Q^2, GeV^2	$p_0, \text{GeV}/c$	$\chi_\theta, ^\circ$
2.5	2.0676	108.5

Table 5.2: Central precession angle χ_θ for the HMS at $Q^2 = 2.5 \text{ GeV}^2$.

In this model, we neglect any precession in the non-dispersive plane. Since the transverse polarization component is along the direction of the dipole field, it will not precess. Therefore the polarization components at the target and at the focal plane are related by:

$$\begin{pmatrix} P_t^{FPP} \equiv P_y^{FPP} \\ P_n^{FPP} \equiv -P_x^{FPP} \\ P_\ell^{FPP} \equiv P_z^{FPP} \end{pmatrix} = \begin{pmatrix} 1 & 0 & 0 \\ 0 & \cos \chi_\theta & \sin \chi_\theta \\ 0 & -\sin \chi_\theta & \cos \chi_\theta \end{pmatrix} \begin{pmatrix} P_t \\ P_n \\ P_\ell \end{pmatrix}$$

In the first vector of this expression we have specified that the the transverse component at the focal plane P_t^{FPP} is measured along the +x axis (corresponding to the +y axis of the transport coordinate system) and the normal component at the focal plane P_n^{FPP} is measured along the +y axis (corresponding to the -x axis of the transport coordinate system). In the Born approximation, the normal component is equal to 0.

5.2.2 Geometric Model

In this model, the precession in the non-dispersive plane is accounted for. Furthermore, precession in the dispersive and non-dispersive plane give rise to independent deflections in both

planes in which the dipole approximation is applied inducing dispersive χ_θ and non-dispersive χ_ϕ precession angles given by:

$$\chi_\theta = \gamma\kappa_p(\theta_{HMS} + \theta_{tgt} - \theta_{fp}) \quad (5.8)$$

$$\chi_\phi = \gamma\kappa_p(\phi_{fp} - \phi_{tgt}) \quad (5.9)$$

With ϕ_{fp} and ϕ_{tgt} defined by the arctan of the horizontal slopes at the focal plane and at the target respectively. We can now rewrite the relation between the polarization components at the target and at the focal plane:

$$\begin{pmatrix} P_t^{FPP} \equiv P_y^{FPP} \\ P_n^{FPP} \equiv -P_x^{FPP} \\ P_\ell^{FPP} \equiv P_z^{FPP} \end{pmatrix} = \begin{pmatrix} \cos \chi_\phi & 0 & \sin \chi_\phi \\ -\sin \chi_\phi \sin \chi_\theta & \cos \chi_\theta & \cos \chi_\phi \sin \chi_\theta \\ -\sin \chi_\phi \cos \chi_\theta & -\sin \chi_\theta & \cos \chi_\phi \cos \chi_\theta \end{pmatrix} \begin{pmatrix} P_t \\ P_n \\ P_\ell \end{pmatrix} \quad (5.10)$$

The helicity difference distribution in Equation 5.2 in the Born approximation ($P_n = 0$) becomes:

$$f^+ - f^- = \frac{A_y}{\Delta\varphi} [(P_t \cos \chi_\phi + P_\ell \sin \chi_\theta) \cos \varphi + (P_\ell \cos \chi_\phi \sin \chi_\theta - P_t \sin \chi_\phi \sin \chi_\theta) \sin \varphi] \quad (5.11)$$

We see that each individual component we measure at the focal plane is a mix of the transverse and longitudinal polarization components at the target. This mix is induced by the spin precession in the non-dispersive plane corresponding to a horizontal rotation by an angle χ_ϕ and in the dispersive plane corresponding to a vertical rotation by an angle χ_θ .

5.2.3 COSY Model

The full spin precession calculation is performed by the differential based code COSY [57] which integrates the Thomas-Bargmann-Michel-Telegdi (Thomas-B.M.T.) equation along the full magnetic length of the HMS. For a given central momentum value, a map of coefficients is produced in the output of the program. Since each individual proton has different target coordinates, each proton will have its own trajectory through the HMS magnet. Thus, each of them will experience a different magnetic field integral. The spin precession matrix needs to be calculated on an event-

by-event basis. For this purpose, a polynomial expansion of the spin transport matrix in power of the reconstructed target quantities $(x_{tgt}, y_{tgt}, x'_{tgt}, y'_{tgt})$ and δ up to the fifth order is performed:

$$P_{ij}(x_{tgt}, y_{tgt}, x'_{tgt}, y'_{tgt}, \delta) = \sum_{k,l,m,n,p=0}^{k+l+m+n+p \leq 5} C_{ij}^{klmnp} (x_{tgt})^k (y_{tgt})^l (x'_{tgt})^m (y'_{tgt})^n (\delta)^p \quad (5.12)$$

where the C_{ij} are the COSY expansion coefficients. The spin matrix coefficients are calculated in the fixed transport coordinate system. The components at the target are expressed in the scattering plane and in the co-moving coordinate system of the proton at the focal plane. Therefore two additional small rotations, a first one F from the scattering plane to the transport system and a second Q from the transport system to the focal plane frame, need to be included in the total spin rotation matrix $S = QPF$.

We define the scattering plane as:

$$\begin{aligned} \hat{n} &\equiv \frac{\vec{k}_i \times \vec{k}_f}{|\vec{k}_i \times \vec{k}_f|} \\ \hat{\ell} &\equiv \frac{\vec{k}_i - \vec{k}_f}{|\vec{k}_i - \vec{k}_f|} \\ \hat{t} &\equiv \hat{n} \times \hat{\ell} \end{aligned} \quad (5.13)$$

where \vec{k}_i and \vec{k}_f are the momenta of the incident and scattered electron respectively and t , n and ℓ stand for transverse, normal and longitudinal. Recalling that the momentum transfer \vec{q} is given by $\vec{q} = \vec{k}_i \times \vec{k}_f$ and in virtue of

$$\vec{k}_i \times \vec{k}_f = \vec{k}_i \times \vec{k}_i - \vec{k}_i \times \vec{q} = \vec{q} \times \vec{k}_i \quad (5.14)$$

the above definitions become:

$$\begin{aligned}\hat{n} &\equiv \frac{\vec{q} \times \vec{k}_i}{|\vec{q} \times \vec{k}_i|} = \frac{\hat{q} \times \vec{k}_i}{|\hat{q} \times \vec{k}_i|} \\ \hat{\ell} &\equiv \frac{\vec{q}}{|\vec{q}|} = \hat{q} \\ \hat{t} &\equiv \hat{n} \times \hat{\ell}\end{aligned}\tag{5.15}$$

In the transport coordinate system:

$$\hat{k} = \begin{pmatrix} 0 \\ \sin \theta_{HMS} \\ \cos \theta_{HMS} \end{pmatrix}\tag{5.16}$$

$$\hat{q} = \frac{1}{\sqrt{1 + x'_{igt}{}^2 + y'_{igt}{}^2}} \begin{pmatrix} x'_{igt} \\ y'_{igt} \\ 1 \end{pmatrix}\tag{5.17}$$

The rotation matrix F from the scattering plane to the transport system is then given by:

$$F = \begin{pmatrix} \hat{t}_x & \hat{n}_x & \hat{\ell}_x \\ \hat{t}_y & \hat{n}_y & \hat{\ell}_y \\ \hat{t}_z & \hat{n}_z & \hat{\ell}_z \end{pmatrix}\tag{5.18}$$

In a similar way the rotation matrix Q from the transport system to the focal plane frame is given by:

$$Q = \begin{pmatrix} \hat{T}_x & \hat{T}_y & \hat{T}_z \\ \hat{N}_x & \hat{N}_y & \hat{N}_z \\ \hat{L}_x & \hat{L}_y & \hat{L}_z \end{pmatrix}\tag{5.19}$$

with

$$\hat{L} = \frac{1}{\sqrt{1 + x'_{fp}{}^2 + y'_{fp}{}^2}} \begin{pmatrix} x'_{fp} \\ y'_{fp} \\ 1 \end{pmatrix} \quad (5.20)$$

$$\hat{N} = \frac{\hat{L} \times \hat{x}_{trans}}{|\hat{L} \times \hat{x}_{trans}|} \quad (5.21)$$

$$\hat{T} = \hat{N} \times \hat{L} \quad (5.22)$$

with \hat{x}_{trans} the unit vector along the fixed x -axis of the transport frame. Therefore, the total spin transport matrix S is given by the product:

$$S = \begin{pmatrix} \hat{T}_x & \hat{T}_y & \hat{T}_z \\ \hat{N}_x & \hat{N}_y & \hat{N}_z \\ \hat{L}_x & \hat{L}_y & \hat{L}_z \end{pmatrix} \begin{pmatrix} \hat{P}_{xx} & \hat{P}_{xy} & \hat{P}_{xz} \\ \hat{P}_{yx} & \hat{P}_{yy} & \hat{P}_{yz} \\ \hat{P}_{zx} & \hat{P}_{zy} & \hat{P}_{zz} \end{pmatrix} \begin{pmatrix} \hat{l}_x & \hat{n}_x & \hat{\ell}_x \\ \hat{l}_y & \hat{n}_y & \hat{\ell}_y \\ \hat{l}_z & \hat{n}_z & \hat{\ell}_z \end{pmatrix} \quad (5.23)$$

and the relation between the polarization components at the focal and at the target is:

$$\begin{pmatrix} P_x^{fpp} \\ P_y^{fpp} \\ P_z^{fpp} \end{pmatrix} = \begin{pmatrix} S_{xx} & S_{xy} & S_{xz} \\ S_{yx} & S_{yy} & S_{yz} \\ S_{zx} & S_{zy} & S_{zz} \end{pmatrix} \begin{pmatrix} P_t = P_x^{tgt} \\ P_n = P_y^{tgt} \\ P_l = P_z^{tgt} \end{pmatrix} \quad (5.24)$$

5.3 Maximum Likelihood Method

In the previous section we derived the relation between the polarization components at the target and at the focal plane, accounting for the total spin precession in the HMS magnets. We can now rewrite the angular probability distribution of a proton for the ± 1 helicity states to scatter with

angles (ϑ, φ) given in Equation (3.9) as:

$$f_i(p, \vartheta, \varphi) = \frac{\epsilon(p, \vartheta)}{2\pi} \left[1 + (a_1 \pm hA_y(p, \vartheta_i) (S_{yx,i}P_x + S_{yz,i}P_z) + A_y(p, \vartheta_i)S_{yy,i}P_y) \cos \varphi + \right. \\ \left. (b_1 \mp hA_y(p, \vartheta_i) (S_{xx,i}P_x + S_{xz,i}P_z) - A_y(p, \vartheta_i)S_{xy,i}P_y) \sin \varphi + \right. \\ \left. + a_2 \cos 2\varphi + b_2 \sin 2\varphi + \dots \right] \quad (5.25)$$

This is the most general expression in which we have included a possible induced normal polarization component P_y coming from inelastic processes, false asymmetries or effects coming from higher order in ep scattering. In the analysis, since we are only interested in elastic events, we neglect the induced polarization, but leave the possibility for a normal polarization component. We build a likelihood function as the product of the N (assuming there are N protons to be analyzed) individual angular probability distributions:

$$\mathcal{L} = \frac{1}{2\pi} \prod_{i=1}^N f_i(p, \vartheta, \varphi) \quad (5.26)$$

Since it is always easier to deal with sums than with products, taking the Napierian logarithm of this expression allows us to transform the product into a sum. We are trying to determine the values of the polarization components P_j $j = x, y, z$ that maximize \mathcal{L} or $\ln(\mathcal{L})$ ¹. The maxima of $\ln(\mathcal{L})$ must satisfy:

$$\frac{\partial \ln \mathcal{L}}{\partial P_j} = 0, \quad j = x, y, z \quad (5.27)$$

As a result we obtain a system of coupled non-linear equations:

$$\frac{\partial \ln \mathcal{L}}{\partial P_j} = 0 \Leftrightarrow \quad (5.28)$$

$$\sum_{i=1}^N \frac{\partial}{\partial P_j} \left[\ln \left(1 + \lambda_{0,i} + \sum_{j=x,y,z} \lambda_{j,i} P_j \right) \right] = 0 \quad (5.29)$$

¹Since the Napierian logarithm is a monotonically increasing function on \mathbb{R}^+ , if P_i is a maximum of $\ln(\mathcal{L})$ it will also be maximum of \mathcal{L}

where the λ_k are defined by

$$\lambda_{0,i} \equiv a_1 \cos \varphi_i + b_1 \sin \varphi_i + a_2 \cos 2\varphi_i + b_2 \sin 2\varphi_i + \dots \quad (5.30)$$

$$\lambda_{x,i} \equiv h\epsilon_i A_{y,i} (S_{yx,i} \cos \varphi_i - S_{xx,i} \sin \varphi_i) \quad (5.31)$$

$$\lambda_{y,i} \equiv A_{y,i} (S_{yy,i} \cos \varphi_i - S_{xy,i} \sin \varphi_i) \quad (5.32)$$

$$\lambda_{z,i} \equiv h\epsilon_i A_{y,i} (S_{yz,i} \cos \varphi_i - S_{xz,i} \sin \varphi_i) \quad (5.33)$$

Assuming small asymmetries and taking the Taylor expansion up to the second order of the Napierian logarithm:

$$\ln(1+x) = \sum_{n=1}^{\infty} (-1)^{n+1} \frac{x^n}{n!} \quad (5.34)$$

we obtain:

$$\begin{aligned} \sum_{i=1}^N \frac{\partial}{\partial P_j} \left[\lambda_{0,i} + \sum_{j=x,y,z} \lambda_{j,i} P_j - \frac{(\lambda_{0,i} + \sum_{j=x,y,z} \lambda_{j,i} P_j)^2}{2} \right] &= 0 \\ \sum_{i=1}^N \frac{\partial}{\partial P_j} \left(\lambda_{0,i} - \frac{1}{2} \lambda_{0,i}^2 + \sum_{j=x,y,z} \lambda_{j,i} P_j - \sum_{j=x,y,z} \lambda_{j,i} P_j \lambda_{0,i} - \sum_{j=x,y,z} \lambda_{j,i} P_j \sum_{k=x,y,z} \lambda_{k,i} P_k \right) &= 0 \\ \sum_{i=1}^N \lambda_{j,i} (1 - \lambda_{0,i}) &= \sum_{i=1}^N \sum_{k=x,y,z} \lambda_{j,i} \lambda_{k,i} P_k \end{aligned}$$

We can rewrite the above system of linear equations in a matrix form $\mathbf{B} = \mathbf{A}P$:

$$\underbrace{\sum_{i=1}^N \begin{pmatrix} \lambda_{x,i} (1 - \lambda_{0,i}) \\ \lambda_{y,i} (1 - \lambda_{0,i}) \\ \lambda_{z,i} (1 - \lambda_{0,i}) \end{pmatrix}}_{\mathbf{B}} = \sum_{i=1}^N \underbrace{\begin{pmatrix} (\lambda_{x,i})^2 & \lambda_{x,i} \lambda_{y,i} & \lambda_{x,i} \lambda_{z,i} \\ \lambda_{y,i} \lambda_{x,i} & (\lambda_{y,i})^2 & \lambda_{y,i} \lambda_{z,i} \\ \lambda_{z,i} \lambda_{x,i} & \lambda_{z,i} \lambda_{y,i} & (\lambda_{z,i})^2 \end{pmatrix}}_{\mathbf{A}} \underbrace{\begin{pmatrix} P_x \\ P_y \\ P_z \end{pmatrix}}_P \quad (5.35)$$

The statistical error on the polarization components are given by the diagonal elements of the covariant matrix \mathbf{A}^{-1} :

$$\Delta P_j = \sqrt{(A^{-1})_{jj}}, \quad j = x, y, z \quad (5.36)$$

The statistical error on the polarization component ratio $R (= KP_t/P_\ell \equiv KP_x/P_z)$, with K the kinematic factor: $K = \frac{E_c + E'_c}{2M_p} \tan \frac{\theta_c}{2}$, is then given by:

$$\left(\frac{\Delta R}{R}\right)^2 = \sqrt{\left(\frac{\Delta P_t}{P_t}\right)^2 + \left(\frac{\Delta P_\ell}{P_\ell}\right)^2 - 2\frac{\rho}{P_t P_\ell}} \quad (5.37)$$

with the correlation factor or covariance between P_t and P_ℓ given by:

$$\rho = (A^{-1})_{xz} \quad (5.38)$$

5.4 False Asymmetries

Until now, we assumed and treated the false asymmetry as an additive helicity-independent term in the angular distribution of events. A more general form of this distribution, with the inclusion of a multiplicative false asymmetry term $A(\varphi)$ is given by:

$$\begin{aligned} f^\pm &= A(\varphi) \frac{1}{2\pi} (1 \pm P_y \cos \varphi \mp P_x \sin \varphi + \lambda_0) \\ &= A(\varphi) \frac{1}{2\pi} (1 \pm P_y \cos \varphi \mp P_x \sin \varphi + a_1 \cos \varphi + b_1 \sin \varphi + a_2 \cos 2\varphi + b_2 \sin 2\varphi) \end{aligned} \quad (5.39)$$

A multiplicative false asymmetry will induced helicity-dependent high order (>1) terms and modify the lowest order. However, it has been shown [60] that the false asymmetries induced by a multiplicative term cancel out to all order using the weighted sum estimators, as we do in the maximum likelihood method, under the assumption $A(\varphi) = A(\varphi + \pi)$ which is satisfied through the helicity reversal. The fit parameters of order >1 in the difference spectra are two orders of magnitude smaller than the ones of the first order which support a cancellation of any multiplicative false asymmetry.

Based on the formalism of [60] we can see what is the effect on the polarization estimator of an additive false asymmetry. The polarization estimators \hat{P}_x, \hat{P}_y are given by the difference of the weighted sum estimators of the coefficients of $\sin \varphi$ and $\cos \varphi$ of both helicity states respectively:

$$\hat{P}_x = -\frac{1}{2}(\hat{B}^+ - \hat{B}^-) \quad (5.40)$$

$$\hat{P}_y = \frac{1}{2}(\hat{A}^+ - \hat{A}^-) \quad (5.41)$$

The \hat{B}_\pm and \hat{A}_\pm satisfy the matrix equation:

$$\begin{pmatrix} \int_0^{2\varphi} f^\pm \cos^2 \varphi d\varphi & \int_0^{2\varphi} f^\pm \cos \varphi \sin \varphi d\varphi \\ \int_0^{2\varphi} f^\pm \cos \varphi \sin \varphi d\varphi & \int_0^{2\varphi} f^\pm \sin^2 \varphi d\varphi \end{pmatrix} \begin{pmatrix} \hat{A}^+ \\ \hat{B}^+ \end{pmatrix} = \begin{pmatrix} \int_0^{2\varphi} f^\pm \cos \varphi d\varphi \\ \int_0^{2\varphi} f^\pm \sin \varphi d\varphi \end{pmatrix} \quad (5.42)$$

Solving the integrals, inverting the matrix by neglecting the quadratic terms we obtain the estimators \hat{A}^\pm and \hat{B}^\pm :

$$\begin{pmatrix} \hat{A}^\pm \\ \hat{B}^\pm \end{pmatrix} = \begin{pmatrix} 1 - \frac{a_2}{2} & \frac{s_2}{2} \\ \frac{s_2}{2} & 1 + \frac{a_2}{2} \end{pmatrix} \begin{pmatrix} \pm P_y + a_1 \\ \mp P_x + b_1 \end{pmatrix} \quad (5.43)$$

The polarization estimators are then given by:

$$\hat{P}_x = \frac{b_2}{2} P_y + P_x \left(1 + \frac{a_2}{2}\right) \quad (5.44)$$

$$\hat{P}_y = \frac{b_2}{2} P_x + P_y \left(1 - \frac{a_2}{2}\right) \quad (5.45)$$

We see that only the 2φ components of the additive false asymmetry modify the polarization estimator. Knowing the a_2 and b_2 coefficients (by a Fourier analysis of the sum distribution spectrum) we can correct for the additive false asymmetry. One can show that we need to apply a correction of the form: $f^\pm(1 + \lambda_0)$ in the weighted sum estimators to finally have:

$$\hat{P}_x = P_x \quad (5.46)$$

$$\hat{P}_y = P_y \quad (5.47)$$

This result is counter intuitive but if we were applying a correction of the form: $f^\pm(1 - \lambda_0)$ this

would double the effect of the false asymmetry. In the analysis we binned the sum spectra in 14 bins of the scattering angle ϑ_{FPP} (see Table 5.3) and determined the Fourier coefficients up to the third harmonic.

ϑ_{FPP} bins ($^\circ$)	1.7	3	5	7	10	13	15	17	20	23	26	29	32	35	40
-------------------------------------	-----	---	---	---	----	----	----	----	----	----	----	----	----	----	----

Table 5.3: False asymmetry ϑ_{FPP} bins.

5.5 CH₂ Analyzing power at $p_0 = 2.0676$ GeV/c

The analyzing power $A_y(\vartheta_{FPP}, p)$ of the $\vec{p} + CH_2 \rightarrow$ one charged particle + X reaction, which depicts the size of the asymmetries, was originally unknown. Despite the fact that it cancels out in the polarization component ratio, since we measure $\hbar A_y P_t$ and $\hbar A_y P_\ell$ (as shown in Equation 5.48), it is a quantity of primary importance in the determination of the ratio of the longitudinal polarization component to its Born value, P_ℓ / P_ℓ^{Born}

$$R = K \frac{\hbar A_y P_t}{\hbar A_y P_\ell} \quad (5.48)$$

Assuming the knowledge of the Born value of P_ℓ , the analyzing power is determined by taking the ratio between the measured asymmetry $A_y P_\ell$ to P_ℓ . The Born value P_ℓ^{Born} is expressed in terms of the beam energy E_{beam} , the momentum p and the fitted value of the polarization component ratio obtained in this experiment.

$$A_y = \frac{(A_y P_\ell)_{meas.}}{P_\ell^{Born}(E_{beam,p,R})} \quad (5.49)$$

P_ℓ^{Born} is given by:

$$P_\ell^{Born}(E_{beam,p,R}) = \sqrt{1 - \epsilon^2} \frac{1}{1 + \frac{\epsilon R^2}{\tau}} \quad (5.50)$$

Recalling the expression of the proton kinetic energy: $T = \sqrt{p^2 + M^2} - M$, τ and ϵ can be written in terms of T and thus of p :

$$\tau = \frac{Q^2}{4M^2} = \frac{1}{2M} \underbrace{\frac{Q^2}{2M}}_T = \frac{T}{2M} \quad (5.51)$$

ϵ requires a little bit more work. We start from its usual expression:

$$\epsilon = \frac{1}{1 + 2(1 + \tau) \tan^2 \frac{\vartheta_e}{2}} \quad (5.52)$$

From:

$$Q^2 = 4E_{beam} E'_e \sin^2 \frac{\vartheta_e}{2} \Rightarrow \sin^2 \frac{\vartheta_e}{2} = \frac{TM}{2E_{beam} (E_{beam} - T)} \quad (5.53)$$

and

$$1 + \tan^2 \vartheta = \frac{1}{\cos^2 \vartheta} = \frac{1}{1 - \sin^2 \vartheta} \Rightarrow \tan^2 \frac{\vartheta_e}{2} = \frac{\sin^2 \frac{\vartheta_e}{2}}{1 - \sin^2 \frac{\vartheta_e}{2}} \quad (5.54)$$

we obtain:

$$\tan^2 \frac{\vartheta_e}{2} = \frac{TM}{2E_{beam}^2 - T(2E_{beam} + M)} \quad (5.55)$$

Therefore:

$$\epsilon = \frac{1}{1 + (2M + T) \frac{T}{2E_{beam}^2 - T(2E_{beam} + M)}} \quad (5.56)$$

We could have determined the analyzing power from the measured transverse polarization component P_t . However P_t is known with a larger relative uncertainty than P_ℓ . The analyzing power is parametrized as a function of the transverse momentum $p_T = p \sin \vartheta_{FP}$ corrected for energy loss up to the interaction vertex in the analyzer. A functional of the form $A_y = A p_T^B e^{C p_T^D}$ was used where A , B , C , and D are the fit parameters. This parametrization has for effect to decrease the statistical uncertainty of the result by giving less weight to small and large angle events. The distribution of A_y as a function of p_T for single, multiple track events and for the average of the two types (all) is shown in Figure 5.3. We see a clear dichotomy between the distributions for single-track and multiple-track events.

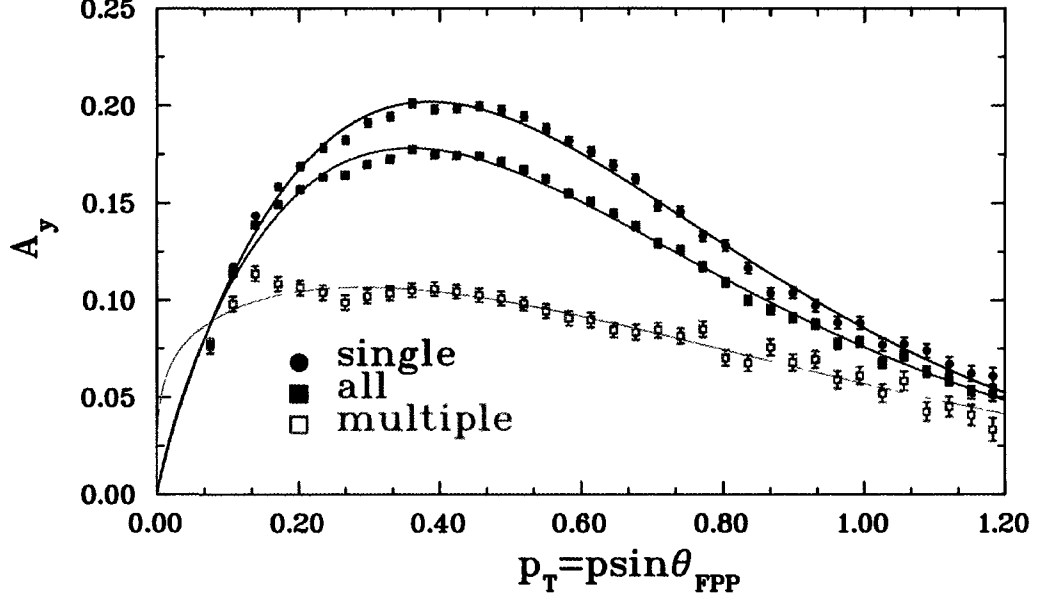


Figure 5.3: Analyzing power distribution as a function of the transverse momentum p_T at $Q^2 = 2.5 \text{ GeV}^2$ for all single and multi-track events and all (single + multi).

The energy loss was calculated using the Bethe-Bloch formula [15]:

$$E_{loss} = Kz^2 \frac{Z}{A} \frac{1}{\beta^2} \left[\frac{1}{2} \ln \left(\frac{2m_e c^2 \beta^2 \gamma^2 T_{max}}{I^2} \right) - \beta^2 - \ln \left(\frac{\hbar \omega_p}{I} \right) + \ln(\beta \gamma) - \frac{1}{2} \right] L \quad (5.57)$$

where $K = 0.307075 \text{ MeV g}^{-1} \text{ cm}^2$, $I = 57.4 \text{ eV}$ is the mean excitation energy, $\hbar \omega_p = \sqrt{\rho Z/A} * 28.816 \text{ eV}$ is the plasma energy, L (=54 cm for one analyzer) is the length of the absorber and T_{max} is the maximum kinetic energy which can be imparted to a free electron in a single collision given by:

$$T_{max} = \frac{2m_e c^2 \beta^2 \gamma^2}{1 + 2\gamma \frac{m_e}{M} + \left(\frac{m_e}{M} \right)^2} \quad (5.58)$$

For CH_2 , $Z/A = 0.57034$ and the density $\rho = 0.89 \text{ g/cm}^3$, we obtain $E_{loss} \approx 112 \text{ MeV}$ (224 MeV for both analyzer). Translating this energy loss into a momentum loss we have for the corrected momentum for energy loss after a passage through the whole width of first analyzer:

$$p_{corr} = \sqrt{(\gamma M - E_{loss})^2 - M^2} \approx 1.94 \text{ GeV}/c \quad (5.59)$$

We obtain $p_{corr} = 1.81$ GeV/c after a passage through the whole width of both analyzers. The effect of this correction on the momentum is shown on Figure 5.4. As expected at the exit of the first analyzer for a momentum central value of $p_0 = 2.0676$ GeV/c and for $\epsilon = 0.152$, the momentum corrected for energy loss is about 1.94 GeV/c. The colours can be misleading but looking at the colour scale we see that the protons scattered within the whole width of the analyzers more or less uniformly. The width in momentum of this distribution, corresponds to the momentum width of the kinematic ($\delta = (p - p_0)/p_0 = \pm 2\%$).

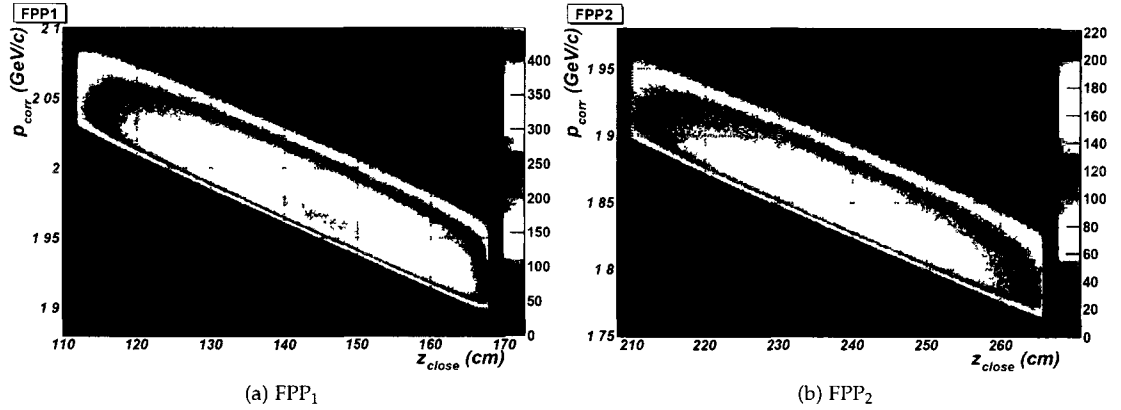


Figure 5.4: Momentum corrected for energy loss p_{corr} as a function of z_{close} for FPP₁ and FPP₂

L. S. Azghirey *et al.* [55], in an experiment in Dubna, Russia aiming at measuring analyzing powers for the reaction $\vec{p} + \text{CH}_2$ at $p_p = 1.75\text{-}5.3$ GeV/c, found that the maximum analyzing power behaves linearly with the inverse of the incident proton momentum:

$$A_y^{max} = \alpha \frac{1}{p} + \beta \quad (5.60)$$

Figure 5.5 presents a comparison between the previous Dubna and Gayou [61] data and the results from the GE_pIII and GE_p2 γ experiments. If the empirical linear behaviour of A_y^{max} versus $1/p$ (which is also seen for the average analyzing power) is observed, we see that the values obtained

in the latest experiments are systematically higher. The equations of the straight lines are:

$$A_y^{max} = 0.3480 \frac{1}{p} + 0.029 \quad \text{for the GE}_p \text{ experiments} \quad (5.61)$$

$$A_y^{max} = 0.3707 \frac{1}{p} + 0.001 \quad \text{for the Dubna and Gayou data combined} \quad (5.62)$$

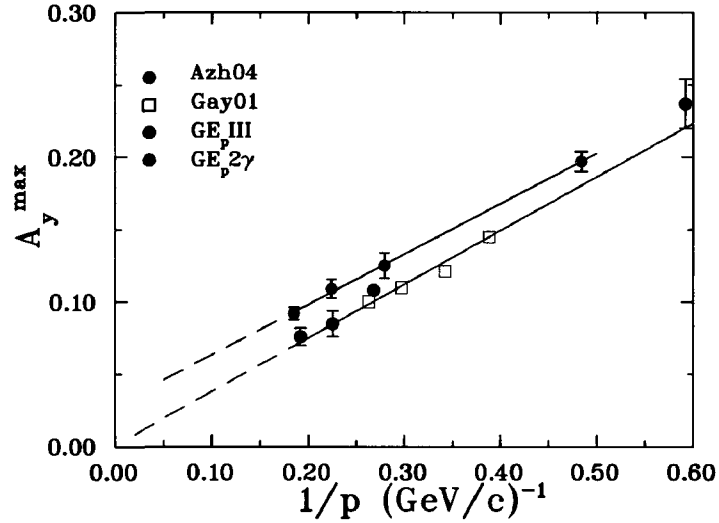


Figure 5.5: CH₂ Analyzing power versus 1/p.

One possible explanation is the suppression of multi-track events. As we have seen above, the analyzing power of multi-track events is significantly lower than the one of single-track events. Assuming that in the experiment we suppress all the multi-track events, we can give a rough estimate of the residual multiple-track event fraction in the Dubna sample. We read on Figure 5.3: $A_{y,single}^{max} \approx 0.2$ and $A_{y,multi}^{max} \approx 0.1$. At $p=2.0676$ GeV/c, in order to get the maximum analyzing power value given by the Dubna and Gayou fit $A_{y,DG}^{max} = 0.179$, the fraction x of multiple-track events must satisfy:

$$A_{y,single}^{max}(1-x) + A_{y,multi}^{max}x = A_{y,DG}^{max} \quad (5.63)$$

which gives $x \approx 20\%$. This rough estimate of the residual multi-track event fraction is high but not unreasonable.

Chapter 6

Results

In this chapter, we will present the results for the polarization component ratio R and for the longitudinal component P_ℓ . We will also describe the different uncertainties identified in the analysis. Finally, after a comparison between the results and the available theoretical models, we will present an empirical determination of the real parts of the TPEX amplitudes.

6.1 Matching Acceptance Cut

In order to have the same spin transport and the same analyzing power for each of the three kinematic, we apply a matching acceptance cut at the focal plane (FP cut). We cut the acceptance of the two largest ϵ points to match the smallest ϵ points (see Figure 6.1). As the HMS magnets are operating in a point-to-point mode, selecting the trajectories at the focal plane within a certain acceptance ensures all the selected protons underwent the same spin transport through the magnetic elements. Of course, depending on the kinematic, the acceptance defined by the cut is not populated the same way, but all along the magnets it is defined by an envelope common to all three kinematics. In Figure 6.1, the original acceptances for $\epsilon=0.635$ and 0.785 (black dots) are cut at $\delta = \pm 2\%$ corresponding to the momentum acceptance of the $\epsilon=0.152$ point, for reason of clarity. Selecting the same acceptance at the focal plane for all the kinematics results in the similar average Q^2 at the 10^{-3} level (see Table 6.1).

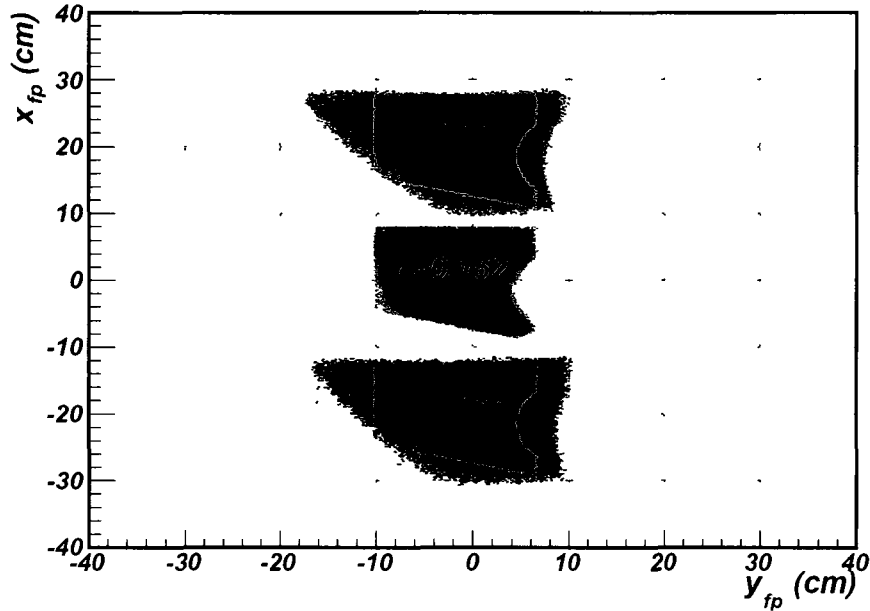


Figure 6.1: x_{fp} versus y_{fp} distribution showing the matching acceptance cut. The distributions for $\epsilon = 0.635$ and $\epsilon = 0.785$ are shifted vertically by +20cm and -20cm in x_{fp} and the original acceptance in black are cut at $\delta = \pm 2\%$ for reason of clarity.

	$\epsilon = 0.152$	$\epsilon = 0.635$	$\epsilon = 0.773$	$\epsilon = 0.791$
$\langle Q^2 \rangle$ (GeV ²) No FP cut	2.493	2.481	2.462	2.458
$\langle Q^2 \rangle$ (GeV ²) FP cut	2.493	2.490	2.490	2.489

Table 6.1: Average Q^2 with and without the FP cut.

The maximum $A_y^{max} \approx 0.2$ and the average analyzing power \bar{A}_y behaves like $1/p$, thus we can look at the average momentum for the three kinematics and check the stability of the results. Table 6.2 shows the ratio of the average proton momentum for $\epsilon = 0.152$ to one of the high ϵ points with and without the matching acceptance cut. The values are the same at the 10^{-3} level when we apply the cut. Therefore we expect the same stability for the analyzing power although we can not verify it experimentally. The stability of the analyzing power is not significant for the determination of the polarization component ratio R (since it exactly cancels out), but it is of primary importance to the extraction of the longitudinal component of the polarization transferred P_L .

	$p_{ave}^{\epsilon=0.152} / p_{ave}^{\epsilon=0.635}$	$p_{ave}^{\epsilon=0.773} / p_{ave}^{\epsilon=0.152}$	$p_{ave}^{\epsilon=0.791} / p_{ave}^{\epsilon=0.152}$
No cut	1.0045	1.0107	1.0107
Match. Acc cut	1.0018	1.0016	1.0019

Table 6.2: Ratio of the average proton momenta with and without matching acceptance cuts.

6.2 z_{close} Dependence of A_y and R

Before presenting the results for the longitudinal component P_ℓ , we will study the z_{close} dependence of the average analyzing power \bar{A}_y and the polarization component ratio. Figure 6.2 shows that \bar{A}_y is constant for the first 2/3 of the width of both analyser blocks before it starts to drop.

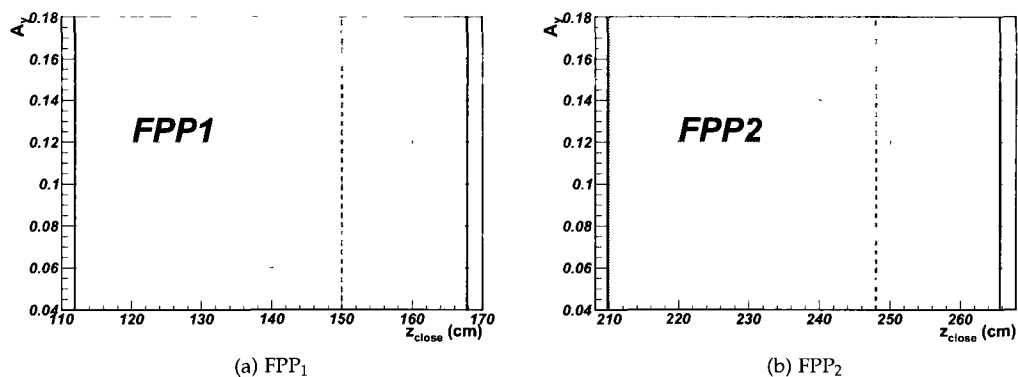


Figure 6.2: \bar{A}_y versus z_{close} for FPP₁ and FPP₂. The dotted line shows the limit above which the events are cut for the longitudinal polarization component extraction.

In contrast, R is constant within the whole width of both FPPs as expected since it is independent of the analyzing power (see Figure 6.3). We interpret this decrease in the average analyzing power as a consequence of mistracked events. We see in the φ_{FPP} versus z_{close} distribution displayed in Figure 6.4, the presence of some peaks at very specific positions. A close look at the figure reveals that the peaks appear every 45° and that each peak is located at a position z corresponding to a drift chamber plane of detection. A simple Monte Carlo simulation showed that the events in these very localized peaks came from Coulomb events for which the FPP track contains at least two hits with a wrong left/right determination. As a results, they are mostly reconstructed in the chambers but also "leak" into the analyzer block as we see in the figure. These wrongly re-

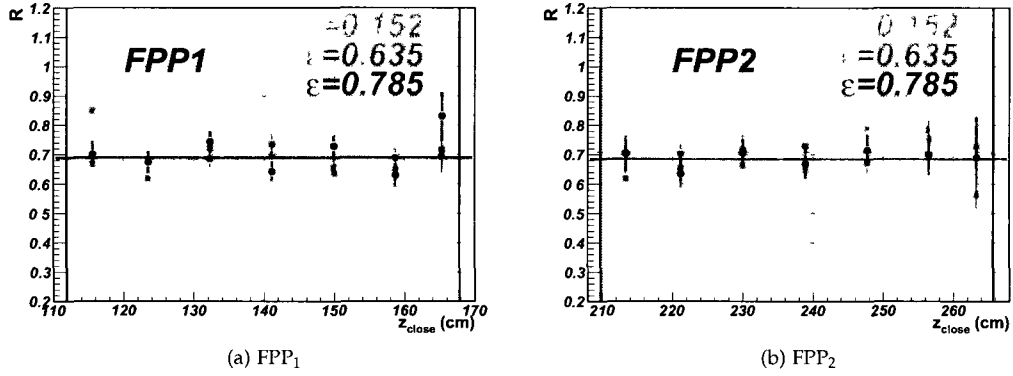


Figure 6.3: R versus z_{close} for FPP₁ and FPP₂.

constructed Coulomb events are also characterized by a smeared scattering angle distribution: $0^\circ \leq \theta_{FPP} \leq 6^\circ$. Since they are originally Coulomb events, they do not carry any analyzing power and thus dilute the analyzing power in the last third of the analyzer blocks. Therefore for P_ℓ , we apply a cut in z_{close} (represented by the vertical dashed line in the Figures 6.2a) and b)) to only select the region of the CH₂ blocks where the analyzing power is constant. A way to suppress, or at least greatly reduce these mistracked events in future experiments using the FPP would be to add a plane to each chamber. This would produce a greater redundancy in the track coordinates and insure a better left-right determination.

6.3 Final Cuts

Global Cuts

Loose cuts were applied on the target slopes x'_{tgt} and y'_{tgt} :

$$|x'_{tgt}| \leq 0.08 \quad (6.1)$$

$$|y'_{tgt}| \leq 0.04 \quad (6.2)$$

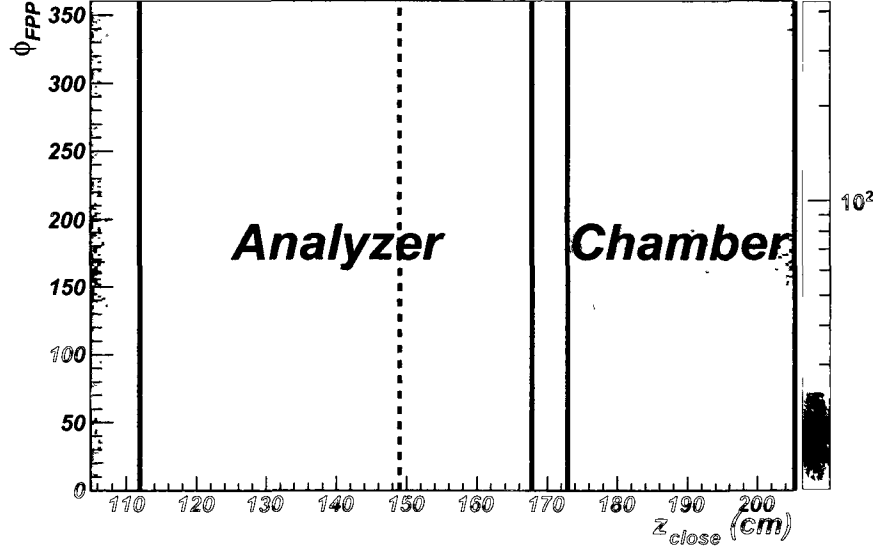


Figure 6.4: ϕ_{FPP} versus z_{close} distribution for the first analyzer block. The solid lines represent the physical width of the block and the drift chambers. The dotted line shows the limit above which the events are cut for the longitudinal polarization component extraction.

Matching Acceptance Cut

For both extractions of R and the longitudinal polarization component P_L , the matching acceptance cut (FP cut) was applied. (see Figure 6.1)

FPP Scattering Cuts

Cut were applied on the number of tracks N_{track} , the distance of closest approach s_{close} , the polar scattering angle θ_{FPP} and the z -coordinate of the interaction point in the analyzer z_{close} for both FPP_1 and FPP_2 :

$$N_{track}^{FPP_{1(2)}} = 1 \quad (6.3)$$

$$s_{close}^{FPP_{1(2)}} \leq 3(6) \text{ cm} \quad (6.4)$$

$$1.7(2.5)^\circ < \theta_{FPP_{1(2)}} < 40^\circ \quad (6.5)$$

For the extraction of R :

$$112 \text{ cm} \leq z_{close}^{FPP_1} \leq 168 \text{ cm} \quad (6.6)$$

$$210 \text{ cm} \leq z_{close}^{FPP_2} \leq 266 \text{ cm} \quad (6.7)$$

For the extraction of P_ℓ :

$$112 \text{ cm} \leq z_{close}^{FPP_1} \leq 150 \text{ cm} \quad (6.8)$$

$$210 \text{ cm} \leq z_{close}^{FPP_2} \leq 247 \text{ cm} \quad (6.9)$$

The conetest was of course also applied, it rejects 0.75% of the elastic events satisfying the FPP scattering and the acceptance cuts described above.

Elastic Event Selection Cuts

The elliptical cut and a cut on p_{miss}^p , as described in Chapter 4, were applied. These cuts are summarized in Table 6.3.

ϵ	x_{cut} , cm	y_{cut} , cm	p_{miss}^p cut, %
0.152	≤ 9.9	≤ 23.9	≤ 0.672
0.152	≤ 9.1	≤ 24.2	≤ 0.672
0.635	≤ 5.9	≤ 21.3	≤ 0.138
0.773	≤ 3.9	≤ 13.9	≤ 0.161
0.791	≤ 3.7	≤ 12.6	≤ 0.161

Table 6.3: Elastic event selection cuts used in the final analysis.

The two rows for $\epsilon=0.152$ correspond to the two parts of the kinematic with two different beam energies. Being kinematically very close, the separate study of these two parts will not be detailed here, but it has been checked that they give statistically compatible results.

6.4 False Asymmetry Correction

As mentioned in the previous chapter, the false asymmetry coefficients were determined by a Fourier analysis of the sum spectra up to the third harmonic. The data were binned in 14 bins of the scattering angle ϑ_{FP} . The analysis code was run a first time without implementing the λ_0 term in the maximum likelihood function (see equation 5.30) and then a second time with it. The difference of the two results gives a small negative correction in R of at most $|\Delta R| \leq 0.012$ as shown in Table 6.4. On the contrary, the correction to P_ℓ is small and positive as displayed in Table 6.5.

	$\epsilon = 0.152$	$\epsilon = 0.635$	$\epsilon = 0.773$	$\epsilon = 0.791$
ΔR No FP cut	-0.012	-0.011	-0.010	-0.009
ΔR FP cut	-0.012	-0.012	-0.011	-0.012

Table 6.4: Shift ΔR in R induced by the false asymmetries.

	$\epsilon = 0.152$	$\epsilon = 0.635$	$\epsilon = 0.773$	$\epsilon = 0.791$
ΔP_ℓ No z_{close} cut	0.009	0.005	0.004	0.004
ΔP_ℓ z_{close} cut	0.002	0.001	0.001	0.001

Table 6.5: Shift ΔP_ℓ in the longitudinal polarization component P_ℓ induced by the false asymmetries.

As expected, the false asymmetries induce a shift in R which is kinematically independent. These asymmetries come from the geometry, the acceptance and a residual misalignment of the detector as well as detection efficiencies affected by a biased track reconstruction. The FP cut has almost no influence on the correction in R . The z_{close} cut reduced the false asymmetry correction considerably since we thereby suppressed mistracked events in the last third of the analyzer blocks.

6.5 Radiative Corrections

The "standard" radiative corrections to the polarization transfer observables were calculated using the model independent calculation of A. Afanasev *et al.* [14]. They consist of the vacuum polarization correction, the electron vertex correction and the internal and external Bremsstrahlung. The

external Bremsstrahlung contribution to the polarization asymmetries is suppressed by reversing the beam polarization. Unlike cross section measurements, polarization transfer experiments are rather insensitive to radiative corrections. Indeed, polarization measurements are a ratio of a polarized cross section σ_p to an unpolarized one σ_u :

$$\sigma_{obs}^{u,p} = (1 + \delta)\sigma_0^{u,p} + \sigma_B^{u,p} \quad (6.10)$$

where δ is the radiative correction coming from the vertex and vacuum polarization correction and $\sigma_B^{p,u}$ is the unfactorized contribution from the Bremsstrahlung process. The relative correction to the measured asymmetry is given by:

$$\begin{aligned} \Delta A &\equiv \frac{\sigma_{obs}^p - \sigma_{obs}^u}{\sigma_{obs}^u} \\ &= \frac{(1 + \delta)\sigma_0^p \sigma_0^u + \sigma_R^p \sigma_0^u}{(1 + \delta)\sigma_0^u \sigma_0^p + \sigma_R^u \sigma_0^p} - 1 \\ &= \frac{\delta_p - \delta_u}{1 + \delta + \delta_u} \end{aligned} \quad (6.11)$$

where $\delta_{u,p} = \sigma_B^{u,p} / \sigma_0^{u,p}$. The δ term can be as large as 30%, but it cancels exactly in the numerator. This is why the radiative correction to the polarization observable are expected to be small and much smaller than the corrections to the cross section. The Bremsstrahlung contribution can be reduced drastically by applying a missing mass cut or inelasticity cut (this was done by the elastic events selection). Furthermore, R being the ratio of two polarization asymmetries is then a ratio of a ratio of cross section, and as a consequence, it will be even less sensitive to radiative corrections. The radiative corrections to R were computed using the program MASCARAD developed and written by A. Afanasev [14]. Table 6.6 presents the small positive corrections ΔR_{rad} found for the different ϵ points. Because both parts of the highest ϵ are kinematically very close to each other, the two inelasticity cuts are almost identical. Therefore, the radiative corrections were found to be very similar and it was not important to separate them in this calculation. The corrections to the longitudinal polarization components were found to be even smaller [14] and are not displayed here.

	$\epsilon = 0.152$	$\epsilon = 0.635$	$\epsilon = 0.785$
$\Delta R_{rad.}$	1.2×10^{-3}	1.4×10^{-4}	0.7×10^{-4}

Table 6.6: Radiative corrections to R obtained from the program MASCARAD.

6.6 Polarization Component Ratio Results

In Chapter 3 it was shown (see Equation (3.11)) that the statistical uncertainties on the polarization components are inversely proportional to the square root of the number of events as well as the square of the analyzing power:

$$\Delta P \propto \frac{1}{\sqrt{NA_y^2}} \quad (6.12)$$

This behaviour can also be seen in Equation (5.35), since the diagonal elements of the covariant matrix \mathbf{A}^{-1} are proportional to $(NhA_y)^2$. The results of R with and without the FP cut and corrected for the false asymmetries are given in Table 6.7.

	$\epsilon = 0.152$	$\epsilon = 0.635$	$\epsilon = 0.773$	$\epsilon = 0.791$
$R \pm \Delta R_{stat.}$ No FP cut	0.695 ± 0.009	0.680 ± 0.007	0.684 ± 0.010	0.668 ± 0.008
$R \pm \Delta R_{stat.}$ FP cut	0.695 ± 0.009	0.688 ± 0.011	0.706 ± 0.018	0.684 ± 0.014

Table 6.7: Results for R corrected for the false asymmetries with and without the FP cut.

The FP cut has a significant effect on R by pulling it up for the highest ϵ points. However, the results before and after the cuts are still statistically compatible. There is also a noticeable difference between the results at $\epsilon = 0.773$ and $\epsilon = 0.791$ which are also statistically compatible. The averages of the two parts with and without the FP cut are $R = 0.674 \pm 0.006$ and $R = 0.692 \pm 0.011$, respectively.

6.7 Longitudinal Component Polarization Results

Rather than looking at the longitudinal polarization component P_ℓ alone, it is customary in the literature when studying the TPEX effect to consider its variation with ϵ with respect to its Born

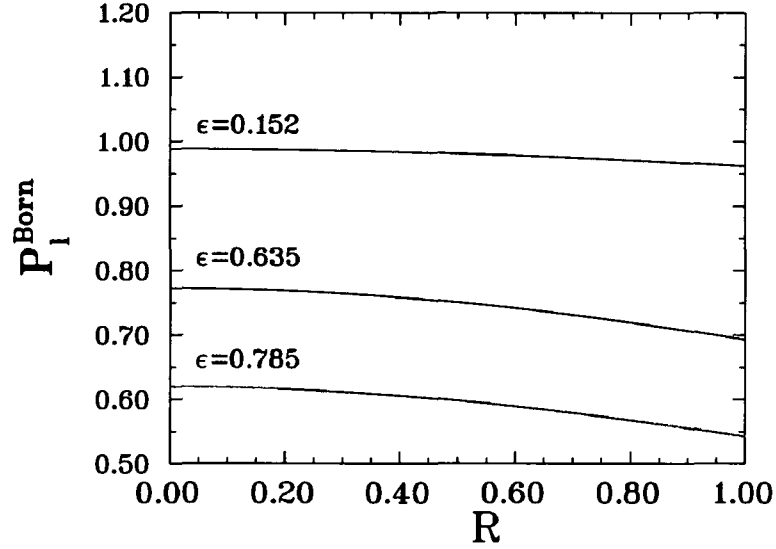


Figure 6.5: P_l^{Born} versus R

value P_l^{Born} . The Born value was calculated from the beam energy, the momentum and the fitted value of R obtained in this experiment as described in Section 5.5. In the experiment, we are measuring the asymmetry $P_e A_y P_\ell$. The beam polarization is known from the Möller measurements, but we need to determine the analyzing power. As we are measuring the asymmetry at three different values of ϵ , we cannot at the same time determine A_y and three values of P_ℓ . In the limit $\epsilon \rightarrow 0$, the angular momentum conservation requires $P_\ell \rightarrow 1$ (seen in Equation 1.98) and is independent of R [62]. Furthermore, from Figure 6.5 we see that at $\epsilon = 0.152$, P_l^{Born} varies at most by $\pm 1.4\%$ for $0 \leq R \leq 1$ against $\pm 5\%$ and $\pm 6.7\%$ at $\epsilon = 0.635$ and $\epsilon = 0.785$. So its variation around the value of R obtained in this experiment is negligible. Therefore, the first kinematic at $\epsilon = 0.152$ is used to determine A_y . Its average value, \bar{A}_y , is found to be equal to:

$$\bar{A}_y = 0.15260 \pm 0.00038 \quad (6.13)$$

Table 6.8 presents the P_ℓ/P_l^{Born} ratio results obtained with and without the z_{close} cut. The FP cut was applied in both cases. The data show an enhancement in the ratio P_ℓ/P_l^{Born} up to $3.1\% \pm 0.5\%$ at high ϵ when both parts are combined. This effect is reduced by the z_{close} cut to 2.3%

	$\epsilon = 0.635$	$\epsilon = 0.773$	$\epsilon = 0.791$	$\epsilon = 785$ (ave.)
$P_\ell / P_\ell^{Born} \pm stat.$ No z_{close} cut	1.012 ± 0.004	1.023 ± 0.008	1.035 ± 0.006	1.031 ± 0.005
$P_\ell / P_\ell^{Born} \pm stat.$ z_{close} cut	1.008 ± 0.005	1.021 ± 0.009	1.024 ± 0.007	1.023 ± 0.005

Table 6.8: P_ℓ / P_ℓ^{Born} results corrected for the false asymmetries with and without the z_{close} cut. The last column shows the results of the two parts of the highest ϵ point averaged.

$\pm 0.6\%$. The application of a more severe z_{close} cut does not reduce this effect any further. Indeed, selecting only the first third (18 cm) of both analyzers, we obtained $P_\ell / P_\ell^{Born} = 1.009 \pm 0.007$ for $\epsilon = 0.635$ and 1.029 ± 0.008 for $\epsilon = 0.785$. In other words, we see an enhancement of $2.9\% \pm 0.8\%$ at the highest ϵ . This result reflects the statistical fluctuations in the loss of 50% of the events with respect to the nominal case where we keep the first thirds of both analyzers.

6.8 Systematic Uncertainties

The advantage of the ratio method, compared to individual determination of P_t and P_ℓ is that beam polarization and the analyzing power cancel out exactly, reducing the sources of systematic uncertainties significantly. As a consequence, the spin precession calculation makes the largest contribution. Other sources are the proton momentum, the beam energy and the scattering azimuthal angle in the FPP; they have been accounted for in the analysis. For each source, an offset was applied in both directions in the considered quantity and the average resulting shifts in R and P_ℓ were recorded. Half of the false asymmetry correction was taken as the systematic contribution from the false asymmetry for R and P_ℓ .

The nominal $\Delta\delta = 0.1\%$ momentum resolution of the HMS was taken as a systematic shift in the proton momentum. Table 3.1 shows that the beam energy has an uncertainty of $\Delta E_{beam} \approx 0.05\%$. A ϑ_{FPP} dependent systematic uncertainty was accounted for in the azimuthal FPP scattering angle φ_{FPP} . With estimated uncertainties of 0.1 mrad in the slopes x' and y' of a track in the FPP, the uncertainty $\Delta\varphi_{FPP}$ in φ_{FPP} behaves like $0.14 \text{ mrad} / \sin \vartheta_{FPP}$.

To estimate the sensitivity of R to the dispersive precession angle χ_θ and the non-dispersive precession angle χ_ϕ , we use the Equation (5.10) with $P_n = 0$. Solving for the polarization components at the target P_t and P_ℓ , taking their ratio in the limit $\chi_\phi \rightarrow 0$ (since along the central ray the

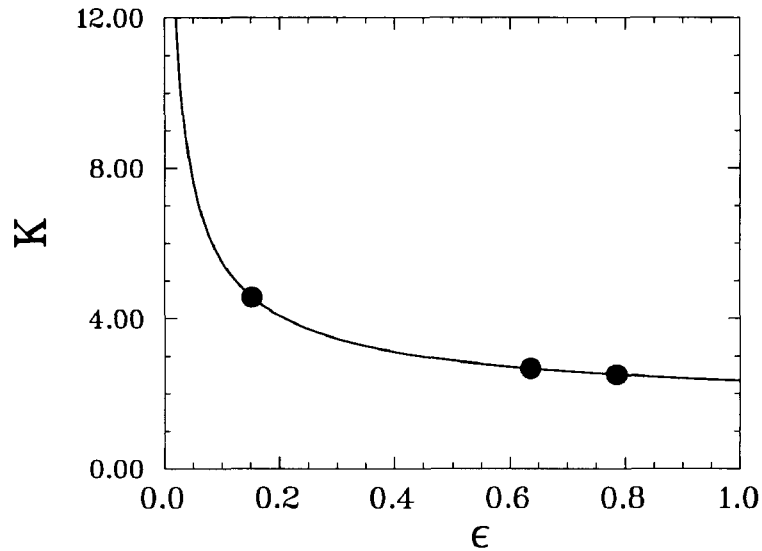


Figure 6.6: Kinematic factor K versus ϵ . The dots represent the three ϵ values of interest during the experiment.

average χ_ϕ over the full acceptance (≈ 0) we obtain:

$$\frac{P_t}{P_\ell} \approx -\chi_\phi - \sin \chi_\theta \frac{P_t^{FPP}}{P_\ell^{FPP}} \quad (6.14)$$

The uncertainty due to the non dispersive precession angle is directly proportional to $\chi_\phi = \gamma\kappa\phi_{bend}$ whereas the contribution of χ_θ enters as $\sin \chi_\theta$. Therefore R will be less sensitive to variation in the dispersive bend angle than to the non dispersive one. The uncertainty in R due to the non dispersive bend angle depends upon the kinematics through the kinematic factor $K = \sqrt{\tau(1+\epsilon)}/2\epsilon$ in front of the ratio of the polarization components:

$$\Delta R_{\phi_{bend}} \approx \gamma\kappa K \phi_{bend} \quad (6.15)$$

The uncertainty due to ϕ_{bend} will follow the evolution of K with respect to ϵ . From Figure 6.6 we expect the uncertainty to be almost twice as large at small ϵ as at the largest ϵ considered in the experiment. A misalignment in the quadrupoles with respect to the central axis results in an uncertainty in ϕ_{bend} . A dedicated study, aiming at quantifying the possible quadrupole offsets in

θ_{bend} (mrad)	ϕ_{bend} (mrad)	E_{beam} (%)	δ (%)	φ_{FPP} (mrad/sin ϑ_{FPP})
2	0.5	0.5	0.3	0.14

Table 6.9: Offsets applied in θ_{bend} , ϕ_{bend} , E_{beam} , δ and φ_{FPP} in the determination of the systematic uncertainties.

	$\epsilon = 0.152$	$\epsilon = 0.635$	$\epsilon = 0.785$
$\Delta\theta_{bend}$	0.0018	0.0018	0.0019
$\Delta\phi_{bend}$	0.0102	0.0061	0.0058
ΔE_{beam}	0.0015	0.0001	5.8×10^{-5}
$\Delta\delta$	0.0036	4.4×10^{-5}	0.0002
$\Delta\varphi_{FPP}$	0.0039	0.0025	0.0024
False Asymmetry (F.A.)	0.0062	0.0062	0.0058
TOTAL	0.0133	0.0092	0.0088

Table 6.10: Absolute systematic uncertainties in R

term of the non-dispersive bend angle, was carried out. Extensive details can be found in [59]. An uncertainty of 0.5 mrad in ϕ_{bend} and 2 mrad in θ_{bend} were found. Table 6.9 summarizes the shifts in the different quantities applied to determine the systematic uncertainties in R and P_ℓ/P_ℓ^{Born} . The same shift in E_{beam} and δ were applied in P_ℓ^{Born} for additional systematic uncertainties. Unlike the ratio R , the determination of P_ℓ/P_ℓ^{Born} is sensitive to the beam polarization. Relative uncertainty of 1% (or 0.5% point to point) in the beam polarization from the Möller measurements was taken into account. This uncertainty is by far the most dominant contribution in the systematic uncertainty budget of P_ℓ/P_ℓ^{Born} . Table 6.10 shows the systematic uncertainties in R obtained from the different sources described above for the three ϵ points. The systematic uncertainty budget is dominated by the contribution of the non-dispersive bend angle ϕ_{bend} as expected; but also by the false asymmetry correction. The effect of the kinematic factor K is noticeable at small ϵ , it magnifies the systematic uncertainty coming from an error on the non-dispersive bend angle by almost a factor two relative to the highest ϵ point. This kinematic factor is also the cause of the strong difference in the uncertainty coming from an error in δ for the different ϵ . Table 6.11 summarizes the systematic uncertainties in P_ℓ/P_ℓ^{Born} . Additional uncertainties on P_ℓ^{Born} resulting from errors in the beam energy and δ were included. We see that the systematics are dominated by the uncertainties on the beam polarization; the uncertainties from the other sources are negligible.

	$\epsilon = 0.635$	$\epsilon = 785$
$\Delta\theta_{bend}$	0.0020	0.0016
$\Delta\phi_{bend}$	0.0004	0.0003
$\Delta\delta$	3.9×10^{-5}	0.0003
$\Delta\varphi_{FPP}$	0.0002	0.0002
False Asymmetry	0.0007	0.0005
ΔE_{beam} from P_ℓ^{Born}	0.0008	0.0007
$\Delta\delta$ from P_ℓ^{Born}	0.0003	0.0003
Möller	0.01	0.01
TOTAL	0.0104	0.0104

Table 6.11: Absolute systematic uncertainties in P_ℓ/P_ℓ^{Born}

The point-to-point (p.t.p.) systematic uncertainties were estimated by summing in quadrature the differences between each systematic contribution from two considered kinematics. For example, the p.t.p. systematic uncertainties between the kinematic $\epsilon = 0.785$ and $\epsilon = 0.152$ will be:

$$\Delta R_{p.t.p.} \equiv \sqrt{\sum_i (\Delta R_i^{\epsilon=0.785} - \Delta R_i^{\epsilon=0.152})^2} \quad (6.16)$$

where i stands for the source of systematic uncertainty: $i = \theta_{bend}, \phi_{bend}, E_{beam}, \delta, \varphi_{FPP}$ and *F.A.*. Table 6.12 gives the p.t.p. systematics for R relative to the highest $\epsilon = 0.785$ point.

	$\epsilon = 0.152$	$\epsilon = 0.635$	$\epsilon = 0.785$
$\Delta R_{p.t.p.}$	0.0060	0.0006	0.0000

Table 6.12: Point-to-point (p.t.p.) systematic uncertainties for R relative to the highest $\epsilon = 0.785$ point.

The same procedure is repeated for P_ℓ/P_ℓ^{Born} . The relative systematic uncertainty coming from the beam polarization measurement is 0.5%. As we can see in Table 6.13, they largely dominate the p.t.p. systematic uncertainty given, this time, relative to the smallest $\epsilon = 0.152$ point.

	$\epsilon = 0.635$	$\epsilon = 0.785$
$\Delta P_\ell/P_\ell^{Born}_{p.t.p.}$	0.0051	0.0052

Table 6.13: Point-to-point (p.t.p.) systematic uncertainties for P_ℓ/P_ℓ^{Born} relative to the smallest $\epsilon = 0.152$ point.

We checked the quality of the spin precession calculation by looking at the dependence of R or $A_y P_\ell$ upon the reconstructed target variables and δ . Figures 6.7, 6.8 and 6.9 show that R and $A_y P_\ell$ are independent of the reconstructed target variables and δ . The results obtained with the simplistic dipole model and the COSY model are shown in open triangles and filled circles respectively. In each panel, the data are integrated and displayed over the full acceptance of the other three variables of the considered kinematic. The significant non-physical dependence of R upon ϕ_{tgt} in the dipole approximation is due to the absence of quadrupole effect corrections (which affect mainly P_t), since in the non-dispersive plane, the precession mixes P_t and P_ℓ . In the dispersive plane, the quadrupoles do not affect P_t significantly and their effects on P_ℓ compensate each other for trajectories with symmetric ϕ_{tgt} , which explains the weak dependence of R and P_ℓ upon θ_{tgt} even in the dipole approximation. The similar dependence upon δ reflects the correlation between momentum and scattering angle in two-body kinematics. A χ^2 of at most 2 attests of the excellent quality of these high statistics data and demonstrates a very good understanding of the spin precession calculation through the HMS magnets.

6.9 Summary and Discussion of the Results

The final results for R and P_ℓ / P_ℓ^{Born} are summarized in Table 6.14 together with the range of ϵ resulting from the focal plane cut, the statistical uncertainties (stat.), the total systematic uncertainty (tot.) and the point-to-point (p.t.p.) uncertainties relative to the highest ϵ point for R and to the lowest ϵ point for P_ℓ / P_ℓ^{Born} . The results of both parts of the highest ϵ point are averaged.

ϵ	$R \pm stat. \pm p.t.p.$	tot.	$P_\ell / P_\ell^{Born} \pm stat. \pm p.t.p.$				tot.
$0.152 \pm_{0.030}^{0.025}$	$0.695 \pm 0.009 \pm 0.006$	0.013	—	—	—	—	—
$0.635 \pm_{0.017}^{0.013}$	$0.688 \pm 0.011 \pm 0.001$	0.009	1.007	± 0.005	± 0.005	0.010	
$0.785 \pm_{0.010}^{0.008}$	$0.692 \pm 0.011 \pm 0.000$	0.009	1.023	± 0.006	± 0.005	0.011	

Table 6.14: Kinematic table with the average kinematical parameter ϵ . Both the ratio R and longitudinal polarization P_ℓ divided by Born approximation P_ℓ^{Born} are given with statistical (stat.), total systematic (tot.) and point-to-point (p.t.p.) uncertainties relative to the highest ϵ point for R and to the lowest ϵ point for P_ℓ / P_ℓ^{Born} .

Figure 6.10 shows the results for R as a function of ϵ together with all available theoretical

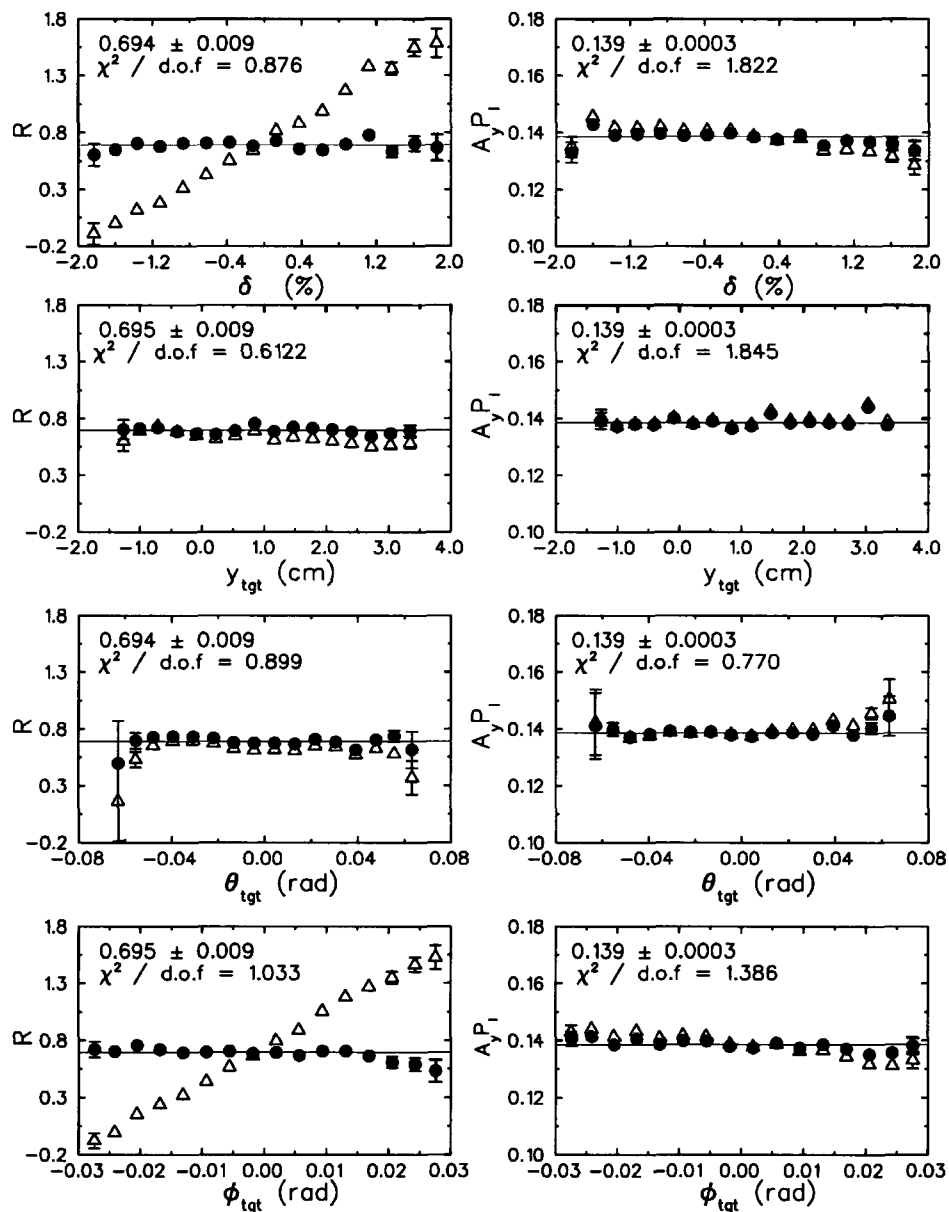


Figure 6.7: R (left column) and $A_y P_l$ (right column) versus δ , y_{tgt} and the dispersive (vertical) θ_{tgt} , non-dispersive (horizontal) ϕ_{tgt} angles for $\epsilon = 0.152$ using the COSY model (filled circles) and the dipole model (open triangles).

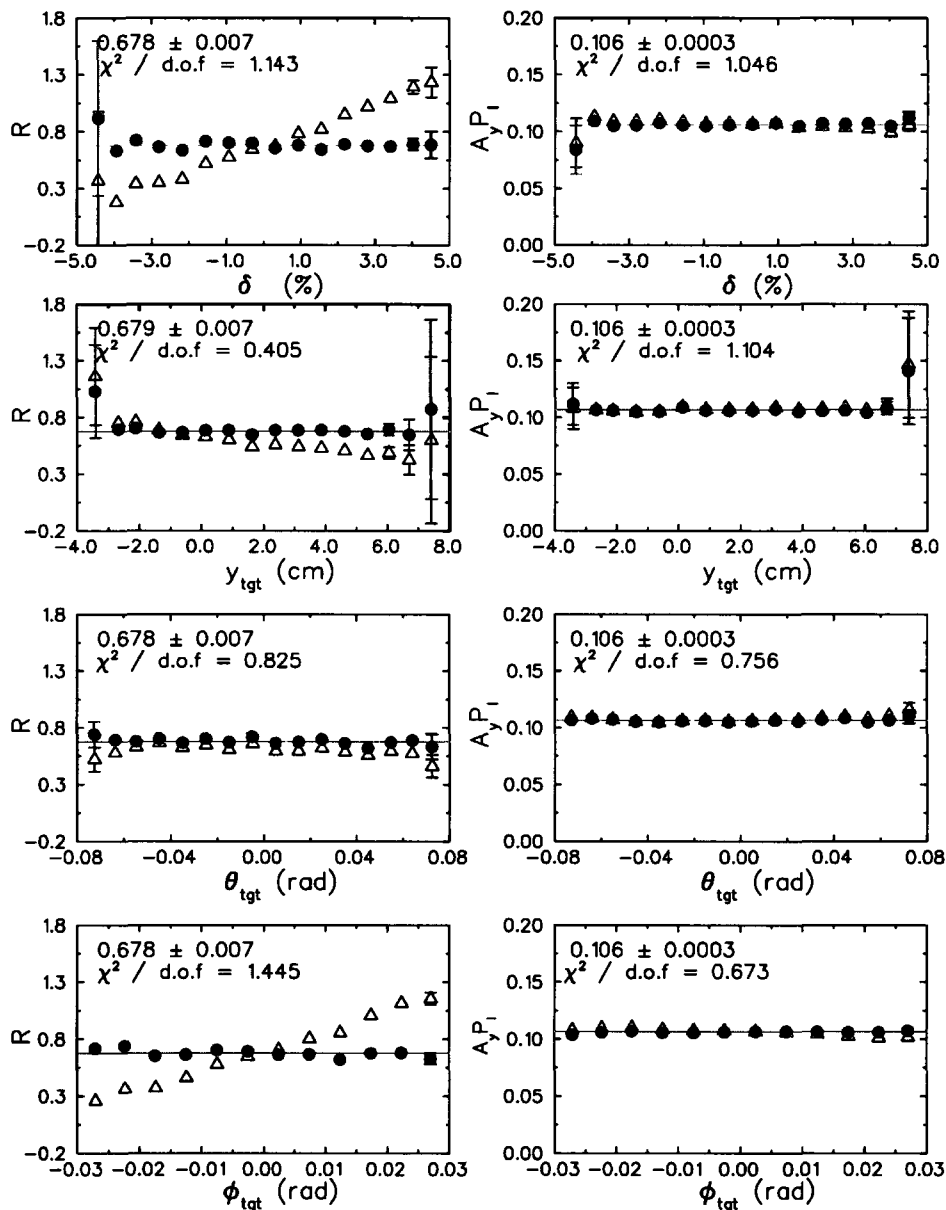


Figure 6.8: R (left column) and $A_y P_l$ (right column) versus δ , y_{tgt} and the dispersive (vertical) θ_{tgt} , non-dispersive (horizontal) ϕ_{tgt} angles for $\epsilon = 0.635$ using the COSY model (filled circles) and the dipole model (open triangles).

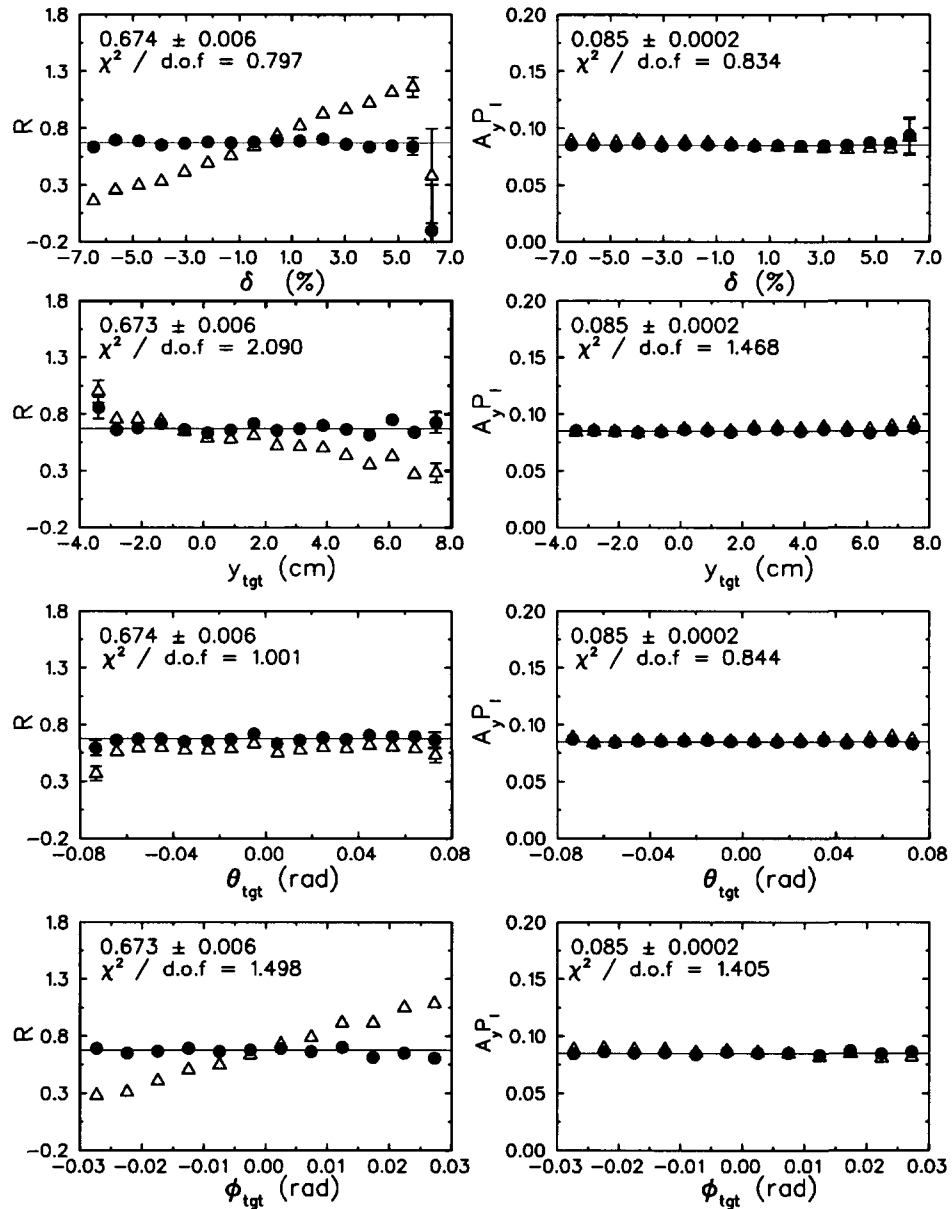


Figure 6.9: R (left column) and $A_y P_l$ (right column) versus δ , y_{tgt} and the dispersive (vertical) θ_{tgt} , non-dispersive (horizontal) ϕ_{tgt} angles for $\epsilon = 0.785$ using the COSY model (filled circles) and the dipole model (open triangles).

estimates. The data of this experiment are represented by the filled circles and the open triangle shows the result obtained from the GEPI experiment [8]. The point-to-point uncertainties are represented by a black band at the bottom of the figure. The solid horizontal line represents the linear fit to the data:

$$R = 0.6920 \pm 0.0058 \quad (6.17)$$

Allowing a linear variation in ϵ of the form $a\epsilon + b$ gives $a = 0.696 \pm 0.012$ and $b = -0.008 \pm 0.021$ which gives statistically compatible results with the constant fit since the error on the slope is at the same level as its value. The total systematic uncertainty imposes an overall uncertainty of the order of 0.01 in our knowledge of the constant value. Another way to describe the systematic uncertainties is to consider the correlated systematic uncertainties obtained by subtracting the point-to-point from the total systematics. Due to the small point-to-point uncertainties, the correlated uncertainties are found to be close to the total systematics. Thus if the point at $\epsilon = 0.785$ moves up by 0.009 the points at $\epsilon = 0.152$ and $\epsilon = 0.635$ will move up by their respective correlated uncertainties. Our confidence in the fit function is also reinforced by the small point-to-point uncertainties, which tell us that the relative variation between the two extreme ϵ points is at most 0.006. We conclude that the data do not show any evidence of an ϵ -dependence of R at $Q^2=2.5$ GeV².

As described in Chapter 2, the theoretical estimates make widely varying predictions for the ϵ -dependence of R . It is appropriate here to recall the main characteristics and predictions of these different models. The hadronic model of Blunden *et al.* [30], where a number of the proton intermediate states are taken into account via a complete calculation of the loop integral using 4-point Passarino-Veltman functions [32], shows a significant positive TPEX contribution at small ϵ . Kondratyuk *et al.* [35] showed that the inclusion of higher resonances, such as the Δ , makes almost no difference. In contrast, the partonic model of Afanasev *et al.* [23], where the TPEX takes place in a hard scattering of the electron by a quark which is "embedded" in the nucleon through the GPDs, predicts a significant negative TPEX contribution. The pQCD calculation of Kivel and Vanderhaeghen [43], which uses two different light front proton distribution amplitude parametrizations, one from Chernyak *et al.* (COZ) [37] and the other one from Braun *et al.* (BLW)

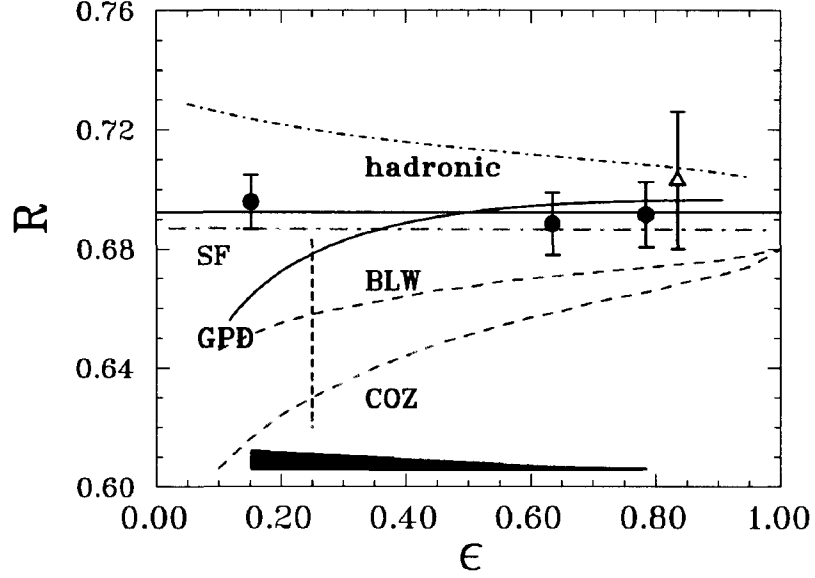


Figure 6.10: R as a function of ϵ with statistical uncertainties, filled circles from this experiment and open triangle from [8]. The point-to-point systematic uncertainties, shown with a band at the bottom of the panel, are relative to the largest ϵ kinematic.

[44], presents a behaviour similar to the partonic model. The lower ϵ limit of applicability of the GPD and pQCD models is shown by the vertical dotted line in Figure 6.10. The electron structure function (SF) based model developed by Bystritskiy *et al.* [46], which takes into account all high-order radiative corrections in the leading logarithm approximation, does not predict any measurable ϵ -dependence of R . While in good agreement with the other available data, the GPD, hadronic and pQCD models predict a deviation of R at small ϵ which is not seen in the results presented here. Referring to Equation (1.101), R is directly proportional to the Born value $R_{Born} = G_E/G_M$, so all the theory predictions which use a G_E/G_M value from [7, 8, 9], can be renormalized by an overall multiplicative factor.

Figure 6.11 shows the results for P_ℓ/P_ℓ^{Born} as a function of ϵ together with its estimates from the hadronic and GPD models. The data show an enhancement of $2.3\% \pm 0.6\%$ at large ϵ which is not predicted by these models.

To ensure that this effect is not biased from the analyzing power determination, we applied a series of cuts on the two variables that A_y depends upon: the proton momentum p and the

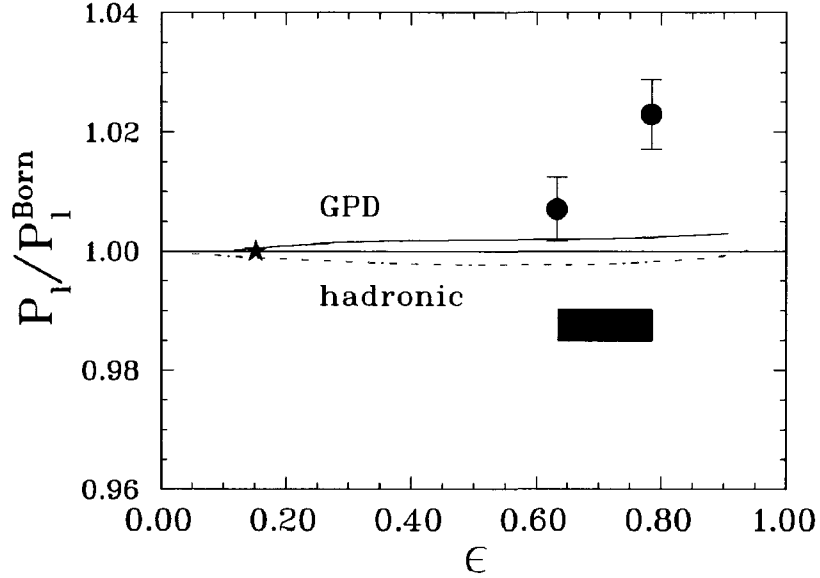


Figure 6.11: $P_\ell / P_\ell^{\text{Born}}$ as a function of ϵ with statistical uncertainties. The point-to-point systematic uncertainties, shown with a band at the bottom of the panel, are relative to the smallest ϵ kinematic. The star indicates the ϵ value at which the analyzing power is determined.

scattering angle ϑ_{FPP} . Figure 6.12 shows the ratio between the ϑ_{FPP} distributions of the different kinematics. The ratio is constant for most of the accepted ϑ_{FPP} range but differences exist at small and large angles between the smallest and the other two ϵ points. We applied a cut (represented by the vertical lines in the figure) to reject events with $\vartheta_{FPP} \leq 6^\circ$ and $\vartheta_{FPP} \geq 33^\circ$. Additional cuts are defined on the $\delta = (p - p_0)/p_0$ distributions: the first to select the common width of the δ acceptance: $-1.3\% \leq \delta \leq 1.3\%$ and the second, more drastic, to reject events with $|\delta| > 1\%$. They are represented by solid and dashed lines respectively in the Figure 6.13. More severe cuts are not possible because they would induce drastic statistical losses. Figure 6.14 displays the results obtained with different combinations of the cuts described above. The points obtained with the cuts are intentionally shifted in ϵ with respect to the nominal point for the benefit of clarity. All results for a particular kinematic are very similar. In particular, depending on the kinematic, the cuts have different effects. While the cuts ($-1.3\% \leq \delta \leq 1.3\%$) and ($-1.3\% \leq \delta \leq 1.3\%$, $6^\circ \leq \vartheta_{FPP} \leq 33^\circ$) decrease the values of $P_\ell / P_\ell^{\text{Born}}$ at $\epsilon = 0.785$, they increase it at $\epsilon = 0.635$. The most drastic combination of cuts represented by hollow circles in Figure 6.14 tends to decrease the

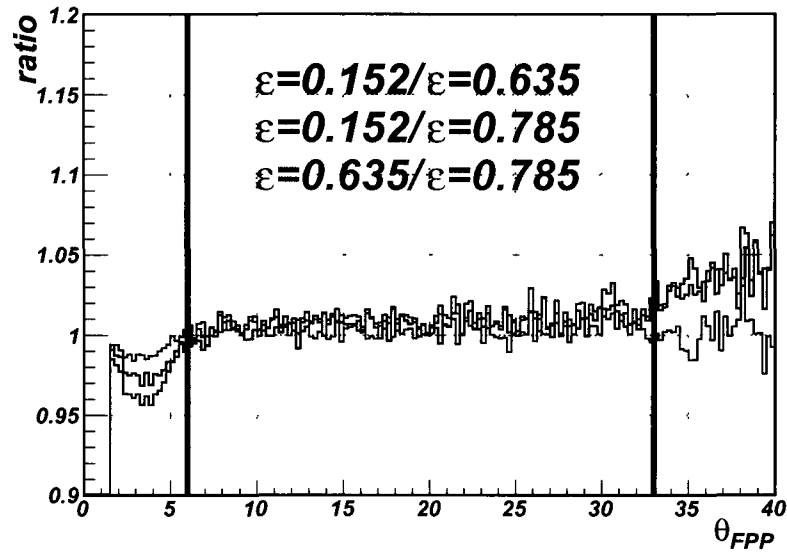


Figure 6.12: Ratio of the ϑ_{FPP} distributions between the different kinematics. The vertical lines represent the cut. Events between the lines are kept.

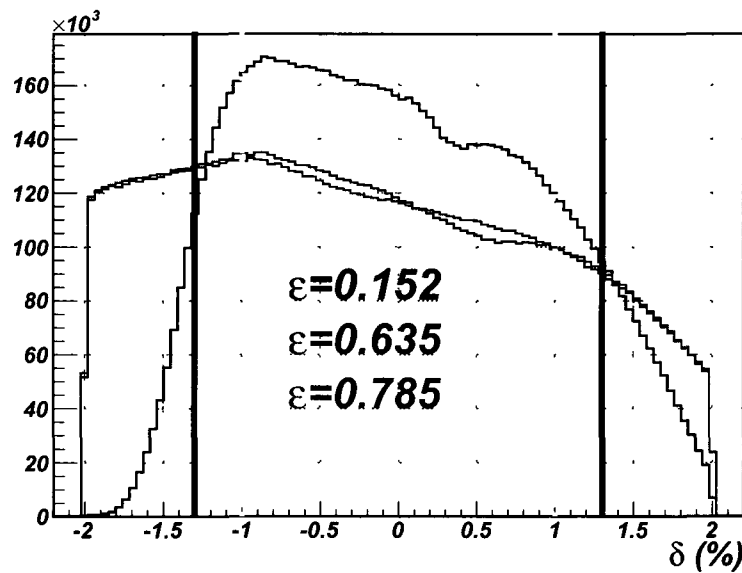


Figure 6.13: δ distribution of the three kinematics. The vertical solid and dashed lines represent the two sets of cuts. Events between the two sets of lines are kept.

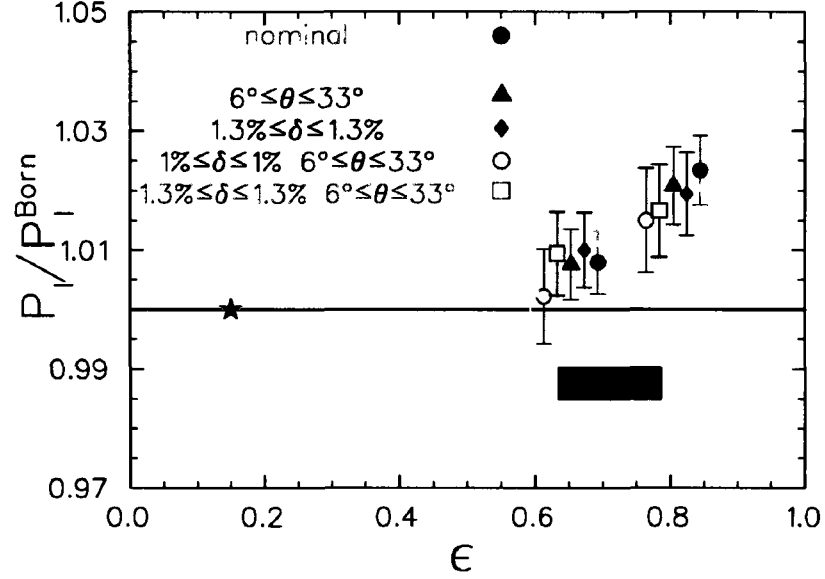


Figure 6.14: Results of P_ℓ/P_ℓ^{Born} obtained with various combinations of cuts in θ_{FPP} and δ . The points are intentionally shifted in ϵ with respect to the nominal value for the benefit of clarity.

ratio resulting in an enhancement of $1.5\% \pm 1\%$ but still remains statistically compatible with the nominal case shown with filled circles. The different sets of cuts result in an important increase of statistical uncertainty which masks any actual variation of the ratio P_ℓ/P_ℓ^{Born} .

6.10 Empirical Determination of the TPEX amplitudes.

This section presents the results of the analysis from [63] aimed at determining the TPEX amplitudes Y_M , Y_E and Y_3 defined in Chapter 1 from the published results presented in this thesis [64] and from the Jlab Hall A cross section measurements [6].

To extract the 3 TPEX amplitudes, the knowledge of G_E/G_M and G_M is needed. The problem is under-determined since we only extract separately three observables: R and P_ℓ/P_ℓ^{Born} from the polarization measurements and $\sigma_r/(\mu_p G_D)^2$ from the cross section measurements and we need to determine five unknowns: G_E/G_M , G_M and the three TPEX amplitudes. We make then two assumptions. In the first, since no evidence of an ϵ -dependence was found so far in R , we take the fitted value of R obtained in the experiment to fix G_E/G_M . In the second, the TPEX correction

to the reduced cross section vanish in the Regge limit ($\epsilon = 1$). The result of the linear fit to the reduced cross section $\sigma_r/(\mu_p G_D)^2$ allows the determination of G_M . The P_ℓ/P_ℓ^{Born} data were fitted with two different functional forms (driven by a perturbative QCD calculation). Figure 6.15 shows the ϵ -evolution of the three TPEX amplitudes Y_M , Y_E and Y_3 defined in Chapter 1. The two colours represent the results for the two functional forms. In Chapter 1 we showed

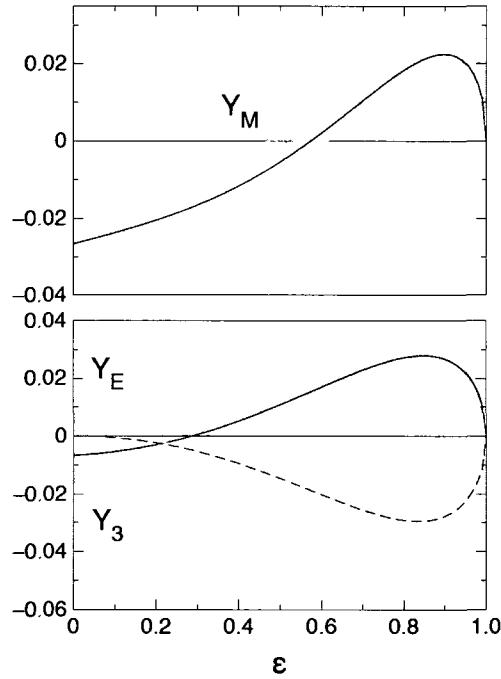


Figure 6.15: TPEX amplitudes as a function of ϵ for the two fits of P_ℓ , with their 1σ statistical error bands. Fit 1 : grey bands; Fit 2 : red bands. The horizontal bands at the bottom of the plots indicate the systematic errors.

that the TPEX correction to the reduced cross section behave like $\sigma_r^{2\gamma} \approx Y_M + \epsilon Y_3$. The linearity of the cross section imposes that Y_M is linear for most of the ϵ -range $[0,1]$. At large ϵ , Y_M has to become non-linear in order that $Y_M + \epsilon Y_3$ remains linear. The Y_M is the best constrained of the TPEX amplitudes and is not sensitive to the functionals used to fit P_ℓ/P_ℓ^{Born} since the two sets of error bands overlap. The TPEX corrections to R being proportional to $Y_E + Y_3$, the ϵ -independence of R implies that Y_E and Y_3 compensate each other. P_ℓ/P_ℓ^{Born} entirely defines Y_3 since its TPEX correction is dominated by Y_3 . The two fits to P_ℓ/P_ℓ^{Born} gives similar results at

large ϵ where the data exist but have different behaviours at small ϵ . These results are the best of what we can possibly achieve with the presently available cross section and polarization data in the determination of the TPEX amplitudes. A better accuracy in the polarization measurements is needed to improve the determination of the Y_E and Y_3 amplitudes.

Epilogue

This thesis presents the results of the E04-019 (GEp2 γ) experiment carried out at Jefferson Lab in Hall C. The experiment was a search for effects beyond the Born Approximation in elastic $\bar{e}p$ scattering at a fixed momentum transfer $Q^2 = 2.5 \text{ GeV}^2$ spanning a wide range of ϵ . The ratio $R = -\mu_p \sqrt{(1+\epsilon)\tau/2\epsilon} P_t/P_\ell$ and the longitudinal polarization component P_ℓ were measured separately with statistical and systematic uncertainties of $\Delta R \approx \pm 0.01(\text{stat}) \pm 0.013(\text{syst})$ and $\Delta P_\ell/P_\ell^{\text{Born}} \approx \pm 0.006(\text{stat}) \pm 0.01(\text{syst})$

A longitudinally polarized electron beam was scattered elastically off a 20 cm liquid hydrogen target. A new electromagnetic calorimeter BigCal was used to detect the electrons while a new focal plane polarimeter (FPP) detected the coincidence protons. The polarization of the recoil proton was determined from the azimuthal asymmetry in the difference of the angular distributions for the two states of the beam helicity. Careful checks were made to ensure that the spin precession calculation through the HMS magnets, which represents the main source of systematic uncertainties, was understood and performed correctly.

While most of the theoretical models predict a deviation of R at small ϵ and are in good agreement with the available cross section data, no evidence of an ϵ -dependence was found in R at the 1.5% level. $P_\ell/P_\ell^{\text{Born}}$ shows an enhancement at large ϵ of $2.3 \pm 0.6\%$ not predicted by any models. The data presented in this thesis put more experimental constraints on the TPEX process and allow for the first time an empirical determination of the real part of the TPEX amplitudes.

The study of the ϵ dependence of the polarization observables is not the only possible test to put in evidence a possible TPEX effect. A direct signature of this effect can be accessed from the ratio $R_{e^+e^-} \equiv \sigma_{e^+}/\sigma_{e^-}$ of the e^\pm cross sections. Indeed one can expand the reduced cross section

in powers of the fine structure constant α :

$$\sigma_{e^-p, e^+p} = \alpha^2 M_{1\gamma}^2 \mp \alpha^3 M_{1\gamma} \Re(M_{2\gamma}) + \dots \quad (6.18)$$

where $M_{1\gamma}$ is the one-photon amplitude and $\Re(M_{2\gamma})$ is the real part of the two-photon amplitude. The interference term between the Born and two-photon terms is T-odd. It changes sign when one replaces electrons with positron. The ratio $R_{e^+e^-}$ becomes [65]:

$$R_{e^+e^-} \approx 1 + 4 \frac{\Re(M_{2\gamma})}{M_{1\gamma}} \quad (6.19)$$

Most of the theoretical models presented in Chapter 2 [30, 23, 36, 43] predict a deviation of few percents of this ratio from unity. There are several experiments aiming at measuring $R_{e^+e^-}$. One has already been carried out in Novossibirsk, Russia at VEPP-3 [66] and the analysis is underway; another one at Jlab Hall-B [67] was recently completed (March 2011), and a third one, OLYMPUS at DESY, Germany [68], is expected to run in 2012. Another test of the TPEX is to look at the beam (target) single spin asymmetry accessible with a polarized (unpolarized) electron beam scattering off an unpolarized (polarized) target. The polarization of either the beam or the target is normal to the scattering plane. This type of measurement studies the imaginary (absorptive) part of the TPEX amplitudes. Several experiments [69, 70, 71, 72] measured the transverse spin beam asymmetry up to an electron beam energy of 3 GeV. A recent Jlab Hall A experiment, E-05-015 [73], carried out in 2009 will provide additional data on the single spin target asymmetries. Finally, the linearity of the reduced cross section is still an open question. In this regards, the E05-017 experiment at Jlab Hall C [74], which measured the reduced cross section over a wide range of Q^2 and ϵ , will give important results about a possible non linearity of the Rosenbluth plot.

This shows the intensive experimental efforts that have been deployed to understand the TPEX. Only a combination of the results presented in this thesis and the forthcoming experiments will provide the information required to fully understand, quantify and characterize the TPEX mechanism in electron-proton scattering.

Appendix A

Dirac Matrices, Dirac Equation and Trace Identities

A.1 Dirac Formalism

Dirac matrices are defined by the anti-commutation relation:

$$\{\gamma^\mu, \gamma^\nu\} = \gamma^\mu \gamma^\nu + \gamma^\nu \gamma^\mu = 2\eta^{\mu\nu} = \begin{pmatrix} 1 & 0 & 0 & 0 \\ 0 & -1 & 0 & 0 \\ 0 & 0 & -1 & 0 \\ 0 & 0 & 0 & -1 \end{pmatrix} \quad (\text{A.1})$$

where $\eta^{\mu\nu}$ is the metric tensor.

In the general case, there exists an infinity of solutions to the above relation. Considering the 4×4 matrices, the ensemble of solutions defines a Clifford algebra, noted $Cl_{1,3}\mathbb{C}$, where the 4 Dirac matrices form a basis. The choice of the basis implies a different representation of the Dirac

matrices. We will consider the so-called standard Dirac representation:

$$\gamma^\mu = (\gamma^0, \vec{\gamma}) \quad (\text{A.2})$$

$$\gamma^0 = \gamma_0 = \begin{pmatrix} \mathbb{I}_2 & 0 \\ 0 & -\mathbb{I}_2 \end{pmatrix} \quad (\text{A.3})$$

$$\vec{\gamma} = \begin{pmatrix} 0 & \vec{\sigma} \\ -\vec{\sigma} & 0 \end{pmatrix} \quad (\text{A.4})$$

$$\gamma^5 \equiv i\gamma^0\gamma^1\gamma^2\gamma^3 = \gamma_5 = \begin{pmatrix} 0 & \mathbb{I}_2 \\ \mathbb{I}_2 & 0 \end{pmatrix} \quad (\text{A.5})$$

with the 2×2 unit matrix \mathbb{I}_2 and the 3 Pauli spin matrices $\vec{\sigma} = (\sigma_x, \sigma_y, \sigma_z)$ defined as:

$$\sigma_x = \begin{pmatrix} 0 & 1 \\ 1 & 0 \end{pmatrix}, \quad \sigma_y = \begin{pmatrix} 0 & -i \\ i & 0 \end{pmatrix}, \quad \sigma_z = \begin{pmatrix} 1 & 0 \\ 0 & -1 \end{pmatrix} \quad (\text{A.6})$$

The matrix γ^5 , given by a combination of Dirac matrices, obeys the anti-commutation relation:

$$\{\gamma^5, \gamma^\mu\} = 0 \quad (\text{A.7})$$

The Dirac representation is obtained from the Weyl representation, which is found when one derives the Dirac equation from the irreducible representation of the Lorentz group, by the transformation:

$$\gamma_D^\mu = U\gamma_W^\mu U^\dagger \quad (\text{A.8})$$

where D, W stand for the Dirac and Weyl representation respectively and the unitary operator U is

$$U = \frac{1}{\sqrt{2}} \begin{pmatrix} 1 & 1 \\ -1 & 1 \end{pmatrix} \quad (\text{A.9})$$

The gamma matrices satisfy the commutation relation:

$$\sigma^{\mu\nu} = \frac{i}{2}[\gamma^\mu, \gamma^\nu] = \frac{i}{2}(\gamma^\mu\gamma^\nu - \gamma^\nu\gamma^\mu) \quad (\text{A.10})$$

Finally, the Pauli matrices obey the commutation and anti-commutation relations:

$$[\sigma^i, \sigma^j] = 2i\epsilon_{ijk}\sigma_k \quad (\text{A.11})$$

$$\{\sigma^i, \sigma^j\} = 2\delta_{ij} \quad (\text{A.12})$$

where ϵ_{ijk} is the Levi-Civita tensor:

$$\epsilon_{ijk} = \begin{cases} +1 & \text{if } ijk \text{ is an even permutation of } 123 \\ -1 & \text{if } ijk \text{ is an odd permutations of } 123 \\ 0 & \text{otherwise} \end{cases} \quad (\text{A.13})$$

A.2 Dirac Equation

The Dirac equation for a free spin 1/2 particle with positive energy is:

$$(\gamma^\mu p_\mu - m)u(p, s) = (\not{p} - m)u(p, s) = (\gamma \cdot p - m)u(p, s) = 0 \quad (\text{A.14})$$

The solutions of this equation are:

$$u(p, s) = \sqrt{E + M} \begin{pmatrix} \xi_s \\ \frac{\vec{\sigma} \cdot \vec{p}}{E + M} \xi_s \end{pmatrix} \quad (\text{A.15})$$

and its adjoint by: $\bar{u}(p, s) \equiv u^\dagger(p, s)\gamma^0$

The Dirac spinors obey the normalization condition:

$$\sum_{\alpha} \bar{u}_{\alpha}(p, s_1) u_{\alpha}(p, s_2) = \bar{u}(p, s_1) u(p, s_2) = 2m \delta_{s_1 s_2} \quad (\text{A.16})$$

$$\sum_{\alpha} u_{\alpha}^{\dagger}(p, s_1) u_{\alpha}(p, s_2) = u^{\dagger}(p, s_1) u(p, s_2) = 2E \delta_{s_1 s_2} \quad (\text{A.17})$$

$$(\text{A.18})$$

The unpolarized spin sum is given by:

$$\sum_s \bar{u}(p, s) u(p, s) = \not{p} - m \quad (\text{A.19})$$

In the polarized case, the spin sum of the Dirac spinors becomes:

$$\sum_s \bar{u}(p, s) u(p, s) = (\not{p} - m) \left(\frac{1 - \gamma_5}{2} \right) \quad (\text{A.20})$$

It is important to point out that in the above expressions the Dirac indices are tacit. For example an explicit form of the unpolarized spin sum is:

$$\sum_s (\bar{u}(p, s))_{\alpha} (u(p, s))_{\beta} = (\not{p})_{\alpha\beta} - m (\mathbb{I}_4)_{\alpha\beta} \quad (\text{A.21})$$

with \mathbb{I}_4 the 4×4 unit matrix.

A.3 Useful Trace theorems

$$\begin{aligned}
 \text{Tr}[\gamma^\mu] = \text{Tr}[\gamma^5] &= 0 \\
 \text{Tr}[\mathbb{I}_4] &= 4 \\
 \text{Tr}[a \cdot b] &= 4a \cdot b \\
 \text{Tr}[\gamma_5 a \cdot b \cdot c \cdot d] &= 4i\epsilon_{\alpha\beta\rho\sigma}a^\alpha b^\beta c^\rho d^\sigma \\
 \text{Tr}[\gamma^\mu\gamma^\nu\gamma^\rho\gamma^\sigma] &= 4(g^{\mu\nu}g^{\rho\sigma} - g^{\mu\rho}g^{\nu\sigma} + g^{\mu\sigma}g^{\nu\rho})
 \end{aligned} \tag{A.22}$$

The trace of any odd number of gamma matrices is equal to zero.

This list of theorems is far from being exhaustive but only shows the identities used to carry out the calculations of the polarization components in Chapter 1 and the unpolarized cross section in the next Appendix section.

Appendix B

Unpolarized cross section calculation using the trace technique

B.1 General definitions

The general expression of the unpolarized cross section for two-body scattering is:

$$d\sigma = \frac{d^3k'}{(2\pi)^3 2k'^0} \frac{d^3p'}{(2\pi)^3 2p'^0} \frac{(2\pi)^4}{4k \cdot p} \delta^{(4)}(k + p - k' - p') |\bar{T}|^2 \quad (\text{B.1})$$

We consider elastic electron-proton scattering:

$$e(k, h) + p(p, \lambda_p) \rightarrow e(k', h') + p(p', \lambda'_p) \quad (\text{B.2})$$

where h, h', λ_p and λ'_p are the helicities and adopt the definitions:

$$q = k - k' = p' - p, \quad q^2 = -Q^2, \quad P = \frac{p + p'}{2}, \quad K = \frac{k + k'}{2} \quad (\text{B.3})$$

and define the Mandelstam variables:

$$s = (p + k)^2, \quad t = q^2 = -Q^2 = (k - k')^2, \quad u = (p - k')^2 = (k - p')^2 \quad (\text{B.4})$$

A possible T -matrix expansion is:

$$T = \frac{e^2}{Q^2} \bar{u}(k', h) \gamma_\mu u(k, h) \times \bar{u}(p', \lambda'_N) \left(\tilde{G}_M \gamma^\mu - \tilde{F}_2 \frac{P^\mu}{M} + \tilde{F}_3 \frac{\gamma \cdot KP^\mu}{M^2} \right) u(p, \lambda_N) \quad (\text{B.5})$$

We can also write the T-matrix as:

$$\bar{T}^2 = \frac{e^4}{Q^4} L_{\mu\nu} W^{\mu\nu} \quad (\text{B.6})$$

The leptonic (for a massless electron) and hadronic tensors, $L_{\mu\nu}$ and $W_{\mu\nu}$ are defined respectively by:

$$\begin{aligned} L_{\mu\nu} &= \frac{1}{2} \sum_{h, h'} \bar{u}(k', h') \gamma_\mu u(k, h) \bar{u}(k, h) \gamma_\nu u(k', h') \\ &= \frac{1}{2} \text{Tr}[\gamma_\mu (\not{k} + m_e) \gamma_\nu (\not{k}' + m_e)] \\ &\stackrel{m_e \rightarrow 0}{=} \frac{1}{2} \text{Tr}[\gamma_\mu \not{k} \gamma_\nu \not{k}'] \end{aligned} \quad (\text{B.7})$$

$$\begin{aligned} W^{\mu\nu} &= \frac{1}{2} \sum_{\lambda_N, \lambda'_N} \bar{u}(p', \lambda'_N) \Gamma^\mu u(p, \lambda_N) \bar{u}(p, \lambda_N) \Gamma^{*\nu} u(p', \lambda'_N) \\ &= \frac{1}{2} \text{Tr}[\Gamma_\mu (\not{p} + M) \Gamma_\nu (\not{p}' + M)] \end{aligned} \quad (\text{B.8})$$

with Γ^μ , the vertex function: $\Gamma^\mu = \tilde{G}_M \gamma^\mu - \tilde{F}_2 \frac{P^\mu}{M} + \tilde{F}_3 \frac{\gamma \cdot KP^\mu}{M^2}$

The factor $\frac{1}{2}$ in (B.7) and (B.8) comes from the average over the initial spin states.

B.2 Trace calculation

There is a total of 10 traces to calculate. One for the leptonic tensor and 9 for the hadronic tensor. The amplitude \tilde{F}_3 , which exists only at the 2γ level and beyond, is of order e^2 (relative to the factor e^2 in (B.5)). As a consequence we will neglect the term of order e^4 proportional to $|\tilde{F}_3|^2$. Using the identities in (A.22), the nine traces are then:

$$\text{Tr}[\gamma_\mu \not{k} \gamma_\nu \not{k}'] = 2(k_\mu k'_\nu + k_\nu k'_\mu - (k \cdot k') g_{\mu\nu}) \quad (\text{B.9})$$

$$\begin{aligned} \text{Tr}[\gamma^\mu (\not{p} + M) \gamma^\nu (\not{p}' + M)] &= \text{Tr}[\gamma^\mu \not{p} \gamma^\nu \not{p}'] + M^2 \text{Tr}[\gamma^\mu \gamma^\nu] \\ &= 4[p^\mu p'^\nu + p^\nu p'^\mu + (M^2 - p \cdot p') g^{\mu\nu}] \end{aligned} \quad (\text{B.10})$$

$$\begin{aligned} \text{Tr}[\gamma^\mu (\not{p} + M) (\not{p}' + M)] &= M \text{Tr}[\gamma^\mu \not{p} + \gamma^\mu \not{p}'] \\ &= 4M(p^\mu + p'^\mu) \end{aligned} \quad (\text{B.11})$$

$$\text{Tr}[(\not{p} + M) \gamma^\nu (\not{p}' + M)] = 4M(p^\nu + p'^\nu) \quad (\text{B.12})$$

$$\begin{aligned} \text{Tr}[(\not{p} + M) (\not{p}' + M)] &= \text{Tr}[\not{p} \not{p}' + M^2] \\ &= 4(M^2 + p \cdot p') \end{aligned} \quad (\text{B.13})$$

$$\begin{aligned} \text{Tr}[\gamma^\mu (\not{p} + M) (\not{k}' + \not{k}) (\not{p}' + M)] &= \text{Tr}[\gamma^\mu \not{p} (\not{k}' + \not{k}) \not{p}' + \gamma^\mu (\not{k}' + \not{k}) M] \\ &= \text{Tr}[\gamma^\mu \not{p} (\not{k}' + \not{k}) \not{p}'] + 4M^2(k^\mu + k'^\mu) \\ &= \text{Tr}[\gamma^\mu \gamma^\alpha p_\alpha \gamma^\beta k_\beta \gamma^\tau p'_\tau + \gamma^\mu \gamma^\alpha p_\alpha \gamma^\beta k'_\beta \gamma^\tau p'_\tau] + 8M^2 K^\mu \\ &= 4(p_\alpha k_\beta p'_\tau + p_\alpha k'_\beta p'_\tau) (g^{\mu\alpha} g^{\beta\tau} - g^{\mu\beta} g^{\alpha\tau} + g^{\mu\tau} g^{\alpha\beta}) \\ &\quad + 8M^2 K^\mu \end{aligned}$$

$$\begin{aligned}
&= 4[p^\mu(k \cdot p') - k^\mu(p \cdot p') + p'^\mu(k \cdot p)] + \text{same}(k \rightarrow k') \\
&\quad + 8M^2 K^\mu \\
&= 4[p^\mu(k \cdot p' + k' \cdot p') + p'^\mu(k \cdot p' + k' \cdot p) \\
&\quad - 2(M^2 - p \cdot p')K^\mu] \tag{B.14}
\end{aligned}$$

$$\begin{aligned}
\text{Tr}[(\not{K}' + \not{K})(\not{p} + M)\gamma^\nu(\not{p}' + M)] &= 4[p^\nu(k \cdot p' + k' \cdot p') + p'^\nu(k \cdot p' + k' \cdot p) \\
&\quad - 2(M^2 - p \cdot p')K^\nu] \tag{B.15}
\end{aligned}$$

$$\begin{aligned}
\text{Tr}[(\not{p} + M)(\not{K}' + \not{K})(\not{p}' + M)] &= \text{Tr}[\not{p}(\not{K}' + \not{K})M] + \text{Tr}[M(\not{K}' + \not{K})\not{p}'] \\
&= 4M(k' + k) \cdot (p + p') \\
&= 16MK \cdot P \tag{B.16}
\end{aligned}$$

$$\begin{aligned}
\text{Tr}[(\not{K}' + \not{K})(\not{p} + M)(\not{p}' + M)] &= 4M(k' + k) \cdot (p + p') \\
&= 16MK \cdot P \tag{B.17}
\end{aligned}$$

B.3 Kinematic identities

We define the 4-momenta of the incident electron (proton) and scattered electron (proton), respectively to be:

$$k^\mu = (k^0, \mathbf{k}) = (E_e, 0, 0, E_e) \tag{B.18}$$

$$p^\mu = (p^0, \mathbf{0}) = (M, 0, 0, 0) \tag{B.19}$$

$$k'^\mu = (k'^0, \mathbf{k}) = (E'_e, E'_e \sin \theta_e, 0, E'_e \cos \theta_e) \tag{B.20}$$

$$p'^\mu = (p'^0, \mathbf{p}') = (E_p, -p_p \sin \theta_p, 0, p_p \cos \theta_p) \tag{B.21}$$

Those equations show that the incident electron direction is along the z axis, and that the xz plane is the scattering plane. We are now ready to derive the dot products needed in the different trace

calculations and other useful identities:

$$k \cdot k' = \frac{Q^2}{2} \quad (\text{B.22})$$

$$p \cdot p' = \frac{Q^2}{2} + M^2 \quad (\text{B.23})$$

$$k \cdot p = k' \cdot p' = ME_e \quad (\text{B.24})$$

$$k' \cdot p = k \cdot p' = ME'_e = ME_e - \frac{Q^2}{2} + M^2 \quad (\text{B.25})$$

The Mandelstam variables become:

$$s = M^2 + 2k \cdot p = M^2 + 2k' \cdot p' = M^2 + 2ME_e \quad (\text{B.26})$$

$$t = (k - k')^2 = (p - p')^2 = -2k \cdot k' = 2(M^2 - p \cdot p') \quad (\text{B.27})$$

$$u = M^2 - 2k \cdot p' = M^2 - 2k' \cdot p \quad (\text{B.28})$$

Momentum and energy conservation give us:

$$\frac{\nu}{M^2} \equiv \frac{s - u}{4M^2} = \frac{E_e + E'_e}{2M} = K \cdot P \quad (\text{B.29})$$

$$Q^2 = 2E_e E'_e (1 - \cos \theta_e) = 4E_e E'_e \sin^2 \frac{\theta_e}{2} \quad (\text{B.30})$$

$$= 2(p \cdot p' - M^2) = 2M\nu \quad (\text{B.31})$$

$$E'_e = \frac{E_e}{1 + \frac{2E_e}{M} \sin^2 \frac{\theta_e}{2}} \quad (\text{B.32})$$

B.4 Leptonic-hadronic tensor contraction

We divide the hadronic tensor into 3 parts: $W^{\mu\nu} = W_{M2}^{\mu\nu} + W_{M3}^{\mu\nu} + W_{23}^{\mu\nu}$. The first part contains terms proportional to $|\tilde{G}_M|^2$, $|\tilde{F}_2|^2$ and a cross term $\tilde{G}_M \tilde{F}_2$. The second and third parts contain only interference terms between \tilde{G}_M and \tilde{F}_3 and \tilde{F}_2 and \tilde{F}_3 , respectively. Using (B.10) - (B.13) we

find:

$$\begin{aligned}
W_{M2}^{\mu\nu} = & 2|\tilde{G}_M|^2[p^\mu p'^\nu + p^\nu p'^\mu + (M^2 - p \cdot p')g^{\mu\nu}] + \frac{1}{2} \frac{|\tilde{G}_E - \tilde{G}_M|^2}{(1+\tau)^2 M^2} (p^\mu + p'^\mu)(p^\nu + p'^\nu)(M^2 + p \cdot p') \\
& + \frac{1}{(1+\tau)} [\tilde{G}_M(\tilde{G}_E^* - \tilde{G}_M^*) + \tilde{G}_M^*(\tilde{G}_E - \tilde{G}_M)] (p^\mu + p'^\mu)(p^\nu + p'^\nu)
\end{aligned} \tag{B.33}$$

The use of

$$|\tilde{G}_E - \tilde{G}_M|^2 = |\tilde{G}_E|^2 + |\tilde{G}_M|^2 - (\tilde{G}_E^* \tilde{G}_M + \tilde{G}_E \tilde{G}_M^*) \tag{B.34}$$

$$M^2 + p \cdot p' = 2M^2 + \frac{Q^2}{2} = 2M^2 \left(1 + \frac{Q^2}{4M^2}\right) = 2M^2(1 + \tau) \tag{B.35}$$

gives:

$$W_{M2}^{\mu\nu} = 2|\tilde{G}_M|^2[p^\mu p'^\nu + p^\nu p'^\mu + (M^2 - p \cdot p')g^{\mu\nu}] + \frac{|\tilde{G}_E|^2 - |\tilde{G}_M|^2}{(1+\tau)} (p^\mu + p'^\mu)(p^\nu + p'^\nu) \tag{B.36}$$

The contraction of $L_{\mu\nu}$ and $W_{M2}^{\mu\nu}$ is equal to:

$$\begin{aligned}
L_{\mu\nu} W_{M2}^{\mu\nu} = & 2(k_\mu k'_\nu + k_\nu k'_\mu - (k \cdot k')g_{\mu\nu}) \times \left[2|\tilde{G}_M|^2[p^\mu p'^\nu + p^\nu p'^\mu + (M^2 - p \cdot p')g^{\mu\nu}] \right. \\
& \left. + \frac{|\tilde{G}_E|^2 - |\tilde{G}_M|^2}{(1+\tau)} (p^\mu + p'^\mu)(p^\nu + p'^\nu) \right] \\
= & 4|\tilde{G}_M|^2 \left[2((k \cdot p)(k' \cdot p') + (p \cdot k')(p' \cdot k)) - 2(k \cdot k')(p \cdot p') - 4M^2(k \cdot k') \right. \\
& \left. + 4(k \cdot k')(p \cdot p') + 2M^2(k \cdot k') - 2(k \cdot k')(p \cdot p') \right] \\
& + 2 \frac{|\tilde{G}_E|^2 - |\tilde{G}_M|^2}{(1+\tau)} \left[2k \cdot (p' + p)k' \cdot (p' + p) - k \cdot k'(p + p')^2 \right] \\
= & 8|\tilde{G}_M|^2 \left[(k \cdot p)(k' \cdot p') + (p \cdot k')(p' \cdot k) - M^2 k \cdot k' \right] \\
& + 4 \frac{|\tilde{G}_E|^2 - |\tilde{G}_M|^2}{(1+\tau)} \left[k \cdot (p' + p)k' \cdot (p' + p) - k \cdot k'(M^2 + p \cdot p') \right]
\end{aligned} \tag{B.37}$$

The contraction of $L_{\mu\nu}$ and $W_{M3}^{\mu\nu}$ is equal to:

$$\begin{aligned}
L_{\mu\nu}W_{M3}^{\mu\nu} &= (k_\mu k'_\nu + k_\nu k'_\mu - (k \cdot k')g_{\mu\nu}) \times \left[\frac{\tilde{G}_M \tilde{F}_3^*}{M^2} [p^\mu (k \cdot p' + k' \cdot p') + p'^\mu (k \cdot p + k' \cdot p)] \right. \\
&\quad \left. + (M^2 - p \cdot p')(k^\mu + k'^\mu)(p^\nu + p'^\nu) \right] + \tilde{G}_M^* \tilde{F}_3 \text{same}(\mu \rightarrow \nu) \\
&= \frac{\tilde{G}_M \tilde{F}_3^* + \tilde{G}_M^* \tilde{F}_3}{M^2} \left[[(k \cdot p)k' \cdot (p + p') + k \cdot p + p'(k' \cdot p) - (k \cdot k')p \cdot (p + p')][k \cdot p' + k' \cdot p] \right. \\
&\quad \left. + [k \cdot p'k' \cdot (p + p') + k \cdot (p + p')k' \cdot p' - (k \cdot k')p' \cdot (p + p')][k \cdot p' + k' \cdot p] \right. \\
&\quad \left. + \underbrace{[k \cdot (k + k')k' \cdot (p + p') + k \cdot (p + p')k' \cdot (k + k') - (k \cdot k')(p + p') \cdot (k + k')]}_{=0} [M^2 - p \cdot p'] \right] \quad (\text{B.38})
\end{aligned}$$

The contraction of $L_{\mu\nu}$ and $W_{23}^{\mu\nu}$ is equal to:

$$\begin{aligned}
L_{\mu\nu}W_{23}^{\mu\nu} &= -(k_\mu k'_\nu + k_\nu k'_\mu - (k \cdot k')g_{\mu\nu}) \frac{\tilde{F}_2 \tilde{F}_3^* + \tilde{F}_2^* \tilde{F}_3}{2M^2} (k' + k) \cdot (p + p')(p^\mu + p'^\mu)(p^\nu + p'^\nu) \\
&= -\frac{\tilde{F}_2 \tilde{F}_3^* + \tilde{F}_2^* \tilde{F}_3}{M^2} \underbrace{(k' + k) \cdot (p + p')}_{4\nu} [k \cdot (p + p')k' \cdot (p + p') - k \cdot k'(M^2 + p \cdot p')] \\
&= -4\nu \frac{\tilde{F}_2 \tilde{F}_3^* + \tilde{F}_2^* \tilde{F}_3}{M^2} [k \cdot (p + p')k' \cdot (p + p') - k \cdot k'(M^2 + p \cdot p')] \quad (\text{B.39})
\end{aligned}$$

Using the relations (B.22) - (B.25) we find:

$$\begin{aligned}
L_{\mu\nu}W_{M2}^{\mu\nu} &= 8|\tilde{G}_M|^2 \left[M^2 E_e^2 + \left(M E_e - \frac{Q^2}{2} \right)^2 - \frac{M^2 Q^2}{2} \right] \\
&\quad + 4 \frac{|\tilde{G}_E|^2 - |\tilde{G}_M|^2}{(1 + \tau)} \left[\left(2 M E_e - \frac{Q^2}{2} \right)^2 - Q^2 M^2 (1 + \tau) \right] \\
&= 8 \left\{ |\tilde{G}_M|^2 \left[2 M^2 E_e^2 - Q^2 M E_e - \frac{M^2 Q^2}{2} + Q^2 M^2 \tau \right] \right. \\
&\quad \left. + \frac{|\tilde{G}_E|^2 - |\tilde{G}_M|^2}{(1 + \tau)} \left[2 M^2 E_e^2 - Q^2 M E_e - \frac{M^2 Q^2}{2} \right] \right\} \\
&= 8 M^2 \left[|\tilde{G}_M|^2 Q^2 \tau + \frac{|\tilde{G}_E|^2 + \tau |\tilde{G}_M|^2}{(1 + \tau)} \left(2 E_e^2 - \frac{Q^2 E_e}{M} - \frac{Q^2}{2} \right) \right] \quad (\text{B.40})
\end{aligned}$$

$$\begin{aligned}
L_{\mu\nu}W_{M3}^{\mu\nu} &= \frac{\tilde{G}_M\tilde{F}_3^* + \tilde{G}_M^*\tilde{F}_3}{M^2} \left[\left(2ME_e - \frac{Q^2}{2}\right) ME_e \left(2ME_e - \frac{Q^2}{2}\right) + \left(ME_e - \frac{Q^2}{2}\right) \right. \\
&\quad \left. \times \left(2E_e - \frac{Q^2}{2}\right)^2 - Q^2 \left(2ME_e - \frac{Q^2}{2}\right) \left(2M^2 + \frac{Q^2}{2}\right) \right] \\
&= \frac{\tilde{G}_M\tilde{F}_3^* + \tilde{G}_M^*\tilde{F}_3}{M^2} \left(2ME_e - \frac{Q^2}{2}\right) \left[2 \left(2ME_e - \frac{Q^2}{2}\right)^2 - Q^2 \left(2M^2 + \frac{Q^2}{2}\right) \right] \\
&= 4 (\tilde{G}_M\tilde{F}_3^* + \tilde{G}_M^*\tilde{F}_3) \left(2ME_e - \frac{Q^2}{2}\right) \left(2E_e^2 - \frac{Q^2E_e}{M} - \frac{Q^2}{2}\right) \\
&= 8\nu (\tilde{G}_M\tilde{F}_3^* + \tilde{G}_M^*\tilde{F}_3) \left(2E_e^2 - \frac{Q^2E_e}{M} - \frac{Q^2}{2}\right) \tag{B.41}
\end{aligned}$$

The last term between brackets in (B.37) is the same as the term between brackets in (B.39). So we can directly rewrite the contraction of $L_{\mu\nu}$ and $W_{23}^{\mu\nu}$:

$$L_{\mu\nu}W_{23}^{\mu\nu} = -8\nu (\tilde{F}_2\tilde{F}_3^* + \tilde{F}_2^*\tilde{F}_3) \left(2E_e^2 - \frac{Q^2E_e}{M} - \frac{Q^2}{2}\right) \tag{B.42}$$

From (B.30) and (B.32) it follows:

$$2E_e^2 = \frac{Q^2}{2\sin^2\frac{\theta}{2}} \left(1 + \frac{2E_e}{M} \sin^2\frac{\theta}{2}\right) \implies 2E_e^2 - \frac{Q^2E_e}{M} - \frac{Q^2}{2} = \frac{Q^2}{2} \cot^2\frac{\theta}{2} \tag{B.43}$$

Futhermore:

$$\begin{aligned}
\tilde{F}_2\tilde{F}_3^* + \tilde{F}_2^*\tilde{F}_3 &= -((\tilde{G}_E - \tilde{G}_M)\tilde{F}_3^* + (\tilde{G}_E^* - \tilde{G}_M^*)\tilde{F}_3) \frac{1}{1+\tau} \\
&= -((G_E + \delta\tilde{G}_E - G_M - \delta\tilde{G}_M)\tilde{F}_3^* + (G_E + \delta\tilde{G}_E^* - G_M - \delta\tilde{G}_M^*)\tilde{F}_3) \frac{1}{1+\tau} \\
&= -2\frac{G_E - G_M}{1+\tau} \mathfrak{R}(\tilde{F}_3) \tag{B.44}
\end{aligned}$$

$$\begin{aligned}\tilde{G}_M \tilde{F}_3^* + \tilde{G}_M^* \tilde{F}_3 &= (G_M + \delta \tilde{G}_M) \tilde{F}_3^* + (G_M + \delta \tilde{G}_M^*) \tilde{F}_3 \\ &= 2G_M \Re(\tilde{F}_3)\end{aligned}\tag{B.45}$$

$$|\tilde{G}_E|^2 = G_E^2 + 2G_E \Re(\delta \tilde{G}_E)\tag{B.46}$$

$$|\tilde{G}_M|^2 = G_M^2 + 2G_M \Re(\delta \tilde{G}_M)\tag{B.47}$$

Where \Re stands for the real part

The total contraction of $L_{\mu\nu}$ and $W^{\mu\nu}$ is then:

$$\begin{aligned}L_{\mu\nu} W^{\mu\nu} &= 8M^2 Q^2 \cot^2 \frac{\theta_e}{2} \left[\frac{G_E^2 + 2G_E \Re(\delta \tilde{G}_E) + \tau(G_M^2 + 2G_M \Re(\delta \tilde{G}_M))}{2(1 + \tau)} \right. \\ &\quad \left. + \tau \tan^2 \frac{\theta_e}{2} (G_M^2 + 2G_M \Re(\delta \tilde{G}_M)) + \frac{\nu}{M^2} \Re(\tilde{F}_3) \left(G_M - \frac{G_E - G_M}{1 + \tau} \right) \right]\end{aligned}\tag{B.48}$$

B.5 Unpolarized cross Section

We can show that the differential cross section for the reaction is:

$$\frac{d\sigma}{d\Omega_e} = \frac{|\bar{T}|^2}{64\pi^2 M^2} \left(\frac{E'_e}{E_e} \right)^2 = \frac{L_{\mu\nu} W^{\mu\nu}}{64\pi^2 M^2} \left(\frac{e}{Q} \right)^4 \left(\frac{E'_e}{E_e} \right)^2\tag{B.49}$$

Using (B.30) and $e^4 = (4\pi\alpha)^2$ we obtain:

$$\begin{aligned}\frac{d\sigma}{d\Omega_e} &= \underbrace{\frac{\alpha^2}{4E_e^2 \sin^4 \frac{\theta_e}{2}} \frac{E'_2}{E_e} \cos^2 \frac{\theta_e}{2}}_{\sigma_{Mott}} \left[\frac{G_E^2 + 2G_E \Re(\delta \tilde{G}_E) + \tau(G_M^2 + 2G_M \Re(\delta \tilde{G}_M))}{(1 + \tau)} \right. \\ &\quad \left. + 2\tau \tan^2 \frac{\theta_e}{2} (G_M^2 + 2G_M \Re(\delta \tilde{G}_M)) + \frac{2\nu}{M^2} \Re(\tilde{F}_3) \left(G_M - \frac{G_E - G_M}{1 + \tau} \right) \right]\end{aligned}\tag{B.50}$$

With $\epsilon = \left(1 + 2(1 + \tau) \tan^2 \frac{\theta_e}{2}\right)^{-1}$, (B.50) becomes:

$$\begin{aligned}
\frac{d\sigma}{d\Omega_e} &= \sigma_{Mott} \frac{\tau}{\epsilon(1+\tau)} \left[(G_E^2 + 2G_E \Re(\delta\tilde{G}_E)) \frac{\epsilon}{\tau} + \tau(G_M^2 + 2G_M \Re(\delta\tilde{G}_M)) \right. \\
&\quad \left. + \frac{\epsilon(1+\tau)}{\tau} \frac{2\nu}{M^2} \Re(\tilde{F}_3) \left(G_M - \frac{G_E - G_M}{1+\tau} \right) \right] \\
&= \sigma_{Mott} \frac{\tau}{\epsilon(1+\tau)} \left[(G_E^2 + 2G_E \Re(\delta\tilde{G}_E)) \frac{\epsilon}{\tau} + \tau(G_M^2 + 2G_M \Re(\delta\tilde{G}_M)) \right. \\
&\quad \left. + 2 \frac{\nu\epsilon}{\tau M^2} (G_E \Re(\tilde{F}_3) - G_M \Re(\tilde{F}_3) + (1+\tau)G_M \Re(\tilde{F}_3)) \right] \\
&= \sigma_{Mott} \frac{\tau}{\epsilon(1+\tau)} \left[G_M^2 + \frac{\epsilon}{\tau} G_E^2 + 2G_M \Re\left(\delta\tilde{G}_M + \frac{\nu\epsilon}{M^2} \tilde{F}_3\right) \right. \\
&\quad \left. + 2 \frac{\epsilon}{\tau} G_E \Re\left(\delta\tilde{G}_E + \frac{\nu}{M^2} \tilde{F}_3\right) \right] \tag{B.51}
\end{aligned}$$

The reduced unpolarized cross section including the two-photon exchange correction is then:

$$\sigma_r = G_M^2 + \frac{\epsilon}{\tau} G_E^2 + 2G_M \Re\left(\delta\tilde{G}_M + \frac{\nu\epsilon}{M^2} \tilde{F}_3\right) + 2 \frac{\epsilon}{\tau} G_E \Re\left(\delta\tilde{G}_E + \frac{\nu}{M^2} \tilde{F}_3\right) \tag{B.52}$$

Appendix C

FPP Scattering Quantities

Reconstruction

In this appendix, we will derive the expressions for the scattering quantities in the FPP: the polar scattering angle ϑ_{FPP} , the azimuthal scattering angle φ_{FPP} , the distance of closest approach s_{close} between the incoming and outgoing track, and the z-coordinate of the point of closest approach z_{close} .

C.1 Tracks Equations

Giving two tracks in the space \mathcal{D}_1 and \mathcal{D}_2 , two points P_1 at $z = z_1$ and P_2 at $z = z_2$ belonging to \mathcal{D}_1 and \mathcal{D}_2 respectively, have for coordinates:

$$P_1 : \begin{pmatrix} m_x^1 z_1 + x_1 \\ m_y^1 z_1 + y_1 \\ z_1 \end{pmatrix}, \quad P_2 : \begin{pmatrix} m_x^2 z_2 + x_2 \\ m_y^2 z_2 + y_2 \\ z_2 \end{pmatrix}$$

with $m_x^{1,2} \equiv \frac{dx^{1,2}}{dz}$ and $m_y^{1,2} \equiv \frac{dy^{1,2}}{dz}$ the slope in x and y of the tracks \mathcal{D}_1 and \mathcal{D}_2 respectively.

The unit vectors of \mathcal{D}_1 and \mathcal{D}_2 are given by:

$$\hat{u}_1 : \frac{1}{N_1} \begin{pmatrix} m_x^1 \\ m_y^1 \\ 1 \end{pmatrix}, \quad \hat{u}_2 : \frac{1}{N_2} \begin{pmatrix} m_x^2 \\ m_y^2 \\ 1 \end{pmatrix}$$

with N_1 and N_2 the normalization factors:

$$\begin{cases} N_1 = \sqrt{(m_x^1)^2 + (m_y^1)^2 + 1} \\ N_2 = \sqrt{(m_x^2)^2 + (m_y^2)^2 + 1} \end{cases}$$

C.2 z-coordinate z_{close} of the point of closest approach

If the distance between P_1 and P_2 is the distance of closest approach, the vector $\overrightarrow{P_1P_2}$ and the unit vectors \hat{u}_1 and \hat{u}_2 must satisfy the relations:

$$\begin{cases} \hat{u}_1 \cdot \overrightarrow{P_1P_2} = 0 \\ \hat{u}_2 \cdot \overrightarrow{P_1P_2} = 0 \end{cases}$$

which is equivalent to:

$$\begin{cases} \frac{m_x^1}{N_1}(m_x^1 z_1 + m_x^2 z_2 + x_1 - x_2) + \frac{m_y^1}{N_1}(m_y^1 z_1 + m_y^2 z_2 + y_1 - y_2) + \frac{1}{N_1}(z_1 - z_2) = 0 \\ \frac{m_x^2}{N_2}(m_x^1 z_1 + m_x^2 z_2 + x_1 - x_2) + \frac{m_y^2}{N_2}(m_y^1 z_1 + m_y^2 z_2 + y_1 - y_2) + \frac{1}{N_2}(z_1 - z_2) = 0 \end{cases}$$

Solving for z_1 and z_2 we obtain:

$$z_1 = \frac{(x_1 - x_2) \left[m_x^1(1 + (m_y^2)^2) - m_x^2(1 + m_y^1 m_y^2) \right] + (y_1 - y_2) \left[m_y^1(1 + (m_x^2)^2) - m_y^2(1 + m_x^1 m_x^2) \right]}{2(1 + m_x^1 m_x^2 + m_y^1 m_y^2) - N_1^2 - N_2^2 - (m_x^1 m_y^2 - m_y^1 m_x^2)^2}$$

$$z_2 = \frac{(x_1 - x_2) \left[m_x^1(1 + m_y^1 m_y^2) - m_x^2(1 + (m_y^1)^2) \right] + (y_1 - y_2) \left[m_y^1(1 + m_x^1 m_x^2) - m_y^2(1 + (m_x^2)^2) \right]}{2(1 + m_x^1 m_x^2 + m_y^1 m_y^2) - N_1^2 - N_2^2 - (m_x^1 m_y^2 - m_y^1 m_x^2)^2}$$

The z-coordinate z_{close} of the point of closest approach is then given by:

$$z_{close} = \frac{z_1 - z_2}{2} \quad (C.1)$$

C.3 Distance of closest approach s_{close}

The distance of closest approach is equal to the magnitude of $\overrightarrow{P_1 P_2}$:

$$s_{close} \equiv \|\overrightarrow{P_1 P_2}\| = \sqrt{(x_1 - x_2)^2 + (y_1 - y_2)^2 + (z_1 - z_2)^2} \quad (C.2)$$

C.4 Polar scattering angle ϑ_{FPP}

The polar scattering angle between \mathcal{D}_1 and \mathcal{D}_2 is simply related to the dot product of the unit vector of the incident and scattered tracks:

$$\vartheta_{FPP} = \arccos(\hat{u}_1 \cdot \hat{u}_2) \quad (C.3)$$

C.5 Azimuthal scattering angle φ_{FPP}

To calculate the azimuthal angle between the incident and scattered tracks, we rotate both tracks so that the incident track is the new z-axis. We previously defined the unit vector of the incident and scattered track to be \hat{u}_1 and \hat{u}_2 respectively. Let \hat{v}_1 and \hat{v}_2 be the unit vectors of the rotated incident and scattered track respectively so that: $\hat{v}_{1,2} = \mathbf{M}\hat{u}_{1,2}$ with \mathbf{M} the rotation matrix given

by:

$$\mathbf{M} = \begin{pmatrix} \cos \alpha & -\sin \alpha \sin \beta & -\sin \alpha \cos \beta \\ 0 & \cos \beta & -\sin \beta \\ \sin \alpha & \cos \alpha \sin \beta & \cos \alpha \cos \beta \end{pmatrix}$$

with $m_x^1 = \frac{\tan \alpha}{\cos \beta}$ and $m_y^1 = \tan \beta$ The azimuthal scattering angle φ_{FPP} is then given by:

$$\varphi_{FPP} = \frac{\hat{v}_2^y}{\hat{v}_2^x} = \frac{\cos \beta \hat{u}_2^y - \sin \beta \hat{u}_2^z}{\cos \alpha \hat{u}_2^x - \sin \alpha \sin \beta \hat{u}_2^y - \sin \alpha \cos \beta \hat{u}_2^z} \quad (\text{C.4})$$

C.6 Cone-test

A rectangular detector such as the FPP drift chambers will induce false asymmetries in the azimuthal angle. In order to suppress this effect a cone-test is applied. It requires that the full ellipse described by the intersection of the scattering cone and the plane of detection, lies within the chamber's acceptance.

Mathematically, this is derived as follows: the slopes m_x and m_y in x and y respectively of the incident track, the scattering angle ϑ and the z-coordinate of the point of closest approach z_{close} of the scattered track are known. The intersection between the scattering cone (with an opening angle equal to 2ϑ) and the plane of detection is an ellipse for non perpendicular tracks or a circle otherwise. For this ellipse to lie within the chamber acceptance, the distances $X_1 = x_{close} + x_1$ and $X_2 = x_{close} + x_2$ (see figure) need to be contained in the chamber active area. The coordinates of the interaction vertex M are $(x_{close} = x_{fp} + x'_{fp} z_{close}, y_{close} = y_{fp} + y'_{fp} z_{close}, z_{close})$. Figure C.1 only shows a cut in the x direction, a similar derivation can be done in the y direction leading to the distances Y_1 and Y_2 . According to the figure, with $m_x = \tan \varphi$:

$$\begin{aligned}
X_1 &= x_{close} + Z (\tan \varphi - \tan (\varphi - \vartheta)) \\
&= x_{close} + Z \left(\tan \varphi - \frac{\tan \varphi - \tan \vartheta}{1 + \tan \varphi \tan \vartheta} \right) \\
&= x_{close} + Z \left(m_x - \frac{m_x - \tan \vartheta}{1 + m_x \tan \vartheta} \right)
\end{aligned}$$

$$\begin{aligned}
X_2 &= x_{close} + Z (\tan (\varphi + \vartheta) - \tan \varphi) \\
&= x_{close} + Z \left(\frac{\tan \varphi + \tan \vartheta}{1 - \tan \varphi \tan \vartheta} - \tan \varphi \right) \\
&= x_{close} + Z \left(\frac{m_x + \tan \vartheta}{1 - m_x \tan \vartheta} - m_x \right)
\end{aligned}$$

Similarly in the y-direction:

$$Y_1 = y_{close} + Z \left(m_y - \frac{m_y - \tan \vartheta}{1 + m_y \tan \vartheta} \right)$$

$$Y_2 = y_{close} + Z \left(\frac{m_y + \tan \vartheta}{1 - m_y \tan \vartheta} - m_y \right)$$

with $z = z_{plane} - z_{close}$ the distance between the interaction vertex and the last plane of the drift chamber considered. A track will pass the cone-test if the following conditions are satisfied:

$$X_1 \leq x_{center} + \frac{D_x}{2} \tag{C.5}$$

$$X_1 \geq x_{center} - \frac{D_x}{2} \tag{C.6}$$

$$Y_1 \leq y_{center} + \frac{D_y}{2} \tag{C.7}$$

$$Y_1 \geq y_{center} - \frac{D_y}{2} \tag{C.8}$$

with the (x_{center}, y_{center}) the coordinates of the center of the FPP drift chamber

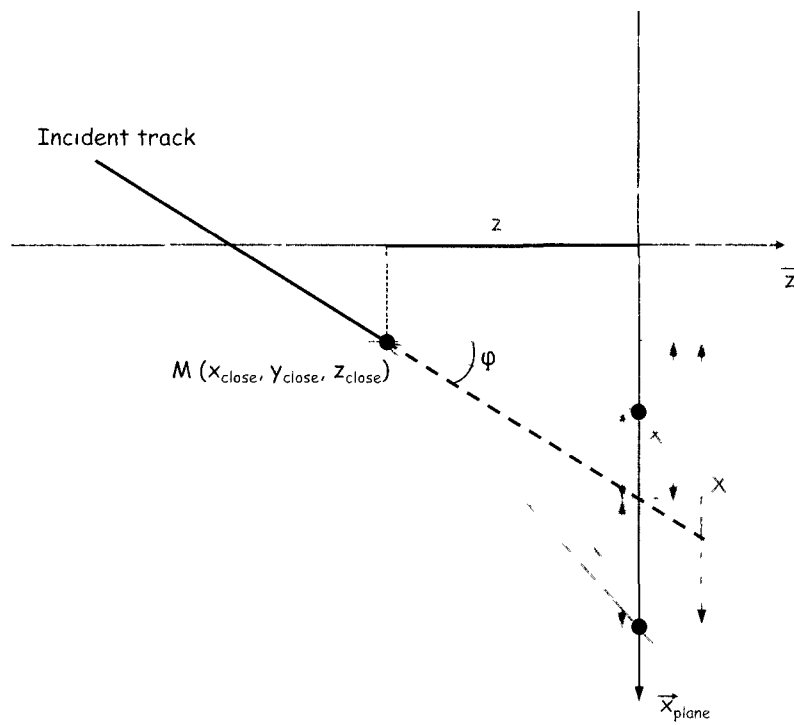


Figure C.1: Diagram showing the cone-test in the FPP.

Bibliography

- [1] O. Stern, "Magnetic Moment of the Proton," *Nature*, vol. 132, p. 169, 1933.
- [2] R. Hofstadter, "Electron Scattering and Nuclear Structure," *Rev. Mod. Phys.*, vol. 28, no. 3, p. 214, 1956.
- [3] M. N. Rosenbluth, "High Energy Elastic Scattering of Electrons on Protons," *Phys. Rev.*, vol. 79, no. 4, p. 615, 1950.
- [4] A. Andivahis *et al.*, "Measurements of the electric and magnetic form factors of the proton from $Q^2=1.75$ to 8.83 $(\text{GeV}/c)^2$," *Phys. Rev. D*, vol. 50, pp. 5491–5517, Nov 1994.
- [5] M. E. Christy *et al.*, "Measurements of electron-proton elastic cross sections for $0.4 < Q^2 < 5.5(\text{GeV}/c)^2$," *Phys. Rev. C*, vol. 70, p. 015206, Jul 2004.
- [6] I. A. Qattan *et al.*, "Precision Rosenbluth Measurement of the Proton Elastic Form Factors," *Phys. Rev. Lett.*, vol. 94, p. 142301, Apr 2005.
- [7] M. Jones *et al.*, " G_{Ep}/G_{Mp} Ratio by Polarization Transfer in $\bar{e}p \rightarrow e\bar{p}$," *Phys. Rev. Lett.*, vol. 84, pp. 1398–1402, Feb 2000.
- [8] V. Punjabi *et al.*, "Proton elastic form factor ratios to $Q^2 = 3.5 \text{ GeV}^2$ by polarization transfer," *Phys. Rev. C*, vol. 71, p. 055202, May 2005.
- [9] O. Gayou *et al.*, "Measurement of G_{Ep}/G_{Mp} in $\bar{e}p \rightarrow e\bar{p}$ to $Q^2 = 5.6\text{GeV}^2$," *Phys. Rev. Lett.*, vol. 88, p. 092301, Feb 2002.

- [10] A. J. R. Puckett *et al.*, "Recoil polarization measurements of the proton electromagnetic form factor ratio to $Q^2 = 8.5 \text{ GeV}^2$," *Phys. Rev. Lett.*, vol. 104, p. 242301, 2010.
- [11] C. Perdrisat, V. Punjabi, and M. Vanderhaeghen, "Nucleon electromagnetic form factors," *Prog. Part. Nucl. Phys.*, vol. 59, p. 694, 2007.
- [12] R. C. Walker *et al.*, "Measurements of the proton elastic form factors for $1 \leq Q^2 \leq 3 (\text{GeV}/c)^2$ at SLAC," *Phys. Rev. D*, vol. 49, pp. 5671–5689, Jun 1994.
- [13] L. W. Mo and Y. S. Tsai, "Radiative Corrections to Elastic and Inelastic ep and μp Scattering," *Rev. Mod. Phys.*, vol. 41, pp. 205–235, Jan 1969.
- [14] A. Afanasev, I. Akushevich, and N. Merenkov, "Model independent radiative corrections in processes of polarized electron-nucleon elastic scattering," *Phys. Rev. D*, vol. 64, p. 113009, Nov 2001.
- [15] C. Amsler *et al.*, "Review of particle physics," *Physics Letters B*, vol. 667, no. 1-5, pp. 1 – 6, 2008. Review of Particle Physics.
- [16] M. L. Goldberger, Y. Nambu, and R. Oehme, "Dispersion Relations for Nucleon-Nucleon Scattering," *Annals of Physics*, vol. 2, pp. 226 – 282, 1957.
- [17] P. A. M. Guichon and M. Vanderhaeghen, "How to Reconcile the Rosenbluth and the Polarization Transfer Methods in the Measurement of the Proton Form Factors," *Phys. Rev. Lett.*, vol. 91, p. 142303, Oct 2003.
- [18] A. I. Akhiezer and M. P. Rekalo, "Polarization effects in the scattering of leptons by hadrons," *Sov. J. Part. Nucl.*, vol. 3, p. 277, 1974.
- [19] R. G. Arnold, C. E. Carlson, and F. Gross, "Polarization transfer in elastic electron scattering from nucleons and deuterons," *Phys. Rev. C*, vol. 23, no. 1, p. 363, 1981.
- [20] A. De Rujula, J. M. Kaplan, and E. de Rafael, "Elastic scattering of electrons from polarized protons and inelastic electron scattering experiments," *Nuc. Phys. B*, vol. 35, pp. 365–389, Dec 1971.

- [21] M. Gorchtein, P. A. M. Guichon, and M. Vanderhaeghen, "Beam Normal Spin Asymmetry in Elastic Lepton-Nucleon Scattering," *Nuclear Physics A*, vol. 741, pp. 234 – 248, 2004.
- [22] Y.-C. Chen, A. Afanasev, S. J. Brodsky, C. E. Carlson, and M. Vanderhaeghen, "Partonic Calculation of the Two-Photon Exchange Contribution to Elastic Electron-Proton Scattering at Large Momentum Transfer," *Phys. Rev. Lett.*, vol. 93, p. 122301, Sep 2004.
- [23] A. V. Afanasev, S. J. Brodsky, C. E. Carlson, Y.-C. Chen, and M. Vanderhaeghen, "Two-photon exchange contribution to elastic electron-nucleon scattering at large momentum transfer," *Phys. Rev. D*, vol. 72, p. 013008, Jul 2005.
- [24] G. Grammer and D. R. Yennie, "Improved Treatment for the Infrared-Divergence Problem in Quantum Electrodynamics," *Phys. Rev. D*, vol. 8, pp. 4332–4344, Dec 1973.
- [25] A. O. Barut and C. Fronsdal, "Spin-Orbit Correlations in $\mu - e$ and $e - e$ Scattering," *Phys. Rev.*, vol. 120, pp. 1871–1874, Dec 1960.
- [26] J. Brodsky and J. R. Primack, "The electromagnetic interactions of composite systems," *Annals of Physics*, vol. 52, pp. 315–365, Apr 1969.
- [27] E. J. Brash, A. Kozlov, S. Li, and G. M. Huber, "New empirical fits to the proton electromagnetic form factors," *Phys. Rev. C*, vol. 65, p. 051001, Apr 2002.
- [28] J. Arrington, "How well do we know the electromagnetic form factors of the proton?," *Phys. Rev. C*, vol. 68, p. 034325, Sep 2003.
- [29] P. G. Blunden, W. Melnitchouk, and J. A. Tjon, "Two-Photon Exchange and Elastic Electron-Proton Scattering," *Phys. Rev. Lett.*, vol. 91, p. 142304, Oct 2003.
- [30] P. G. Blunden, W. Melnitchouk, and J. A. Tjon, "Two-photon exchange in elastic electron-nucleon scattering," *Phys. Rev. C*, vol. 72, p. 034612, Sep 2005.
- [31] L. C. Maximon and J. A. Tjon, "Radiative corrections to electron-proton scattering," *Phys. Rev. C*, vol. 62, p. 054320, Oct 2000.

- [32] G. Passarino and M. Veltman, "One-loop corrections for e^+e^- annihilation into $\mu^+\mu^-$ in the Weinberg model," *Nuclear Physics B*, vol. 160, no. 1, pp. 151 – 207, 1979.
- [33] G. t. Hooft and M. Veltman, "Scalar one-loop integrals," *Nuclear Physics B*, vol. 153, pp. 365 – 401, 1979.
- [34] D. Borisyuk and A. Kobushkin, "Box diagram in the elastic electron-proton scattering," *Phys. Rev. C*, vol. 74, p. 065203, Dec 2006.
- [35] S. Kondratyuk, P. G. Blunden, W. Melnitchouk, and J. A. Tjon, " δ Resonance Contribution to Two-Photon Exchange in Electron-Proton Scattering," *Phys. Rev. Lett.*, vol. 95, p. 172503, Oct 2005.
- [36] D. Borisyuk and A. Kobushkin, "Perturbative QCD predictions for two-photon exchange," *Phys. Rev. D*, vol. 79, p. 034001, Feb 2009.
- [37] V. L. Chernyak, A. A. Ogloblin, and I. Zhitnitsky, "Wave Function of Octet Baryon," *Z. Phys. C*, vol. 42, p. 569, 1989.
- [38] M. Gari and N. G. Stefanis, "Quark distribution amplitudes for the nucleon from perturbative QCD and QCD sum rules," *Phys. Rev. D*, vol. 35, pp. 1074–1077, Feb 1987.
- [39] N. G. Stefanis and M. Bergmann, "Nucleon distribution amplitude: The heterotic solution," *Phys. Rev. D*, vol. 47, pp. R3685–R3689, May 1993.
- [40] D. Borisyuk and A. Kobushkin, "Phenomenological analysis of two-photon exchange effects in proton form factor measurements," *Phys. Rev. C*, vol. 76, p. 022201, Aug 2007.
- [41] V. Tvaskis, J. Arrington, M. E. Christy, R. Ent, C. E. Keppel, Y. Liang, and G. Vittorini, "Experimental constraints on nonlinearities induced by two-photon effects in elastic and inelastic rosenbluth separations," *Phys. Rev. C*, vol. 73, p. 025206, Feb 2006.
- [42] D. Borisyuk and A. Kobushkin, "Two-photon exchange in a dispersion approach," *Phys. Rev. C*, vol. 78, p. 025208, Aug 2008.

- [43] N. Kivel and M. Vanderhaeghen, "Two-Photon Exchange in Elastic Electron-Proton Scattering: A QCD Factorization Approach," *Phys. Rev. Lett.*, vol. 103, p. 092004, Aug 2009.
- [44] V. M. Braun, A. Lenz, and M. Wittmann, "Nucleon form factors in QCD," *Phys. Rev. D*, vol. 73, p. 094019, May 2006.
- [45] M. Göckeler, R. Horsley, T. Kaltenbrunner, Y. Nakamura, D. Pleiter, P. E. L. Rakow, A. Schäfer, G. Schierholz, H. Stüben, N. Warkentin, and J. M. Zanotti, "Nucleon distribution amplitudes from lattice qcd," *Phys. Rev. Lett.*, vol. 101, p. 112002, Sep 2008.
- [46] Y. M. Bystritskiy, E. A. Kuraev, and E. Tomasi-Gustafsson, "Structure function method applied to polarized and unpolarized electron-proton scattering: A solution of the G_{Ep}/G_{Mp} discrepancy," *Phys. Rev. C*, vol. 75, p. 015207, Jan 2007.
- [47] T. Janssens, R. Hofstadter, E. B. Hughes, and M. R. Yearian, "Proton Form Factors from Elastic Electron-Proton Scattering," *Phys. Rev.*, vol. 142, pp. 922–931, Feb 1966.
- [48] D. T. Pierce, R. J. Celotta, G.-C. Wang, W. N. Unertl, A. Galejs, C. E. Kuyatt, and S. R. Mielczarek, "The GaAs spin polarized electron source," *Review of Scientific Instruments*, vol. 51, no. 4, pp. 478–499, 1980.
- [49] L. S. Cardman, "Polarized electron sources for the 1990's," *Nuclear Physics A*, vol. 546, pp. 317–336, 1992.
- [50] C. Yan, R. Carlini, and D. Neuffer, "Beam energy measurement using the ARC beam line as a spectrometer," *Technical Report CEBAF 93-PR-004*, Jun 1993.
- [51] M. Hauger *et al.*, "A high-precision polarimeter," *Nucl. Instrum. Methods A*, vol. 462, p. 382, 2001.
- [52] C. Yan *et al.*, "Target raster system at CEBAF," *Nucl. Instrum. Methods A*, vol. 365, p. 46, 1995.
- [53] D. Meekins, "Hall C target configuration." Unpublished internal report, Nov. 2007.
- [54] H. P. Blok *et al.*, "Charged pion form factor between $Q^2 = 0.60$ and 2.45 GeV^2 . Measurements of the cross section for the $^1h(e, e' \pi^+)n$ reaction," *Phys. Rev. C*, vol. 78, p. 045202, 2008.

- [55] L. S. Azghirey *et al.*, "Measurement of analyzing powers for the reaction $\vec{p} + \text{CH}_2$ at $p_p = 1.75$ - $5.3 \text{ GeV}/c$," *Nucl. Instrum. Methods A*, vol. 538, p. 431, 2005.
- [56] K. A. Assamagan, D. Dutta, and P. Welch, "Hall C matrix element optimization package (CMOP)." Unpublished internal document, May 1997.
- [57] K. Makino and M. Berz, "COSY infinity version 8," *Nucl. Instrum. Methods A*, vol. 427, p. 338, 1999.
- [58] G. Lynch and O. Dahl, "Approximations to multiple coulomb scattering," *Nucl. Instrum. Methods B*, vol. 58, p. 6, 1991.
- [59] A. J. R. Puckett, *Recoil Polarization Measurements of the Proton Form Factor Ratio to High Momentum Transfer*. PhD thesis, Massachusetts Institute of Technology, 2010. Unpublished Ph.D thesis.
- [60] D. Besset, B. Favier, L. Greeniaus, R. Hess, C. Lechanoine, D. Rapin, and D. Werren, "A set of efficient estimators for polarization measurements," *Nucl. Instrum. Methods*, vol. 166, p. 515, 1979.
- [61] O. Gayou, *Measurements of the Proton Form Factor Ratio $\mu_p G_E^p / G_M^p$ up to $Q^2 = 5.6 \text{ GeV}^2$ by Recoil Polarimetry*. PhD thesis, The College of William and Mary, 2002. Unpublished Ph.D thesis.
- [62] L. Pentchev, "Proton Form Factor Measurements Using Polarization Method: Beyond Born Approximation," *AIP Conference Proceedings*, vol. 1056, no. 1, pp. 357-364, 2008.
- [63] J. Guttmann, N. Kivel, M. Meziane, and M. Vanderhaeghen, "First empirical determination of two-photon exchange amplitudes from elastic electron-proton scattering data," *arXiv:1012.0564v2*, 2011.
- [64] M. Meziane *et al.*, "Search for Effects Beyond the Born Approximation in Polarization Transfer Observables in $\vec{e}p$ Elastic Scattering," *Phys. Rev. Lett.*, vol. 106, p. 132501, Mar 2011.
- [65] J. Mar, B. C. Barish, J. Pine, D. H. Coward, H. DeStaebler, J. Litt, A. Minten, R. E. Taylor, and M. Breidenbach, "Comparison of Electron-Proton and Positron-Proton Elastic Scattering

- at Four-Momentum Transfers up to $5.0 (GeV/c)^2$," *Phys. Rev. Lett.*, vol. 21, pp. 482–484, Aug 1968.
- [66] J. Arrington *et al.*, "Two-photon exchange and elastic scattering of electrons/positrons on the proton," *arXiv:nucl-ex/0408020v1*, 2004. Proposal for an experiment at VEPP-3.
- [67] J. Arrington *et al.*, "Beyond the Born approximation: A Precise Comparison of e^+p and e^-p Elastic Scattering in CLAS." A Proposal to PAC31, 2006.
- [68] M. Kohl *et al.*, "The OLYMPUS experiment at DESY," *AIP Conf. Proc.*, vol. 1160, pp. 19–23, 2009.
- [69] S. P. Wells *et al.*, "Measurement of the vector analyzing power in elastic electron-proton scattering as a probe of the double virtual Compton amplitude," *Phys. Rev. C*, vol. 63, p. 064001, May 2001.
- [70] F. E. Maas *et al.*, "Measurement of the Transverse Beam Spin Asymmetry in Elastic Electron-Proton Scattering and the Inelastic Contribution to the Imaginary Part of the Two-Photon Exchange Amplitude," *Phys. Rev. Lett.*, vol. 94, p. 082001, Mar 2005.
- [71] L. H. C. Kaufmann, "Transverse beam asymmetries measured from 4He and hydrogen targets," *Eur. Phys. A*, 2006. Proc. Parity Violation to Hadronic Structure Milos, Greece.
- [72] D. S. Armstrong *et al.*, "Transverse beam spin asymmetries in forward-angle elastic electron-proton scattering," *Phys. Rev. Lett.*, vol. 99, p. 092301, Aug 2007.
- [73] T. Averett *et al.*, "Measurement of the target single-spin asymmetry in year = 2005, quasi-elastic $^3He^{\uparrow}(e, e')$. A Proposal to PAC27." A proposal to PAC27.
- [74] J. Arrington *et al.*, "A measurement of two-photon exchange in unpolarized elastic electron-proton scattering." A proposal to PAC27, 2004.